Measurement of the Strangeness Spectral Function and the Mass of the Strange Quark in Hadronic τ Decays with the OPAL Detector

Dissertation
zur
Erlangung des Doktorgrades (Dr. rer. nat.)
der
Mathematisch-Naturwissenschaftlichen Fakultät
der
Rheinischen Friedrich-Wilhelms-Universität Bonn

vorgelegt von
Wolfgang Franz Mader
aus
Aschaffenburg

Bonn 2004

Angefertigt mit Genehmigung der Mathematisch-Naturwissenschaftlichen Fakultät der
Rheinischen Friedrich-Wilhelms-Universität Bonn

1. Referent: Prof. Dr. N. Wermes
2. Referent: Prof. Dr. E. Hilger
Tag der Promotion: 10. März 2004

Abstract: Tau lepton decays with open strangeness in the final state are measured with the OPAL detector at LEP to determine the strange hadronic spectral function of the τ lepton and the mass of the strange quark. The decays $\tau^- \rightarrow (\mathrm{K}\pi)^-\nu_\tau$, $(\mathrm{K}\pi\pi)^-\nu_\tau$ and $(\mathrm{K}\pi\pi\pi)^-\nu_\tau$ with final states consisting of neutral and charged kaons and pions, have been studied. The invariant mass distribution of 93.4% of these final states have been experimentally determined. Monte Carlo simulations have been used for the remaining 6.6% and for the strange final states including η mesons. The reconstructed strange final states, corrected for resolution effects and detection efficiencies, yield the strange spectral function of the τ lepton. The moments of the spectral function and the ratio of strange to non-strange moments, which are important input parameters for theoretical analyses, are determined. Furthermore, the branching fractions

$$B(\tau^- \rightarrow \mathrm{K}^-\pi^0\nu_\tau) = (0.471 \pm 0.064_{\mathrm{stat}} \pm 0.021_{\mathrm{sys}})\,\%$$
$$B(\tau^- \rightarrow \mathrm{K}^-\pi^+\pi^-\nu_\tau) = (0.415 \pm 0.059_{\mathrm{stat}} \pm 0.031_{\mathrm{sys}})\,\%$$

have been measured. From the CKM weighted difference of strange and non-strange spectral moments, the mass of the strange quark at the τ mass scale has been determined

$$m_\mathrm{s}(m_\tau^2) = (84 \pm 14_{\mathrm{exp}} \pm 6_{V_{\mathrm{us}}} \pm 17_{\mathrm{theo}})\,\mathrm{MeV}.$$

Evolving this result to customary scales yields

$$m_\mathrm{s}(1\,\mathrm{GeV}^2) = (111^{+26}_{-35})\,\mathrm{MeV}$$
$$m_\mathrm{s}(4\,\mathrm{GeV}^2) = (82^{+19}_{-25})\,\mathrm{MeV}.$$

CONTENTS

1. Introduction 9

2. Theoretical Aspects 13
- 2.1 Theory of Hadronic τ Decays 14
- 2.2 Theoretical Analysis of R_τ 16
- 2.3 Operator Product Expansion 19
- 2.4 R_τ and the Spectral Moments 22
- 2.5 Electroweak Corrections 22
- 2.6 $\mathrm{SU(3)_{Flavor}}$ Breaking 23
- 2.7 The Determination of m_s and the Choice of Moments 25

3. The Experiment 27
- 3.1 The LEP Accelerator 27
- 3.2 The OPAL Detector 28
  - 3.2.1 The Central Tracking System 29
  - 3.2.2 The Outer Detector 30
  - 3.2.3 The Luminosity Detector 31
- 3.3 Coordinate System and Track Parameters 31

4. Experimental Aspects 33
- 4.1 Energy Loss Calibration in the τ Environment 33
  - 4.1.1 Energy Loss of Particles in Matter 33
  - 4.1.2 The Energy Loss Measurement in OPAL 35
  - 4.1.3 The Standard OPAL Calibration 36
  - 4.1.4 Energy Loss Measurement in τ Decays 37
  - 4.1.5 Adjustment of the Experimental Errors 45
- 4.2 Photon Reconstruction and Identification of Neutral Pions 49
  - 4.2.1 Description of Electromagnetic Shower 50
  - 4.2.2 Parametrization of the Shower Shape in the Barrel 51
  - 4.2.3 The Find Photon Algorithm 53
  - 4.2.4 Photon Pairing Algorithm 56
  - 4.2.5 Reconstruction of Neutral Pions 59
- 4.3 Identification of Events Containing K^0 62
  - 4.3.1 Selection of K^0_S Candidates 63
  - 4.3.2 Result of the K^0_S Selection 65
- 4.4 The Monte Carlo Simulation 66
  - 4.4.1 Update of the Three Meson Final States 66
  - 4.4.2 Four-Meson Final States 68
  - 4.4.3 Monte Carlo Samples 69

5. The Event Selection 71
- 5.1 The τ Pair Selection 72
- 5.2 Selection of the Signal Channels 76
  - 5.2.1 $\tau^- \rightarrow \mathrm{K}^-\pi^0\nu_\tau$ 76
  - 5.2.2 $\tau^- \rightarrow \mathrm{K}^0\pi^-\nu_\tau$ 77
  - 5.2.3 $\tau^- \rightarrow \mathrm{K}^-\pi^+\pi^-\nu_\tau$ 78
  - 5.2.4 $\tau^- \rightarrow \mathrm{K}^0\pi^-\pi^0\nu_\tau$ 79

    5.2.5 $\tau^- \to \mathrm{K}^-\pi^+\pi^-\pi^0\nu_\tau$ 79
  5.3 Invariant Mass Spectra 80

6. The Mass Correction Procedure 83
  6.1 Introduction 83
  6.2 Matrix Unfolding 85
    6.2.1 Unfolding ‘Ideal’ Distributions 86
    6.2.2 Iteration Procedure 86
    6.2.3 Test with τ Monte Carlo 89
  6.3 Unfolding Data Events 89

7. Results 93
  7.1 Branching Fractions 93
    7.1.1 Systematic Studies for the Branching Fractions Measurement 95
    7.1.2 Improved Averages for $B(\tau^- \to \mathrm{K}^-\pi^0\nu_\tau)$ and $B(\tau^- \to \mathrm{K}^-\pi^+\pi^-\nu_\tau)$ 95
    7.1.3 Discussion 96
  7.2 The Strangeness Spectral Function 97
  7.3 Systematic Uncertainties on the Spectral Function 98
  7.4 R_τ and the Spectral Moments 100
    7.4.1 The Measurement R_τ 100
    7.4.2 Measurement of the Spectral Moments 101
  7.5 Measurement of the Strange Quark Mass m_s 104
    7.5.1 Measurement of m_s at the τ Mass Scale 105
    7.5.2 The Strange Quark Mass at $\mu^2 = 1\,\mathrm{GeV}^2$ and $\mu^2 = 4\,\mathrm{GeV}^2$ 106
    7.5.3 Discussion 109

8. Conclusion 113

9. Appendix 115
  9.1 Branching Fractions used in Monte Carlo Simulation 115
  9.2 Update of the Non-Strange Spectral Moments 117
  9.3 Kinematic Fit 118
  9.4 Updated Parametrizations of the Three Meson Final States 121

1. INTRODUCTION

In 1975, Martin L. Perl and collaborators observed events for which they had ‘no conventional explanation’ at that time [1]. These events had one electron and one muon in the final state, plus missing energy. From event kinematics, the missing energy had to be due to at least two particles, escaping undetected:

$$\mathrm{e}^+\mathrm{e}^- \to \mathrm{e}^\pm + \mu^\mp + \geq 2\,\text{undetected particles.}$$

They concluded that these events, apparently violating lepton number conservation, are ‘the signature for new types of particles or interactions’. All together 24 of these events were recorded until then, using the SLAC-LBL [3] magnetic detector, operated at the Stanford Linear Accelerator Center (SLAC) colliding beam facility SPEAR at center-of-mass energies at or above $\sqrt{s} = 4\,\mathrm{GeV}$.

By that time, the fermionic particle content of the Standard Model consisted of two leptons, the electron and the muon plus the accompanying neutrinos, and three quarks. The up and the down quark, ordinary matter consists of, and the strange quark. A fourth quark, the charm quark, was already predicted, but then not observed. Apart from theoretical considerations, with the fourth quark, once it were found, one could explain e.g. the absence of flavor changing neutral currents or the small branching fraction for the decay of the long lived neutral kaon into a pair of muons. In addition, the symmetry of the Standard Model would be re-established, having an equal number of generations for quarks and leptons. By that time, there was no need and no experimental hint for third generation fermions.

For the events mentioned above, no immediate explanation was found, though several solutions were proposed. The pair production of charged bosons for example, higher order weak interactions or the production of neutral leptons. But either the mass of those particles would be too large to be produced at the energies accessible at that time, or the cross sections predicted for these processes were too small to explain the observed number of events. However, already in the first publication on the ‘anomalous lepton production’, it was suggested that this type of events could be explained, by pair production of new heavy charged leptons. This assumption was finally established one year later in the publication on ‘Properties of the Proposed τ Charged Lepton’ [2] and so the first fermion of the third generation was found. In this paper, various properties of the new lepton were already determined, like its mass and a limit on the mass of the associated neutrino was set. Its leptonic branching fractions, the production cross section and the τ-neutrino coupling were measured. The discovery of the third generation lepton was later confirmed by the experiments PLUTO [4] and DASP [5] at the DORIS storage ring at DESY.

Today, the third generation is established in the lepton sector and in the quark sector. The fermionic content of the Standard Model of particle physics, as we know it today, consists of three generations of charged leptons plus the associated neutrinos ((e, ν_e), (μ, ν_μ) and (τ, ν_τ)) and three generations of quarks ((u, d$'$)[†], (c, s$'$)[†] and (t, b$'$)[†]). Compared to the leptons, they carry in addition a color charge. The left-handed particles are grouped in doublets of weak isospin $T = \frac{1}{2}$, its right-handed partners are singlets with weak isospin $T = 0$. The forces of the electroweak interaction are mediated by bosons of spin one. There are two neutral bosons, the Z^0 and the photon, and two charged bosons, the W^+ and the W^-. The photon couples to all charged particles. The W boson couples only to left-handed particles, the coupling of weak neutral boson Z^0 is proportional to the weak isospin and the electric charge and it therefore interacts with all fermions. The eight gluons, which carry color and anti-color at the same time, mediate the strong force, i.e. they couple to all colored particles. The Standard Model is completed by the spin-zero Higgs boson, which has not yet been discovered. It is responsible for the masses of the elementary particles. The non-zero neutrino masses, which were established by neutrino oscillation experiments are the first hint for physics beyond the Standard Model. In the simplest extension, a right-handed neutrino would be added to the list of elementary particles. They were singlets and therefore would not have any Standard Model interactions.

Important contributions to τ physics in the last years came from the four LEP experiments, the CLEO collaboration and the SLD collaboration at SLC. These experiments have meanwhile stopped data taking.

[†] The weak eigenstates labeled with a prime are mixtures of the mass eigenstates d, s, b.

		FERMIONS (S=1/2)							
		LEPTONS			**QUARKS**				
T_3	Q							Q	T_3
+1/2 −1/2	−1 0	$\begin{pmatrix} \mathrm{e} \\ \nu_\mathrm{e} \end{pmatrix}_L$	$\begin{pmatrix} \mu \\ \nu_\mu \end{pmatrix}_L$	$\begin{pmatrix} \tau \\ \nu_\tau \end{pmatrix}_L$	$\begin{pmatrix} \mathrm{u} \\ \mathrm{d}' \end{pmatrix}_L$	$\begin{pmatrix} \mathrm{c} \\ \mathrm{s}' \end{pmatrix}_L$	$\begin{pmatrix} \mathrm{t} \\ \mathrm{b}' \end{pmatrix}_L$	+2/3 −1/3	0 0
0	−1	e_R	μ_R	τ_R	u_R	c_R	t_R	+2/3	0
					d'_R	s'_R	b'_R	−1/3	0

Tab. 1.1: The Standard Model of particle physics. In the table, the fermionic content is given, which can be divided into leptons and quarks. The left-handed particles are organized in doublets, the right-handed particles are singlets. For the fermions, in addition the electric charge and the third component of the weak isospin is given, which characterize the coupling of the fermions.

In October 1999 the asymmetric b-factories BaBar at PEP-II and Belle at KEKB have started operation. Until the end of 2003, over 300 fb^{-1} of data have been recorded. At these experiments, the analysis of τ data has only just begun and the amount of data will allow for even more stringent tests of the Standard Model or the discovery of possible new phenomena in particle physics.

With its mass of $m_\tau = (1776.99\,^{+0.29}_{-0.26})$ MeV[‡], the τ lepton is the heaviest lepton known to date. In the more than two decades since its discovery, it has provided us with high precision measurements on the percent level, which helped to improve our understanding of particle physics. Due to its high mass, it could be particularly sensitive to new physics beyond the Standard Model and thus the study of τ leptons is also an interesting field for the search for new phenomena. The τ lepton is the only lepton that can decay either leptonically or hadronically. It therefore provides an ideal tool to study the leptonic as well as the hadronic current. In the following, some examples are given.

In leptonic decays, the structure of the leptonic current and the universality of the coupling of leptons to the W boson can be studied. Exploiting the polarization of τ leptons from Z^0 decays, one can determine the leptonic Michel parameters ρ_ℓ, δ_ℓ, ξ_ℓ and η_μ which characterize the nature of the leptonic current. In particular, the parameter η_μ is sensitive to a possible right handed coupling and thus to the mass of the charged Higgs boson, which is predicted in extensions of the Standard Model.

Hadronic τ decays allow for a study of strong interaction effects. This includes studies of the structure of the hadronic current, the determination of resonance parameters and radial excitations and the search for CP violating effects beyond the Standard Model. A comparison of the inclusive hadronic decay rate of the τ lepton with QCD predictions allows the measurement of some fundamental parameters of the theory. The inputs to these studies are the spectral functions that measure the transition probability to create hadrons of invariant mass $m = \sqrt{s}$ in the hadronization process. The energy regime accessible in τ-lepton decays can be divided into two different regions. Non-perturbative QCD effects dominate in the low energy regime with a rich resonance structure. At the kinematic limit at $s = m_\tau^2 = (1.777\,\mathrm{GeV})^2$, perturbative QCD dominates. Thus τ-lepton decays provide an environment where the strong coupling constant α_s can be measured [6–10, 12] without large influence from non-perturbative effects, while the perturbative expansion still converges well. The measurement of the non-strange spectral function of hadronic τ decays [40–42] has provided us with one of the most accurate measurements of α_s, and some very stringent tests of perturbative QCD at relatively low mass scales [22].

The spectral function of τ decays with open strangeness will allow additional and independent tests of QCD and a measurement of the mass of the strange quark [6, 15, 20, 21]. Among the free parameters of the Standard Model, the quark masses are the ones less precisely known. In particular, the comparison of strange and non-strange spectral functions allows to pin down the $\mathrm{SU}(3)_\mathrm{Flavor}$ breaking effects, and thus allows for determination of the mass of the strange quark.

The strange spectral function of the τ lepton is obtained from the invariant mass spectra of hadronic τ decay modes with net strangeness. From an experimental point of view, the key issues of this analysis are the separation of charged kaons and pions in the dense environment of multiprong τ decays via energy loss measurement in the Opal Jet Chamber. Substantial improvements have been achieved compared to previous analyses [43]. In particular, those improvements have made it possible to obtain a reliable $\mathrm{d}E/\mathrm{d}x$ measurement in the environment where three tracks are very close to each other. The reconstruction of π^0 is based on the study of shower profiles in the electromagnetic calorimeter. Furthermore, the identification

---

[‡] $\hbar = c = 1$

and reconstruction of τ decays involving neutral kaons has been achieved with high efficiency and good mass resolution.

For this analysis, data collected with the OPAL detector during the LEP-I period from 1991 to 1995 has been used. Applying the standard τ selection [39], the data sample comprises a total of 162 477 τ candidate events.

This thesis is organized as follows. Chapter 2 gives a short overview over the theoretical framework hadronic τ decays are analyzed in. In Chapter 3, a description of the OPAL detector is given, concentrating on those components that are important for this analysis. Chapter 4 continues with a discussion of the experimental aspects of this work. The Monte Carlo samples used in the analysis and the selection of the strange final states are described in Chapter 4.4 and Chapter 5, respectively. A presentation of the unfolding procedure employed in this thesis is given in Chapter 6. The results are presented in Chapter 7. This includes the measurement of the branching fractions, the strange spectral function and the spectral moments derived from it. From the comparison of strange and non-strange spectral moments, a value for the mass of the strange quark is obtained.

2. THEORETICAL ASPECTS

The τ lepton with its mass of $m_\tau = (1776.99\,^{+0.29}_{-0.26})\,\mathrm{MeV}$ is the only lepton heavy enough to decay into leptons and into hadrons. Of particular interest is the τ hadronic width which is often stated as the ratio R_τ of the partial width of τ lepton decays into hadrons normalized to the partial width of τ lepton decays into electrons

$$R_\tau := \frac{\Gamma(\tau \to \nu_\tau \mathrm{hadrons}(\gamma))}{\Gamma(\tau \to \nu_\tau \mathrm{e}\overline{\nu}_\mathrm{e}(\gamma))}. \tag{2.1}$$

Here, γ represents possible additional photons or lepton pairs. On the one hand, this quantity can be studied experimentally under very clean conditions using τ data from $\mathrm{e}^+\mathrm{e}^-$annihilation. On the other hand, its inclusive character guarantees a precise theoretical calculation using analyticity constraints and the Operator Product Expansions (OPE).

In the naïve parton model, where strong and electroweak radiative corrections are ignored and the masses of all final state particles are neglected, the universality of the W coupling to the fermionic charged currents implies that this ratio should be

$$R_\tau = N_\mathrm{C}(|V_\mathrm{ud}|^2 + |V_\mathrm{us}|^2) \approx 3, \tag{2.2}$$

where N_C is the number of colors of the quarks, $|V_\mathrm{ud}|$ and $|V_\mathrm{us}|$ are the corresponding matrix elements of the weak mixing matrix (CKM matrix). However, if calculated from the measured leptonic widths of the τ lepton

$$R_\tau = \frac{1 - \Gamma(\tau \to \nu_\tau \mathrm{e}\overline{\nu}_\mathrm{e}) - \Gamma(\tau \to \nu_\tau \mu\overline{\nu}_\mu)}{\Gamma(\tau \to \nu_\tau \mathrm{e}\overline{\nu}_\mathrm{e})} = (3.632 \pm 0.016), \tag{2.3}$$

the result obtained is about 20% higher. This is due to perturbative radiative corrections and non-perturbative hadronization effects which are neglected in the naïve approach. The energy scale, defined by the mass of the τ lepton is high enough so that R_τ can predominantly be described by perturbative QCD. However, the scale is low enough to be sensitive to non-perturbative QCD effects without affecting the convergence of the perturbative expansion. This allows for a precise determination of parameters of QCD, like e.g. the strong coupling constant, where the analysis of τ data provides one of the most precise measurements [40].

The quark masses only play a minor role in R_τ. Considering the small mass of the light quarks, their associated corrections are on the percent level. The corrections due to the relatively large mass of the strange quark are suppressed by the Cabbibo factor $|V_\mathrm{us}|$, which reduces its correction to R_τ also to the percent level. But predictions can also be made for the τ decay widths associated with specific quark currents:

$$R_\tau = R_{\tau,\mathrm{non-S}} + R_{\tau,\mathrm{S}} \tag{2.4a}$$

$$= R_{\tau,\mathrm{V}} + R_{\tau,\mathrm{A}} + R_{\tau,\mathrm{S}}. \tag{2.4b}$$

One can separately compute strange and non-strange contributions. The non-strange contributions can be further resolved into vector ($R_{\tau,\mathrm{V}}$) and axial-vector ($R_{\tau,\mathrm{A}}$) parts according to whether there are an even or an odd number of pions in the final state[1]. Strange decays ($R_{\tau,\mathrm{S}}$) are identified by the presence of an odd number of kaons. A further separation into vector and axial-vector parts for strange decay modes would require a detailed analysis of the underlying resonance structure. Due to the limited statistics, this is not within the realms of possibility of this work.

By analyzing separately the semi-inclusive decay width of the τ lepton into modes with and without open strangeness, the relatively large value of m_s induces an important effect. The corresponding $R_{\tau,\mathrm{S}}$ prediction is very sensitive to the strange quark mass and can be used to extract information on this parameter. In the following section a short overview is given on the theoretical framework necessary to determine the mass of the strange quark.

---

[1] Electromagnetic decays and decays involving kaons do not respect this relation. Therefore, this assignment does not work for non-strange channels with two kaons in the final state and for decays involving ω or η mesons

2.1 Theory of Hadronic τ Decays

The influence from QCD in hadronic τ decays becomes manifest in the deviation from the predictions of the naïve parton model where free, massless quarks appear in the final state. By analyzing R_τ, which is defined as the partial decay width of the τ lepton into hadrons normalized to the partial width of τ decays into electrons[2]:

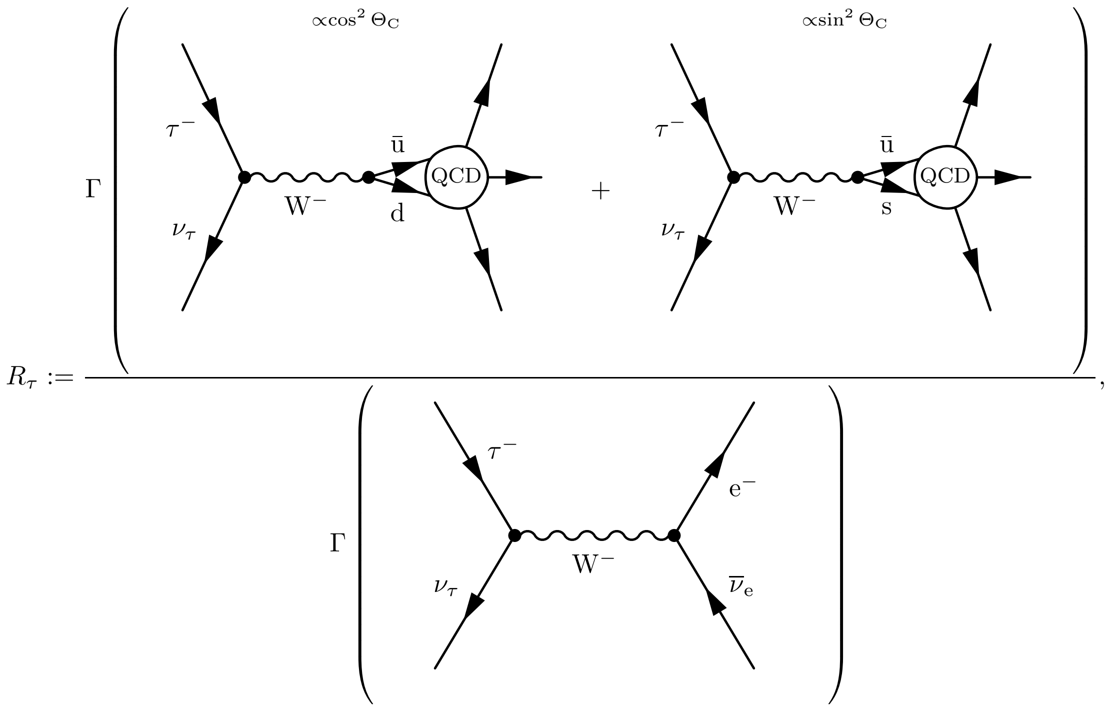

, (2.5)

parameters of the QCD can be determined, like e.g. the strong coupling constant or the mass of the strange quark. There are two contributions to the numerator, the decays into non-strange final states ($\bar{\mathrm{u}}\mathrm{d}$) and decays with open strangeness in the final state ($\bar{\mathrm{u}}\mathrm{s}$), where the partial width is proportional to $\sin^2\Theta_\mathrm{C}$ and $\cos^2\Theta_\mathrm{C}$ for non-strange and strange final states, respectively. The angle Θ_C is the so-called Cabbibo or quark mixing angle, which relates the weak eigenstates to the quark mass eigenstates.

The decay width to electrons in the denominator can be calculated, treating the process as an effective four-fermion contact interaction

$$\Gamma(\tau^- \to \nu_\tau \mathrm{e}^- \overline{\nu}_\mathrm{e}) = \frac{G_\mathrm{F}^2 m_\tau^5}{192\pi^2} \cdot (1+\Delta). \tag{2.6}$$

Here, $G_\mathrm{F} = 1.16639(1) \cdot 10^{-5}\,\mathrm{GeV}^{-2}$ is the Fermi coupling constant. The additional term Δ includes corrections to this lowest order calculation which come from the mass of the final state leptons, QED radiative corrections and corrections due to the W propagator. They are of the order of $\sim 0.5\%$.

The matrix element for τ decays into hadrons

$$\mathcal{M} = \frac{G_\mathrm{F}}{\sqrt{2}} \begin{pmatrix} \sin\Theta_\mathrm{C} \\ \cos\Theta_\mathrm{C} \end{pmatrix} L_\mu H^\mu \tag{2.7}$$

is expressed in terms of the leptonic current

$$L_\mu = \bar{u}\gamma_\mu (g_\mathrm{V} - g_\mathrm{A}\gamma_5) u \tag{2.8}$$

(with $g_\mathrm{V} = g_\mathrm{A} = 1$ in the Standard Model) and the hadronic current

$$H^\mu = \langle \mathrm{h}^- | (J^\mu(0))^\dagger | 0 \rangle = \langle \mathrm{h}^- | V^\mu(0) - A^\mu(0) | 0 \rangle. \tag{2.9}$$

---

[2] In order to simplify the text we refer only to the decays of the negatively charged τ lepton. Simultaneous treatment of the charge conjugate decay is always implied.

The operator $J^{\mu}(x)$ describes the creation of hadronic final states from the vacuum by means of QCD. According to the weak interaction, the hadronic current is decomposed into vector (V^{μ}) and axial-vector (A^{μ}) contribution. The differential τ hadronic width can be expressed in the general Ansatz

$$\mathrm{d}\Gamma_{ij}(\tau^- \to \nu_\tau\,\text{hadrons}^-) = \frac{G_\mathrm{F}}{4m_\tau}|V_{ij}|^2 L_{\mu\nu}H^{\mu\nu}\mathrm{dLips}, \tag{2.10}$$

where $ij \in \{\bar{\mathrm{u}}\mathrm{d},\, \bar{\mathrm{u}}\mathrm{s}\}$ labels the quark flavor involved in the decay. The leptonic (hadronic) tensor is denoted by $L_{\mu\nu}$ ($H^{\mu\nu}$) and dLips is the Lorentz invariant phase space element. Integrating over the phase space except for the integration over the invariant mass of the hadronic system yields the total hadronic width of τ lepton decays into strange and non-strange final states:

$$\begin{aligned}\Gamma(\tau^- \to \nu_\tau\,\text{hadrons}^-) = \frac{G_\mathrm{F}^2 m_\tau^5}{32\pi^2}\int_0^{m_\tau^2}\frac{\mathrm{d}s}{m_\tau^2}\times\\ \times\Bigg(|V_\mathrm{ud}|^2\Big(1-\frac{s}{m_\tau^2}\Big)^2\Big(\Big(1+2\frac{s}{m_\tau^2}\Big)\rho_1^{(0)}+\rho_0^{(0)}\Big)\\ +|V_\mathrm{us}|^2\Big(1-\frac{s}{m_\tau^2}\Big)^2\Big(\Big(1+2\frac{s}{m_\tau^2}\Big)\rho_1^{(1)}+\rho_0^{(1)}\Big)\Bigg).\end{aligned} \tag{2.11}$$

The real functions $\rho_J^{(S)}$ are the spectral functions in strange ($S = 1$) and non-strange ($S = 0$) τ decays. The subscript J denotes the angular momentum in the hadronic rest frame. The spectral functions can be split further into vector (v) and axial-vector (a) parts, referring to the vector and axial-vector part of the weak current

$$\rho_J^{(S)} = v_J^{(S)} + a_J^{(S)}. \tag{2.12}$$

From the experimental point of view, the spectral functions are obtained from the invariant mass spectra of the hadronic final states ($\mathrm{d}N_{V/A}/\mathrm{d}s$), normalized to their respective branching fractions B and divided by the corresponding kinematic factor:

$$\begin{aligned}v_J^{(\mathrm{S})}(s)/a_J^{(\mathrm{S})}(s) = \frac{m_\tau^2}{6|V_{\mathrm{ud/us}}|^2 S_\mathrm{ew}}\left(\left(1-\frac{s}{m_\tau^2}\right)^2\left(1+\frac{2s}{m_\tau^2}\right)^J\right)^{-1}\\ \times\sum_{\tau^-\to\nu_\tau X^-}\frac{B(\tau^-\to\nu_\tau(V/A)^{(S,\,J)})}{B(\tau^-\to\nu_\tau e^-\bar{\nu}_e)}\frac{1}{N_{\mathrm{V/A}}}\frac{\mathrm{d}N_{\mathrm{V/A}}}{\mathrm{d}s},\end{aligned} \tag{2.13}$$

where the sum runs over all final states of a particular spin and strangeness content and S_ew is an electroweak correction factor.

In the non-strange case, the individual contributions to vector and axial-vector spectral functions can be identified by their G parity. It is defined as the eigenvalue of a combination of charge conjugation C and rotation in isospin: $G = C(-1)^I$. The vector (axial-vector) current only couples to states with positive (negative) G parity. Currents which do not obey this rule are called second class currents [62]. They have not yet been found. Since hadronic final states of different G parity also differ in the J^P quantum number, there is no interference between the two states, and the total hadronic width can be written as the linear sum of vector and axial-vector partial widths.

In $\mathrm{e}^+\mathrm{e}^-$ annihilation, the G parity is related to the isospin I of the hadronic final state in the case of non-strange τ decays. Since G parity is a multiplicative quantum number, one obtains isospin $I = 1$ ($I = 0$) for a final state with an even (odd) number of charged or neutral pions in the final state. Therefore, the vector (axial-vector) current only couples to states with positive (negative) G parity and thus to a final state with an even (odd) number of pions.

There is no contribution from scalar final states to the non-strange vector spectral function $v_0^{(0)}$. The conserved vector current (CVC) theorem relates the non-strange part of the vector current to the vector current in $\mathrm{e}^+\mathrm{e}^-$annihilation processes. The contribution from a possible scalar component is proportional to the difference of the masses of the light quarks. This difference is zero to very good approximation. However, this is not the case in strange τ decays. Due to the relatively large mass of the strange quark, contributions to the v_0^1 part of the spectral function exist through the $\mathrm{K}_0^*(1430)$ resonance.

The G parity is not a good quantum number for decay modes involving strange particles. Therefore, a separation into vector and axial-vector parts would require a detailed analysis of the structure of the

Resonance	J^P	Mass/ MeV	Width/ MeV	Decay		Type
				Mode	$B/\%$	
K	0^-	493.677 ± 0.016	-	-	-	pseudoscalar
$\mathrm{K}^*(892)^\pm$	1^-	891.66 ± 0.26	50.8 ± 0.9	$\mathrm{K}\pi$	~ 100	vector
$\mathrm{K}_1(1270)$	1^+	1273 ± 7	90 ± 20	$\mathrm{K}\rho$ $\mathrm{K}_0^*(1430)\pi$ $\mathrm{K}^*(892)\pi$ $\mathrm{K}\omega$	42 ± 6 28 ± 4 16 ± 5 11 ± 2	axial-vector
$\mathrm{K}_1(1400)$	1^+	1402 ± 7	174 ± 13	$\mathrm{K}^*(892)\pi$	94 ± 6	axial-vector
$\mathrm{K}^*(1410)$	1^-	1414 ± 15	232 ± 21	$\mathrm{K}^*(892)\pi$	> 40	vector
$\mathrm{K}_0^*(1430)$	0^+	1412 ± 6	294 ± 23	$\mathrm{K}\pi$	93 ± 10	scalar
$\mathrm{K}_0^*(1680)$	1^-	1717 ± 27	322 ± 110	$\mathrm{K}\pi$ $\mathrm{K}\rho$ $\mathrm{K}^*(892)\pi$	38.7 ± 2.5 31.4 ± 3.4[3] 29.9 ± 3.5[3]	vector

Tab. 2.1: Resonances involved in τ decays with open strangeness. The mass of the resonances, the width of the resonances, spin-parity J^P and the dominant decay modes are given [57].

underlying resonances of the hadronic system. Due to the limited statistics this is not possible in this analysis. The known resonances involved in τ decays with open strangeness are listed in Table 2.1. The $\mathrm{K}\pi$ final state for examples includes contributions from both, vector ($\mathrm{K}^*(892)$ and $\mathrm{K}_0^*(1680)$) and scalar ($\mathrm{K}_0^*(1430)$) resonances. Contributions from different currents can also be found in the $\mathrm{K}^-\pi^+\pi^-\nu_\tau$ final state. Axial-vector resonances ($\mathrm{K}_1(1270/1400)$) contribute as well as scalar ($\mathrm{K}_0^*(1430)$) and vector ($\mathrm{K}_0^*(1680)$) resonances.

2.2 Theoretical Analysis of R_τ

With the expression given in Equation 2.11, a theoretical analysis of the inclusive hadronic τ decay width is not possible. It requires the integration over all hadronic resonances of the invariant mass spectra. This involves large contributions from non-perturbative effects of QCD and thus can not be reliably calculated at present. As discussed later, only phenomenological parametrizations assuming vector dominance models exits. The free parameters of these parametrizations (usually the mass and the width of the corresponding resonance) can not be predicted in QCD, but have to be determined from the data. However, assuming analyticity and using the Operator Product Expansion (OPE), the total hadronic width can be calculated. The central quantities in a theoretical analysis are the so-called two-point correlation functions. These complex functions are given by the time ordered product of the currents involved

$$\Pi^{\mu\nu}_{ij,\mathcal{J}}(q) \equiv \imath \int \mathrm{d}^4x\, e^{\imath qx} \langle 0|T(\mathcal{J}^{\mu}_{ij}(x)\mathcal{J}^{\nu}_{ij}(0)^{\dagger})|0\rangle \tag{2.14}$$

for the vector and axial-vector quark currents ($i, j = \mathrm{u}, \mathrm{d}, \mathrm{s}$)

$$\mathcal{J}^{\mu}_{ij} = V^{\mu}_{ij} = \bar{q}_{\mathrm{j}}\gamma^{\mu}q_{\mathrm{i}} \tag{2.15a}$$

$$\mathcal{J}^{\mu}_{ij} = A^{\mu}_{ij} = \bar{q}_{\mathrm{j}}\gamma^{\mu}\gamma^{5}q_{\mathrm{i}}, \tag{2.15b}$$

respectively. The two-point correlation functions describe the creation of hadronic states with total angular momentum J from the vacuum by means of QCD. The lower indices describe the quark flavors and the type of the current ($ij \in (\bar{\mathrm{u}}\mathrm{d}, \bar{\mathrm{u}}\mathrm{s})$). The correlators have the Lorentz decomposition

$$\Pi^{\mu\nu}_{ij,\mathrm{V/A}}(q) = (-g^{\mu\nu}q^2 + q^{\mu}q^{\nu})\Pi^{(J=1)}_{ij,\mathrm{V/A}}(q^2) + q^{\mu}q^{\nu}\Pi^{(J=0)}_{ij,\mathrm{V/A}}(q^2) \tag{2.16}$$

---

[3] Errors are symmetrized

where the superscript refers to the angular momentum in the hadronic rest frame ($J = 1$: transverse component, $J = 0$: longitudinal component). The correlator can be decomposed according to the quark current involved

$$\begin{aligned}\Pi^{(J)}(s) \equiv \; & |V_{\mathrm{ud}}|^2\Big(\Pi^{(J)}_{\mathrm{ud,V}}(s) + \Pi^{(J)}_{\mathrm{ud,A}}(s)\Big) \\ & +|V_{\mathrm{us}}|^2\Big(\Pi^{(J)}_{\mathrm{us,V}}(s) + \Pi^{(J)}_{\mathrm{us,A}}(s)\Big),\end{aligned} \tag{2.17}$$

into non-strange and strange contributions. The contributions can be split further into vector and axial-vector parts.

The connection between the spectral functions $\rho_J^{(S)}$ in Equation 2.11 and the two-point correlation function in Equation 2.17 is given via the optical theorem, which is illustrated in Figure 2.1. It relates the total cross section of a process to the imaginary part of the forward scattering amplitude. Here, it relates the spectral functions $\rho_J^{(S)}$, that are proportional to the total hadronic width in τ lepton decays, to the two-point correlation function. Using the definition of the spectral functions in Equation 2.13, one identifies the following relation

$$\frac{1}{\pi}\Im\Pi^{(J)}_{ij,\,V/A}(s) = \frac{1}{2\pi^2}(v_J/a_J)(s). \tag{2.18}$$

This relation connects the experimentally measurable quantities, the spectral functions, to the two-point correlation function, calculable with QCD techniques. Equation 2.11 would require the calculation of all exclusive final states which can not be handled by perturbative QCD. The vacuum polarization (Equation 2.17) however already includes all final states and can be calculated theoretically. The hadronic width ratio of the τ lepton as defined in Equation 2.5 can thus be written as an integral over the imaginary part of the correlation functions

$$R_\tau = 12\pi\int_0^{m_\tau^2}\frac{\mathrm{d}s}{m_\tau^2}\left(1-\frac{s}{m_\tau^2}\right)^2\left(\left(1+2\frac{s}{m_\tau^2}\right)\Im\Pi^{(1)}(s) + \Im\Pi^{(0)}(s)\right). \tag{2.19}$$

The integration requires analyticity of the correlation functions. Unfortunately, the correlation functions $\Pi^{(J)}_{ij,V/A}$ are analytic functions in the complex plane except for the positive real axis. This has two reasons. First, there are two poles, the pion pole and the kaon pole at $s = m_\pi^2$ and $s = m_{\mathrm{K}}^2$. Second, the correlation function has a discontinuity as the imaginary part crosses the real axis. The line, where the discontinuity shows up is called branch cut or branch line. Using Cauchy's theorem, however, the integral along the real axis can be transformed into an contour integral

$$\frac{1}{\pi}\int_0^{m_\tau^2}\mathrm{d}s\, g(s)\Im\Pi(s) = -\frac{1}{2\pi\imath}\oint_{|s|=m_\tau^2}\mathrm{d}s\, g(s)\Pi(s). \tag{2.20}$$

The correlation functions are therefore analyzed as depicted in Figure 2.2. As ε approaches zero, the imaginary part again approaches the branch cut. However at $|s| = m_\tau^2$, any possible pole is suppressed by the factor $(1-\frac{s}{m_\tau^2})^2$, so that the integration can safely be performed. The hadronic width ratio R_τ can thus

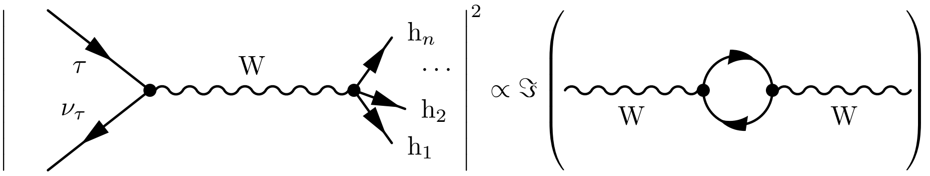

Fig. 2.1: The optical theorem relates the production of hadrons from τ decays to the imaginary part of the forward scattering amplitude. The left hand side requires the calculation of all hadronic final states, while they are implicitly contained on the right hand side.

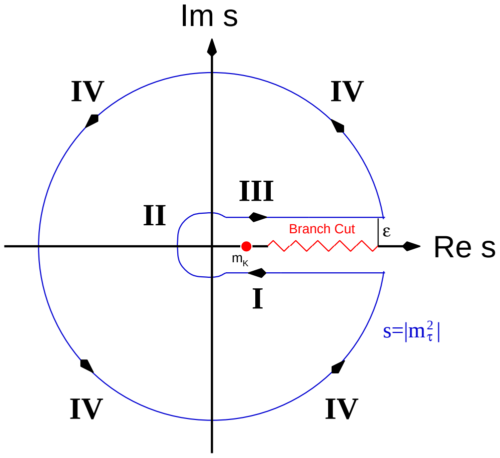

Fig. 2.2: Integration path in the complex plane as used in the analytic calculation of R_τ. The integration path runs counter-clockwise around the circle at $|s| = m_\tau^2$. Since the correlation functions are analytic functions except for the real axis, the integration path has an offset of $\pm\imath\varepsilon$ along the real axis.

be expressed as an integral around the contour that runs counter-clockwise around the circle[4] $s = m_\tau^2$

$$R_{\tau,\mathrm{V/A}} = 6\pi\imath \oint_{|s|=m_\tau^2} \frac{\mathrm{d}s}{m_\tau^2}\left(1-\frac{s}{m_\tau^2}\right)^2 \left(\left(1+2\frac{s}{m_\tau^2}\right)\Pi^{(1)} + \Pi^{(0)}\right). \tag{2.21}$$

The advantage of this expression over Equation 2.19 is that it requires knowledge of the correlator only for complex s of the order m_τ^2, which is significantly larger than the scale associated with non-perturbative effects in QCD. The Operator Product Expansion, which will be discussed in the next section, can therefore be used, to organize perturbative and non-perturbative contributions and to reliably calculate the correlator. The naïve prediction for R_τ is reproduced by inserting the correlators for massless non-interacting quarks into Equation 2.21:

$$\Pi^{(1)}_{\mathrm{ij},V}(s) = \Pi^{(1)}_{\mathrm{ij},A}(s) = -\frac{N_\mathrm{C}}{12\pi^2}\log(-s) + \text{constant} \tag{2.22a}$$

$$\Pi^{(0)}_{\mathrm{ij},V}(s) = \Pi^{(0)}_{\mathrm{ij},A}(s) = 0. \tag{2.22b}$$

For technical reasons, not $\Pi^{(J)}$ but rather the so-called Adler functions are used in the calculations. These are essentially the logarithmic derivatives of the correlation functions

$$D^{\mathrm{L+T}} \equiv -s\frac{\mathrm{d}}{\mathrm{d}s}\left(\Pi^{(0+1)}(s)\right) \tag{2.23}$$

$$D^{\mathrm{L}}(s) \equiv \frac{s}{m_\tau^2}\frac{\mathrm{d}}{\mathrm{d}s}\left(s\Pi^{(0)}(s)\right). \tag{2.24}$$

They satisfy the homogeneous renormalization group equations. This representation avoids renormalization-scheme and scale dependent subtraction constants which do not contribute to any physical observable. The total hadronic width ratio can then be written as

$$R_\tau = -\pi\imath \oint_{|s|=m_\tau^2} \frac{\mathrm{d}s}{s}\left(1-\frac{s}{m_\tau^2}\right)^3 \left(3\left(1+\frac{s}{m_\tau^2}\right)D^{\mathrm{L+T}}(s) + 4D^{\mathrm{L}}(s)\right), \tag{2.25}$$

where L and T denote the longitudinal ($J = 0$) and transversal ($J = 1$) contributions, respectively.

---

[4] Here it has been used that the correlation function depends logarithmically on s, ($s \in \mathbb{R}$), i.e.

$$\Im\Pi^{(J)} = -\frac{\imath}{2}\left(\Pi^{(J)}(s+\imath\varepsilon) - \Pi^{(J)}(s-\imath\varepsilon)\right).$$

2.3 Operator Product Expansion

As explained before, for low momentum transfer the spectral function cannot be described using perturbative QCD. A theory describing non-perturbative processes, dominant in this energy regime, does not exist. For inclusive observables like R_τ however, the Operator Product Expansion (OPE) [35–38] allows to separate the description of perturbative effects (dominant at large momentum transfer) and non-perturbative effects (dominant at low energy transfers).
For scalar correlators, the OPE has the form

$$\Pi^{(J)}(s) = \sum_{D=0,\,2,\,4,\,\ldots} \frac{1}{(-s)^{D/2}} \sum_{\mathrm{dim}\mathcal{O}=\mathcal{D}} \mathcal{C}^{(J)}(s,\,\mu) < \mathcal{O}(\mu) >, \tag{2.26}$$

where the outer sum runs over all energy dimensions D and the inner sum runs over all operators of the same dimension. The parameter μ is an arbitrary factorization scale, separating long distance non-perturbative effects from short distance effects. Long distance effects are described by the vacuum matrix elements $< \mathcal{O}(\mu) >$. Short distance effects are parametrized by the so-called Wilson Coefficients $\mathcal{C}^{(J)}(s,\,\mu)$. They are dimensionless functions of s and the factorization scale μ, which can be computed perturbatively as expansions in powers of $\alpha_s(\mu)$. Here, it is convenient to choose the factorization scale $\mu = m_\tau$ to avoid large logarithms of the form $\log(-s/\mu^2)$ in the perturbation expansion.

Dimension-0 Correction: The dimension-0 operator is the perturbative correction assuming massless quarks. It is therefore identical for the vector and axial-vector parts. The lowest order vacuum polarization diagram contributing is displayed in Figure 2.3. It contains one quark loop inserted into the W propagator. A contribution of second order in α_s is given by the second diagram in Figure 2.3. In addition to the gluon exchange, self-energy diagrams contribute. An example for a third order diagram, containing an additional quark loop is also given. The dimension-0 corrections are described by

$$D^{L+T}_{\mathrm{ij},V/A}(s)\Big|_{D=0} = \frac{1}{4\pi} \sum_{n=0} \tilde{K}_n(\xi) a^n(-\xi^2 s), \tag{2.27}$$

where $a^n = \alpha_s/\pi$ and ξ is an arbitrary scale factor of order unity. The coefficients $\tilde{K}_n$ are constrained by the homogeneous renormalization group equation

$$\frac{\mathrm{d}}{\mathrm{d}\xi}\tilde{K}_0(\xi) = 0 \tag{2.28}$$

$$\xi\frac{\mathrm{d}}{\mathrm{d}\xi}\tilde{K}_n(\xi) = \sum_{k=1}^{n}(k-n)\beta_k \tilde{K}_{n-k}(\xi), \tag{2.29}$$

where β_k are the coefficients of the renormalization group β function which is known to the four-loop level [27]. The coefficients are given in Chapter 7.5.2. The perturbative expansion of the Adler functions is known up to order α_s^3 [28]

$$K_0 = K_1 = 1 \qquad K_2 = \frac{299}{24} - \zeta(3) \qquad K_3 = \frac{58057}{288} - \frac{779}{4}\zeta(3) - \frac{75}{2}\zeta(5), \tag{2.30}$$

where ζ represents the Riemann ζ function($\zeta(3) = 1.20206...$, $\zeta(4) = 1.08232...$ and $\zeta(5) = 1.03693...$).

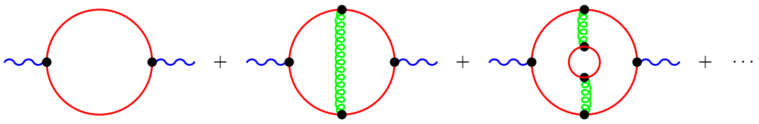

Fig. 2.3: Feynman diagrams for the dimension-0 operators. The wiggled lines represent the W propagator, the solid lines are quark lines. The curled lines represent gluons. Examples for diagrams up to third order in α_s are given.

Dimension-2 Correction: Dimension-2 operators are perturbative corrections of the form $m_i(\mu)m_j(\mu)$, which contain the operator describing running quark masses. For light quark masses ($m_\mathrm{u} = m_\mathrm{d} = 0$), this operator becomes zero. It has however to be taken into account in the case of Cabbibo suppressed decays. Neglecting the light quark masses, the correction is proportional to the mass of the strange quark m_s^2. In terms of the running quark mass and the QCD coupling, the correction is given via

$$D_\mathrm{us}^{L+T}(s)\Big|_{D=2} = \frac{3}{4\pi^2 s} m_s^2(-\xi^2 s) \sum_{n=0} \tilde{d}_n^{L+T}(\xi) a^n(-\xi^2 s) \tag{2.31a}$$

$$D_\mathrm{us}^{L}(s)\Big|_{D=2} = \frac{3}{8\pi^2 m_\tau^2} m_\mathrm{s}^2 \sum_{n=0} \tilde{d}_n^{L}(\xi) a^n(-\xi^2 s). \tag{2.31b}$$

The coefficients $\tilde{d}_n^{L/L+T}$ are constrained by the renormalization group equation

$$\frac{\mathrm{d}}{\mathrm{d}\xi}\tilde{d}_0(\xi) = 0 \tag{2.32a}$$

$$\xi\frac{\mathrm{d}}{\mathrm{d}\xi}\tilde{d}_n(\xi) = \sum_{n=1} \Big(2\gamma_k - (n-k)\beta_k\Big)\tilde{d}_{n-k}(\xi). \tag{2.32b}$$

These equations involve the coefficients of the renormalization group β and γ functions, which are known to the four-loop level [27]. The coefficients are given in Chapter 7.5.2. The $J = L+T$ coefficients are known to order $\mathcal{O}(\alpha_s^2)$, the $J = L$ coefficients are known to order $\mathcal{O}(\alpha_s^3)$ and for $\xi = 1$ the numerical values in the $\overline{\mathrm{MS}}$ scheme are

$$d_0^{L+T} = 1 \qquad d_1^{L+T} = \frac{13}{3} \qquad d_2^{L+T} = \frac{23077}{432} - \frac{32}{9} + \left(\frac{179}{54} + \frac{8}{3}\right)\xi(3) - \frac{520}{27}\xi(5) \tag{2.33a}$$

and

$$d_0^{L} = 1 \qquad d_1^{L} = \frac{17}{3} \qquad \begin{aligned} d_2^L &= \frac{9631}{144} - \frac{35}{2}\xi(3) \\ d_3^L &= \frac{4748953}{5184} - \frac{91519}{216}\xi(3) - \frac{5}{2}\xi(4) + \frac{715}{12}\xi(5). \end{aligned} \tag{2.33b}$$

There are no non-perturbative contributions here. It is impossible to build dynamical operators of dimension-2 from quark and gluon fields. Therefore the leading non-perturbative contribution comes from dimension-4 operators.

Dimension-4 Correction: The dimension-4 corrections contain dynamical contributions from the quark-operator $\langle m\bar{\mathrm{q}}_i \mathrm{q}_i\rangle$ and the gluon-operator $\langle(\alpha_s/\pi)GG\rangle$. Additional contributions from the running quark masses enter to the fourth power in m_s. Given the experimental situation, these contributions can safely be neglected. Feynman diagrams contributing to the so-called quark and gluon condensates are displayed in Figure 2.4. The crosses represent the fact that a particle annihilates into the vacuum and 'condensates' at this point. The condensates parametrize the non-perturbative contributions. In perturbative QCD, the vacuum expectation values of these operators vanish. Non-vanishing vacuum expectation values are a hint for non-perturbative effects. The dimension-4 contribution to the correlation functions is given by

$$\Big(D_{\mathrm{ud},V+A}^{L+T}(s) - D_{\mathrm{us},V+A}^{L+T}(s)\Big)\Big|_{D=4} = -\frac{4}{s^2}\delta O_4(-\xi^2 s)\sum_{n=0}\tilde{q}_n(\xi)a^n(-\xi^2 s) + \mathcal{O}(m_\mathrm{s}^4) \tag{2.34a}$$

$$\big(D_{\mathrm{ud},V+A}^{L}(s) - D_{\mathrm{us},V+A}^{L}(s)\big)\Big|_{D=4} = -\frac{2}{s m_\tau^2}\delta O_4(-\xi^2 s) + \mathcal{O}(m_\mathrm{s}^4), \tag{2.34b}$$

where $\delta O_4(\mu^2)$ is the quark condensate defined in the $\overline{\mathrm{MS}}$ scheme

$$\delta O_4(\mu^2) \equiv \langle 0|m_\mathrm{s}\bar{\mathrm{s}}\mathrm{s} - m_\mathrm{d}\bar{\mathrm{d}}\mathrm{d}|0\rangle. \tag{2.35}$$

It is the only contribution from dimension-4 operators considered here. The scale dependence of the

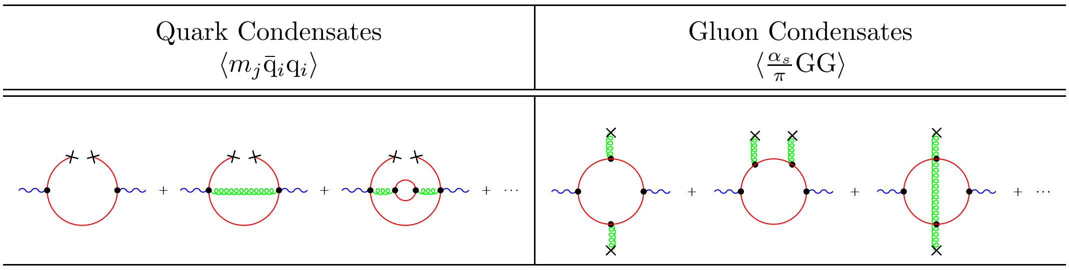

Fig. 2.4: Feynman diagrams for the dimension-4 operators. The wiggled lines represent the W propagator, the solid lines are quark lines. The curled lines represent gluons. The crosses represent the corresponding condensates. Examples of the Feynman diagrams contributing to the quark condensate and to the gluon condensate are given.

perturbative expansion coefficients $\tilde{q}_n$ is fixed by the renormalization group equations

$$\xi \frac{\mathrm{d}}{\mathrm{d}\xi} \tilde{q}_0^{L+T}(\xi) = 0 \tag{2.36a}$$

$$\xi \frac{\mathrm{d}}{\mathrm{d}\xi} \tilde{q}_n^{L+T}(\xi) = \sum_{k=1}^{n} (k-n) \beta_k \tilde{q}_{n-k}^{L+T}(\xi). \tag{2.36b}$$

The coefficients are known to second order in α_s

$$\tilde{q}_0^{L+T}(\xi) = 1 \qquad \tilde{q}_1^{L+T}(\xi) = -1 \qquad \tilde{q}_2^{L+T}(\xi) = -\frac{131}{24} - \frac{9}{2} \ln \xi. \tag{2.37}$$

Dimension⩾6 Correction: The largest contribution to the dimension-6 operator comes from the 4-quark operator. These operators have the form $\bar{\mathrm{q}}_i \Gamma \mathrm{q}_j \bar{\mathrm{q}}_k \Gamma \mathrm{q}_l$, where Γ is the product of a Dirac matrix and an $\mathrm{SU}(3)_{\mathrm{Flavor}}$ color matrix. Further contributions come from the triple gluon condensate $\langle f^{abc} G_\mu^{a\nu} G_\nu^{b\lambda} G_\lambda^{c\mu} \rangle$. Examples of Feynman diagrams contributing to the dimension-6 operators are depicted in Figure 2.5. In addition lower dimension operators multiplied by running quark masses have to be considered. The overall contribution from the dimension-8 operators to R_τ is expected to be small. They arise from quark-quark condensates, quark-gluon and four-gluon condensates [30]. The largest contribution comes from the square of the gluon condensate. The contributions from dimension-10 or higher are even smaller.

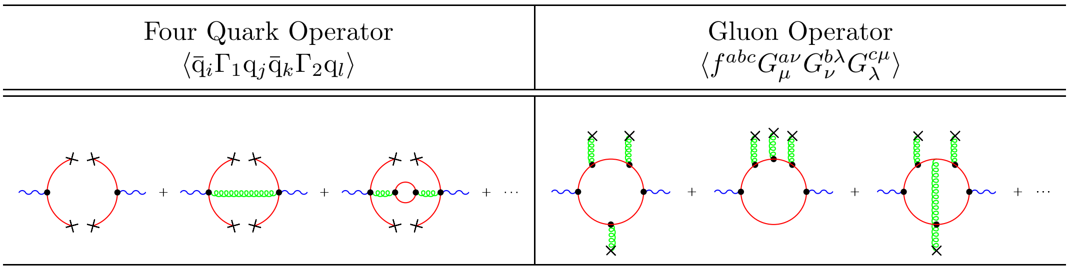

Fig. 2.5: Feynman diagrams for the dimension-6 operators. The wiggled lines represent the W propagator, the solid lines are quark lines. The curled lines represent gluons. The crosses represent the corresponding condensates. Examples of the Feynman diagrams contributing to the four-quark operator and the gluon operator are given.

2.4 R_τ and the Spectral Moments

It is convenient to express the corrections to R_τ from dimension D operators in terms of the fractional corrections $\delta^{(D)}_{ij,\,V/A}$ to the naïve contribution from the current with quantum numbers $ij,\ V/A$

$$\delta^{(D)}_{ij,\,V/A} = \sum_{\dim\mathcal{O}=D} \frac{<\mathcal{O}(\mu)>}{m_\tau^D} 4\pi\imath \oint_{|s|=m_\tau^2} \frac{\mathrm{d}s}{m_\tau^2}\left(\frac{-s}{m_\tau^2}\right)^{-D/2}\left(1-\frac{s}{m_\tau^2}\right)^2 \times$$
$$\times\left(\left(1+2\frac{s}{m_\tau^2}\right)\mathcal{C}^{(0+1)}_{ij,\,V/A}(s,\,\mu) - 2\frac{s}{m_\tau^2}\mathcal{C}^{(0)}_{ij,\,V/A}(s,\,\mu)\right), \tag{2.38}$$

where $\mathcal{C}^{(J)}_{ij,\,V/A}(s,\,\mu)$ are the Wilson coefficients for the correlators $\Pi^{(J)}_{ij,\,V/A}(s)$. The contour integral in Equation 2.38 is dimensionless and depends only on the scales μ and m_τ.

In terms of the fractional corrections defined in Equation 2.38, the three experimentally measurable components of R_τ, the vector and the axial-vector part in the non-strange case and the contribution from the hadronic width into final states with open strangeness, can be expressed as

$$R_{\tau,\,\mathrm{V}} = \frac{3}{2}|V_{\mathrm{ud}}|^2 S_{\mathrm{ew}}\left(1+\delta_{\mathrm{ew}}+\delta^{(0)}+\sum_{D=2,\,4,\,\ldots}\delta^{(D)}_{\mathrm{ud},\,\mathrm{V}}\right) \tag{2.39a}$$

$$R_{\tau,\,\mathrm{A}} = \frac{3}{2}|V_{\mathrm{ud}}|^2 S_{\mathrm{ew}}\left(1+\delta_{\mathrm{ew}}+\delta^{(0)}+\sum_{D=2,\,4,\,\ldots}\delta^{(D)}_{\mathrm{ud},\,\mathrm{A}}\right) \tag{2.39b}$$

$$R_{\tau,\,\mathrm{S}} = 3|V_{\mathrm{us}}|^2 S_{\mathrm{ew}}\left(1+\delta_{\mathrm{ew}}+\delta^{(0)}+\sum_{D=2,\,4,\,\ldots}\delta^{(D)}_{\mathrm{us}}\right). \tag{2.39c}$$

Here, $\delta^{(D)}_{ij}$ is the average of the vector (V) and axial-vector (A) corrections $\delta^{(D)}_{ij} = (\delta^{(0)}_{ij,\,\mathrm{V}} + \delta^{(0)}_{ij,\,\mathrm{V}})/2$. The electroweak correction factors S_{ew} and δ_{ew} are explained in Chapter 2.5. The dimension-0 correction $\delta^{(0)}$ is the purely perturbative correction, neglecting quark masses. It is the same for all components of R_τ.

The measurement of the invariant mass distribution of the hadronic final state provides additional information on QCD dynamics. The invariant mass spectrum can be analyzed by using the spectral moments [11] defined as

$$R^{kl}_\tau \equiv \int_0^{m_\tau}\mathrm{d}s\left(1-\frac{s}{m_\tau^2}\right)^k\left(\frac{s}{m_\tau^2}\right)^l\frac{\mathrm{d}R_\tau}{\mathrm{d}s}. \tag{2.40}$$

Using Equation 2.25, the spectral moments can be rewritten as contour integral in the complex s plane

$$R^{kl}_\tau = -\pi\imath\oint_{|x|=1}\frac{\mathrm{d}x}{x}\left(3\mathcal{F}^{kl}_{L+T}(x)D^{L+T}(m_\tau^2x)+4\mathcal{F}^{kl}_{L}(x)D^{L}(m_\tau^2x)\right), \tag{2.41}$$

where $x = s/m_\tau^2$. All kinematic factors have been absorbed into the kernels, defined via

$$\mathcal{F}^{kl}_{L+T} \equiv 2(1-x)^{3+k}\sum_{n=0}^{l}\frac{l!}{(l-n)!n!}(x-1)^n\frac{(6+k+n)+2(3+k+n)x}{(3+k+n)(4+k+n)} \tag{2.42a}$$

$$\mathcal{F}^{kl}_{L} \equiv 3(1-x)^{3+k}\sum_{n=0}^{l}\frac{l!}{(l-n)!n!}(x-1)^n\frac{1}{3+k+n}. \tag{2.42b}$$

2.5 Electroweak Corrections

In addition to the corrections from QCD, the partial width of the τ lepton for decays into electrons/hadrons also depends on electroweak radiative corrections. Two contributions have to be considered here. The radiation of real photons off the final state fermions and the self-interaction of final state fermions via the exchange of virtual photons and Z^0 bosons. In the ratio of the partial width of the τ lepton into hadrons to the partial width into electrons, however they do not completely cancel. The difference arises from the different charges of the final state fermions involved in hadronic and leptonic τ decays. From the self-interaction diagrams, a finite correction is obtained [31]

$$S_{\text{ew}} = 1 + 4\frac{\alpha}{2\pi}\ln\frac{m_{\text{Z}^0}}{m_\tau} \tag{2.43a}$$

$$= \left(\frac{\alpha(m_{\text{b}})}{\alpha(m_\tau)}\right)^{9/19}\left(\frac{\alpha(m_{\text{W}})}{\alpha(m_{\text{b}})}\right)^{9/20}\left(\frac{\alpha(m_{\text{Z}^0})}{\alpha(m_{\text{W}})}\right)^{36/17} = 1.0194. \tag{2.43b}$$

The following values of α_{QED} have been used $\alpha(m_\tau) = 1./133.29$, $\alpha(m_{\text{b}}) = 1./132.05$, $\alpha(m_{\text{W}}) = 1./127.97$, and $\alpha(m_{\text{Z}^0}) = 1./127.93$. The correction from the radiation of real photons off the final state fermions is implemented as an additive correction [33]

$$\delta_{\text{ew}} = \frac{\alpha}{2\pi}\frac{5}{6} = 0.001, \tag{2.44}$$

which is numerically small. Summing up Equations 2.39(a-c), the τ hadronic width can be written as

$$R_\tau = 3(|V_{\text{ud}}|^2 + |V_{\text{us}}|^2)S_{\text{ew}}\left(1 + \delta_{\text{ew}} + \delta^{(0)} + \sum_{D=2,4,\ldots}\left(\cos^2\Theta_{\text{C}}\delta^{(\text{D})}_{\text{ud}} + \sin^2\Theta_{\text{C}}\delta^{(\text{D})}_{\text{us}}\right)\right). \tag{2.45}$$

2.6 SU(3)$_{\text{Flavor}}$ Breaking

The correlators for strange and non-strange τ lepton decays are identical in the SU(3)$_{\text{Flavor}}$ limit, i.e. in the limit of vanishing quark masses. Rescaling strange and non-strange hadronic widths by their corresponding suppression factors, i.e. the elements of the weak mixing matrix, their difference

$$\delta R^{kl}_\tau \equiv \frac{R^{kl}_{\tau,\,V+A}}{|V_{\text{ud}}|^2} - \frac{R^{kl}_{\tau,\,S}}{|V_{\text{us}}|^2} \tag{2.46}$$

vanishes in the chiral limit. Any non-zero value measured from τ data is due to the mass of the strange quark and thus a sign for breaking of the SU(3)$_{\text{Flavor}}$ symmetry. The separate measurement of Cabbibo allowed and Cabbibo suppressed decays of the τ lepton therefore allows to pin down the SU(3)$_{\text{Flavor}}$ breaking effects. From the theoretical point of view this quantity has the advantage that the theoretical uncertainties are reduced in the difference.

In principle these flavor breaking quantities can also be constructed for the vector part, the axial-vector part or for the sum of both. However, for the strange final states, the separate vector and axial-vector contributions can not be reconstructed due to the limited statistics. Therefore, the vector plus axial-vector spectral distributions are used in the construction of the weighted difference.

Using the Operator Product Expansion, the weighted difference can be rewritten as

$$\delta R^{kl}_\tau = 3S_{\text{ew}}\sum_{D\geq 2}\left(\delta^{kl(D)}_{\text{ud}} - \delta^{kl(D)}_{\text{us}}\right), \tag{2.47}$$

which contains only contributions from dimension-2 and higher. The dimension-0 correction are the purely perturbative corrections calculated in the chiral limit. The contributions are therefore identical for strange and non-strange spectral moments. In the weighted difference (Equation 2.46) they cancel exactly. The same is true for the additive electroweak corrections.

The corrections of various dimensions to the τ hadronic width have already been introduced in Chapter 2.3. Here, the corresponding expressions for δR^{kl}_τ are given and their relevance in the determination of the strange quark mass is discussed.

Dimension-2 Correction:

The contribution of the dimension-2 operator to the weighted difference of non-strange and strange moments δR^{kl} can be written as

$$\delta R^{kl}_\tau\Big|_{D=2} = 24S_{\text{ew}}\frac{m^2_{\text{s}}(m^2_\tau)}{m^2_\tau}(1-\epsilon^2_d)\Delta^{(2)}_{kl}(a_\tau), \tag{2.48}$$

where $a_\tau = \alpha_s(m_\tau^2)/\pi$, $\epsilon = m_\mathrm{d}/m_\mathrm{s} = 0.053 \pm 0.002$ [23] and

$$\Delta^{(2)}_{kl}(a_\tau) = \frac{1}{4}\Big(3\sum_{n=0} \tilde{d}_n^{L+T}(\xi) B^{kl(n)}_{L+T}(a_\xi) + \sum_{n=0} \tilde{d}_n^{L}(\xi) B^{kl(n)}_{L}(a_\xi)\Big) \tag{2.49}$$

$$= \frac{1}{4}\Big(3\Delta^{L+T}_{kl}(a_\tau) + \Delta^{L}_{kl}(a_\tau)\Big) \tag{2.50}$$

is the perturbative contribution of the dimension-2 operators. To the extent that $(m_\mathrm{u} + m_\mathrm{d})/2 \ll m_\mathrm{s}$, this contribution is proportional only to m_s^2 which generates the sensitivity to the mass of the strange quark. The leading quark mass corrections of dimension-2 have been studied in detail in [13, 14, 16–19, 26]. The dimension-2 correction involves the functions $B_{L+T}kl$ and B_L^{kl} which are defined via

$$B^{kl,\,(n)}_{L+T} \equiv \frac{-1}{4\pi\imath}\oint_{|x|=1}\frac{\mathrm{d}x}{x^2}\mathcal{F}^{kl}_{L+T}(x)\left(\frac{m(-\xi^2 m_\tau^2 x)}{(m_\tau^2)}\right)^2 a^n(-\xi^2 m_\tau^2 x) \tag{2.51a}$$

$$B^{kl,\,(n)}_{L} \equiv \frac{1}{2\pi\imath}\oint_{|x|=1}\frac{\mathrm{d}x}{x}\mathcal{F}^{kl}_{L}(x)\left(\frac{m(-\xi^2 m_\tau^2 x)}{(m_\tau^2)}\right)^2 a^n(-\xi^2 m_\tau^2 x). \tag{2.51b}$$

These functions now only depend on $\alpha_s(\xi^2 m_\tau^2)/\pi$, $\log(\xi)$.

Dimension-4 Correction:
The dimension-4 correction to δR_τ^{kl} is given by

$$\delta R_\tau^{kl}\Big|_{D=4} = -12 S_\mathrm{ew}\Big(4\pi^2\frac{\delta O_4(m_\tau^2)}{m_\tau^4}Q_{kl}(a_\tau) + \mathcal{O}\Big(\frac{m_\mathrm{s}^4}{m_\tau^4}\Big)\Big), \tag{2.52}$$

where terms of the order m_s^4 can safely be neglected compared to the mass of the τ. The function Q_{kl} is defined via

$$Q_{kl} = Q_{kl}^{L} + Q_{kl}^{L+T}, \tag{2.53}$$

where

$$Q^{L}_{kl} = \frac{-1}{6\pi\imath}\oint_{|x|=1}\frac{\mathrm{d}x}{x^2}\mathcal{F}^{kl}_{L}(x)\frac{\delta O_4(-\xi^2 m_\tau^2 x)}{\delta O_4(m_\tau^2)} \tag{2.54}$$

$$Q^{L+T}_{kl} = \frac{-1}{4\pi}\oint_{|x|=1}\frac{\mathrm{d}x}{x^3}\mathcal{F}^{kl}_{L+T}(x)\frac{\delta O_4(-\xi^2 m_\tau^2 x)}{\delta O_4(m_\tau^2)}\sum_n \tilde{q}_n^{L+T}(\xi) a^n(-\xi^2 m_\tau^2 x) \tag{2.55}$$

and $x = s/m_\tau^2$. The operator δO_4 denotes the contribution from the quark condensate. The definition of $\tilde{q}_n^{L+T}$ can be found in Chapter 2.3.
In principle, the $\mathrm{SU(3)}_\mathrm{Flavor}$ breaking condensate $\delta O_4(m_\tau^2)$ could be extracted from the τ decay data together with m_s in a combined fit of different δR_τ^{kl} moments. Given the current experimental accuracy of the data, this is not possible. To date, the contribution from $\delta O_4(m_\tau^2)$ is estimated using constraints provided by the chiral symmetry of QCD. To lowest order in Chiral Perturbation Theory [24], $\delta O_4(\mu^2)$ is scale independent and is fully predicted in terms of the pion decay f_π constant and the pion and kaon masses

$$\delta O_4(m_{\tau^2})\Big|_{O(p^2)} = (m_\mathrm{s} - m_\mathrm{d})\langle 0|\bar{\mathrm{q}}\mathrm{q}|0\rangle \simeq -f_\pi^2(m_\mathrm{K}^2 - m_\pi^2) \simeq -1.9\cdot 10^{-3}\,\mathrm{GeV}^4. \tag{2.56}$$

Here, $\langle 0|\bar{\mathrm{q}}\mathrm{q}|0\rangle$ denotes the quark condensate in the chiral limit given by [24, 25]

$$(m_\mathrm{u} + m_\mathrm{d})\langle 0|\mathrm{q}\bar{\mathrm{q}}|0\rangle \simeq \frac{m_\mathrm{u} + m_\mathrm{d}}{2}\langle 0|\mathrm{d}\bar{\mathrm{d}} + \mathrm{u}\bar{\mathrm{u}}|0\rangle \simeq -f_\pi^2 m_\pi^2. \tag{2.57}$$

This estimate is improved by taking into account the leading $O(p^4)$ corrections [10]

$$v_\mathrm{s} \equiv \frac{< 0|\bar{\mathrm{s}}\mathrm{s}|0 >}{< 0|\bar{\mathrm{d}}\mathrm{d}|0 >} = 0.8 \pm 0.2. \tag{2.58}$$

This yields the estimate

$$\delta O_4(m_\tau^2)\Big|_{O(p^4)} = (v_\mathrm{s} m_\mathrm{s} - m_\mathrm{d}) < 0|\bar{\mathrm{d}}\mathrm{d}|0 > \simeq -\frac{m_\mathrm{s}}{m_\mathrm{u} + m_\mathrm{d}}(v_\mathrm{s} - \epsilon_\mathrm{d}) f_\pi^2 m_\pi^2 \tag{2.59}$$

$$\simeq -(1.5 \pm 0.4)\cdot 10^{-3}\,\mathrm{GeV}^4 \tag{2.60}$$

for the quark condensate.

Dimension$\geqslant 6$ Corrections:
The leading order coefficients of dimension six and eight corrections for the two-point functions have been studied in the $\overline{\mathrm{MS}}$ scheme [29]. In view of the theoretical uncertainties in the dimension-2 and dimension-4 corrections and in the view of the unknown values of the dimension six and eight condensates, contributions $D \geqslant 6$ are not considered here. They are regarded as additional theoretical uncertainties.

2.7 The Determination of m_s and the Choice of Moments

The mass of the strange quark at the τ scale can now be determined from the weighted difference of strange and non-strange spectral moments for each combination of kl individually using the following relation

$$m_\mathrm{s}^2(m_\tau^2)\Big|_{kl} = \frac{m_\tau^2}{2(1-\epsilon_d)} \frac{1}{\Delta_{kl}^{(2)}(a_\tau)} \Big(\frac{\delta R_\tau^{kl}}{12 S_\mathrm{ew}} + 4\pi^2 \frac{\delta O_4(m_\tau^2)}{m_\tau^4} Q_{kl}(a_\tau) \Big). \tag{2.61}$$

Contributions from dimension-4 operators other than the quark condensate δO_4 are neglected here. They are suppressed by factors m_s^4, so that the expected experimental uncertainty is larger than these corrections. Corrections of dimension-6 or higher are again much smaller, so that they are not considered here.

In the choice of moments, the experimental and the theoretical uncertainties associated with it have to be taken into account. Using the definition of the weighting function in Equation 2.40, this means that for increasing values of k the low mass range gets higher weights, while for increasing l the high mass range becomes more pronounced.

The low mass range is dominated by the few-meson final states, the kaon pole and the $\mathrm{K}^*(892)$ resonance. These final states have relatively large branching fractions and they are measured with high accuracy. From the theoretical point of view, this is the range where the non-perturbative contributions play an important role. This means that the moments are dominated by the vacuum condensates of higher-dimension operators. The condensates of dimension-6 and higher are either connected with large uncertainties or they are even completely unknown. The theoretical uncertainty associated with these corrections therefore increases with increasing values of k.

The high mass range is dominated by the multi-meson final states. This region becomes more and more pronounced as l increases. Here, the branching fractions become smaller as the invariant mass of the corresponding final state approaches the kinematic limit. From the experimental point of view, this region is dominated by large statistical uncertainties. In addition, not all spectra are determined from data. For the four-meson final states for example, the prediction from Monte Carlo is used, since the statistics is too low to allow for a determination from data. In addition, the Monte Carlo simulation is not based on studies of the resonance structure in this case, because the experimental data in the strange sector to date is not sufficiently precise to allow for these studies. A phase space distribution is assumed instead in the Monte Carlo simulation. The theoretical uncertainty associated with the operator product expansion for increasing l however is smaller than in the case discussed before. As s approaches m_τ^2, contributions from perturbative QCD dominate and the influence from non-perturbative effects is small.

3. THE EXPERIMENT

In this section, a description of the LEP accelerator and the OPAL detector is given. On those detector components that are important for this analysis, i.e. the central tracking chamber and the electromagnetic calorimeter, a detailed description is given.

3.1 The LEP Accelerator

The e^+e^- storage ring LEP (Large Electron Positron Collider) is located at the European Center of Nuclear Research (CERN). The storage ring is 100 m below the surface in a tunnel with a circumference of 26.7 km. During the LEP-I phase from 1989 to 1995, beams of electrons and positrons were accelerated to 45.6 GeV. Several bunches of electrons and positrons were circulating in opposite directions and were brought to collision at four interaction points, where the detectors ALEPH, DELPHI, L3 and OPAL were build. The center of mass energy of $\sqrt{s} = 91.2\,\text{GeV}$ allowed for a study of the production and decay properties of the neutral weak boson Z^0.
From 1989 until fall 1995, an integrated luminosity of $165\,\text{pb}^{-1}$ has been collected per experiment. This corresponds to roughly 6 million Z^0 decays and allowed for many precision tests of the Standard Model in electroweak and strong interactions. In particular, during the LEP-I phase, a total of about 500 000 Z^0 boson decays into a pair of τ leptons have been recorded by the four experiments. This provided a unique environment to study the couplings of the Z^0 boson to heavy leptons, where many extensions of the Standard Model would induce significant modifications to the expectation. In leptonic τ decays, the structure of the leptonic current and the universality of the coupling of leptons to the W boson could be studied. Hadronic τ decays allowed for a study of the structure of the hadronic current and the determination of parameters

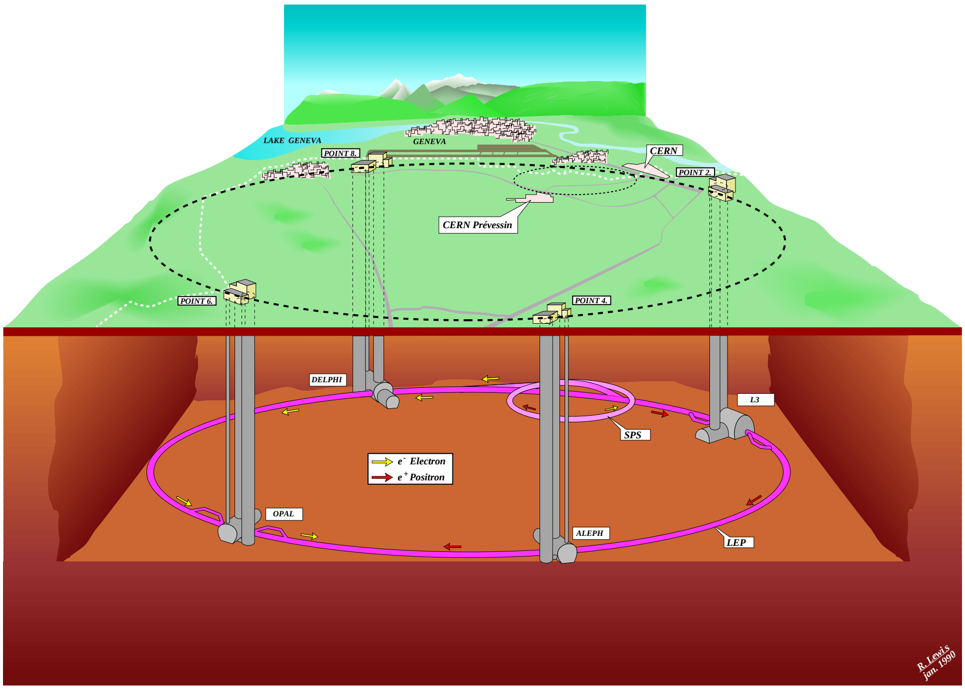

Fig. 3.1: The LEP storage ring.

of the Quantum Chromo Dynamics QCD, like the strong coupling constant α_s or the quark masses.
Since 1995, the energy of the colliding beams was progressively increased. This was achieved by inserting new and replacing old normal conducting cavities by superconducting ones. In 1996, a center of mass energy of $\sqrt{s} = 161\,\mathrm{GeV}$ was achieved which allowed for the study of production and couplings of the charged weak bosons $\mathrm{W}^{\pm}$. In 1997, at center of mass energy of $\sqrt{s} = 183\,\mathrm{GeV}$, the study of the production of Z^0 pairs and anomalous triple gauge couplings was of particular interest.
During the year 2000, the goal was to collect data at the highest energies possible. Finally, a center of mass energy of 208 GeV has been achieved. During the whole LEP period, not only tests of the Standard Model with unprecedented precision were possible. Especially during the last period, the search for new particles which are predicted e.g. by supersymmetric theories (SUSY) came into focus. In particular, the search for Higgs bosons, either the one predicted by the Standard Model or those from extended theories, was one of the main subjects. Since no evidence was found, OPAL was able to set a limit on the mass of the Standard Model Higgs boson of $m_\mathrm{H} > 114.1\,\mathrm{GeV}$ (at 95% CL). In these particle searches, data from τ lepton decays played an important role.
Finally, in the fall of 2000, LEP was switched off and the civil engineering for the LHC (Large Hadron Collider) project began. This accelerator, when started in 2007 will provide proton beams with an energy of $\sqrt{s} = 7\,\mathrm{TeV}$. New physics up to the TeV scale will come into reach.

3.2 The OPAL Detector

The OPAL detector (Omni Purpose Detector for LEP) [44] was one of four detectors at the $\mathrm{e}^+\mathrm{e}^-$ storage ring LEP. The detector had a length of 12 m, a diameter of 10 m and a total weight of roughly 3000 t. The detector, covering 98% of the total solid angle, provided the means for the identification and reconstruction

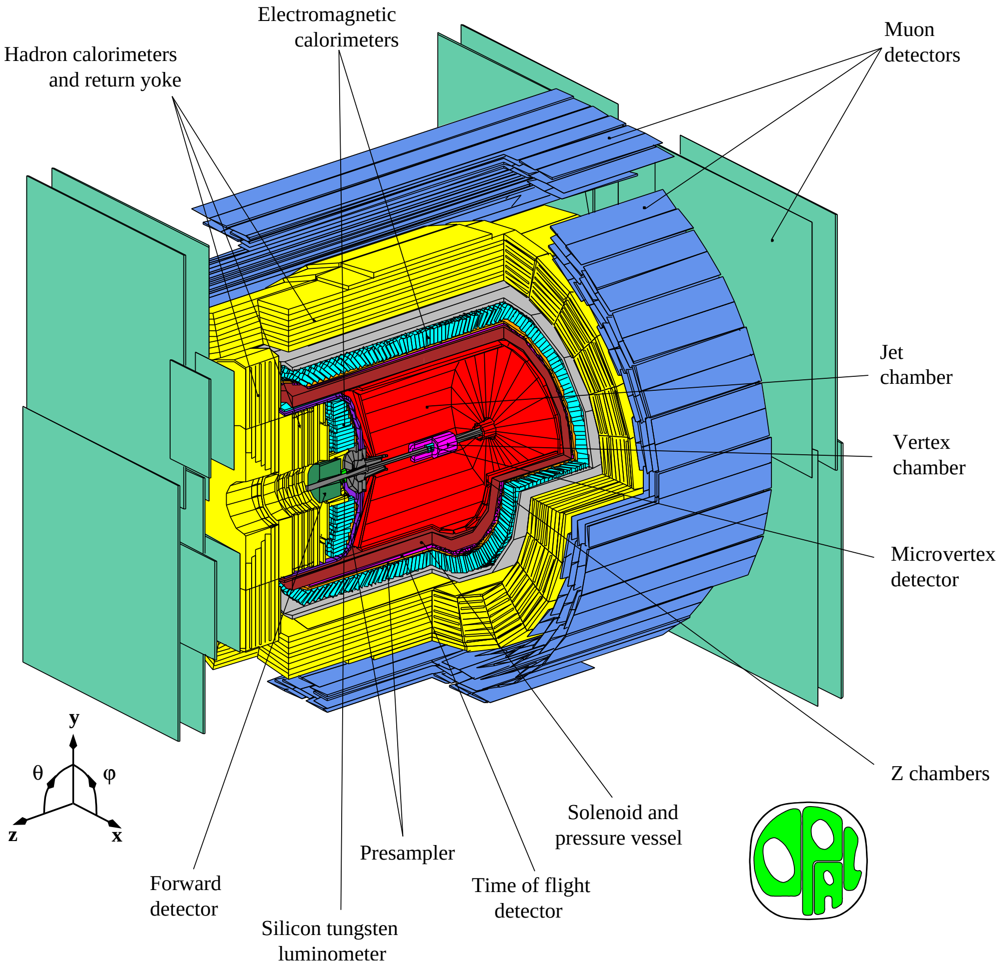

Fig. 3.2: The OPAL detector.

of $e^+e^- \rightarrow \bar{f}f$ events ($f \neq \nu$):

- The central tracking system provided the means for a measurement of direction, momentum and charge of particles. In addition, it provided the possibility of particle identification via measurement of the specific energy loss ($\mathrm{d}E/\mathrm{d}x$). The excellent spatial resolution allowed for the reconstruction of secondary vertices near the interaction region to detect long lived particles like B-mesons or neutral kaons.

- The calorimeter section allowed for the identification of photons and the measurement of their 4-momentum (electromagnetic calorimeter) as well as the identification of hadrons and the measurement of their energy (hadron calorimeter).

- The measurement of the luminosity via Bhabha scattering events in the forward direction using Silicon-Tungsten luminosity detectors.

In the following, a brief description of the components of the detector is given. Components which are vital for this analysis, i.e. the central jet chamber and the electromagnetic calorimeter are described in more detail. A detailed description of all components of the OPAL detector can be found elsewhere [44].

3.2.1 The Central Tracking System

- **Silicon-Microvertex Detector (SI)** consisted of two double layer silicon strip detectors, mounted at radii of 6.1 cm and 7.5 cm. The inner layer consisted of 11 tiles, the outer one of 14 layers. It covered a polar angle range of $|\cos\Theta| < 0.77$ (after the upgrade in 1996 it covered an angular range of $|\cos\Theta| < 0.88$). It played an important role in the reconstruction of secondary vertices, i.e. in the identification of mesons containing b-quarks. A resolution of 5 µm in the $(r-\phi)$-plane and 13 µm in z direction was achieved.

The Microvertex detector was surrounded by a pressure vessel which contained the central tracking system. It was filled with a gas mixture of argon (88.2%), methane (9.8%) and isobutane (2.0%) and it was operated at a pressure of 4 bar. The central tracking system consisted of the following components.

- **The Vertex Chamber (CV)** was a drift chamber of length 1 m. The inner radius of the chamber was at 8.8 cm, the outer radius at 23.5 cm. It was subdivided into 36 sectors, each containing two layers of sense wires. The innermost 12 layers were mounted parallel to the beam pipe. The outer 6 layer had a stereo angle of 4° in order to obtain the full 3D position information. A resolution of 55 µm in $(r-\phi)$ and 300 µm in z direction was achieved.

- **The Jet Chamber (CJ)** was a cylindrical drift chamber with a total length of 4 m. It covered the radial range from $r = 25\,\mathrm{cm}$ to $r = 185\,\mathrm{cm}$. In azimuthal direction it was subdivided into 24 sectors, each containing 159 signal wires with a radial distance of 10 mm. To resolve the left-right ambiguity, the signal wires were staggered by 100 µm. Between each pair of sense wires and between neighboring sectors, field wires were mounted that provided a uniform drift field. An ionization cloud, produced by a particle traversing the sensitive volume, had a drift velocity of 52.7 µm/ ns and a Lorentz angle of 20° relative to the anode plane. All wires were mounted parallel to the beam axis. The maximum drift distance was 3 cm at the innermost radius and up to 25 cm at the outermost radius.

  For every measured point, the full 3D information was obtained from the position of the corresponding sense wire, the measured drift time in $r-\phi$ and the charge collected at each end of the signal wires (z direction). A spatial resolution of 135 µm in the $(r-\phi)$ plane and 6 cm in z direction was achieved. The double track resolution was 2 mm. From the curvature of the track within the magnetic field ($B = 0.435\,\mathrm{T}$), the momentum and the charge of the particle was determined. The transverse momentum resolution achieved was

$$\frac{\sigma_{p_\mathrm{T}}}{p_\mathrm{T}} = \sqrt{(0.02)^2 + 0.0015/\,\mathrm{GeV}\cdot p_\mathrm{T}}.$$

  For particle identification, the specific energy loss ($\mathrm{d}E/\mathrm{d}x$) was used. The relative accuracy was

$$\frac{\sigma_{\mathrm{d}E/\mathrm{d}x}}{\mathrm{d}E/\mathrm{d}x} = 3.8\%.$$

- **The Z-Chamber (CZ)** consisted of 24×8 drift chambers, which covered the polar angular range up to $|\cos\Theta| < 0.72$. Each drift chamber had 6 layers of sense wires which were arranged perpendicular to the beam axis. By using the information from this device, the resolution could be improved to 300 µm in z direction.

The inner detector was contained in a solenoidal, homogeneous magnetic field of 0.435 T. The outer detector consisted of the following components:

3.2.2 The Outer Detector

- **The Time-Of-Flight System (TOF)** was used to measure the time of flight of particles coming from the interaction region. It consisted of 160 scintillation counters, forming a barrel of mean radius 2.36 m. A time resolution of 300 ps in the barrel region was achieved. After 1996 the system was extended to the endcaps ($0.85 < |\cos\Theta| < 0.97$), where a time resolution of 3 ns was achieved. It served mainly as trigger and for the rejection of cosmic ray events.

- **The Presampler (PB, PE)** was mounted in front of the electromagnetic calorimeter. It consisted of two layers of limited streamer tubes in the barrel region and 16 multi-wire proportional chambers in the endcap region. Since the material in front of the electromagnetic calorimeter corresponds to 2 radiation lengths X_0 in the barrel region (and up to 7 radiation lengths in some regions between the barrel and the endcaps), most showers start already within the pressure vessel or inside the solenoidal coil. This reduced the accuracy of the energy measurement. With the presampler, the multiplicity of the shower, which is proportional to the energy lost in the material in front of the calorimeter, was measured and this information could be used to correct the energy in the electromagnetic calorimeter.

- **The Electromagnetic Calorimeter (ECAL)** was used to identify electrons, positrons and photons and to measure their energy in a range from 100 MeV up to 100 GeV. Together with the hadron calorimeter it was used to separate electrons/positrons from hadrons. It was mounted between the magnetic coil and the return yoke. It consisted of the barrel region (covering the angular range of $|\cos\Theta| < 0.68$), the overlap region ($0.68 < |\cos\Theta| < 0.72$) and the endcap region ($|\cos\Theta| > 0.72$). Together they covered 98% of the total angular range.
  - **The Barrel Region** of the ECAL consisted of 9440 lead glass blocks which were mounted at a radius of 2445 mm from the beam pipe. Each block had a $(10 \times 10)\,\mathrm{cm}^2$ cross section and a length of 37 cm ($\widehat{=}24X_0$), so that electrons, positrons and photons were completely absorbed.

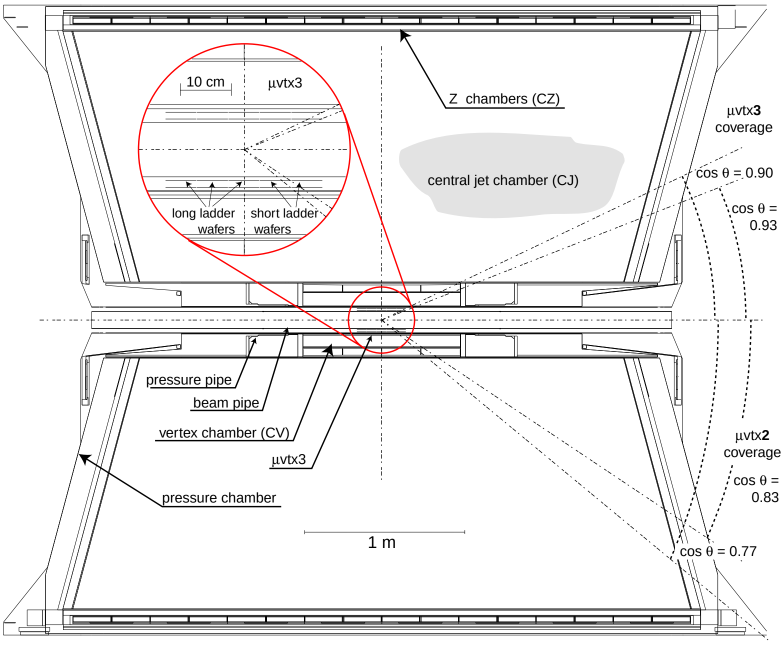

Fig. 3.3: The tracking system of the OPAL detector.

The Čherenkov light emitted when a particle enters a lead glass block was detected via photo multipliers. The calorimeter had a quasi-pointing geometry. Therefore, the total energy was almost completely contained within one single block.

  - **The Endcap Region** consisted of 1132 lead glass blocks with a cross section of $(9.4 \times 9.4)\,\mathrm{cm}^2$. They covered the angular range $0.81 < |\cos\Theta| < 0.98$. Depending on the radial position, they had a length of 380 mm, 420 mm or 520 mm, which corresponds to an average length of $20.4X_0$. All blocks were mounted parallel to the beam pipe.

The energy resolution, taking into account the material in front of the ECAL, was measured to be

$$\frac{\sigma_{E_\gamma}}{E_\gamma} = \left(\frac{0.160 \pm 0.003}{\sqrt{E_\gamma}}\right) \oplus (0.015 \pm 0.003) \tag{3.1}$$

and

$$\frac{\sigma_{E_\gamma}}{E_\gamma} = \left(\frac{0.218 \pm 0.025}{\sqrt{E_\gamma}}\right) \oplus (0.018 \pm 0.013) \tag{3.2}$$

for the barrel and the endcap region, respectively [47].

- **The Hadron Calorimeter** measured the energy of hadrons emerging from the electromagnetic calorimeter and it assisted in the identification of muons. It was subdivided into a barrel part (HB), two endcaps (HE) and two pole tips (HP). In the barrel, it consisted of 9 layers of limited streamer tubes, alternating with 8 iron slabs. It covered the radial range from $r = 339\,\mathrm{cm}$ up to $= 439\,\mathrm{cm}$ and it had a hadronic interaction length of $\sim 5\lambda$. In the endcap region, 8 layers of chambers alternated with 7 slabs of iron. Since there were already about 2.2 interaction lengths of material in front of the hadron calorimeter, the total hadronic energy could only be measured by combining the information from the hadronic and the electromagnetic calorimeter. An energy resolution of

$$\frac{\sigma_E}{E} = 120\%/\sqrt{E}$$

was achieved.

- **The Muon Chambers** consisted of 110 drift chambers in the barrel region that were mounted in four layers. In the endcap region, 2×2 layers of streamer tubes were used, which were oriented perpendicular to each other. The azimuthal and axial resolution was 1.5 mm and 2 mm, respectively.

3.2.3 The Luminosity Detector

To measure the luminosity in OPAL, e^+e^- pairs from Bhabha scattering events were used. This process is very well understood from the theoretical point of view and has a very high event rate. To measure the event rate, two detectors were mounted in forward direction which allow for an accuracy of 0.1%.

- **The Forward Detector (FD)** consisted of a system of drift chambers, proportional counters and a calorimeter of scintillating material with an interaction length of $24X_0$ in sandwich geometry. This detector covered the angular range from 47 mrad to 120 mrad.

- **The Silicon-Tungsten Detector (Si-W)** was mounted at $|z| = 240\,\mathrm{cm}$. It was introduced in 1993 to allow for a precise measurement of the luminosity. It consisted of 19 layers of silicon detectors with one layer of tungsten in between each pair, resulting in 22 interaction lengths. This detector covered the angular range from 25 mrad up to 59 mrad.

3.3 Coordinate System and Track Parameters

The coordinate system used in OPAL is as follows: The positive z axis is pointing parallel to the direction of flight of the electron, the x axis is pointing towards the center of the LEP storage ring. The polar angle Θ is measured relative to the z axis, the azimuthal angle ϕ is measured relative to the x axis and maps the plane perpendicular to the beam axis. In the axial magnetic field the trajectory described by the charged particles in OPAL is parametrized by five track parameters: κ, ϕ_0, d_0, $\tan\lambda$ and z_0. They are defined as follows:

- $\kappa = \frac{1}{2\rho}$ is the curvature of the track and ρ is the radius of the curvature.
- ϕ_0 is the azimuthal angle of the track tangent at the point of closest approach (p.c.a.).
- d_0 is the impact parameter at the p.c.a.. It is defined by

  $$d_0 = \hat{\phi} \times \vec{d} \cdot \hat{z},$$

  where $\hat{\phi}$ is the unit track vector at the p.c.a., $\vec{d}$ is the vector from the origin to the point of closest approach and $\hat{z}$ is the unit vector along the z axis.
- $\tan\lambda = \cot\Theta$ where Θ is the track angle measured relative to the z axis.
- z_0 is the z coordinate of the track at the point of closest approach.

4. EXPERIMENTAL ASPECTS

In this chapter, the experimental aspects of the analysis are discussed. This includes the calibration of the energy loss measurement in the central drift chamber. It had to be optimized for the use in the τ pair environment, which is described in detail in Chapter 4.1. In Chapter 4.2, the identification of photons from shower shapes in the electromagnetic calorimeter and the reconstruction of neutral pions is discussed. The Find Photon algorithm, which was developed for the measurement of non-strange spectral function was improved using a pairing scheme in order to reduce the number of fake photons and to increase the energy resolution. In Chapter 4.3, the identification and reconstruction of the four-momentum of neutral kaons is described. After the selection, all $\mathrm{K^0_S}$ candidates are subject to a 2C kinematic fit, which is explained in detail. Finally, in Chapter 4.4, the update of the τ Monte Carlo is discussed. This became necessary in order to include four-meson final states with kaons, which were not simulated so far.

4.1 Energy Loss Calibration in the τ Environment

The most important part in this analysis is the kaon identification via energy loss measurement ($\mathrm{d}E/\mathrm{d}x$) in the jet chamber. Since this is the only possibility to distinguish between pions and kaons in OPAL, a very good understanding of the effects caused by the dense multi-track environment in τ decays is vital for any analysis that requires particle identification.

The high Lorentz boost ($\gamma \approx 25$) of the τ lepton results in its decay products being contained in a narrow cone with a typical opening angle of 5°. In those cases, where the final state consists of more than one track, the $\mathrm{d}E/\mathrm{d}x$ measurement is known to be no longer reliable [43]. A systematic shift in the $\mathrm{d}E/\mathrm{d}x$ distribution was observed which lead to a misidentification of pions as kaons and thus to a reduced sensitivity in those cases where particle identification is required. A detailed study of the calibration procedure therefore has been carried out, using τ decays with at least three tracks in the final state. The effect, two very close tracks have on the measured energy loss has been studied on a hit-by-hit basis using drift time information.

This chapter starts with an introduction on particle identification via energy loss measurement. In Chapter 4.1.2, the standard OPAL calibration corrections are described. They can be split into corrections applied on a hit-by-hit bases and those applied on track level. The improvements in the energy loss calibration, using events from τ decays are described in Chapter 4.1.4. The adjustment of the experimental error is discussed in Chapter 4.1.5.

4.1.1 Energy Loss of Particles in Matter

The only means to distinguish pions from kaons in OPAL is via the measurement of the specific energy loss in the jet chamber. The mean energy loss per unit length of an incident particle of charge 1 is described by the Bethe-Bloch equation [48, 49]

$$-\frac{\mathrm{d}E}{\mathrm{d}x} = C_1 \rho \frac{Z}{A}\frac{1}{\beta^2}\left(\frac{1}{2}\ln\left(\frac{2m_\mathrm{e}c^2\eta}{I^2}\right) - \beta^2 + \ln\beta\gamma - \frac{\delta(\beta)}{2} - \frac{C_2}{Z}\right), \tag{4.1}$$

where C_1 is defined as

$$C_1 = 4\pi N_\mathrm{A} r_\mathrm{e}^2 m_\mathrm{e} c^2 = 0.307\,\mathrm{MeV\,cm^2/g}$$

and

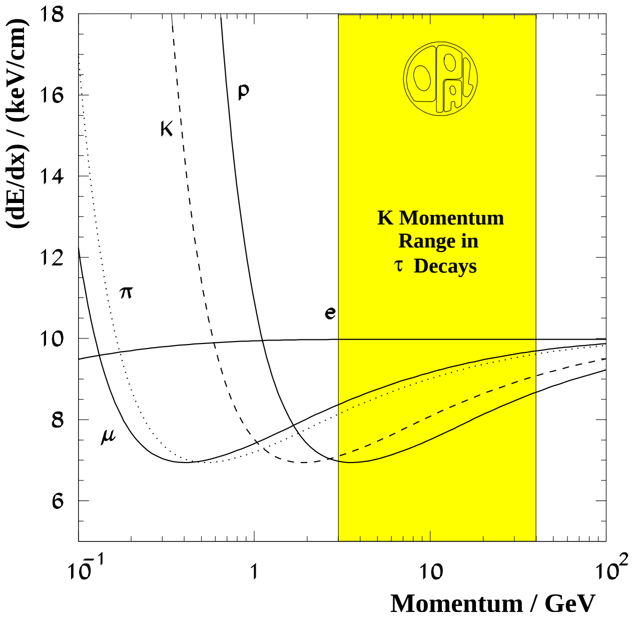

Fig. 4.1: Energy loss as a function of the particle momentum. The predicted energy loss in keV/ cm for different particle species is displayed. The expectation for kaon (pion) tracks is given by the dashed (dotted) curve. The momentum range relevant in this analysis ($3\,\mathrm{GeV} \leq p \leq 35\,\mathrm{GeV}$) is indicated by the shade area. In this range, the expected separation between kaons and pions is at least 1.5σ.

- r_e is the classical electron radius
- m_e^2 is the mass of the electron $\times c^2$
- N_A is Avogadro's number
- I is the mean excitation energy
- Z is the atomic number of the absorbing material
- A is the atomic weight of the absorbing material
- ρ is the density of the absorbing material
- δ is the density correction described below
- η is the maximum energy transfer in a single collision.

There are two additional corrections in Equation 4.1, $\delta/2$ and C_2/Z, which apply for high and low energetic particles, respectively.

- The density correction $\delta(\beta)/2$ accounts for the fact that the electric field of high energetic particles tends to polarize the atoms along their path. Electrons at some distance from the path of the particle will be shielded from the full electric field intensity. Collisions with these outer lying electrons will therefore contribute less to the total energy loss than predicted by the Bethe-Bloch formula. This effect, which depends on the density of the material, becomes more important as the particle energy increases.
- The shell correction C_2/Z depends on the atomic number of the material and becomes important as the velocity of the incident particle approaches the orbital velocity of the bound electrons. At such energies, the assumption that the electron is stationary with respect to the incident particle is no longer valid. Because of the high energy of the particles considered here, this term is neglected.

For a given material, the mean energy loss per unit length is a universal function of $\beta\gamma$ for all particle types. It shows a characteristic decrease of the energy loss proportional to $1/\beta^2$ for low energetic particles, and it reaches a minimum at around $\beta\gamma \sim 3$. Such particles are called minimum ionizing particles (MIPS). In the region beyond this point, a logarithmic rise is observed (however partly canceled by the density correction) which ends in the Fermi plateau.

The mean energy loss as a function of the particle momentum in the OPAL jet chamber is displayed in Figure 4.1. As a function of momentum, the curve is no longer universal but still shows the characteristic behavior discussed above. By measuring simultaneously the mean energy loss and the momentum of a track, particle identification becomes possible. The momentum range relevant for this analysis ($3\,\mathrm{GeV} \leq p \leq 35\,\mathrm{GeV}$) is

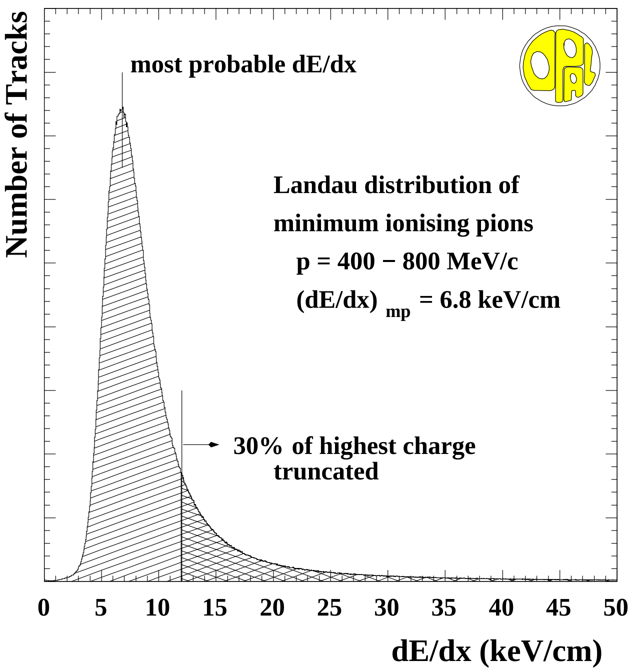

Fig. 4.2: Landau distribution for minimum ionizing pions ($p = (0.4 - 0.6)$ GeV). A cut at $|\cos\Theta| < 0.7$ was applied and a minimum of 40 dE/dx hits was required. The most probably value is about 6.8 keV/ cm. In order to determine the average energy loss from a couple of dE/dx samples, the method of truncated mean is used. The 30% highest energy loss samples are rejected and are not used to calculate the average energy loss.

indicated by the shaded area. In this region, the expected energy loss for electrons as a function of the momentum does not vary much. Electrons have the highest dE/dx of all particles considered. The energy loss for protons is the smallest. Protons are too heavy to occur in τ decays, however they occur in $q\bar{q}$ background events with low multiplicity. Muon tracks have an energy loss quite similar to the one for pions. They can be reliably identified by the muon chambers, so that no dE/dx measurement is necessary in this case. The expectations for kaons and pions, which are of particular interest here, are displayed as dashed and dotted lines, respectively.
The distribution of energy loss of individual particles follows a Landau distribution which is displayed in Figure 4.2. It peaks at low energy transfers which originates from distant collisions. One-sided non-gaussian tail is due to high energy knock-on collisions with shell electrons.

4.1.2 The Energy Loss Measurement in OPAL

Details of the OPAL jet chamber have already been discussed in Chapter 3.2.1 and will not be repeated here. When a charged particle passes through the jet chamber it produces an ionization cloud. This cloud travels at a constant speed of $v_D \approx 53\,\mu\text{m/ns}$ in the homogeneous drift field to the sense wires, where it produces a signal pulse. This signal pulse is integrated over $\Delta t = 200$ ns, which corresponds to a drift distance of ~ 1 cm. The integral is proportional to the energy loss of the particle in this particular drift volume. There is a maximum sample size of 159 individual measurements for a given track. Certain quality criteria are imposed on each individual hit and on the total hit sample used to evaluate the mean energy loss for each track [51].

- Only hits, which are assigned to a track in the track fit are used. A hit is discarded, if a second one is recorded on the same wire within $\Delta t = 200$ ns. Hits are rejected, if a second one is expected within 3 mm as calculated from the track parameters, since these hits could no longer be resolved. If a hit is as close as 2 mm to the anode plane, it is discarded since the drift field is no longer homogeneous, which affects the energy loss measurement. For tracks crossing the sector boundaries, hits are rejected for the same reason if they have a distance of 1 cm or less to the field wires. In the following, all hits fulfilling these quality criteria are called ‘dE/dx hits’.

- Each sample of hits recorded for a given track has to have a minimum size in order to determine the mean energy loss with sufficient accuracy. The large inherent width of the energy loss distribution as explained above, makes it necessary to require at least 20 of them along each track where particle identification is required.

The individual samples for a given track are distributed according to a Landau distribution. To calculate the mean energy loss, the method of truncated mean [50] is used, where 30% of the highest measured charges is discarded. No truncation at the lower tail of the distribution is applied. The mean is then calculated using the remaining 70% of the measured hits. Following this procedure, basically the gaussian like peak from soft collisions is used for the calculation. Requiring at least 20 hits in each sample has the advantage, that in the limit of many tracks, the distribution of the truncated means follows a gaussian distribution.

4.1.3 The Standard OPAL Calibration

The measured energy loss for kaons and pions is quite similar in the momentum range considered here (see Figure 4.1). The relative difference is of the order of 10% or less depending on the particle momentum. The uncertainty of the measurement, which depends e.g. on the sample size for a given track and on its polar angle, is of the order of 3%. A reliable particle separation is therefore possible with a significance of more than 1.5σ over the full momentum range relevant here. This however requires an accurate and bias-free measurement of the energy loss.

In the following, the standard OPAL calibration corrections are described. They can be split into corrections applied on a hit-by-hit basis and those applied on the mean energy loss of the corresponding track. These corrections were determined using high multiplicity $q\bar{q}$ events. A summary of all corrections applied either to data events and/or events from Monte Carlo simulation are summarized in Table 4.1.

- **Corrections on a Hit-by-Hit Basis:**
  - Effective Charge: If a high number of charged particles passes one sector of the drift chamber at the same time, the amplitude, homogeneity and stability of the drift field as created by the field wires is affected. The size of the effect depends on the rate of tracks, the synchrotron radiation and the gas gain.
  - Saturation Correction: Due to the high gas gain of 10^4, saturation effects have an impact on the accuracy of the energy loss measurement. Near the sense wires, a screening effect is observed, which is due to the remaining ions from the amplification of the electrons arriving first. The effect is largest for tracks perpendicular to the wires, where the electrons reach the wire almost all at the same spot. In addition, for short drift times, the electron cloud is not spread out much by diffusion. For large drift distances or tracks with a small polar angle relative to the direction of the wire, where the ions are distributed longitudinally and the space charge density is low, the effect becomes smaller.
  - Attachment Correction: The energy deposition of a charged particle in the jet chamber is not completely recorded at the sense wires. Contaminations of electronegative material (e.g. oxygen) in the drift chamber gas leads to an absorption of the electrons produced by the passage of the charged particles. The size of this effect depends on the drift distance.
  - Relative Gain Correction/Asymmetry Correction: The amplification factors are different due to differences in the electric field or the gain constants of the amplifiers. Systematic differences also arise from field distortions in the vicinity of the sector boundaries. The gain differences are corrected using calibration factors derived from the data.
  - Gas Density Correction: During data taking, the pressure and the density of the chamber gas varied. This effect was corrected for by analyzing muon tracks from dimuon events as function of the gas density. A typical time scale for readjustments of the density correction was of the order of one week.
  - Wine Bottle Effect: As the ionization cloud approaches the anode wires, the field is no longer homogeneous. The electrons are drifting radially towards the sense wire. This effect is called wine bottle effect. Correction factors are applied depending on the sector and wire number and on the track angle relative to the drift direction.

ID	MC	Data	Description
0	√	√	Saturation (theta)
1	-	√	Cross Talk (local phi)
2	-	√	Correlation (theta x local phi)
3	-	√	Attachment
4	-	√	Wire to Wire Gain
6	-	√	Sector to Sector Gain (if no gas density)
8	-	√	Wine Bottle
9	√	√	Geometric Track Length (theta)
10	√	√	Geometric Track Length (local phi)
11	-	-	Curvature
12	-	√	Logarithmic Track Length
14	√	-	Smear MC
15	√	√	Correction of Truncated Mean
16	-	√	Asymmetry Correction
17	√	√	Correction to Number of Hits
18	√	√	Correction to Effective Charge
19	√	-	MC Rescaling to Different Bethe-Bloch Curve

Tab. 4.1: Standard corrections to the energy loss measurement applied to $\mathrm{d}E/\mathrm{d}x$ hits in data and/or Monte Carlo events.

  - True Track Length: The measured charge on each individual wire depends on the projected track length on the direction of the wire. Therefore the measured charged is normalized to 1 cm track length. This normalization depends on the polar angle θ with respect to the beam axis and on the angle relative to the drift direction given by the Lorentz angle.

- **Corrections on Track Basis:**
  - In the calculation of the truncated mean, 30% of the highest energy loss measurements are discarded. However, 0.3 times the number of $\mathrm{d}E/\mathrm{d}x$-hits is not always an integer number. This leads to a shift in the calculated truncated mean, which depends on the total number of measured hits.
  - The value obtained for the mean energy loss via the calculation of the truncated mean depends on the number of hits in the sample. This dependence has been studied using isolated tracks as well as tracks in dense particle environments. This correction is only applied to hits with $|\cos\Theta| < 0.8$.
  - Cross Talk: If a signal is recorded on one wire, a signal of opposite polarity is observed on the two neighboring wires. This effect depends on the azimuthal angle ϕ_{local} of the track relative to the sense wire plane.

4.1.4 Energy Loss Measurement in τ Decays

Before any of the corrections mentioned above is applied, either on hit level or on track level, a drift time correction is calculated for each individual hit. This correction is explained in the following text and is illustrated in Figure 4.3(b).

The measurement procedure of the energy loss for a single track traversing the jet chamber has been described in Chapter 4.1.2. If an additional track passes through the same sector, a second pulse will be created on each sense wire, which overlaps with the tail of the first one. The contribution of the tail is estimated via extrapolation using a reference pulse [51], where the normalization of that pulse is proportional to the integral over the first pulse. This estimated contribution is then subtracted from the measured integral over the second signal pulse.

In τ decay events, where the final state consists of more than one track, the $\mathrm{d}E/\mathrm{d}x$ measurement is known not to be reliable [43]. The number of tracks that were identified as kaons was much higher than the expectation and this could not be explained e.g. by the uncertainty on the branching fraction in strange τ decays (see Figure 4.15). Therefore, in previous analyses of 3-prong τ decays, only the energy loss information of the first track relative to the anode plane in the corresponding sector has been used for particle identification purposes. All subsequent tracks have not been considered. This reduces the available statistics by roughly

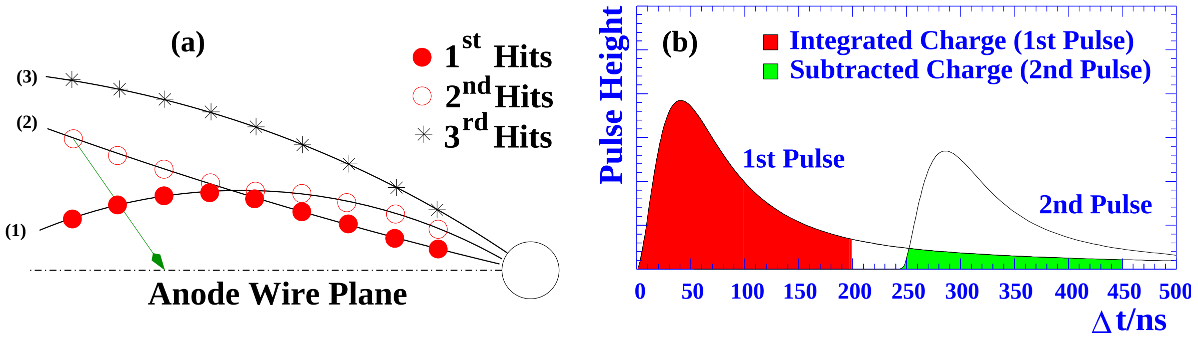

Fig. 4.3: Illustration of the tail subtraction procedure. (a) shows one half-sector of the OPAL central drift chamber with three tracks. The arrow indicates the drift direction of the ionization cloud following a path given by a Lorentz angle of 20°; (b) illustrates the signal seen on the sense wire for two successive pulses.

a factor of three. In addition, without particle identification for all tracks, the expected background rate is higher. In the selection of a $K^-\pi^+\pi^-\nu_\tau$ final state, the contributions from $K^-K^+\pi^-\nu_\tau$ and $K^-K^+K^-\nu_\tau$ events represent an irreducible background if particle identification is not required for all tracks.

The reference pulse used in the correction of the energy loss measurement was determined using $q\bar{q}$ events. Compared to τ decay events, they have on average a larger track multiplicity and therefore a lower energy. The lower energy of the decay products leads to a larger spatial separation of the tracks in the event. This means that the drift time difference between two subsequent hits on the same anode wire on average is larger in multihadronic events compared to τ decay events and thus, the correction required is considerably smaller. The distribution of the average drift time difference as observed in multihadronic events and in τ decays is illustrated in Figure 4.4. Especially drift time differences in the range $(200 - 400)$ ns, where the correction is particularly large, are much more frequent in τ decays than in multihadronic events. If, in the above correction procedure, the tail correction for 'second pulses' is overestimated, this leads to a systematic shift in the energy loss measurement towards lower values and thus to a misidentification of pions as kaons (see Figure 4.1).

4.1.4.1 Drift Time Correction

In order to quantify the systematic shift in the energy loss measurement as a function of the drift time difference between two subsequent hits, and in order to determine an optimized reference pulse, the following track topology was selected from the data. Tracks that have 'first hits' as well as 'second hits' and a

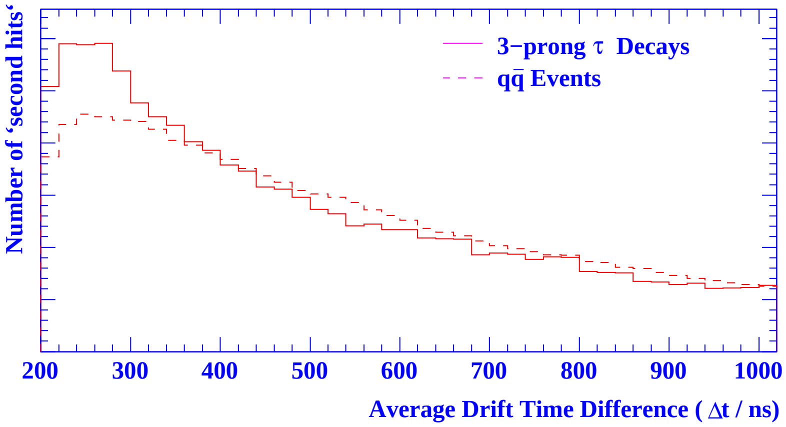

Fig. 4.4: Distribution of the drift time differences in τ decays compared to $q\bar{q}$ events. The distribution obtained using τ decays is given by the solid line. The distribution obtained using high multiplicity multi-hadronic events is displayed as dashed histogram. For τ decays, the average distance between two successive hits on the same sense wire is considerably smaller.

momentum greater than 3 GeV were used. This means that only events have been used, where a second track traverses the same sector of the drift chamber and these two tracks have an intersection point in the $r - \phi$ plane within the sensitive volume. This is illustrated in Figure 4.3(a). The tracks (1) and (2) fulfill the above requirements. The 'first hits' ('second hits') on each track are illustrated by the full (open) dots. Thus, for a given track, some of the hits do not need tail subtraction ('first hits') and some hits do need tail subtraction ('second hits'). Using 'first hits' only (given there are at least 20 of them) the expected energy loss $(\mathrm{d}E/\mathrm{d}x)_{\mathrm{exp}}$ for a the track is calculated. The 'second hits' of the same track were then used to obtain the measured energy loss $(\mathrm{d}E/\mathrm{d}x)_{\mathrm{meas}}$. The measured energy loss, normalized to the expectation was then analyzed as a function of the drift time difference Δt between two successive hits on the same anode wire[1]. The result obtained is displayed in Figure 4.6(a). For two hits that are as close as $\Delta t = 200$ ns, the observed deviation is of the order of 10% of the expected energy loss. In the region between $400\,\mathrm{ns} < \Delta t < 900\,\mathrm{ns}$ the measured $\mathrm{d}E/\mathrm{d}x$ is slightly overestimated. The standard correction is finally switched off for pulses with a drift time difference of more than 1000 ns which produces the step visible there. Weighted with the Δt distribution of all measured hits, this gives on average the correct mean energy loss for high multiplicity events. For multiprong τ decays, however, the distribution of drift time differences, as illustrated in Figure 4.4, is different and the mean energy loss for the corresponding track tends to be too low. This leads to the systematic misidentification of kaons as pions.

The same procedure can be used in those cases where a third track is present in the same sector. Again, the measured energy loss, normalized to the expectation is calculated and displayed in Figure 4.6(b). The distribution is analyzed as a function of the drift time relative to the first hit observed on the corresponding anode wire. Since a minimum drift time difference of 200 ns is required for two successive hits by the quality criteria, the distribution starts only at a Δt of ~ 400 ns.

For this analysis, a new reference pulse has been developed that avoids the shortcomings of the standard one using the distribution as obtained from the analysis of 'second hits'. A parametrized pulse shape was used here instead of a binned one in order to avoid artifacts from the binning like the dip at $\Delta t \approx 500$ ns. The new reference pulse is of the form

$$\begin{aligned} P_{\mathrm{norm}} = & \Big(p_1 \Delta t \exp\left(-\frac{\Delta t}{p_2}\right) + p_3 (\Delta t)^2 \exp\left(-\frac{(\Delta t)^2}{p_4}\right)\Big) \\ & + \Big(p_5 \Delta t \exp\left(-\frac{\Delta t}{p_6}\right) + p_7 (\Delta t)^2 \exp\left(-\frac{(\Delta t)^2}{p_8}\right)\Big) \\ & + \Big(\tilde{p}_1 + \tilde{p}_2 \Delta t\Big) \end{aligned} \tag{4.2}$$

to describe the short-range and the long range part respectively plus a linear contribution. The p_i are parameters that are optimized using the dense environment in τ decays. The numerical values are given

---

[1] The left-right ambiguity, which in principle exists if two tracks pass on different sides of the anode plane, is treated properly here, since the correction is applied based on measured drift times and not on the spatial separation of the tracks.

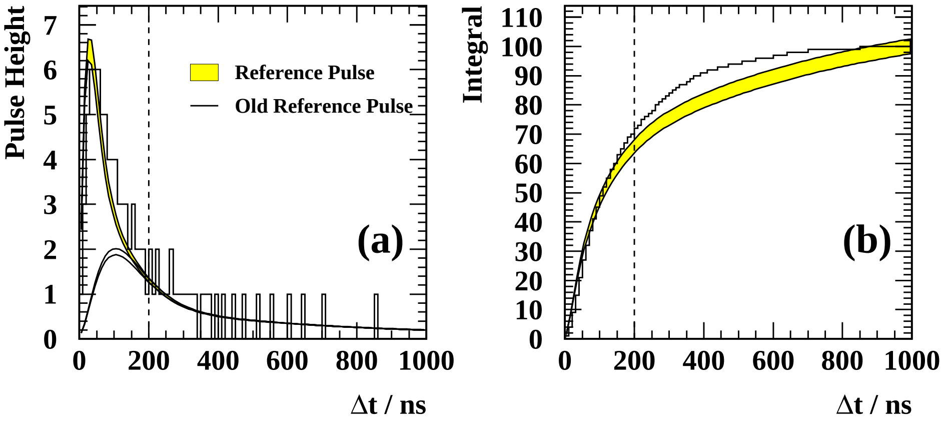

Fig. 4.5: In (a), the new normpulse is shown as shaded band in arbitrary units. The long range part is shown separately. The width represents the uncertainty on the parametrization. The old, binned normpulse is shown as histogram. In (b), the integral over the reference pulses as used in the tail subtraction is displayed.

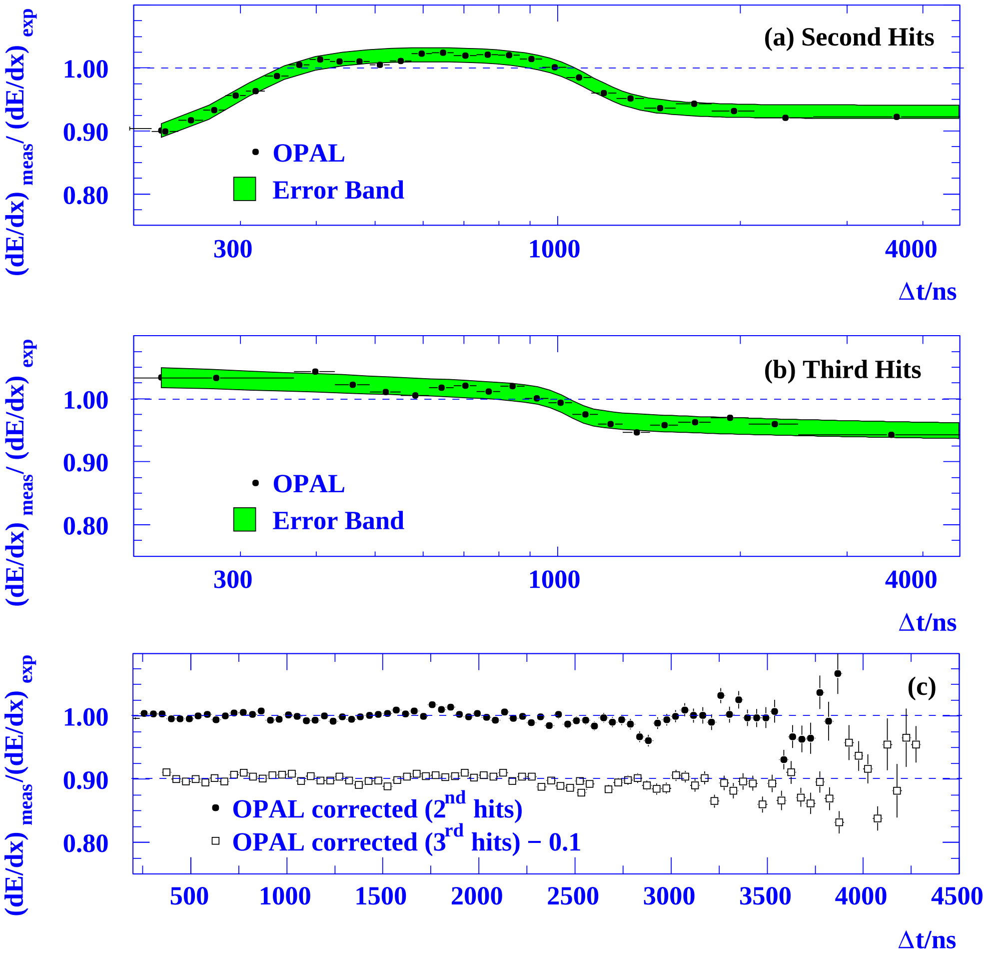

Fig. 4.6: Measured energy loss normalized to the expectation as a function of time difference between two measured hits (200 ns $\widehat{=}$ 1.054 cm). The observed deviations using the standard correction are shown for (a) 'second hits' and (b) 'third hits'. The error band reflects the 1σ error band of the parametrization. (c) shows the same distribution after all corrections have been applied. For better visibility, the distribution for 'third hits' is shifted by -0.1 in the plot.

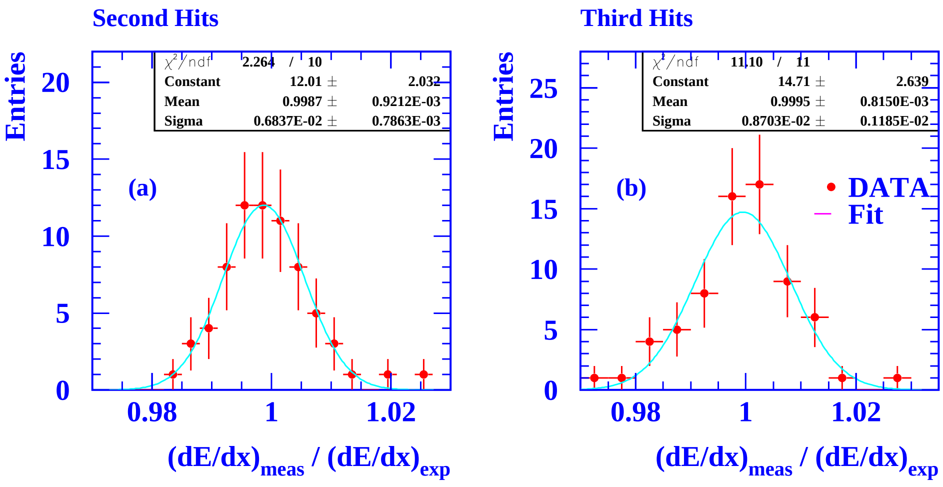

Fig. 4.7: Systematic bias in $(\mathrm{d}E/\mathrm{d}x)_{\mathrm{meas}}/(\mathrm{d}E/\mathrm{d}x)_{\mathrm{exp}}$ for second and third hits in plot (a) and (b), respectively. No significant bias was observed in both cases. The resolution in the plotted quantity is below 1%.

Normpulse Parametrization

Long Range Part		Short Range Part		Linear Part ($\times 10^{-2}$)	
p_1	5.43 ± 0.13	p_5	0.0407 ± 0.0001	$\tilde{p}_1$	-8.69 ± 0.8
p_2	2.17 ± 0.03	p_6	26.03 ± 0.13	$\tilde{p}_2$	-0.02 ± 0.004
p_3	1.04 ± 0.12	p_7	0.117 ± 0.004		
p_4	1.72 ± 0.07	p_8	4.96 ± 0.04		

Tab. 4.2: Parameters of the optimized pulse shape. The parameters are given separately for the short range and the long range part, respectively.

in Table 4.2. The shaded band in Figure 4.6(a) and (b) represents the uncertainty in the parametrization of the pulse shape. The new correction is applied to all hits, not only to those where the preceding hit is within $\Delta t \approx 1000\,\mathrm{ns}$ (5 cm) of the preceding pulse, to avoid the s-shaped structure. The new reference pulse is displayed in Figure 4.5. The new pulse is displayed as a smooth curve. The binned histogram represents the old, binned pulse as used in the standard OPAL correction. The new pulse has a steeper rise for very small Δt and a smaller tail for higher drift time differences.

The measured energy loss, normalized to the expectation as a function of the drift time difference using the new reference pulse, is displayed in Figure 4.6(c). The corresponding distribution for 'second hits' is displayed as full dots. The distribution shows a flat behavior over the whole range of observed drift time differences.

The correction procedure using a reference pulse is applied iteratively, i.e. the first pulse is used to correct the second one, the first and corrected second pulse are used to correct a possible third pulse and so on. Therefore, the chosen reference pulse is valid for any jet topology [51]. The same reference pulse is therefore used to correct the sample of 'third hits'. The corrected distribution in this case in displayed as open dots in Figure 4.6(c). Also this distribution shows a flat behavior over the full range of observed drift time differences. This distribution is shifted by -0.1 for illustration purposes. As a result of this procedure, a $\mathrm{d}E/\mathrm{d}x$ bias reduction to better than 1% in $(\mathrm{d}E/\mathrm{d}x)_{\mathrm{meas}}/(\mathrm{d}E/\mathrm{d}x)_{\mathrm{exp}}$ has been achieved, which is illustrated in Figure 4.7.

4.1.4.2 Cross Talk Correction

When a signal is present at a sense wire, a signal of opposite polarity is induced in the neighboring wires, which affects the accuracy of the energy loss measurement. This effect is called cross talk. It has been analyzed on a hit-by-hit basis as a function of the time difference $\Delta t = t_2 - t_1$ between signals recorded on neighboring wires for the same track (see Figure 4.8(a)). It is a function of the local azimuthal angle ϕ_{local} of the track within the corresponding sector and a function of the curvature of the track.

This effect is analyzed using muon tracks from $\mathrm{Z}^0 \to \mu^-\mu^+$ events. Since the effect is also a function of the curvature of the track, i.e. a function of the momentum, muons from τ decays involving muons are also used. For a given track, the measured energy loss, normalized to the expectation as calculated using the Bethe-Bloch parametrization, is analyzed as a function of the drift time difference $\Delta t = t_2 - t_1$ between signals on two neighboring anode wires. The size of the effect was found to be dependent on the polar angle. It was therefore analyzed in seven bins in the range $-0.9 \leq \cos\Theta \leq 0.9$. The result is displayed in Figure 4.8 for the bin $-0.1 \leq \cos\Theta \leq 0.1$, where the effects is largest (crosses) and as integral over the full $\cos\Theta$ range as full dots. The effect is of the order of -5% with respect to the expectation for $\Delta t = 0$. In this case the tracks have very high momentum and they traverse the jet chamber very close to the anode plane. The effect is $+5\%$ with respect to the expectation for a high momentum track that passes the sector close to the cathode plane or for low momentum tracks with large curvature.

The observed effect is parametrized as a function of Δt

$$C(\cos\Theta,\, \Delta t) = \sum_{i=1}^{3} A_i(\cos\Theta) \cdot (\Delta t)^{i-1}, \qquad (4.3a)$$

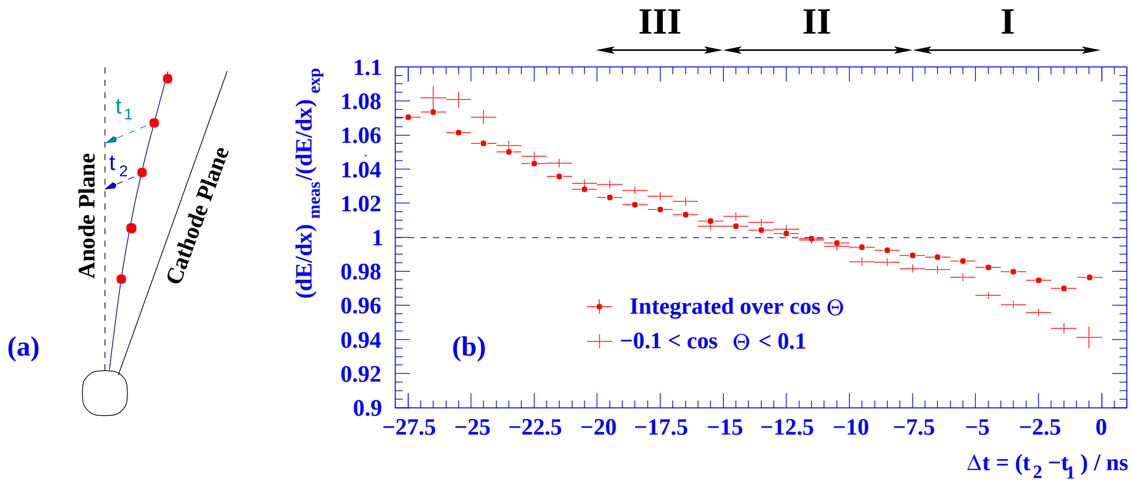

Fig. 4.8: Illustration of the cross talk correction. In plot (a), the drift time difference $\Delta(t_2 - t_1)$ as used in the analysis of the cross talk correction is illustrated. In plot (b), the cross talk correction as determined using muons from τ decays and $Z^0 \to \mu^+\mu^-$ events is displayed. This effect was studied in seven $\cos\theta$ bins. The results is displayed for the bin $-0.1 \leq \cos\Theta \leq 0.1$, where the effects is largest (crosses) and integrated over the full momentum range (full dots). The size of the correction is up to 5%. The regions marked on top of the plot refer to the explanations as given in the text.

where the A_i are functions of the polar angle $\cos\Theta$

$$A_i(\cos\Theta) = \sum_{j=1}^{4} a_i^{(j)} \cdot |\cos\Theta|^{j-1}. \tag{4.3b}$$

The numerical values for the parameters a_i are given in Table 4.3.
In [43], an additional correction as a function of the local azimuthal angle of the track ϕ_{local} in the sector of the jet chamber was introduced. This effect was found by analyzing $Z^0 \to \mu^+\mu^-$ on track level, i.e. the mean energy loss of the track. This effect is displayed in Figure 4.9 as open dots. The mean energy loss for high energetic muons from $Z^0 \to \mu^+\mu^-$ is expected to be 9.7 keV/ cm. For $\phi_{\text{local}} = 0$ this value is observed within the experimental uncertainties. Close to the anode plane ($|\phi_{\text{local}}| \approx 1^\circ$) the observed mean energy loss for a high energetic muon tracks is $\sim 2\%$ below the expectation. This corresponds very well to the results obtained in Figure 4.8 in region I. Due to the influence from cross talk, the measured energy loss is lower than the expectation. With increasing $|\phi_{\text{local}}|$, this effect becomes smaller (region II). At the sector boundaries, close to the cathode plane, the measured energy loss is again overestimated (region III). The same event type was analyzed as in [43]. With the hit based cross talk correction, used instead of the track based one, the ϕ_{local} dependence is no longer visible in Figure 4.9. The effect can therefore be fully explained by cross talk effects, which have been corrected using the hit-based procedure, developed in this work.

4.1.4.3 Anode/Cathode Plane Correction

If a track is within one or two cm of the anode- or cathode plane in the jet chamber, the drift field is no longer homogeneous. This affects the accuracy of the energy loss measurement for tracks near the sector boundaries. In order to study the size of this effect and to determine a correction function, $Z^0 \to \mu^-\mu^+$ events have been used. These events were tagged by requiring exactly two tracks in the event. One muon was

	$a_i^{(1)}$	$a_i^{(2)}$	$a_i^{(3)}$	$a_i^{(4)}$
A_1	0.947	0.156	-0.283	0.192
A_2	-0.004	0.0188	-0.0330	0.0204
$A_3(\times 10^{-3})$	0.0202	0.276	-0.328	0.119

Tab. 4.3: Parameters for the cross talk correction.

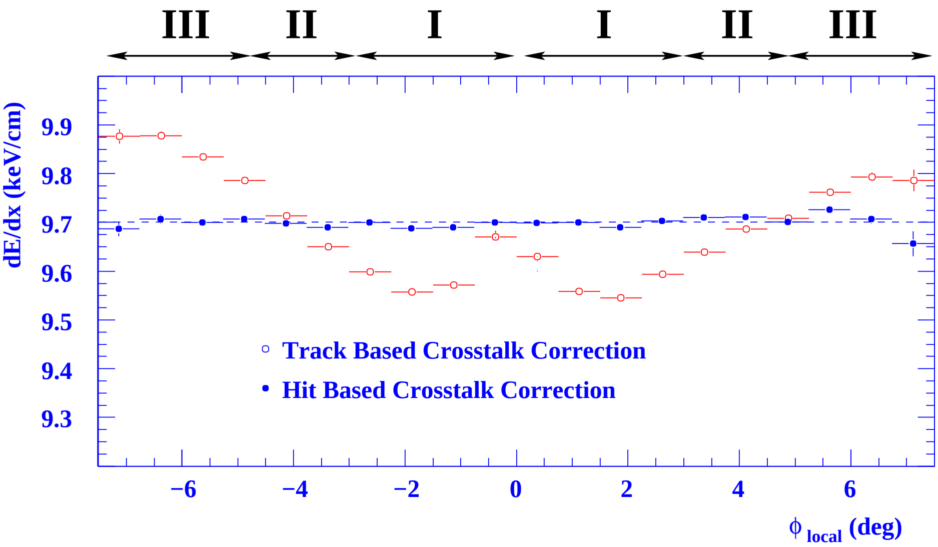

Fig. 4.9: The measured mean energy loss for tracks from $Z^0 \to \mu^+\mu^-$ events. The open dots represent the distribution using the standard OPAL cross talk correction. The full dots represent the same distribution using the hit-based cross talk correction developed in this work. The regions marked on top of the plot refer to the explanations as given in the text.

tagged by cutting on its energy ($|E_{\text{beam}} - E_{\mu^-}| < 2\,\text{GeV}$). Background contributions from other di-lepton events were reduced by requiring associated hits in the muon chambers and an energy deposition of less than 1 GeV in the electromagnetic calorimeter. Remaining muons from τ decays, which will not have the expected energy due to the additional neutrino are discarded by requiring an acollinearity angle of less than 1°.

The energy loss measurement is then analyzed as a function of the distance to the anode/cathode plane using the muon in the opposite hemisphere. Since the energy of the muon is known in this case, the expected energy loss can be calculated using the prediction from the Bethe-Bloch parametrization.

The measured energy loss, normalized to the expectation is displayed in Figure 4.10 and Figure 4.11 separately for μ^- (full dots) and μ^+ (open dots) as a function of the distance to the cathode plane and the anode plane, respectively. A deviation of up to 3% relative to the expectation was observed for drift times of $\approx 200\,\text{ns} \mathrel{\hat{=}} 1\,\text{cm}$. For drift times larger than $600\,\text{ns} \mathrel{\hat{=}} 3\,\text{cm}$, no correction is necessary any more in all cases. Linear functions $A(\Delta t)$ and $C(\Delta t)$ were used to correct for the observed effects close to the anode

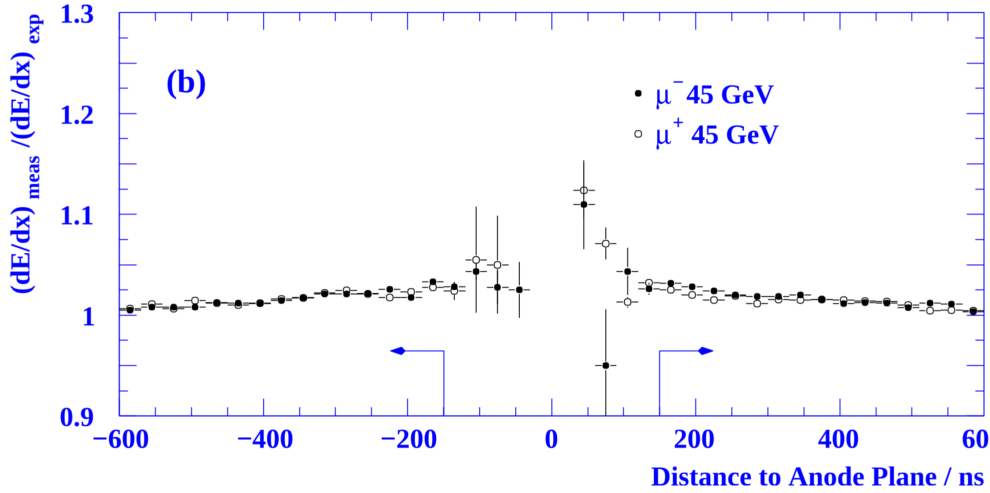

Fig. 4.10: Anode and cathode plane corrections, determined using $Z^0 \to \mu^+\mu^-$ events. The measured energy loss, normalized to the expectation as calculated from the Bethe-Bloch parametrization, is displayed as a function of the distance to the anode plane.

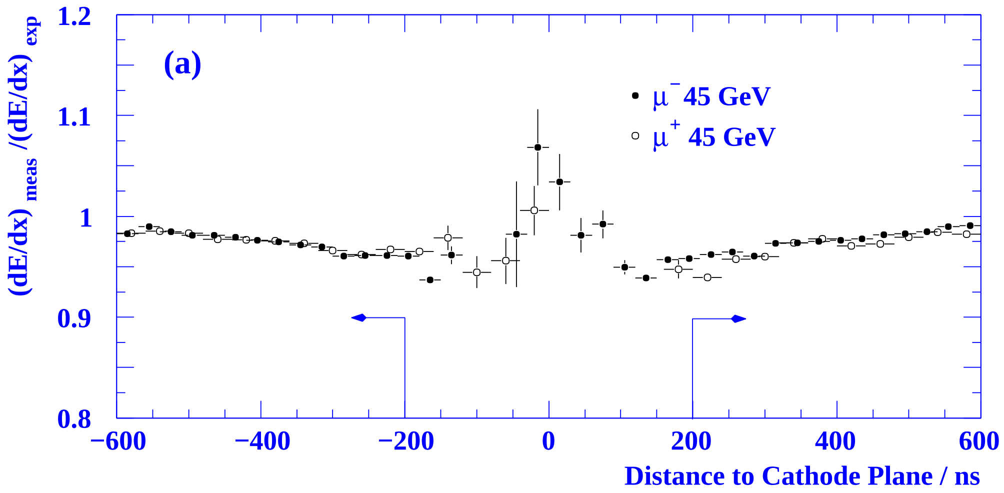

Fig. 4.11: Anode and cathode plane corrections, determined using $Z^0 \rightarrow \mu^+\mu^-$ events. The measured energy loss, normalized to the expectation as calculated from the Bethe-Bloch parametrization is displayed as a function of the distance to the cathode plane.

and cathode plane, respectively:

$$A(\Delta t) = 1.04 \ {}^{+}/_{-} \ 0.67 \cdot 10^{-4} \Delta t \tag{4.4}$$

$$C(\Delta t) = 0.95 \ {}^{+}/_{-} \ 0.69 \cdot 10^{-4} \Delta t \tag{4.5}$$

The sign in front of the second term corresponds to particle approaching from the left or from the right side.

4.1.4.4 Correlation between Corrections

In principle, correlations exist between the individual corrections applied to each individual hit. For example the attachment correction, which compensates the charge loss of an ionization cloud due to electronegative gas like oxygen in the drift chamber, is a function of the drift distance. The improved drift time correction as developed in this analysis could in principle affect the standard Opal corrections.

Therefore, the effect on each of the standard corrections, with and without the above improvements applied, has been studied. The effect was found to be largest for the attachment correction and the gain correction. This is illustrated in Figure 4.12. In these cases, the effect was found to be of the order of 1%

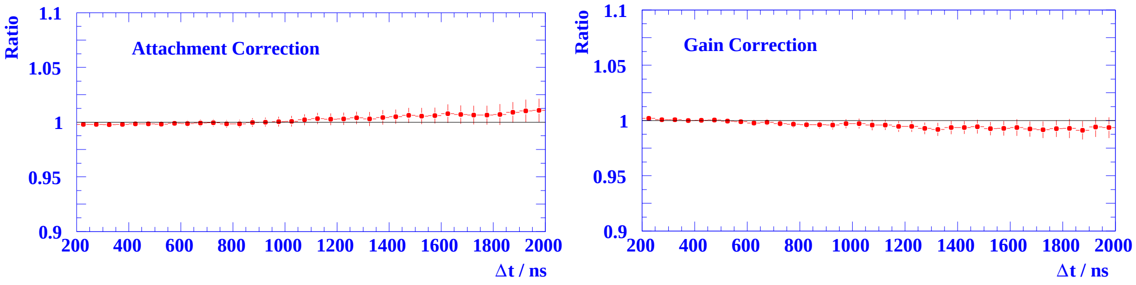

Fig. 4.12: Correlation to the standard correction. The influence of the new corrections on the attachment correction (left plot) and the gain correction (right plot) is illustrated as function of the drift time difference. The effect is of the order of 1%

4.1.5 Adjustment of the Experimental Errors

After all the corrections described above, the systematic bias of the energy loss measurement in the τ environment could be reduced from $\mathcal{O}(10\%)$ to $\mathcal{O}(1\%)$. From the measured energy loss, its error and the expectation calculated using the Bethe-Bloch equation, χ^2 probabilities are calculated that the measured energy deposition is in accordance with the expectation for a given particle type, as

$$P(\chi^2_{\mathrm{meas}},\,\nu) = \int_{\chi^2_{\mathrm{meas}}}^{\infty} \Gamma(\chi^2,\,\nu)\,\mathrm{d}\chi^2, \tag{4.6}$$

where $\Gamma(\chi^2,\,\nu)$ is the χ^2-p.d.f. and $\nu = 1$ the number of degrees of freedom. Pion- and kaon-weights, W_π and W_K are then calculated by taking one minus the value of this probability. These weights acquire a sign depending on whether the actual energy loss lies above or below the expectation for a certain particle hypothesis. This means that W_π is expected to be close to -1 for kaons since their energy loss per unit length is smaller in the momentum range relevant in this analysis. For electron tracks, W_π is expected to be close to $+1$ due to the higher energy loss in this case. Whenever these quantities are used in the selection, a cut on at least 20 $\mathrm{d}E/\mathrm{d}x$ hits for this track is implicitly made.

To calculate the probability that the measured energy loss is in agreement with the expectation for a given particle type, an accurate description of the experimental uncertainty is necessary. In order to verify this and to determine correction factors if needed, distributions of residuals R are studied:

$$\mathrm{R} = \frac{(\mathrm{d}E/\mathrm{d}x)_{\mathrm{meas}} - (\mathrm{d}E/\mathrm{d}x)_{\mathrm{exp}}}{\sigma_{\mathrm{exp}}^{\mathrm{d}E/\mathrm{d}x}}, \tag{4.7}$$

which is the measured energy loss for a given particle observed in the detector, minus the expectation as calculated from the Bethe-Bloch equation for a particular particle hypothesis, divided by the expected error of the measurement. For a sample of a single particle species and for the right particle hypothesis, this results in a unit Gaussian with mean zero and unit width. Any deviation in shape and position from this expectation is an indication for either the wrong particle hypothesis, a systematic shift in the energy loss measurement or an inaccurate description of the experimental uncertainties.

The track sample analyzed here contains three different particle species: pions, kaons and electrons. The distribution of residuals as defined in Equation 4.7 is therefore a superposition of three distributions. The number of muon tracks in the sample considered here is negligible. For those tracks, the probability for final state radiation and a subsequent conversion of the photon (to fake a 3-prong event) is very low. The rate is below 1% and these tracks are absorbed in the peak produced by the pions. Using pion hypothesis, one observes one Gaussian peak originating from pion tracks which is centered around zero. The peak from the kaons in the sample is situated left from the pion peak, since the energy loss for kaons is less than the one expected for pions in the momentum range considered here (see Figure 4.1). The contribution from electron tracks is expected right from the pion peak. The shape of the contributions from kaon and electron tracks are not Gaussian-like since the difference in energy loss for these two particle species is not constant as a function of the particle momentum relative to the expectation from pions. The individual contributions as described above are illustrated in Figure 4.13.

The residual under pion hypothesis is then analyzed in a χ^2-fit as explained below. To assess possible correction factors, for every track in the sample the residual under pion hypothesis R^π_{meas} is calculated

$$R^\pi_{\mathrm{meas}} = \frac{\left(\frac{\mathrm{d}E}{\mathrm{d}x}\right)_{\mathrm{meas}} \cdot P_{\mathrm{scal}} - \left(\frac{\mathrm{d}E}{\mathrm{d}x}\right)^\pi_{\mathrm{exp}}}{\sigma^{\mathrm{d}E/\mathrm{d}x}_{\mathrm{meas}} \cdot P_{\mathrm{err}} \cdot \frac{\left(\frac{\mathrm{d}E}{\mathrm{d}x}\right)^\pi_{\mathrm{exp}}}{\left(\frac{\mathrm{d}E}{\mathrm{d}x}\right)_{\mathrm{meas}}}} - P_{\mathrm{mean}}. \tag{4.8}$$

The parameters P_{scal} and P_{err} are multiplicative scaling factors for the measured energy loss and the experimental error. P_{mean} is an additive correction factor, to allow for an overall shift of the whole distribution. They are free parameters in the fit. After all corrections, P_{scal} and P_{mean} are expected to be one. Since the bias of the $\mathrm{d}E/\mathrm{d}x$ measurement has been substantially improved, the experimental uncertainty is expected to be smaller. P_{err} is therefore expected to be less than one, which is then used as scaling factor for the experimental uncertainty. For small enough momentum bins, the difference in energy loss is in good approximation constant and the expected distribution of measured residuals can be described by the sum of three Gaussians.

$$D_{\mathrm{theo}} = \sum_{i\in\{\mathrm{K},\pi,\mathrm{e}\}} C_i \exp\left(-\frac{1}{2}\frac{x_i^2}{\sigma_i^2}\right), \tag{4.9}$$

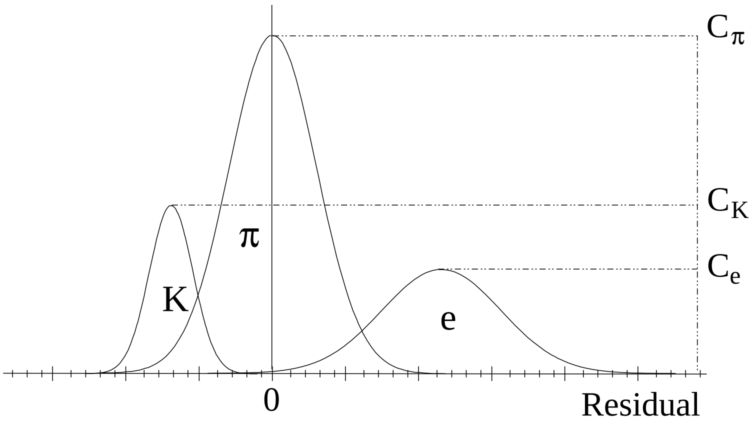

Fig. 4.13: Distribution of residuals as expected for the particles species considered here.

where x_i is the expected residual as calculated from the Bethe-Bloch formula for each of the particle hypotheses using the measured momentum of the track. The parameters C_i are normalization factors that represent the relative size of the contributions of each of the three particle species relevant here. Two of them, C_{K} and C_{e} are free parameters of the fit. The fraction of pion tracks is not a free parameter since it can be calculated via $C_\pi = 1 - C_{\mathrm{K}} - C_{\mathrm{e}}$. The error σ_i is the expected width of the Gaussian, which is $\sigma_\pi = 1$ for the central peak and $\sigma_i = \left(\frac{\mathrm{d}E}{\mathrm{d}x}\right)^i_{\mathrm{exp}} / \left(\frac{\mathrm{d}E}{\mathrm{d}x}\right)_{\mathrm{meas}}$ for kaons and electrons.
In the fit, the following χ^2 is minimized

$$\chi^2 = \frac{\sum_{\mathrm{Tracks}} R^\pi_{\mathrm{meas}} - \sum_{\mathrm{Tracks}} D_{\mathrm{theo}}}{\sigma_{\mathrm{stat}}}. \tag{4.10}$$

The fit was tested using Monte Carlo track samples. Here, the particle species for each individual track is known, and the distribution of the residual and the relative size of the contribution of each particle species can be compared to the result obtained in the fit. This is illustrated in Figure 4.14. In the upper row, the momentum distribution of all tracks considered in the fit is displayed separately for all three particle species. The dots represent the distribution used in the Monte Carlo simulation and the histogram is the prediction of the fit as calculated from the fit parameters $C_{\mathrm{K,\,e,\,}\pi}$. The shaded area represents the uncertainty as obtained in the fit. Below, the residual for each individual particle species as obtained from the fit is compared to the expectation. In general, a good agreement between the Monte Carlo and the results of the fit is observed. The scaling factor P_{err} for the experimental uncertainty of the energy loss measurement were found to be one within the errors of the fit. The corrections described in the previous section are relevant for data tracks only. They are not present in the Opal detector simulation, therefore no scaling of $\sigma^{\mathrm{d}E/\mathrm{d}x}_{\mathrm{meas}}$ is necessary. The same is true for P_{scal} and P_{mean}, which were found to one and zero within statistical uncertainty, respectively.

This fit is now applied to the track sample in data events. The tracks in 1-prong and in multi-prong τ decay environment are fitted separately for each year of data taking. The results obtained for the parameters of the fit are given in Table 4.4. For the error on the energy loss measurement $\sigma^{\mathrm{d}E/\mathrm{d}x}_{\mathrm{meas}}$ a scaling factor of up to 0.9 was obtained in the multi-prong environment. This means a 10% reduction of the experimental uncertainty. Furthermore, in this environment, a shift of the order of 0.05 was observed. In the 1-prong environment, as expected only small corrections are obtained from the fit.
The effect of all corrections can be seen in figure 4.15. It shows the $\mathrm{d}E/\mathrm{d}x$ pull distribution under a pion-hypothesis for all like-sign tracks from 3-prong tau decays. The full dots represent the result obtained using tracks in data events with all corrections applied. The solid line represents the prediction from the fit as explained above. In addition, the distribution of residuals with the default Opal correction only is shown as open dots. Due to the effects explained above, a significant excess of events is observed in the range where the kaon tracks are expected.

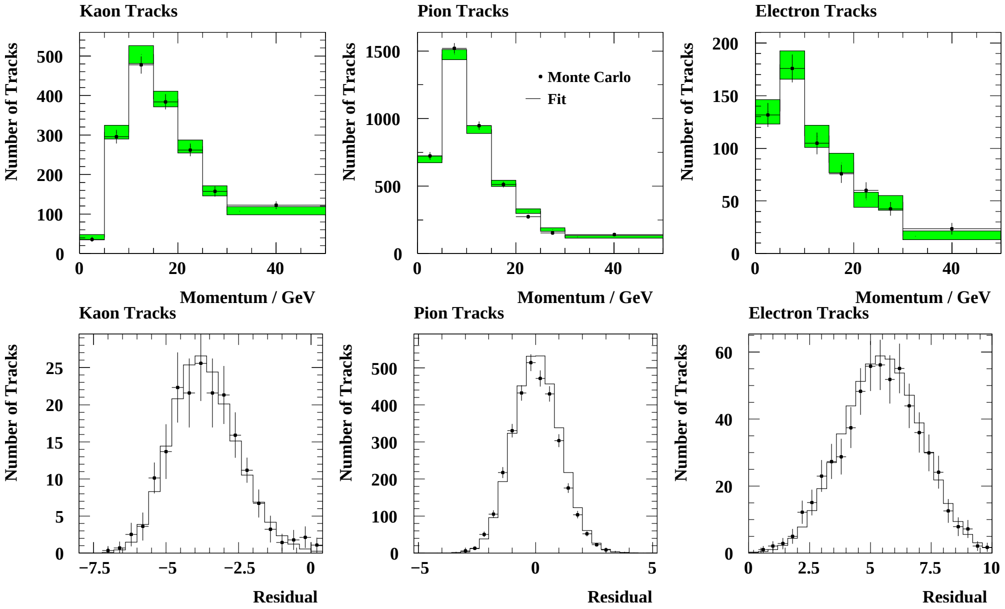

Fig. 4.14: Test of the fit procedure using tracks from Monte Carlo simulation. In the upper row, the momentum distribution in the Monte Carlo (dots) is compared to the distribution as obtained from the fit (histogram). The shaded area represents the uncertainty from the fit. Below, the distribution of residuals for the individual particle species as obtained from the fit (histogram) is compared to the prediction from the Monte Carlo simulation.

	1-prong		
Year	P_{mean}	P_{err}	P_{scal}
91	0.0077 ± 0.0015	0.9810 ± 0.0073	0.9989 ± 0.0022
92	0.0078 ± 0.0049	1.0128 ± 0.0054	0.9995 ± 0.0016
93	0.0048 ± 0.0027	1.0013 ± 0.0063	0.9995 ± 0.0070
94	0.0012 ± 0.0013	1.0018 ± 0.0090	0.9971 ± 0.0057
95	0.1128 ± 0.0032	1.0100 ± 0.0056	0.9994 ± 0.0062
91	0.0533 ± 0.0091	0.9293 ± 0.0077	1.0074 ± 0.0015
92	0.0517 ± 0.0056	0.9365 ± 0.0065	1.0099 ± 0.0012
93	0.0499 ± 0.0046	0.9021 ± 0.0074	1.0064 ± 0.0006
94	0.0371 ± 0.0039	0.9509 ± 0.0097	1.0085 ± 0.0010
95	0.0355 ± 0.0083	0.9657 ± 0.0120	1.0081 ± 0.0022
Year	P_{mean}	P_{err}	P_{scal}
	multi-prong		

Tab. 4.4: Result of the fit to the residuals. The mean of the parameters P_{mean}, P_{err} and P_{scal} are given separately for each year of data taking and for tracks in 1-prong and multi-prong environment separately.

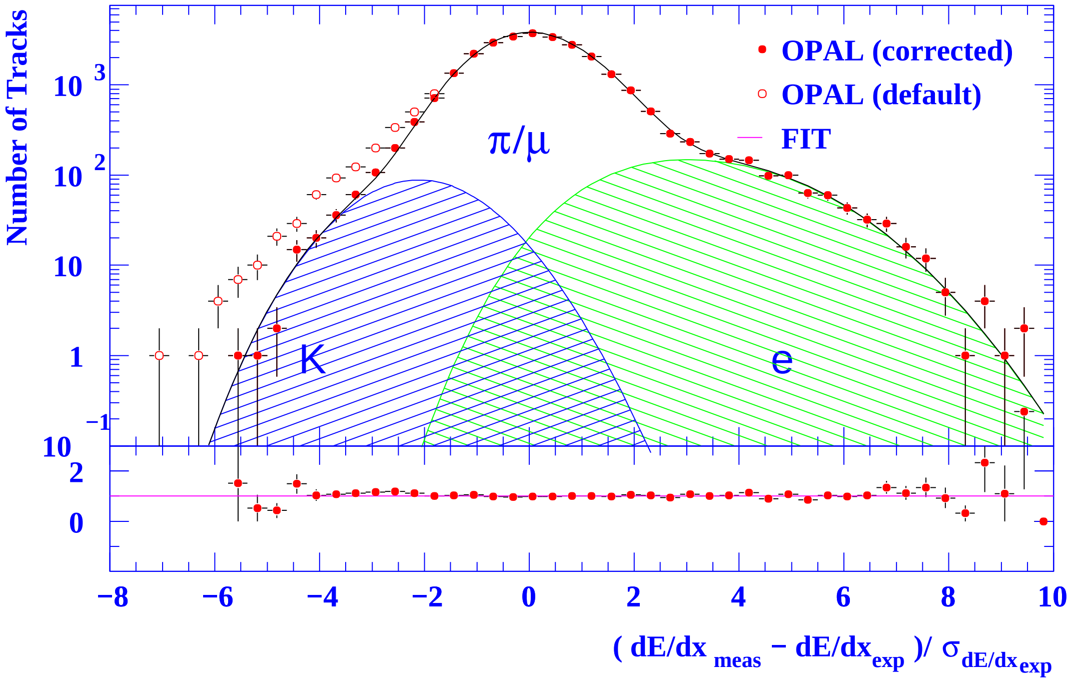

Fig. 4.15: Pull distribution obtained under a pion hypothesis for all tracks in 3-prong τ decays with a minimum momentum of 3 GeV and a minimum number of 20 hits in the dE/dx measurement. Only the tracks with the same charge as the decaying τ are shown. The full points with error bars are data after all corrections and the histograms shows the expectation as explained in the text. The open points in the range between -8 to -2 show the same distribution but without the corrections mentioned in the text. The smaller plot at the bottom shows the ratio of the full data points to the histogram.

4.2 Photon Reconstruction and Identification of Neutral Pions

For a classification of the final states in hadronic τ decays, a reliable identification of the number of neutral pions involved is therefore essential. The neutral pion decays after a mean lifetime of $\tau_{\pi^0} = (0.084 \pm 0.006)\,\mathrm{fs}$ into two photons. The identification of photons and the reconstruction of their four-momenta is therefore necessary for the reconstruction of the invariant mass of the hadronic system. This requires the analysis of electromagnetic showers observed in the OPAL lead glass calorimeter. It includes the identification and the correct treatment of electromagnetic cluster with or without an associated track pointing to it.

The algorithm used here is based on a shower parametrization described in [61] and the 'Find Photon Package' [40], which determines the number of photons and their four-momenta for a given electromagnetic cluster observed in the detector. This package was originally developed for the measurement of the non-strange spectral function. In this analysis, the algorithm had to be optimized for the use in strange τ decays for two reasons.

1) The algorithm has the tendency to reconstruct too many photons. While the high energy tail is described precisely, the low energy part shows some clear discrepancies. In particular in 3-prong τ decays, too many photons with energies below 2 GeV are reconstructed. Pairing algorithms, originally developed to reconstruct jets in multihadronic events, are used to reduce the number of low energy photons and to improve the energy resolution.

2) The relative size of the branching fractions for the multi-meson final states in τ decays are different in the strange and in the non-strange case. Two effects contribute here:

   - The $(J^P = 1^-)$ final state in strange decays is dominated by the $\mathrm{K}^*(892)$ resonance. Assuming isospin symmetry and an equal contribution from decays involving K^0_S and K^0_L, the three decay channels of the $\mathrm{K}^*(892)$($\mathrm{K}^-\pi^0$, $\mathrm{K}^0_\mathrm{S}\pi^-$ and $\mathrm{K}^0_\mathrm{L}\pi^-$) should contribute equally. The decay channel involving a neutral pion is therefore suppressed by the ratio [2]

     $$\frac{B(\tau^- \to \mathrm{K}^0\pi^-\nu_\tau)}{B(\tau^- \to \mathrm{K}^-\pi^0\nu_\tau)} = \frac{2}{1}. \tag{4.11}$$

     There is no such effect in the corresponding two-meson final state in the non-strange case.

   - The relative size of τ decays into a single kaon is enhanced with respect to the non-strange counterpart ($\tau^- \to \pi^-\nu_\tau$). This can be explained by 'helicity suppression' of the spin-0 final states. In the restframe of the W boson, the decay products are produced back-to-back. In the chiral limit, only left-handed fermions and right-handed anti-fermions exist. Therefore, the decay products have to be in a spin-1 state. If the final state fermions have mass, the decay into a spin-0 state is possible. However it is still suppressed by a factor which is proportional to the masses of the quarks involved:

     $$\frac{m_\mathrm{u}}{m_\tau} + \frac{m_\mathrm{d/s}}{m_\tau} + \mathcal{O}\left(\frac{m^2_\mathrm{u/d/s}}{m^2_\tau}\right). \tag{4.12}$$

     In the case of non-strange final states, where the masses of the quarks are still very small, this leads to a strong suppression of the decay $\tau^- \to \pi^-\nu_\tau$ $(J^P = 0^-)$ over $\tau^- \to \pi^-\pi^0\nu_\tau$ $(J^P = 1^-)$, while from phase space considerations alone. The latter would be expected to be smaller.

     In strange decays, however, the situation is different due to the relatively large mass of the strange quark. Here, the single kaon final state $(J^P = 0^-)$ is enhanced with respect to the $\tau^- \to \mathrm{K}^*(892)\nu_\tau$ final state $(J^P = 1^-)$.

The ratios of the branching fractions in the strange and non-strange case are

$$\frac{B(\tau^- \to \pi^-\nu_\tau)}{B(\tau^- \to \pi^-\pi^0\nu_\tau)} = \frac{(11.06 \pm 0.11)\%}{(25.41 \pm 0.14)\%} \approx \frac{1}{2} \tag{4.13a}$$

$$\frac{B(\tau^- \to \mathrm{K}^-\nu_\tau)}{B(\tau^- \to \mathrm{K}^-\pi^0\nu_\tau)} = \frac{(0.686 \pm 0.023)\%}{(0.450 \pm 0.030)\%} \approx \frac{1.5}{1}. \tag{4.13b}$$

---

[2] Corrections due to the masses of the final state particles involved are neglected in this explanation.

> Since the background contribution from the single kaon in the $K^0\pi^-\nu_\tau$ final state is higher than in the corresponding non-strange decay channels for the reasons explained above, the reconstruction and selection criteria had to be optimized for the use in strange τ lepton decays.

Therefore, in the optimization of the photon reconstruction and the identification of neutral pions, only those events where used, where at least one kaon candidate track was found. This section starts with an introduction on the description of electromagnetic shower and the parametrization of the shower shape in the barrel part of the OPAL lead glass calorimeter is explained. In Section 4.2.3 the Find Photon algorithm is explained which is used to identify photon candidates and to reconstruct their four-momenta. A pairing algorithm in then applied to these candidates in order to reduce the number of fake photons and to increase the energy resolution. Finally, the reconstruction of neutral pions from photon candidates is described in Section 4.2.5

4.2.1 Description of Electromagnetic Shower

For an electromagnetic shower, the longitudinal energy distribution scales with the radiation length X_0 of the matter it develops in. The lateral distribution scales with the so-called Molière radius R_{M} [55], which describes the average deviation of an electron of energy E_C from the incident direction by Coulomb scattering. It is given by

$$R_{\mathrm{M}} = X_0 \frac{E_S}{E_C} \tag{4.14}$$

where E_S is the scale energy $E_S = \sqrt{4\pi/\alpha}\, m_e c^2 = 21.1\,\mathrm{MeV}$. In material containing fractions w_j of the element with critical energy $E_{c,\,j}$ and radiation length X_j, the Molière radius is given by

$$\frac{1}{R_{\mathrm{M}}} = \frac{1}{E_S} \sum_j \frac{w_j E_{c,\,j}}{X_j}. \tag{4.15}$$

The OPAL lead glass calorimeter in the central region consists of SF-57 with a density of $5.54\,\mathrm{g/cm}^3$ and a radiation length of $X_0 = 1.50\,\mathrm{cm}$ which leads to a critical energy of $E_C = 13.0\,\mathrm{MeV}$ and a Molière radius of $R_{\mathrm{M}} = 2.92\,\mathrm{cm}$.
This analysis is restricted to the barrel part of the OPAL detector ($|\cos\Theta| < 0.68$). Since there is no segmentation in longitudinal direction, the development of the shower can only be analyzed considering the lateral development. The density of the lateral energy distribution can be described by the sum of two exponentials [56]

$$f(\rho) = a_1 \lambda_1^2 \cdot \exp\big(-\lambda_1 \rho\big) + a_2 \lambda_2^2 \cdot \exp\big(-\lambda_2 \rho\big), \tag{4.16}$$

where Bremsstrahlung is responsible for the narrow part which is called the 'core' of the shower. The broad component is due to Coulomb scattering and is called the 'halo'. The factors a and b are normalization constants which add up to unity. The variable ρ is the radial distance from the shower axis. The integral

$$\int_0^R f(\rho)\rho \mathrm{d}\rho \tag{4.17}$$

then gives the fraction of the total energy of the shower, which is contained within a radius R around the axis of the shower. Measurements now show, that 90% of the total shower energy is contained within one Molière radius and 99% is contained within $3.5R_{\mathrm{M}}$. Requiring that the integral in Equation 4.17 goes to unity as the radius R goes to infinity, leads to three constraints

$$\int_0^\infty f(\rho)\rho \mathrm{d}\rho = 1 \tag{4.18a}$$

$$\int_0^{R_{\mathrm{M}}} f(\rho)\rho \mathrm{d}\rho = 0.9 \tag{4.18b}$$

$$\int_0^{3.5\,R_{\mathrm{M}}} f(\rho)\rho \mathrm{d}\rho = 0.99. \tag{4.18c}$$

The value of $c = b/a$ of the relative contribution of halo to core, and the parameters λ_1 and λ_2 were determined in a fit to the observed lateral energy distribution using (2−10) GeV electrons (see [61]). Equation 4.16 can then be rewritten as

$$f(\rho) = 0.89 \cdot (1.81)^2 \cdot \exp\big(-1.81\rho\big) + 0.11 \cdot (0.39)^2 \cdot \exp\big(-0.39\rho\big), \tag{4.19}$$

using $c = 0.12$, $\lambda_1 = 1.81$ and $\lambda_2 = 0.39$.

4.2.2 Parametrization of the Shower Shape in the Barrel

Equation 4.19 can now be used to predict the energy of a photon shower deposited in each calorimeter block as a function of the center of the shower. The energy is given by

$$E_i = \frac{1}{2\pi} \int_{x_i^{\min}}^{x_i^{\max}} \mathrm{d}x \int_{y_i^{\min}}^{y_i^{\max}} \mathrm{d}y \frac{\mathrm{d}E}{\mathrm{d}\rho} \tag{4.20}$$

with

$$\frac{\mathrm{d}E}{\mathrm{d}\rho} = E_0 \cdot \Big(0.89 \cdot (1.81)^2 \cdot \exp\big(-1.81\rho\big) + 0.11 \cdot (0.39)^2 \cdot \exp\big(-0.39\rho\big)\Big) \tag{4.21}$$

and

$$\rho = \sqrt{(x - x_0)^2 + (y - y_0)^2}. \tag{4.22}$$

Here (x_0, y_0) are the cartesian coordinates of the point of incidence, and E_0 is the energy of the photon. Performing this integration for each photon shower is time consuming. Therefore, in [61] the simulated energy distribution of an electromagnetic shower in a lead glass block cluster was calculated using Equation 4.20 for showers with centroids at 441 distinct points within the central block of the cluster. The front side of each block in the barrel has a cross section of $(10 \times 10)\,\mathrm{cm}^2$ and two points in the grid therefore have a distance of 0.5 cm. The energy fractions deposited in each block as a function of the coordinates of the centroid in the central block are displayed in Figure 4.16. Only those showers that have their center close to the edge of a block, deposit a significant amount of energy in the neighboring block. There are two effects that are small and that are therefore neglected in the calculations.

1. Only those blocks are considered that are direct neighbors of the block the center of the shower is located in. In this 3 × 3 lead glass block cluster, at least 98.9% of the total energy of the incident particle is deposited. Other blocks further away are not considered.
2. The lead glass blocks in the barrel region of the ECAL have a quasi-pointing geometry. This means that they are not directly pointing to the primary vertex, but they have a small tilt angle of 2.25° in φ-direction and of $\sim 1.9°$ in z-direction. By this configuration, it is excluded that photons exactly hit the gap between two blocks, where they are not recognized. This small tilt is neglected in the calculations.

The calculated fractions were found to be smooth functions of the position of the center of the shower and can therefore be parametrized using higher order polynomials. Five different polynomials were used

$$\text{Block } 1: (a_1 + a_2 x^6)(a_3 + a_4 y^6) \tag{4.23a}$$

$$\begin{aligned}\text{Block } 2, 4: &(a_1 + a_2 x + a_3 x^2 + a_4 x^3 + a_5 x^4 + a_7 x^6 + \\ &a_8 x^7 + a_9 x^8)(a_{10} + a_{11} y^4)\end{aligned} \tag{4.23b}$$

$$\begin{aligned}\text{Block } 3, 5: &(a_1 + a_2 y + a_3 y^2 + a_4 y^3 + a_5 y^4 + a_7 y^6 + \\ &a_8 y^7 + a_9 y^8)(a_{10} + a_{11} x^4)\end{aligned} \tag{4.23c}$$

$$\begin{aligned}\text{Block } 6, 8: &a_1 + a_2(x+y) + a_3(x+y)^2 + a_4(x+y)^3 + a_5(x+y)^4 + \\ &a_7(x+y)^6 + a_8(x+y)^7 + a_9(x+y)^8 + a_{10}(x+y)^9 + a_{11}(x+y)^{10}\end{aligned} \tag{4.23d}$$

$$\begin{aligned}\text{Block } 7, 9: &a_1 + a_2(x-y) + a_3(x-y)^2 + a_4(x-y)^3 + a_5(x-y)^4 + \\ &a_7(x-y)^6 + a_8(x-y)^7 + a_9(x-y)^8 + a_{10}(x-y)^9 + a_{11}(x-y)^{10}.\end{aligned} \tag{4.23e}$$

The numbering scheme for each block within the cluster is given in Figure 4.16 and the parameters a_i are given in Table 4.5.

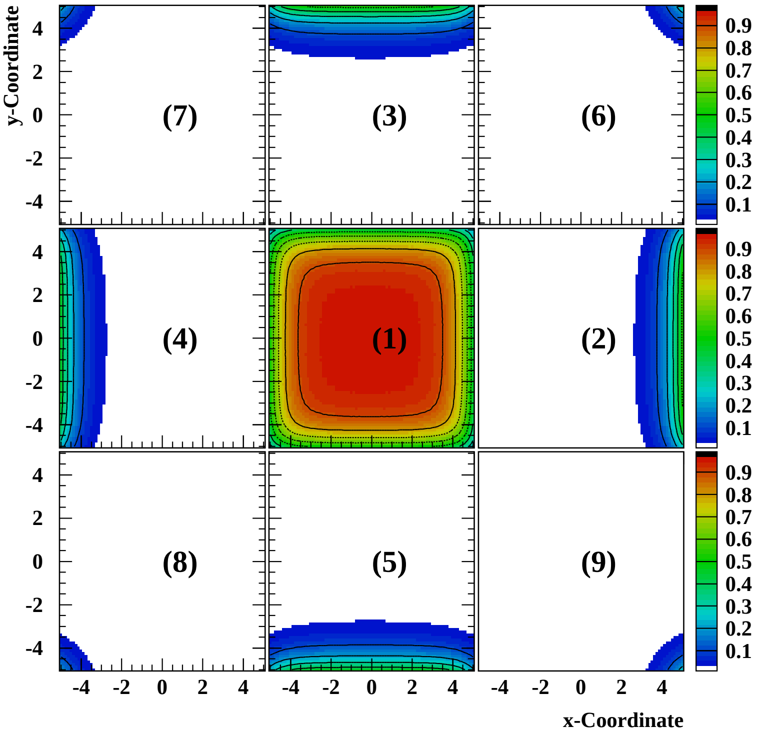

Fig. 4.16: Fraction of the total energy deposited in each block in a cluster of the size 3 × 3 blocks. The coordinates given in each always correspond to the incident coordinates of the photon in the central block. For better visibility, only fractions larger than 0.05 are displayed. The numbers given in the center of each block correspond to the numbering scheme of the parametrization as used in Equations 4.23.

Block	a_1	a_2	a_3	a_4	a_5	a_6
1	$8.732\cdot10^{-1}$	$-3.667\cdot10^{-5}$	1.092	$-4.588\cdot10^{-5}$	-	-
2	3.168	-1.269	$5.191\cdot10^{-2}$	$-1.665\cdot10^{-2}$	$5.468\cdot10^{-2}$	$-1.345\cdot10^{-2}$
3	$5.791\cdot10^{-1}$	$-2.264\cdot10^{-1}$	$6.683\cdot10^{-2}$	$-2.195\cdot10^{-2}$	$1.127\cdot10^{-3}$	$3.354\cdot10^{-4}$
4	1.374	$5.413\cdot10^{-1}$	$1.501\cdot10^{-1}$	$4.746\cdot10^{-2}$	$3.733\cdot10^{-3}$	$-1.343\cdot10^{-4}$
5	$5.035\cdot10^{-1}$	$2.175\cdot10^{-1}$	$5.156\cdot10^{-2}$	$5.578\cdot10^{-3}$	$7.610\cdot10^{-7}$	$1.225\cdot10^{-3}$
6	$1.399\cdot10^{-3}$	$-4.106\cdot10^{-4}$	$3.720\cdot10^{-5}$	$5.261\cdot10^{-6}$	$4.000\cdot10^{-6}$	$-1.425\cdot10^{-6}$
7	$1.403\cdot10^{-3}$	$4.202\cdot10^{-4}$	$3.715\cdot10^{-5}$	$-6.639\cdot10^{-6}$	$3.896\cdot10^{-6}$	$1.480\cdot10^{-6}$
8	$1.399\cdot10^{-3}$	$4.136\cdot10^{-4}$	$3.678\cdot10^{-5}$	$-6.456\cdot10^{-6}$	$3.924\cdot10^{-6}$	$1.494\cdot10^{-6}$
9	$1.395\cdot10^{-3}$	$-4.187\cdot10^{-4}$	$3.970\cdot10^{-5}$	$7.002\cdot10^{-6}$	$3.645\cdot10^{-6}$	$-1.514\cdot10^{-6}$

Block	a_7	a_8	a_9	a_{10}	a_{11}
1	-	-	-	-	-
2	$2.466\cdot10^{-3}$	$-1.015\cdot10^{-3}$	$1.379\cdot10^{-4}$	$2.498\cdot10^{-3}$	$-2.228\cdot10^{-6}$
3	$7.642\cdot10^{-4}$	$-2.967\cdot10^{-4}$	$2.878\cdot10^{-5}$	$1.295\cdot10^{-2}$	$-1.153\cdot10^{-5}$
4	$1.812\cdot10^{-3}$	$6.774\cdot10^{-4}$	$6.572\cdot10^{-5}$	$5.483\cdot10^{-3}$	$-4.862\cdot10^{-6}$
5	$8.677\cdot10^{-4}$	$2.071\cdot10^{-4}$	$1.674\cdot10^{-5}$	$1.524\cdot10^{-2}$	$-1.363\cdot10^{-5}$
6	$-6.850\cdot10^{-8}$	$4.487\cdot10^{-8}$	$-8.048\cdot10^{-10}$	$-5.051\cdot10^{-10}$	$3.027\cdot10^{-11}$
7	$-6.381\cdot10^{-8}$	$-4.585\cdot10^{-8}$	$-8.903\cdot10^{-10}$	$5.123\cdot10^{-10}$	$3.092\cdot10^{-11}$
8	$-6.162\cdot10^{-8}$	$-4.609\cdot10^{-8}$	$-9.431\cdot10^{-10}$	$5.114\cdot10^{-10}$	$3.103\cdot10^{-11}$
9	$-5.290\cdot10^{-8}$	$4.648\cdot10^{-8}$	$-1.064\cdot10^{-9}$	$-5.148\cdot10^{-10}$	$3.172\cdot10^{-11}$

Tab. 4.5: Table of coefficients for the parametrization of the fraction of energy deposited in a 3 × 3 cluster of lead glass blocks in the barrel region (see Equations 4.23). The numbering scheme is illustrated in Figure 4.16.

4.2.3 The Find Photon Algorithm

The above parametrization is now used to describe the measured shower shape in each cluster[3] as a function of the four-momentum of the incident photons. The hypothesis that up to $n = 8$ photons are responsible for the observed shower shape is tested. For each photon, the energy and its azimuthal and polar angle (E_i, φ_i, θ_i) are fitted, which gives a total number of $3n$ parameters in a fit, where the hypothesis is tested, that n photons are responsible for the measured shower shape. In this fit, only those blocks within a cluster are considered that have a minimum energy of $E_{\mathrm{min}}^{\mathrm{Block}} = 150\,\mathrm{MeV}$. The distribution of block energies can be found in Figure 4.17(a) and (b) for cluster without and with associated track, respectively. The data is well described by the Monte Carlo simulations for block energies above 150 MeV. The number of blocks observed in a given cluster is displayed in Figure 4.18 for minimum block energies of 50 MeV and 150 MeV for cluster with and without associated tracks. With the more stringent energy cut applied, the distribution observed in the data is well described by the Monte Carlo simulation, while for the looser cut significant discrepancies are observed.

In Figure 4.19(a) the energy distribution for clusters without associated track is given. The dashed line denotes the contribution from those clusters in the Monte Carlo, where on generator level a photon from a π^0 decay is pointing to it. By requiring a minimum cluster energy of $E_{\mathrm{min}}^{\mathrm{Cluster}} = 600\,\mathrm{MeV}$, the rate of fake clusters is significantly reduced.

Not only photons and electrons/positrons are expected to leave an energy deposit in the electromagnetic calorimeter. Due to hadronic interactions, pions/kaons or muons also leave a certain amount of energy. Therefore, the energy deposit of a minimum ionizing muon is subtracted from the measured energy in each block a track is pointing to. The energy deposit of a minimum ionizing muon was determined using muons from τ decays and it was found to be 420 MeV in the barrel region [40]. The total energy observed in the clusters with associated tracks is displayed in Figure 4.19(b). The peak from minimum ionizing particles is

---

[3] A cluster is a group of neighboring blocks with minimum energy $E_{\mathrm{min}}^{\mathrm{Block}} \geq 50\,\mathrm{MeV}$.

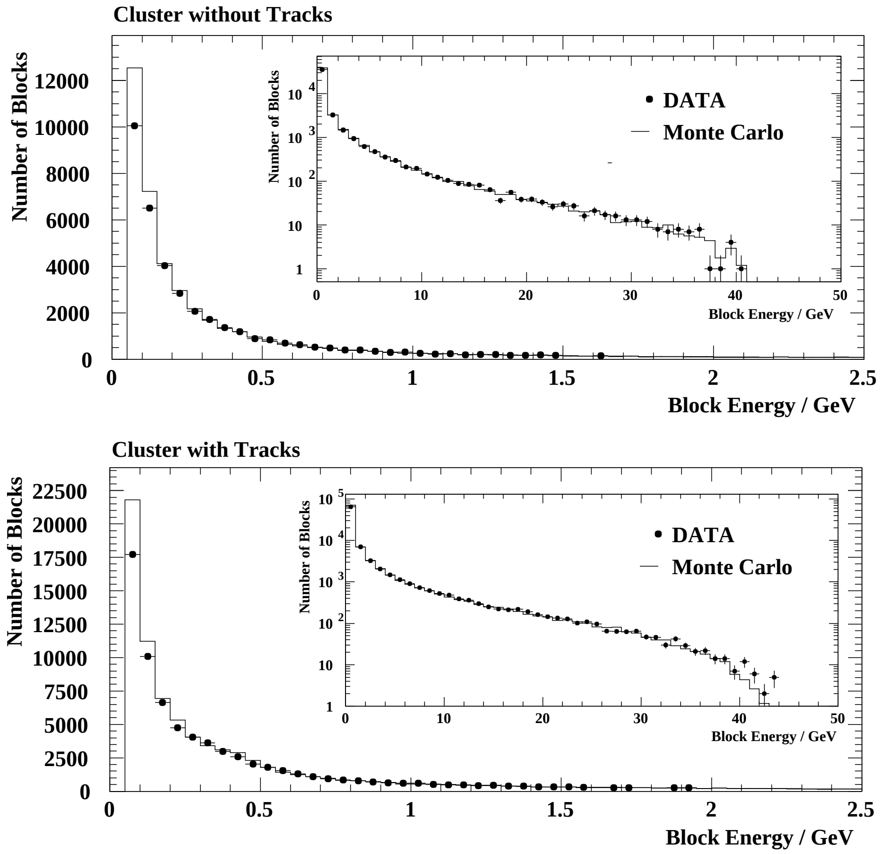

Fig. 4.17: Block energy in cluster with and without associated tracks. The dots are the data and the histogram is the Monte Carlo simulation. The small insert shows a logarithmic plot of the whole energy range. The plots are normalized to the number of τ decays.

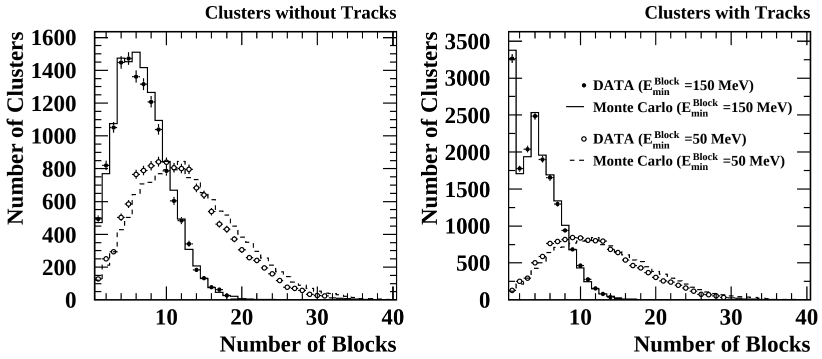

Fig. 4.18: Number of blocks in clusters with and without associated tracks. The dots are the data and the histogram denotes the predicted distribution from Monte Carlo simulation. The open dots and the dashed histogram show the distribution considering all blocks with a minimum energy of 50 MeV. The full dots and the solid histogram denote the same distribution considering only blocks with a minimum energy of 150 MeV. The left (right) plot shows the corresponding distribution for clusters without (with) associated tracks. The plots are normalized to the number of τ decays.

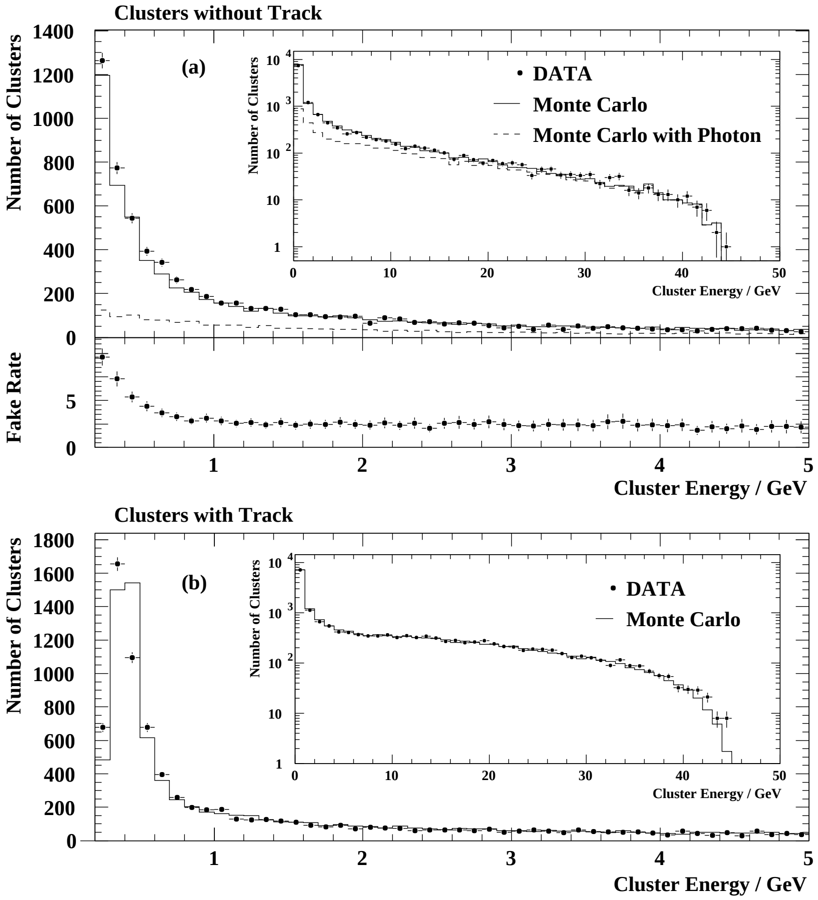

Fig. 4.19: Energy distribution of clusters without (plot (a)) and with (plot (b)) associated tracks. A minimum block energy of $E_{\mathrm{min}}^{\mathrm{Block}} = 150\,\mathrm{MeV}$ is required. The dots are the data and the solid histogram denotes the prediction from Monte Carlo simulation. The small inserts show a logarithmic version of the plot over the whole energy range. In the upper plot, the dashed line denotes those clusters in the Monte Carlo, where a photon on tree-level is pointing to it. Below, the fake rate is given. The peak from the energy deposition of minimum ionizing particles is visible in plot (b). The plots are normalized to the number of τ decays. A minimum cluster energy of 600 MeV is required for the further analysis in both cases.

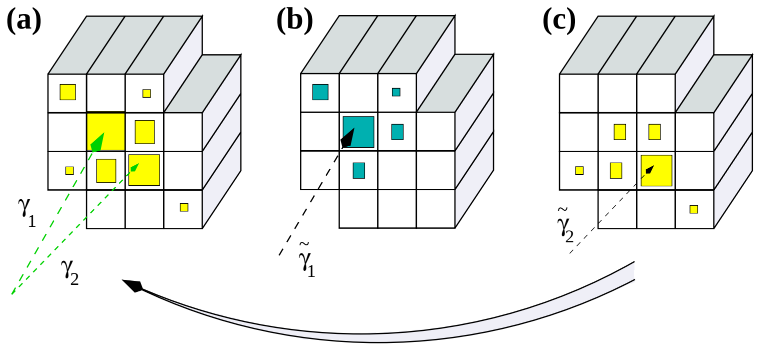

Fig. 4.20: Illustration of the iteration procedure for the Find Photon algorithm. In (a) the original configuration is displayed where two photons, γ_1 and γ_2, generate the shower shape observed in the cluster. (b) shows the energy distribution as predicted in the first iteration step by a single simulated photon $\tilde{\gamma}_1$. This contribution is then subtracted from the original energy deposition in each block. In the next iteration step, the second simulate photon $\tilde{\gamma}_2$ is fitted, using the energy and center of the block with highest energy residual as starting values.

clearly visible. This peak is not very well described by the Monte Carlo simulation. Therefore, a minimum cluster energy of $E_{\text{min}}^{\text{Cluster}} = 600\,\text{MeV}$ is required for further analysis.

The energy deposit of a hadron or muon, however, is not always the one expected for a minimum ionizing particle. Therefore, an additional photon is fitted for each track pointing to a block in the cluster under investigation. For these photons, only the energy is a free parameter. The direction of the photon, i.e. the azimuthal and polar angles, is fixed and is extrapolated from the track parameters measured in the central jet chamber.

Now, in an iterative algorithm, the hypotheses are tested that up to eight photons (plus one photon for each track pointing to the cluster) are responsible for the observed energy deposit in a given cluster. In the first iteration step, the energy and the center of the block with the highest energy in the cluster are chosen as starting values for the photon parameters in the fit. The parameters are then varied, until the best agreement is achieved between the measured block energies in the cluster and the energy deposition of the simulated photon as calculated from the shower parametrization. A χ^2 criterion is used

$$\chi^2 = \sum_{\text{Block } i=1}^{m} \frac{\left(E_i - \sum_{j=1}^{n} E_\gamma(i) - \sum_{k=1}^{l} E_\gamma^{\text{track}}(i) \right)^2}{\sigma_i^2}, \tag{4.24}$$

where the outer sum goes over all m blocks in the cluster under investigation and E_i is the energy as measured in the corresponding block. The sum over j (k) includes the energy deposit in this particular block from all photons ('track' photons) considered in the fit. The energy as predicted by the parametrization for each of the photons for the particular block i is labeled $E_\gamma(i)$ ($E_\gamma^{\text{track}}(i)$) for the fitted photons ('track' photons). The error of the energy measurement is assumed to be 100 MeV for each block.

The energies as predicted by the parametrization for the fitted photons are then subtracted from the measured block energies. In the next iteration step, the block with the highest remaining energy deposit is chosen, and its energy and center are used as starting values for an additional photon. For the other photons, the results obtained from the previous iteration step are used as starting values. In this iteration step, all photons are again fitted simultaneously. This iteration procedure is illustrated in Figure 4.20. In this example, two photons were responsible for the observed shower shape. The true photons are denoted by γ_1 and γ_2, the fitted photons by $\tilde{\gamma}_1$ and $\tilde{\gamma}_2$.

This procedure is repeated until the maximum energy remaining in the highest energetic block is less than 150 MeV or the number of reconstructed photons exceeds eight. The four-vectors of the photons and their error matrix is then taken from the iteration step with the minimum χ^2/n.d.o.f.. All photon candidates with an energy less than $E_\gamma^{\text{min}} < 50\,\text{MeV}$ are discarded.

4.2.4 Photon Pairing Algorithm

Using the parametrization of the shower shape and the Find Photon Algorithm described above, the number of reconstructed photons tends to be too high compared to the expectation. This can be explained by several effects.

- The parametrization of the shower shape has been developed using electrons from τ decays with an energy of $(2-10)\,\mathrm{GeV}$ [61]. A ratio of halo to core of $c = 0.12$ has been found there. In [56] a ratio of $c = 0.14$ using TF-1 lead glass has been found. This difference in the halo to core ratio affects the shower shape and thus the fraction of energy deposited in the individual blocks of a given cluster. The residuals are compensated by fitting additional low energetic photons which reduces the energy resolution.
- The electromagnetic calorimeter is situated outside the magnetic coil and the pressure vessel, containing the central tracking detectors. The radiation length a photon has to traverse before it enters the electromagnetic calorimeter is $\sim 2X_0$. There is a certain probability, that the electromagnetic shower starts developing, before the photon enters a lead glass block. The amount of material in front of the electromagnetic calorimeter is a function of the polar angle $\cos\theta$ of the photon which might change the shape of the shower. This has not been considered in [61].
- The energy distribution in a shower which is initiated by hadronic interaction is expected to be broader than the corresponding showers initiated by photons or electrons/positron. The width of the shower initiated by hadrons scales with the hadronic interaction length which is given by $\lambda \sim 35\mathrm{g/cm}^2 A^{-1/3}$, where A denotes the atomic weight of the material. The energy deposit from hadronic interactions is therefore not expected to be described correctly by the 'track' photons, since the same parametrization is used as for photons and hadrons. The residuals are compensated by fitting additional low energetic photons, which reduces the energy resolution.
- The calorimeter has some showers that are not caused by photons and are not directly the result of track hits. These extra showers arise for instances when a hadron strikes the calorimeter and some secondary particles are created in the interaction. These particles may cause the reconstruction of additional photons if they deposit their energy in the calorimeter sufficiently displaced from the track. This is called 'hadronic split-offs'.
- Depending on the energy of the neutral pion, the two photons from its decay are too close together so that they cannot be resolved, given the size of the calorimeter blocks and the intrinsic resolution of

Algorithm	Resolution	Combination	Remarks
E	$\frac{(p_i+p_j)^2}{s}$	$p_k = p_i + p_j$	Lorentz invariant
JADE	$\frac{2E_iE_j(1-\cos\theta_{ij})}{s}$	$p_k = p_i + p_j$	conserves $\sum E$, $\sum \vec{p}$
D	$\frac{2\cdot\min(E_i^2,E_j^2)\cdot(1-\cos\theta_{ij})}{s}$	$p_k = p_i + p_j$	conserves $\sum E$, $\sum \vec{p}$;
E0	$\frac{(p_i+p_j)^2}{s}$	$\vec{p}_k = \frac{E_k}{\lvert\vec{p}_i+\vec{p}_j\rvert}(\vec{p}_i+\vec{p}_j)$ $E_k = E_i + E_j$	conserves $\sum \vec{p}$ violates $\sum E$
p0	$\frac{(p_i+p_j)^2}{s}$	$\vec{p}_k = \vec{p}_i + \vec{p}_j$ $E_k = \lvert\vec{p}_k\rvert$	conserves $\sum \vec{p}$ violates $\sum E$
G	$\frac{8E_iE_j(1-\cos\theta_{ij})}{9(E_i+E_j)^2}$	$p_k = p_i + p_j$	conserves $\sum E$, $\sum \vec{p}$

Tab. 4.6: Selection of the pairing algorithms. The resolution parameter used in the corresponding algorithms is given as well as the instructions used in the combination of objects. The table includes algorithms obeying energy and momentum conservation (E, JADE, D, G) and those that violate either energy or momentum conservation (E0, p0).

the photon fit. The fit tends to reconstruct one high energetic photon and the remaining residuals are described by additional low energetic photons, which again reduces the energy resolution.

These affects described above reduce the energy resolution of the photons and thus the invariant mass resolution in τ decays with neutral pions in the final state. A Jet-Pairing algorithm is used to recombine the additional photons in order to increase the resolution. An overview over jet pairing algorithms is given in Table 4.6. It includes the resolution parameter and the instructions to recombine neutral objects to photon candidates. These algorithms were applied iteratively.

1. The resolution parameter is calculated for all possible combinations of photon candidates, reconstructed by the Find Photon Algorithm in a given electromagnetic cluster.
2. For the combination with the lowest value for the resolution parameter, the four-vectors of these two objects are combined using the instructions for the corresponding algorithm given in Table 4.6.
3. This procedure is repeated with all remaining photon candidates in the cluster. The procedure stops, when the resolution parameter for all possible combinations exceeds a certain value y_{cut}. This parameter has to be optimized for the use in strange τ decays.

For the reasons explained above, the shower shapes are different for clusters with and without associated tracks. Therefore, two y_{cut} values have been determined. The following procedure has been applied. First, the number of expected photons has to be calculated. To do this, an angular resolution is assumed in the Monte Carlo, e.g. $\Delta_{\mathrm{MC}} = 1.3°$. The Monte Carlo tree is analyzed and all photons found with an angular separation of less than the assumed resolution are combined to a new photon object by adding their corresponding four-vectors. This procedure is repeated until all neutral object have a separation of more than 1.3° on tree-level.

Then, the objects found by the Find Photon Algorithm are analyzed. Here, a pairing algorithm is used to combine the neutral objects found on detector level. The y_{cut} value was varied in the range from -7 to -2 in 50 steps, which results in different numbers of photon candidates. For each step, the χ^2 is calculated from the number of photons expected (assuming some angular resolution on tree-level as explained above) and the number of photons candidates found by the pairing algorithm. For the above example, i.e. an angular

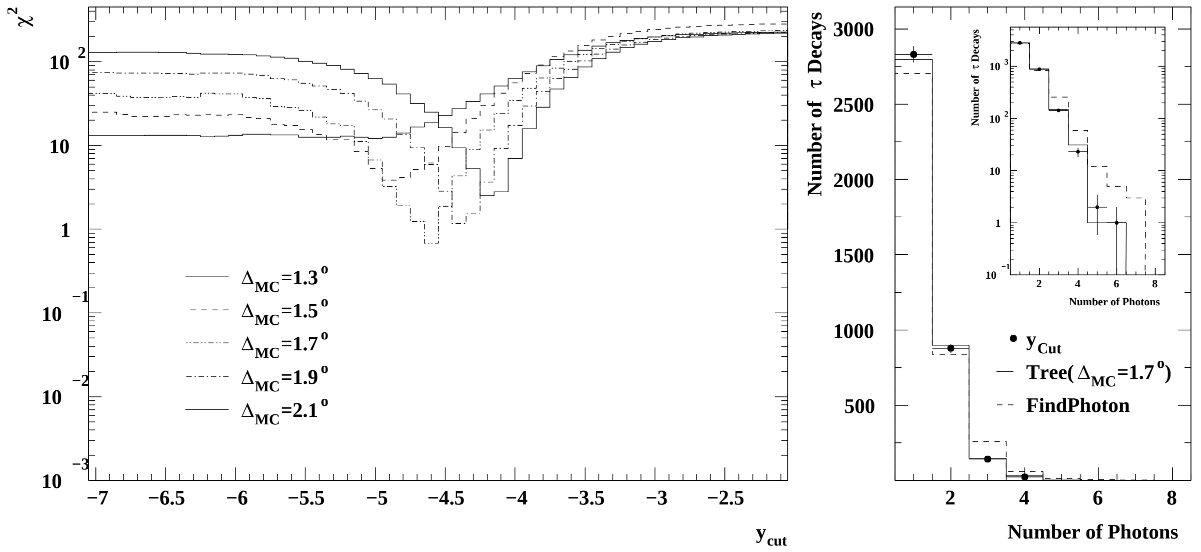

Fig. 4.21: Determination of the y_{cut} value for cluster without associated tracks. The left plot shows the χ^2 as calculated from the number of observed photons and the number of predicted photons as function of y_{cut}. Each curve corresponds to a particular resolution of the photon reconstruction algorithm assumed to determine the number of expected photons as explained in the text. The minimum χ^2 is obtained assuming a resolution of 1.7° at a y_{cut} value of -4.6 using the p0 scheme. In the right plot, the number of reconstructed photons is shown. The dashed histogram shows the number of photons obtained using the Find Photon algorithm. The solid histograms shows the predicted number of photons assuming a resolution of 1.7°. The dots represent the number of reconstructed photons using the p0 algorithm with a y_{cut} value of -4.6. The small insert shows a version of the same plot using a logarithmic y-axis.

resolution of 1.3°, the solid line in Figure 4.21 is obtained. In the next step, the assumed angular resolution is increased, the number of expected photons on tree-level is re-evaluated and the pairing algorithm is again applied to all objects originally found by the Find Photon Package. Again, the χ^2 as function of the $y_{\rm cut}$ value is plotted.

The result of this procedure is illustrated in Figure 4.21 for angular resolutions between 1.3° and 2.1°, using the p0 recombination scheme, which was found to give the best results. The minimum χ^2 was found for an angular resolution of 1.7° and a $y_{\rm cut}$ value of -4.6. The corresponding distribution of the number of photon candidates found is displayed on the right hand side of Figure 4.21. Here the number of photons expected (solid histogram), the original number of photon candidates from Find Photon (dashed histogram) and the reconstructed number of photons with the combination scheme applied (dots) is displayed. The smaller insert is the same distribution on a logarithmic scale.

For clusters with associated tracks, the expected resolution is worse. Here, an angular resolution of 2.1° with a $y_{\rm cut}$ value of -3 was found to give the optimal result again using the p0 combination scheme.

The resolution achieved with and without the pairing algorithm applied is shown in Figure 4.22. The corresponding distribution for the energy resolution and the resolution in the polar and azimuthal angle are displayed for clusters with and without associated track. The energy distribution was improved for both types of cluster. Even with the pairing algorithm applied, a small shift in the energy is observed and the distribution is slightly asymmetric. This is due to the fact, that approximately $2X_0$ of material are situated in front of the electromagnetic calorimeter. For a shower that starts before the photon actually reaches a lead glass block, a certain fraction of the energy is deposited in the detector material rather than in the calorimeter. The resolution in the azimuthal and polar angles are only slightly improved.

If a photon candidate is too close to an entrance point of a track into the ECAL, the track's hadronic interaction can distort the photon energy measurement. Therefore a minimum angle between a photon candidate and a the entrance point of the electromagnetic calorimeter of 2.8° is required. This value is obtained from studies of the rate of fake π^0 in the decay $\tau^- \rightarrow \mathrm{K}^- \nu_\tau$. The energy in the hadron calorimeter is not considered here.

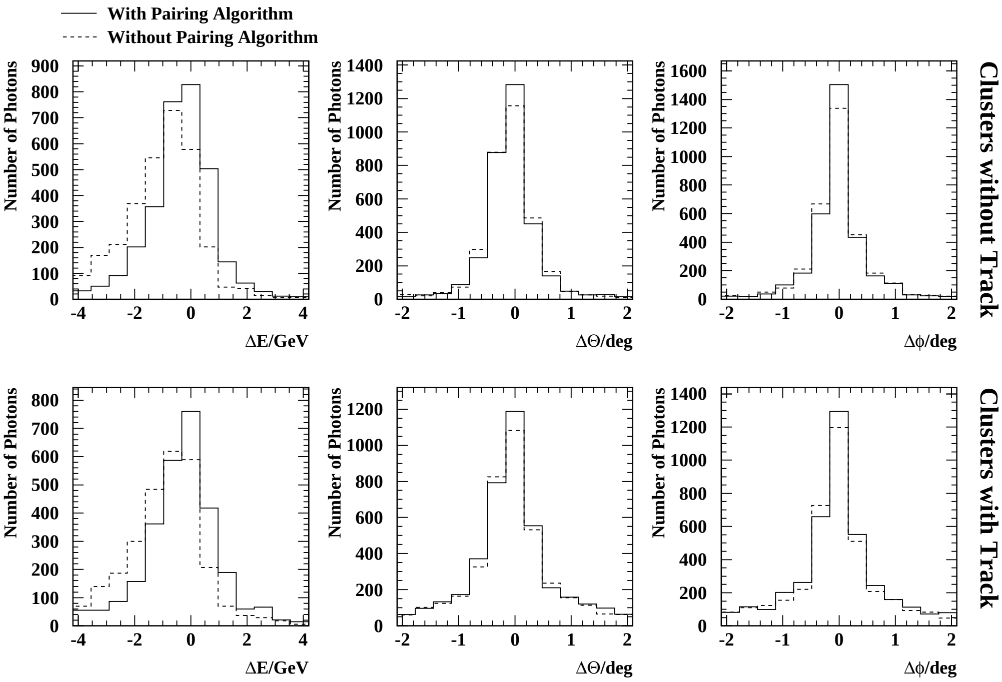

Fig. 4.22: Resolution of the reconstructed photons after applying the photon pairing algorithm. The upper (lower) plots correspond to cluster without (with) associated track. In each row, the resolution in energy and the resolution in the polar and azimuthal angles is given. The solid line corresponds to the resolution distribution with the pairing algorithm applied to the reconstructed photons, the dashed histogram corresponds to the distribution without pairing algorithm.

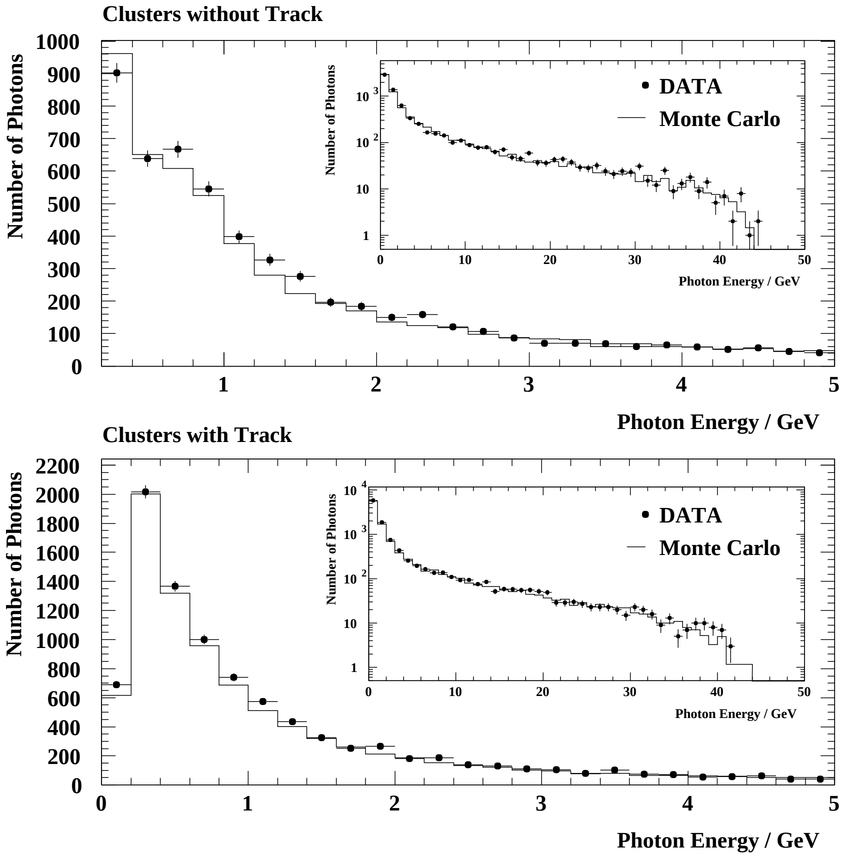

Fig. 4.23: Energy of reconstructed photons. In the upper (lower) plot, the corresponding distribution for clusters without (with) associated track is displayed. The dots are the data, the histogram is the predicted distribution from Monte Carlo simulation. The smaller insert shows a logarithmic version of the plot over the whole energy range.

The neutral objects remaining after the pairing procedure are called photons. The energy of the reconstructed photons can be found in Figure 4.23. The energy distribution for clusters with and without associated tracks in general is very good up to the highest photon energies observed in τ decay events. For photon energies below $\sim 1.5\,\mathrm{GeV}$, the number of photons reconstructed is still slightly underestimated in the Monte Carlo simulation compared to the data.

4.2.5 Reconstruction of Neutral Pions

The angular resolution of the photon reconstruction using the algorithm explained above, was found to be $1.7°$ $(2.1°)$ for clusters without (with) an associated track pointing to one of its blocks. From this resolution, the minimum energy of a neutral pion can be calculated for which the two photons from its decay can no longer be separately reconstructed by the algorithm applied. Therefore, reconstructed photons with an energy of more than $7.5\,\mathrm{GeV}$ were directly interpreted as neutral pions. To account for the mass of the π^0, the momentum vector of the photon is corrected by a factor x:

$$x = \frac{\sqrt{E_\gamma^2 - m_{\pi^0}^2}}{E_\gamma} \qquad \rightarrow \qquad \vec{p}_{\pi^0} = x \cdot \vec{p}_\gamma, \tag{4.25}$$

which is calculated from the energy of the reconstructed photon and the nominal mass of the neutral pion.

For the remaining photons, each possible combination of two photons is tested, whether they can be combined to a neutral pion. The number N_{π^0} of neutral pions that can be reconstructed from N_γ photons (where $N_{\pi^0} \leq N_\gamma/2$) identified in a τ cone by the above algorithm is given by

$$M_{N_{\pi^0}}^{N_\gamma} = \binom{N_\gamma}{2N_{\pi^0}} \frac{(2N_{\pi^0})!}{(N_{\pi^0})!\; 2^{N_{\pi^0}}}. \tag{4.26}$$

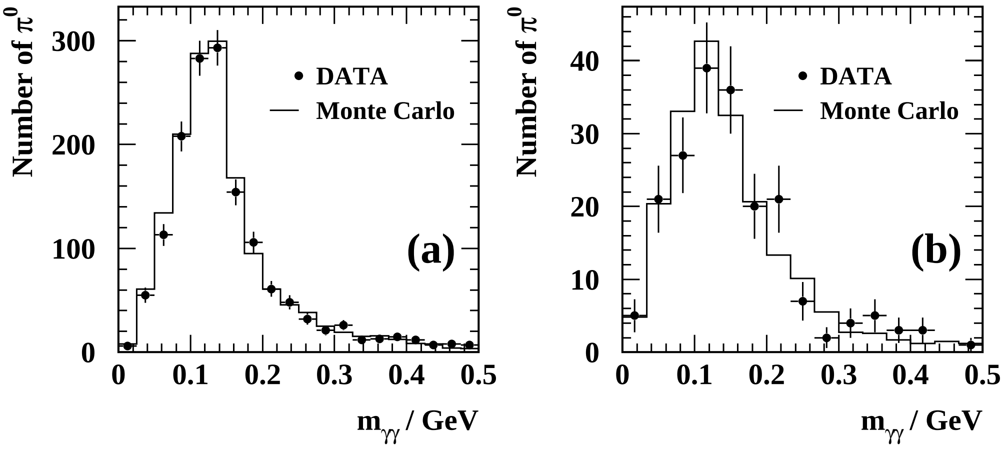

Fig. 4.24: Invariant two-photon mass for 1-prong and 3-prong τ decays in plot (a) and (b), respectively. The dots are the data and the histogram denotes the prediction from Monte Carlo simulation. A minimum energy of 1.5 GeV (2.0 GeV) is required for the neutral pion in the 1-prong (3-prong) case.

The combination which results in the maximum number of neutral pions is chosen, where the two-photon invariant mass may have a maximum deviation of 1.5σ from the nominal π^0 mass. For 1-prong τ decays, a minimum energy for the neutral pion of $E_{\mathrm{min}}^{1-\mathrm{prong}} = 1.5\,\mathrm{GeV}$ is required. In the 3-prong case, all π^0-candidates with an energy less than $E_{\mathrm{min}}^{3-\mathrm{prong}} = 2.0\,\mathrm{GeV}$ were rejected. The energy distribution is displayed in Figure 4.25.

To increase the mass resolution, these π^0 candidates are then subjected to a kinematic fit, that constrains the invariant two photon mass to the nominal mass of the π^0. The invariant two photon mass before the kinematic fit can be found in Figure 4.24. The distribution from data is well described by the Monte Carlo simulation. All π^0 candidates where the kinematic fit converges are called neutral pions. The invariant two photon mass found in 3-prong τ decays is broader compared to that from 1-prong decays. This reflects the reduced resolution (see Figure 4.22) in the presence of an associated track in the electromagnetic cluster. The number of neutral pions reconstructed in 1-prong and 3-prong τ decays is displayed in Figure 4.26. The data is well described by the Monte Carlo simulation.

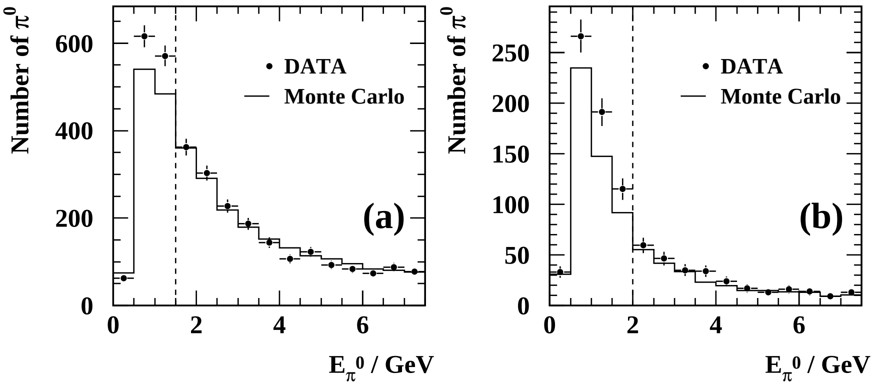

Fig. 4.25: The energy of the reconstructed neutral pions is displayed for 1-prong (3-prong) τ decays in plot (a) (plot (b)).The dots are the data and the histogram denotes the prediction from Monte Carlo simulation. The cut on the minimum energy of the π^0 is indicated by the dashed line and is placed at $E_{\mathrm{min}}^{1-\mathrm{prong}} = 1.5\,\mathrm{GeV}$ and $E_{\mathrm{min}}^{3-\mathrm{prong}} = 2.0\,\mathrm{GeV}$, respectively.

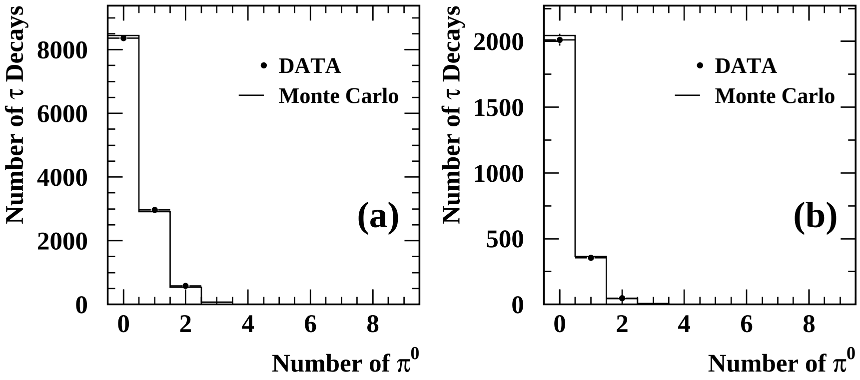

Fig. 4.26: The Number of reconstructed neutral pions in 1-prong and 3-prong τ decays is displayed in plot (a) and (b), respectively. The dots are the data and the histogram denotes the prediction from the Monte Carlo simulation.

4.3 Identification of Events Containing K^0

A neutral kaon is involved in roughly 1.8% of all τ decays and in about 30% of all decays with open strangeness. It is produced in weak interactions with definite strangeness $S = 1$ and -1 for the $\mathrm{K}^0(\mathrm{d\bar{s}})$ and the $\overline{\mathrm{K}}^0(\mathrm{\bar{d}s})$, respectively. It is the lightest meson containing a strange quark and since strangeness is conserved in strong and electromagnetic interaction, it can only decay weakly. Weak decays, however, are expected to be eigenstates of CP[4], which the neutral kaon is not. Linear combinations of K^0 and $\overline{\mathrm{K}}^0$ however are CP eigenstates

$$|\mathrm{K}^0_\mathrm{S}\rangle = \frac{1}{\sqrt{2}}(|\mathrm{K}^0\rangle + |\overline{\mathrm{K}}^0\rangle) \qquad \mathrm{CP} = +1$$

$$|\mathrm{K}^0_\mathrm{L}\rangle = \frac{1}{\sqrt{2}}(|\mathrm{K}^0\rangle - |\overline{\mathrm{K}}^0\rangle) \qquad \mathrm{CP} = -1.$$

In the absence of orbital angular momentum and zero net spin, possible hadronic final states are 2π and 3π, which have CP eigenvalues +1 and −1, respectively. The K^0 signal therefore consists of 50% K^0_L and 50% K^0_S. The phase space factors for the 2π and 3π decay modes are substantially different, and therefore substantially different lifetimes are expected.

The K^0_L has a lifetime $\tau_{\mathrm{K}^0_\mathrm{L}} = (51.7 \pm 0.4)\,\mathrm{ns}$ which corresponds to a decay length of $\tau_{\mathrm{K}^0_\mathrm{L}} = 31\,\mathrm{m\,GeV}^{-1}$. In τ decays, neutral kaons on average are produced with a $\gamma \approx 30$, the K^0_L is therefore not expected to decay within the central detector. Its signature is a large energy deposit in the hadron calorimeter without associated tracks pointing to it. An event display of a K^0_L decay can be found below. The resolution of the hadron calorimeter does not allow for a clean reconstruction of this channel, thus it is not considered in this analysis.

The K^0_S has a lifetime of $\tau_{\mathrm{K}^0_\mathrm{S}} = (89.37 \pm 0.12)\,\mathrm{ps}$ and a decay length of $\tau_{\mathrm{K}^0_\mathrm{S}} = 5.4\,\mathrm{cm\,GeV}^{-1}$. In 68% of all decays, two charged pions are produced. The signature of this decay mode is a secondary vertex which is separated from the interaction point. Due to the mass of the K^0, a non-zero opening angle of the decay products is observed, which helps in the rejection of track pairs originating from a photon conversion ($\gamma \to \mathrm{e}^+\mathrm{e}^-$). In 32% of all cases the K^0_S decays into two neutral pions. Since the photon reconstruction algorithm explicitly exploits the quasi-pointing geometry of the electromagnetic calorimeter in the barrel, only photons coming from the primary vertex can be properly reconstructed. Therefore, this decay mode is not considered in this analysis. An example for a K^0_S decay into two charged pions can be found below.

The aim of this selection is to reduce the background in the K^0_S candidate sample and to have an efficient selection. Two background contributions are distinguished. The background from photon conversions and

---

[4] neglecting CP violation

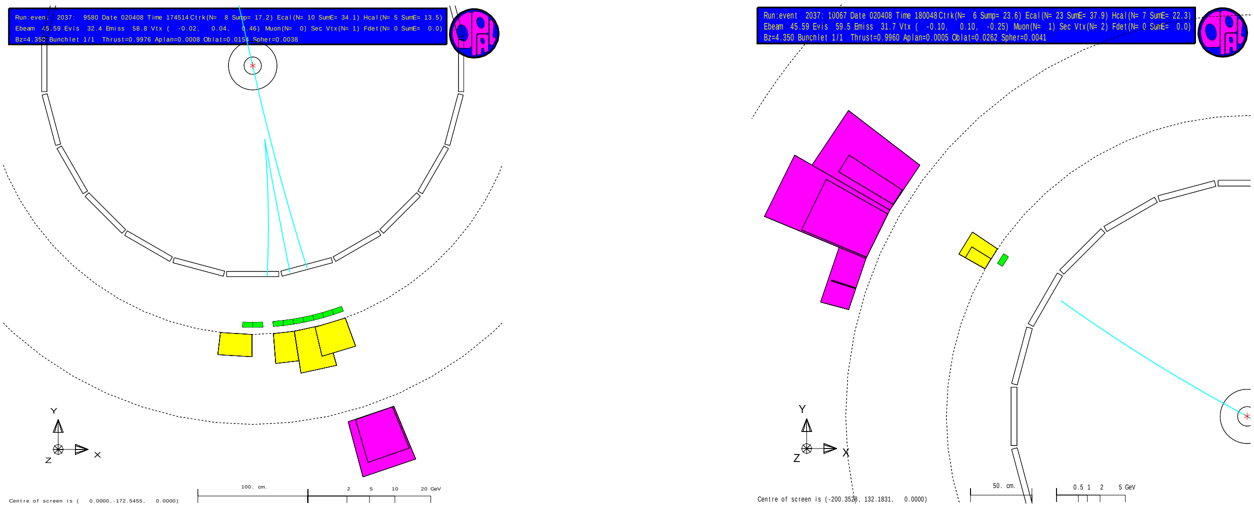

Fig. 4.27: Event display of τ decays involving neutral kaons. The left plot shows a decay $\tau^- \to \nu_\tau \mathrm{K}^0_\mathrm{S}\pi^-$ with the neutral kaon decaying into two charged pions. The secondary vertex is clearly separated from the interaction point. The right plot shows a decay $\tau^- \to \nu_\tau \mathrm{K}^0_\mathrm{L}\pi^-$. This signature is a large energy deposit in the hadron calorimeter without a track associated to it.

the combinatorial background which comes from the wrong combination of tracks.

4.3.1 Selection of K^0_S Candidates

The selection starts by combining each pair of oppositely charged tracks in a τ decay event. Each track considered has to have a transverse momentum with respect to the beam axis of $p_\mathrm{T} \geq 150\,\mathrm{MeV}$. Tracks with less energy have a large curvature and cannot be properly reconstructed. Furthermore the combinatorial background is reduced, since these tracks are most likely produced by δ electrons. A minimum of 20 out of 159 possible hits in CJ, at least 20% of all geometrically possible hits, are required for each track. A maximum χ^2 for the track fit of 50 is allowed. This guarantees a good momentum resolution. For each combination of tracks, their intersection points in the plane perpendicular to the beam axis are calculated. At least one intersection point within the sensitive volume of the central drift chamber is required. A radial distance of $r \leq 150\,\mathrm{cm}$ is required for the secondary vertex candidate. For vertices with $r > 150\,\mathrm{cm}$ there are not enough measured points in CJ so that the tracks can not be properly reconstructed. Due to the mass of the K^0, the opening angle of the decay products is non-zero and at least one intersection point is found in almost all K^0_S decays. The requirement to find at least one intersection point within the sensitive volume of the central drift chamber already reduces the background contribution from photon conversions, where the opening angle is zero. In this case it is more likely to find no intersection point at all due to resolution effects. If two vertices are found which fulfill the above requirements, the one with the first measured hit closest to the intersection point is selected. In addition the z-coordinate of the vertex has to satisfy $|z_\mathrm{V}| < 80\,\mathrm{cm}$.

The variables used in the selection described below are shown in Figure 4.29. For each K^0_S candidate, the angle between the reconstructed momentum of the candidate vertex and the K^0_S direction of flight must be less than $|\Theta_\mathrm{V}| < 0.5°$ (see Figure 4.28). This guarantees, that the neutral particle, reconstructed from the two tracks actually was produced at the primary vertex. With this cut the contribution from combinatorial background is reduced. If the number of $\mathrm{d}E/\mathrm{d}x$-hits is more than 20 on at least one of the tracks, the energy loss information is used to veto photon conversions. All candidates where at least one track has a pion weight of more than 0.98 are rejected. To further reduce this kind of background, the invariant mass of the K^0_S candidate is calculated using electron hypothesis for the masses of the two tracks. All combinations with a mass $m_\mathrm{ee} < 0.1\,\mathrm{GeV}$ are rejected.

The remaining background from 3prong τ decays can be reduced by applying cuts on the impact parameter d_0 of the two tracks. For tracks coming from a K^0_S decay, due to the opening angle of the decay products and the lifetime of the K^0_S, they are expected to have on average a large impact parameter. Tracks from decays not involving K^0_S are expected to have small $|d_0|$, since they are produced at the primary vertex (neglecting the flight distance of the τ lepton, which is small compared to that of the neutral kaon). The minimum and the maximum of the absolute value of the impact parameters from the two tracks in K^0 candidates can be found in Figure 4.29(c/d). Cuts are placed at 0.03 cm for the minimum and 0.1 cm for the maximum. The

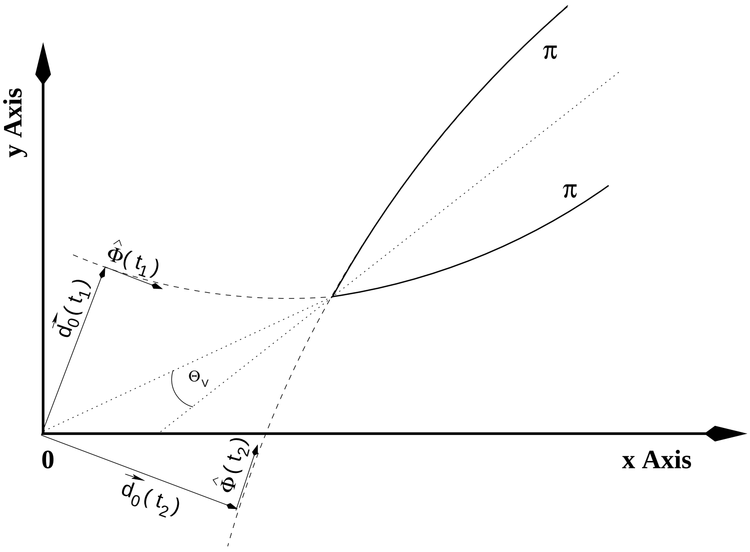

Fig. 4.28: Illustration of selection quantities in K^0_S decays.

d_0 values have to have opposite signs according to the OPAL convention. Using this convention, the impact parameter is defined as

$$d_0 \equiv \hat{\Phi} \times \vec{d} \cdot \hat{z} \tag{4.27}$$

where

- $\hat{\Phi}$ is the unit vector along the track trajectory at the point of closest approach (p.c.a)
- $\vec{d}$ is the vector from the interaction point to the p.c.a.
- $\hat{z}$ unit vector along the z axis.

The cross product in the above equation leads to different signs of the impact parameter for track pairs of opposite charge as illustrated in Figure 4.28.

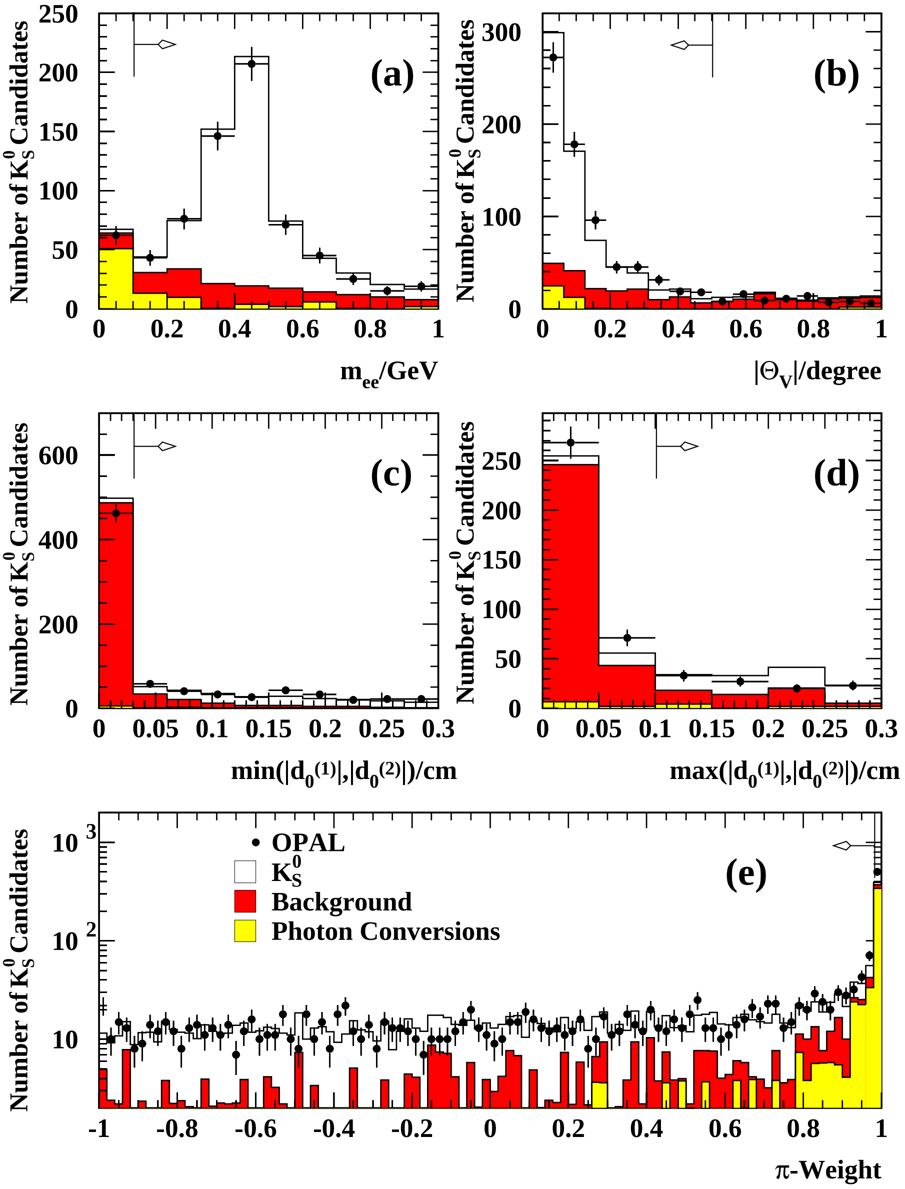

Fig. 4.29: Variables used in the K^0_S selection. A detailed description of all variables is given in the text. The dots represent data and the open histogram is Monte Carlo signal. The shaded areas show the background where photon conversions are marked separately. Events on the side of the direction of the arrow are kept. For all plots all selection cuts have been applied except for the cut on the variable shown.

4.3.2 Result of the K^0_S Selection

The remaining K^0_S candidates have to have a total momentum of $p_{K^0_S} > 3\,\mathrm{GeV}$. To those the 3D vertex fit as explained in Appendix 9.3 is applied including a constraint of the invariant two-track mass under pion-hypothesis to the nominal K^0_S mass.

The invariant two-track mass under pion hypothesis before the kinematic fit can be found in Figure. The radius of the reconstructed secondary vertex is displayed in Figure 4.30(a). This does not exhibit an exponential behavior, as might be expected. This is due to reduced efficiency near the primary vertex. Two effects contribute. As the radius of the secondary vertex becomes smaller, the resolution of the track parameters and thus the reconstruction of the secondary vertex does not allow for a clean and efficient separation from the primary vertex. The second contribution comes from background events not containing K^0_S or from photon conversions.

The χ^2 probability of the kinematic fit can be seen in Figure 4.30(c). It shows a nice flat behavior down to 10^{-5}. The background from conversions and the background from true 3-prong τ decays piles up at low probabilities and is removed by a cut at 10^{-5}. If more than one K^0_S candidate share the same track, the one with the smaller deviation from the nominal K^0_S mass before the fit is selected. After this selection procedure a total of 535 K^0_S remains with an estimated purity of 82%. About 70% of the background consists of wrong combinations of tracks, 30% comes from conversions. In one data event two K^0_S candidates are found within one cone. This event is considered as background.

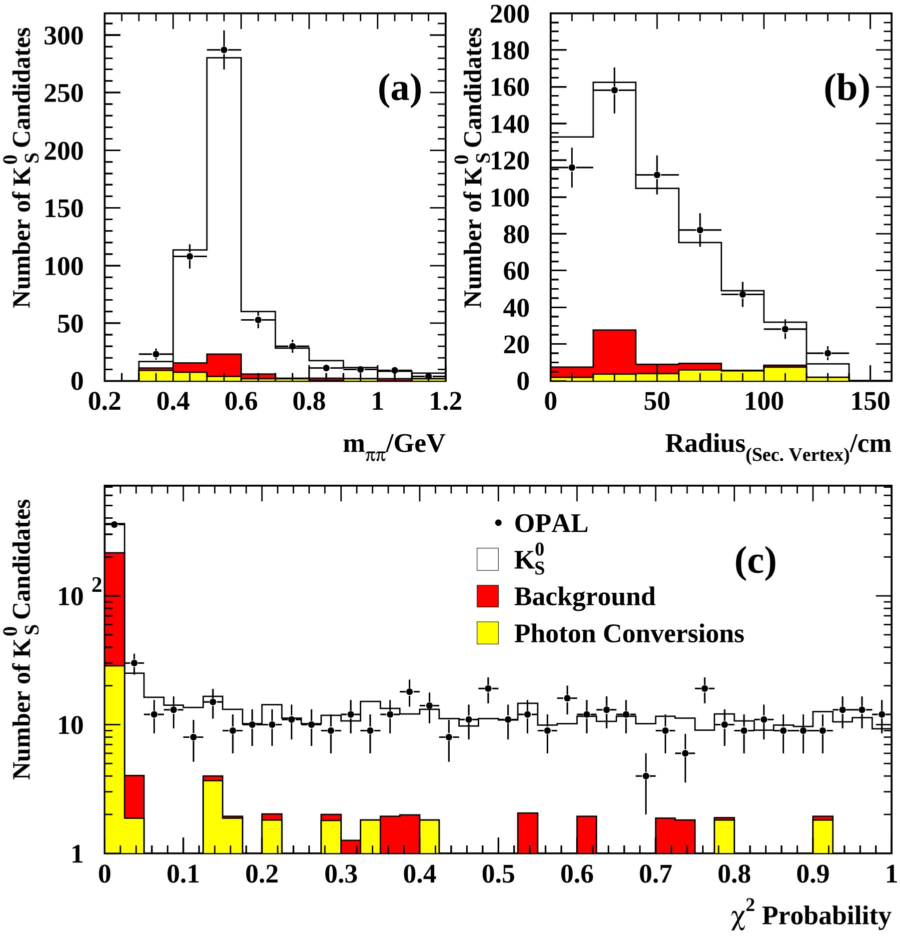

Fig. 4.30: Result of the K^0_S selection. Plot (a) shows the invariant mass distribution of the K^0_S candidates under pion hypothesis before the kinematic fit. Plot (b) shows the radius of the reconstructed secondary vertex and plot (c) the distribution of the χ^2-probability of the 2C-fit. A cut is applied on the probability at 10^{-5}. The dots represent the data and the open histogram is Monte Carlo signal. The shaded areas show the background where conversions are marked separately.

4.4 The Monte Carlo Simulation

Kaons are involved in roughly 3% of all τ final states with open strangeness. The single kaon and the two meson final states are the largest ones. The three meson final states are of about the size of the single kaon channel. Though the four-meson final states with strangeness together make up only 5% of all strange final states, they are of particular importance since they populate the high end of the mass spectrum. For final states with an invariant mass above $\sim 1\,\mathrm{GeV}$ for example, they already make up $\sim 20\%$ of all reconstructed events. In the standard τ Monte Carlo, these final states are missing. The corresponding background channels (i.e. four-meson final states with an even number of kaons) are also not simulated. In addition, strange τ decays involving η mesons are also not implemented in the standard τ Monte Carlo.

This section starts with a short introduction on the parametrization of multi-meson final states including intermediate resonances. In this chapter, the update of the resonance structure of the three meson final states and the simulation of the missing τ decay modes is discussed. In the last section, an overview over the complete set of Monte Carlo samples used in this analysis is given.

4.4.1 Update of the Three Meson Final States

Hadronic τ decays occur often via intermediate vector or axialvector resonances. For example the decay into a three pions occurs via the a_1 resonance, which then decays via the intermediate ρ resonance. Another example is the $\mathrm{K}^0\pi^-\nu_\tau$ final state, which has the $\mathrm{K}^*(892)$ as intermediate resonance. Those decays can described in the so-called Vector Dominance Model (VDM), where the resonances are parametrized by Breit-Wigner form factors. The mass and the width of the resonances involved can not be predicted in this model. They are free parameters which have to be determined by experiment. In contrast to the non strange final states which can be assigned to a vector or axialvector current by simply counting the number of pions[5], decay modes involving kaons allow for vector and axialvector contributions at the same time.

The most general Ansatz for the matrix element of the quark current J^μ, describing the creation of three mesons, is given via

$$\begin{aligned} J^\mu &= \langle \pi_1(q_1)\pi_2(q_2)\pi_3(q_3)|J^\mu_A(0)+J^\mu_V(0)|0\rangle \\ &= V_1^\mu F_1 + V_2^\mu F_2 + \imath V_3^\mu F_3 + V_4^\mu F_4. \end{aligned} \tag{4.28}$$

It is characterized by four complex form factors F_i, which are functions of the Dalitz variables $s_1=(q_2+q_3)^2$, $s_2=(q_1+q_3)^2$, $s_3=(q_1+q_2)^2$ and Q^2, the invariant mass of the hadronic system. The form factors F_1 and F_2 originate from the $J^P=1^+$ spin-1 axial vector current and F_3 originates from the $J^P=1^-$ spin-1 vector state. The F_4 form factor corresponds to the $J^P=0^+$ spin-0 part of the axial current matrix element. It is assumed to be negligible here. The current components V_i can be calculated from the four-vectors of the final state particles q_i^μ:

$$\begin{aligned} V_1^\mu &= q_1^\mu - q_3^\mu - Q^\mu\frac{Q(q_1-q_3)}{Q^2} \qquad & V_3^\mu &= \varepsilon^{\mu\alpha\beta\gamma}q_{1\alpha}q_{2\beta}q_{3\gamma} \\ V_2^\mu &= q_2^\mu - q_3^\mu - Q^\mu\frac{Q(q_2-q_3)}{Q^2} \qquad & V_4^\mu &= q_1^\mu + q_2^\mu + q_3^\mu = Q. \end{aligned}$$

The form factors are given by

$$F_1(Q^2,\, s_2,\, s_3) = \frac{2\sqrt{2}A}{3f_\pi}G_1(Q^2,\, s_2,\, s_3) \tag{4.29a}$$

$$F_2(Q^2,\, s_1,\, s_3) = \frac{2\sqrt{2}A}{3f_\pi}G_2(Q^2,\, s_1,\, s_3) \tag{4.29b}$$

$$F_3(Q^2,\, s_1,\, s_2) = \frac{A}{2\sqrt{2}\pi^2 f_\pi^3}G_3(Q^2,\, s_1,\, s_2), \tag{4.29c}$$

where A and the functions G_i are given in Table 9.2 [78]. They contain Breit-Wigner functions which contain

---

[5] neglecting decays involving the ω and η resonance

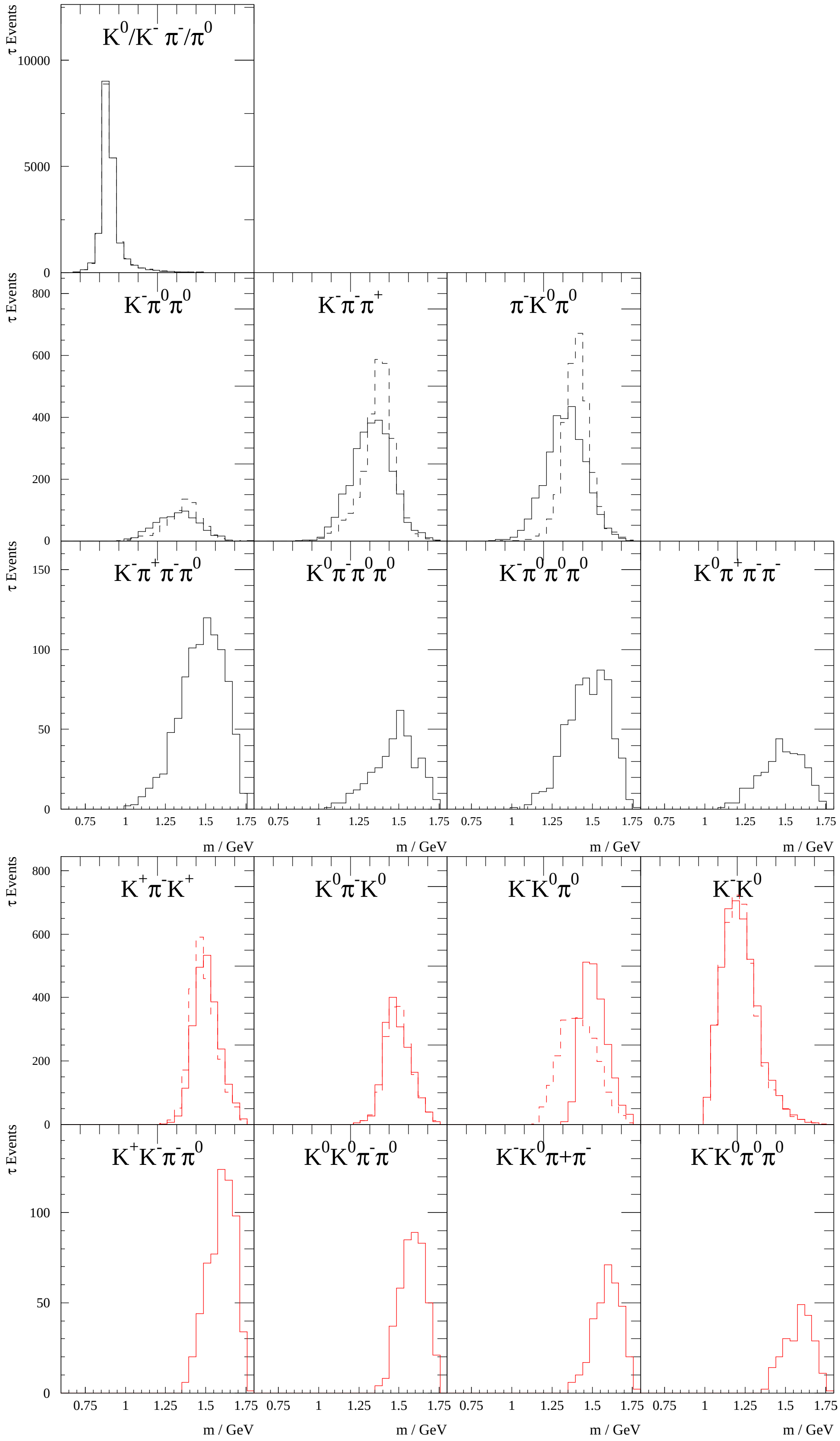

Fig. 4.31: Comparison of the invariant mass spectra between the standard Monte Carlo (dashed histograms) and the updated event sample.

admixtures of radial excitations.

$$T^{2m} = \frac{\mathrm{BW}_i + \beta \mathrm{BW}_j}{1+\beta} \tag{4.30a}$$

$$T^{3m} = \frac{\mathrm{BW}_i + \beta \mathrm{BW}_j + \gamma \mathrm{BW}_k}{1+\beta+\gamma} \tag{4.30b}$$

In Equations 4.30a and 4.30b, BW denote normalized Breit-Wigner propagators with an energy dependent width:

$$\mathrm{BW}_{\mathrm{X}}(Q^2) = \frac{m_X^2}{m_X^2 - Q^2 - \imath\sqrt{Q}^2\Gamma_X(Q^2)}. \tag{4.31}$$

The factors β and γ denote the relative strength of the contributions from the higher excitations.
The three meson final states with kaons are updated using the parametrizations given in [78]. A comparison of the new and the old parametrization of the three meson final states with kaons is displayed in Figure 4.31.

4.4.2 Four-Meson Final States

For the four-meson final states, the structure of the resonances involving kaons is basically unknown. Unfortunately, the statistics in this analysis is by far not sufficient, to gain insights into the structure. Though the branching fractions for these decay channels are small and the statistical error is large, they make important contributions to the invariant mass spectrum and the spectral function near the kinematic limit. This can be seen in Figure 4.32(b). The dashed histogram represents the strangeness spectral function as obtained using the standard τ Monte Carlo. Close to the kinematic, the measured distribution is expected to approach the prediction from the naïve parton model. Due to the missing four-meson strange final states this is not the case.

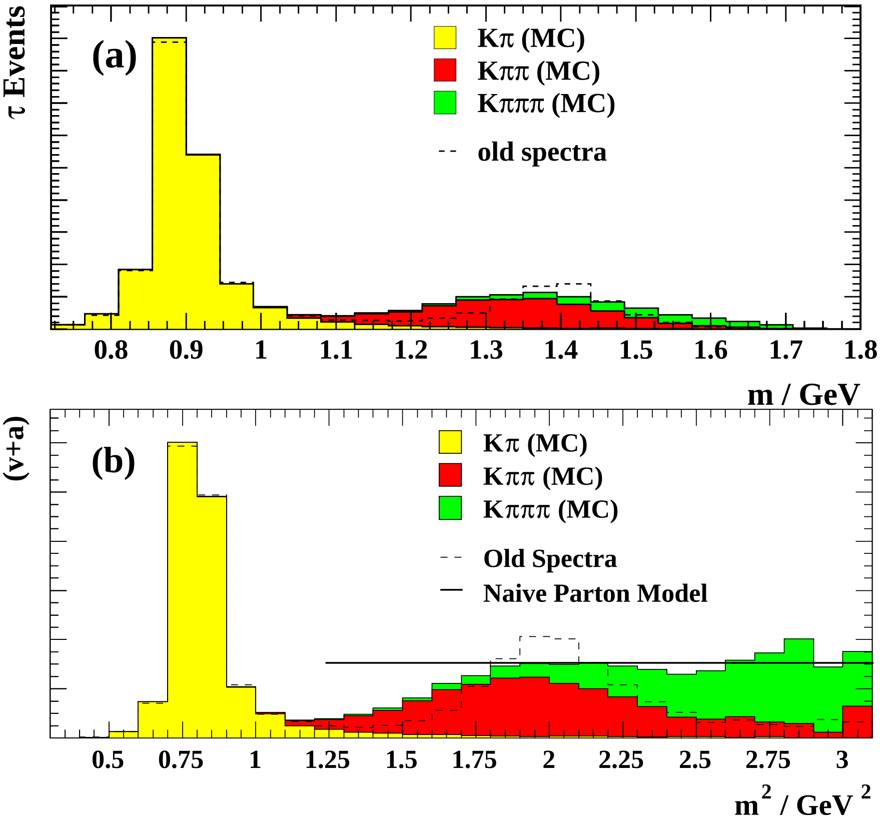

Fig. 4.32: Comparison between the standard τ Monte Carlo and the updated simulation for the invariant mass distribution(a) and the spectral function (b). The contributions from the different multi meson final states are marked separately. The distributions as obtained from the standard τ Monte Carlo is denoted by the dashed line.

In addition, the background in the corresponding signal channels, as predicted by the standard Monte Carlo is not correct. The four-meson final states either with an odd or an even number of kaons contribute for example to the measured three meson spectra. Therefore, the four-meson final states with kaons are implemented into the τ Monte Carlo, assuming an invariant mass distribution according to phase space. The invariant mass spectra for the corresponding channels are displayed in Figure 4.31. The invariant mass distribution for the strange final states and the strangeness spectral function as simulated in the Monte Carlo including the updated resonance structure for the three meson final states and the new four-meson final states is displayed in Figure 4.32(a) and (b), respectively. The exclusive contributions from the various multi meson final states are marked separately.

4.4.3 Monte Carlo Samples

The τ Monte Carlo sample used consists of 200 000 τ pair events generated at $\sqrt{s} = m_{Z^0}$ using KoralZ 4.02 [80] and a modified version of Tauola 2.4 [81], including the modifications described above. The branching fractions of the decay channels with kaons are enhanced in this sample so that it comprises roughly a factor of ten more τ decays with kaons than expected from data. The Monte Carlo events are then reweighted to the latest branching fractions given in [57], which are used throughout the selection procedure. The Monte Carlo events were processed through the GEANT OPAL detector simulation [79].

The non-τ background was simulated using Monte Carlo samples that consist of q$\bar{\text{q}}$ events generated with Jetset [82], Bhabha events generated with Bhwide [83], μ-pair events generated with KoralZ [80] and two-photon events using Phojet [84], F2Gen [85] and Vermaseren [86,87]. The non-τ background Monte Carlo samples used are summarized in Table 4.7. The number of events generated for each physics process and the integrated luminosity the size of the Monte Carlo sample corresponds to is given. The last column contains the weight as used in the event selection.

	MCID	Physics Process	Events	Luminosity/ pb^{-1}	Event Weight
Bhabha Events	1360	$e^+e^- \rightarrow e^+e^-$	574 000	139.9	0.982
μ Pair Events	1618	$e^+e^- \rightarrow \mu^+\mu^-$	792 000	534.1	0.257
Multihadron Events	2790/4	$e^+e^- \rightarrow \bar{q}q$	4 000 000	129.9	1.061
Two Photon Events	1014	$\gamma\gamma \rightarrow \bar{q}q$	999 999	209.0	0.656
	1039	$\gamma\gamma^* \rightarrow \bar{q}q$	100 000	660.0	0.906
	1099	$\gamma\gamma \rightarrow \mu^+\mu^-$	250 000	492.0	0.270
	1098	$\gamma\gamma \rightarrow e^+e^-$	350 000	687.0	0.270
	1017	$\gamma\gamma \rightarrow \tau^+\tau^-$	55 000	202.0	0.504

Tab. 4.7: Summary of the non-τ background Monte Carlo samples used in the analysis strangeness spectral function. The physics process is given, the number of events and the integrated luminosity of the Monte Carlo sample. The last column contains the event weights as used in the selection.

5. THE EVENT SELECTION

The data analyzed in this work was recorded with the OPAL detector during the years 1991 to 1995 at a center of mass energy which corresponds to the mass of the neutral weak boson Z^0 ($\sqrt{s} = m_{Z^0} = 91.2\,\mathrm{GeV}$). A total integrated luminosity of $\mathcal{L} = 121\,\mathrm{pb}^{-1}$ has been recorded. In 3.37% of all decays of the Z^0 boson, a pair of τ leptons is produced, which are subject to this analysis.
In this chapter the separation of the τ pair events from non-τ background and the selection of τ decays with open strangeness is described. These channels make up a total of $B_{\mathrm{strange}} = 2.94\%$ of all τ decays (using the branching fractions given in [57]). The following final states are contributing, which are summarized in Table 5.1.

- $(\mathrm{K})^-$: The single kaon channel has a branching fraction of $B = (0.686 \pm 0.023)\%$. No invariant mass reconstruction is possible, since the energy resolution in the hadron calorimeter is not sufficient.
- $(\mathrm{K}\pi)^-$: The two-meson final states with a total branching fractions of 1.340% consist of two decay channels. The decay[1] $\tau^- \rightarrow \mathrm{K}^-\pi^0\nu_\tau$ has a branching fraction of 0.450% and can be fully reconstructed. The $\tau^- \rightarrow \mathrm{K}^0\pi^-\nu_\tau$ channel ($B = 0.890\%$) consists of two decay chains: $\tau^- \rightarrow \mathrm{K}^0_{\mathrm{L}}\pi^-\nu_\tau$ (50%) and $\tau^- \rightarrow \mathrm{K}^0_{\mathrm{S}}\pi^-\nu_\tau$ (50%). For reasons explained in Chapter 4.3, the long lived neutral kaon is not considered here. The $\mathrm{K}^0_{\mathrm{S}}$ decays to two neutral (charged) pions in roughly 32% (68%) of all cases. Only the charged decay mode is considered here.
- $(\mathrm{K}\pi\pi)^-$: The decay channels $\tau^- \rightarrow \mathrm{K}^-\pi^+\pi^-\nu_\tau$ ($B = 0.280\%$) and $\tau^- \rightarrow \mathrm{K}^0\pi^-\pi^0\nu_\tau (B = 0.370\%)$ are fully reconstructed. The decay $\tau^- \rightarrow \mathrm{K}^-\pi^0\pi^0\nu_\tau$ with two neutral pions in the final state, is taken from Monte Carlo simulation. The three meson final states with strangeness together make up a total of $(0.708 \pm 0.068)\%$ of all τ final states.

---

[1] In order to simplify the text we refer only to the decays of the negatively charged τ lepton. Simultaneous treatment of the charged conjugate decay is always implied.

		Measured in this Analysis		Not Measured	
	$B_{\mathrm{total}}/\%$	τ Decay	$\mathrm{B_{PDG}}/\%$	τ Decay	$\mathrm{B_{PDG}}/\%$
$(\mathrm{K})^-$	0.686 ± 0.023			$\tau^- \rightarrow \mathrm{K}^-\nu_\tau$	0.686 ± 0.023
$(\mathrm{K}\eta)^-$	0.027 ± 0.006			$\tau^- \rightarrow \mathrm{K}^-\eta\nu_\tau$	0.027 ± 0.006
$(\mathrm{K}\pi)^-$	1.340 ± 0.050	$\tau^- \rightarrow \mathrm{K}^-\pi^0\nu_\tau$	0.450 ± 0.030		
		$\tau^- \rightarrow \mathrm{K}^0\pi^-\nu_\tau$	0.890 ± 0.040		
$(\mathrm{K}\pi\pi)^-$	0.708 ± 0.068	$\tau^- \rightarrow \mathrm{K}^0\pi^-\pi^0\nu_\tau$	0.370 ± 0.040		
		$\tau^- \rightarrow \mathrm{K}^-\pi^+\pi^-\nu_\tau$	0.280 ± 0.050		
				$\tau^- \rightarrow \mathrm{K}^-\pi^0\pi^0\nu_\tau$	0.058 ± 0.023
$(\mathrm{K}\eta\pi)^-$	0.029 ± 0.009			$\tau^- \rightarrow \mathrm{K}^*(892)\eta\pi^0\nu_\tau$	0.029 ± 0.009
$(\mathrm{K}\pi\pi\pi)^-$	0.150 ± 0.045	$\tau^- \rightarrow \mathrm{K}^-\pi^+\pi^-\pi^0\nu_\tau$	0.064 ± 0.024		
				$\tau^- \rightarrow \mathrm{K}^0\pi^-\pi^0\pi^0\nu_\tau$	0.026 ± 0.024
				$\tau^- \rightarrow \mathrm{K}^-\pi^0\pi^0\pi^0\nu_\tau$	0.037 ± 0.021
				$\tau^- \rightarrow \mathrm{K}^0\pi^-\pi^+\pi^-\nu_\tau$	0.023 ± 0.020
$\sum B^{\mathrm{total}}_{\mathrm{strange}}$	2.940 ± 0.099	$\sum B^{\mathrm{meas}}_{\mathrm{strange}}$	2.054 ± 0.085	$\sum B^{\mathrm{notmeas}}_{\mathrm{strange}}$	0.886 ± 0.051

Tab. 5.1: Overview of all channels with net strangeness and their respective branching fractions as given in [57]. The numbers are given separately for those τ final states that have been measured in this analysis and for those that were taken from Monte Carlo simulation.

- $(K\pi\pi\pi)^-$: The four-meson final state with a total branching fraction of $(0.150 \pm 0.045)\%$ is detected via the decay $\tau^- \rightarrow K^-\pi^+\pi^-\pi^0\nu_\tau$ $(0.064 \pm 0.024)\%$ which has the largest branching fraction among the four-meson final states. The remaining channels are taken from Monte Carlo simulation.

- $(K\eta)^-$ and $(K\eta\pi)^-$: The final states involving η mesons have a branching fraction of $(0.027 \pm 0.006)\%$ and $(0.029 \pm 0.009)\%$ [66], respectively. These channels are taken from Monte Carlo simulation.

Of the multi-meson final states with open strangeness, $(K\pi)^-$, $(K\pi\pi)^-$ and $(K\pi\pi\pi)^-$, 93.4% of all decay channels involved are measured. The remaining 6.6% are taken from Monte Carlo simulation.

This chapter is organized as follows: First the τ selection is described. It separates the τ pair events from Z^0 decays into electron pairs, muon pairs or a pair of quarks and from Bhabha scattering events and two photon background. In the second section the identification of final states with open strangeness is described and finally the invariant mass spectra are presented in Chapter 5.3.

5.1 The τ Pair Selection

The Z^0 decays in $(3.370 \pm 0.008)\%$ of all cases into a pair of τ leptons. They are produced back-to-back in the lab frame[2] with an energy of $E_{\text{beam}} = \sqrt{s}/2 = 45.6\,\text{GeV}$. In most of the cases, they decay into final states with one or three charged particles plus possible associated neutral pions or kaons. The typical signature is therefore a low multiplicity event with energy deposition in the electromagnetic and/or hadron calorimeter. Decays into five charged particles occur in only 0.1% of all cases, τ decays into seven charged particles have not been observed, yet ($B(\tau \rightarrow \nu_\tau 7-\text{prong}) < 2.4 \cdot 10^{-6}$ at CL= 90%). Due to the Lorentz boost of the τ lepton ($\gamma \approx 25$), all decay products are contained in a narrow cone of opening angle of typically 5°. At least one neutrino is involved in τ decays and therefore the measured total energy in τ pair events is less than the beam energy. Due to the τ-lifetime of $\tau = (290.6 \pm 1.1)\,\text{fs}$, a secondary vertex can be observed which is on average 2 mm displaced from the primary interaction point. An example for a Feynman diagram of a τ decay is given below where one τ decays leptonically, the other hadronically.

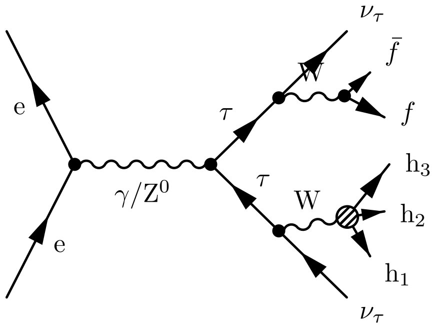

$f \in (e, \mu, \nu)$

$h_i \in (\pi, K)$

A typical τ pair event can be seen in the event display in Figure 5.1. The left plot shows the event in the $(r-\phi)$ plane as recorded with the OPAL detector. The tracks are recorded in the central drift chambers represented, by the inner circle. The light shaded bars represent the energy deposited in the electromagnetic calorimeter. Every bar represents one cluster, where the size is proportional to the energy measured therein. The dark shaded blocks represent the energy deposited in the hadron calorimeter. Hits in the muon chambers are indicated by arrows. In the box above the display, parameters of the event are given, e.g. run and event numbers, beam energy and visible energy.

In the upper hemisphere, a τ decay into three charged particles (pions or kaons) is seen. Besides the energy deposition in the hadron calorimeter, there is a large amount of energy in the electromagnetic calorimeter, which indicates the presence of additional neutral pions or final state radiation. The right plot is a zoom of the event. A secondary vertex can be clearly identified for the 3-prong τ decay.

In the lower hemisphere, a τ decay into one charged particle is seen. There is only little energy deposition in the electromagnetic calorimeter and a large amount of energy in the hadron calorimeter, which indicates that the charged track is a hadron (pion or kaon). The hit in the muon chamber, represented by the arrow, comes from a punch-through of the shower particles in the hadron calorimeter.

In the following, only events are considered where all decay products of the two τ leptons are contained in exactly two cones with a maximum half-angle of 35°. This includes all tracks in the jet chamber and all

---

[2] Neglecting initial and final state radiation

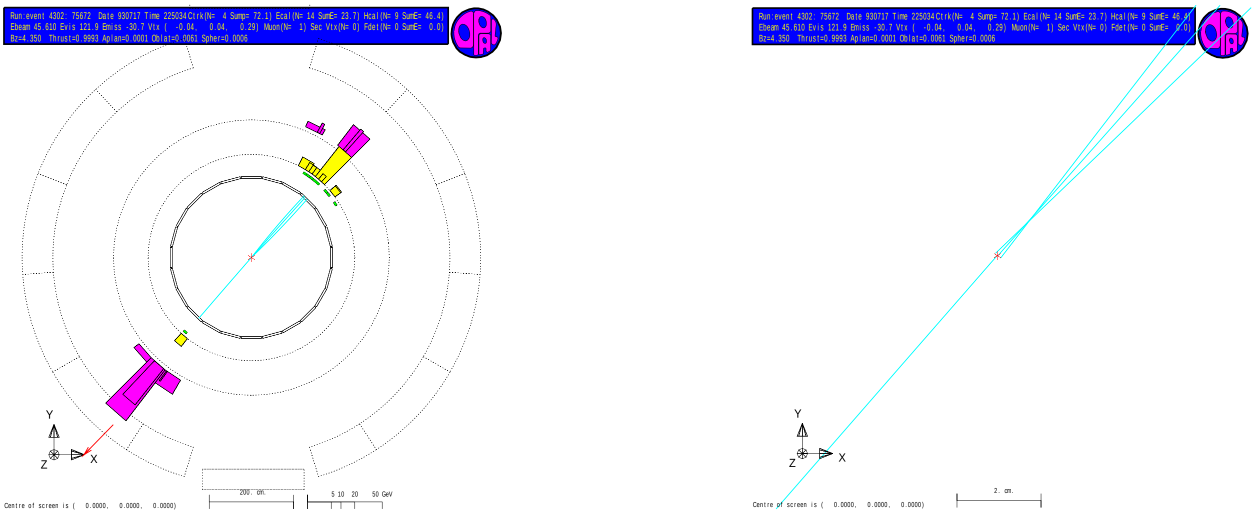

Fig. 5.1: Event display of τ decay in the $r - \phi$ plane. In the upper hemisphere of the left plot, a 3-prong τ decay can be seen. The lower hemisphere is a 1-prong decay. Details are given in the text. The right plot shows a zoom of the same event to region of the primary vertex. For the 3-prong decay, a displaced vertex is observed which is due to the lifetime of the τ lepton.

clusters reconstructed in the electromagnetic calorimeter. A maximum acollinearity angle of 15° is allowed for these cones. The tracks and clusters considered have to fulfill the following quality criteria.

- A **good track** has to have at least 20 hits in the jet chamber in order to guarantee a proper reconstruction of the trajectory. A maximum radial distance of the first measured hit of $r_{\mathrm{max}} = 75\,\mathrm{cm}$ from the primary vertex is allowed. The point of closest approach has to be less than $d_0 < 2\,\mathrm{cm}$ away from the primary vertex. In z direction the maximum distance is $|z_{\mathrm{max}}| = 75\,\mathrm{cm}$. A minimum transverse momentum of $p_{\mathrm{T}} > 0.1\,\mathrm{GeV}$ is required for each reconstructed track.

- A **good cluster** has to have at least one block with a minimum energy of $E_{\mathrm{min}} = 100\,\mathrm{MeV}$ if the cluster is reconstructed in the barrel part of the detector. A minimum of two blocks with an energy sum exceeding $E_{\mathrm{min}} = 200\,\mathrm{MeV}$ is required if the cluster is in the endcaps. In that case, the most energetic block must not contain more than 99% of the total total electromagnetic energy in the cluster.

In the following the individual sources of non-τ background are discussed and the selection criteria applied to remove them are explained.

$\mathrm{q\bar{q}}$ **Events:**

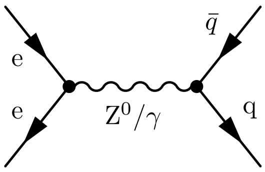

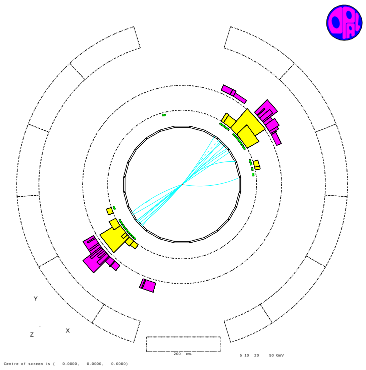

The $\mathrm{Z^0}$ decays with a branching fraction of $B = (69.91 \pm 0.06)\%$ into a pair of quarks. A typical hadronic $\mathrm{Z^0}$ decay can be seen in the event display above. Due to the high center of mass energy this results in a final state with two back-to-back jets of high multiplicity[3] and significant energy deposition in the electromagnetic and hadron calorimeters. The radiation of gluons off the final state quarks would result in additional jets. To remove hadronic events, the following cuts are applied.

---

[3] The average multiplicity of a hadronic events is of the order of 15.

- A maximum of two cones with half-angle of 35° are allowed in the event. The energy in each cone has to exceed 1% of the beam energy.
- At least one 'good' track per cone is required. The maximum number of tracks in the event must not exceed six.
- A maximum of ten 'good' clusters in the electromagnetic calorimeter is allowed in the event.

Two Photon Events:

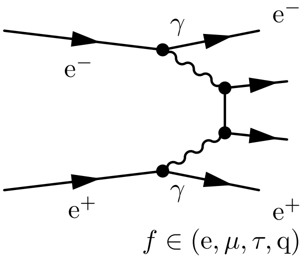

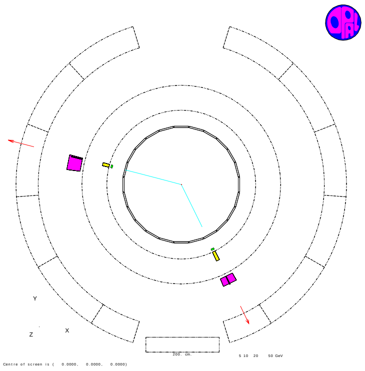

In these events, a photon is radiated off each of the two initial state electrons/positrons. The interaction of these photons can produce either a leptonic or a hadronic final state. A typical two-photon event can be seen in the event display above. Since the energy of the two photons is different, the resulting final state is boosted. The event looks in general asymmetric. Furthermore, the energy of this final state is usually less than the beam energy, since the initial state particles escape undetected. The following cuts are applied to remove two-photon events.

- The maximum acollinearity angle allowed between the two cones in the event is 15°.
- The event is removed if the visible energy in one of the cones is less than 3% of the beam energy.
- If the visible energy is in the range $3\% < E_{\text{vis}} < 20\%$, the transverse momentum as calculated from tracks and clusters has to exceed 2 GeV.

Muon Pair Events:

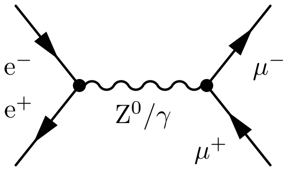

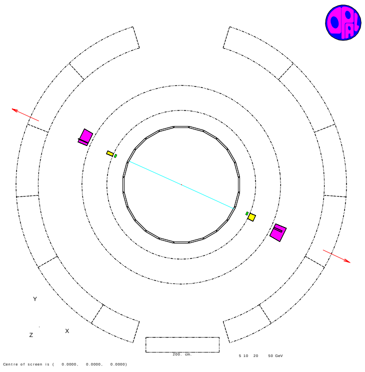

In $(3.366 \pm 0.007)\%$ of all cases, the Z^0 decays into a pair of muons. The experimental signature is two high energetic ($E_\mu \approx \sqrt{s}/2 = 45.6\,\text{GeV}$) back-to-back tracks in the central detector, small or no energy deposition in the electromagnetic and hadron calorimeters and hits in the muon chambers which can be assigned to the tracks. A typical muon pair event can be seen in the event display above. The two muons are identified separately by requiring that at least one of the following criteria is fulfilled.

- The total energy deposited in the electromagnetic calorimeter must not exceed 2 GeV. A minimum ionizing particle on average deposits an energy of $E = 420\,\text{MeV}$ in the OPAL lead glass calorimeter.
- The sum of the number of fired layers in the muon chamber and the last three layers of the HCAL must be larger than 5.

- At least two hits are found in the muon chambers.

If both muon candidates fulfill these requirements and if the sum of the energy measured in the jet chamber and in the electromagnetic calorimeter exceeds 60% of the center of mass energy, the event is identified as a muon pair.

$e^+e^- \rightarrow e^+e^-$ **Events:**

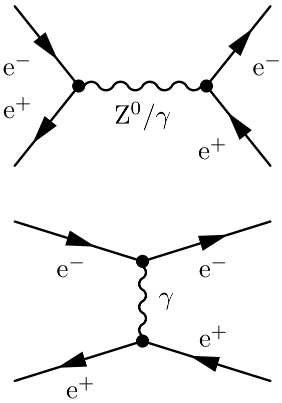

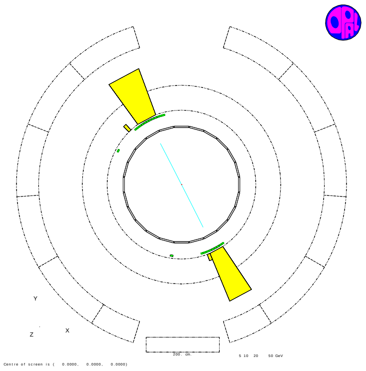

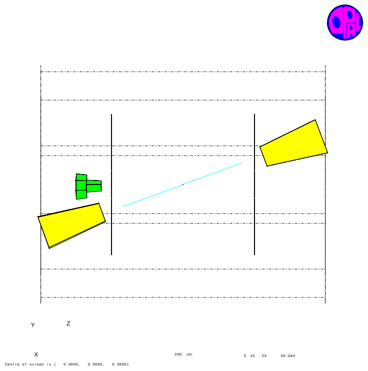

The experimental signature is two back-to-back high energetic tracks in the jet chamber with an energy close or equal to the beam energy. Since electrons are completely absorbed in the electromagnetic calorimeter, one high energetic cluster is expected per hemisphere, which can be assigned to the corresponding track. No or very little energy deposition is measured in the hadron calorimeter and no hits are expected in the muon chambers.

Two physics processes contribute to this final state. In the s-channel process, which is shown by the upper Feynman diagram, electron and positron annihilate to a Z^0 or γ which then decays into an electron-positron pair. The angular distribution of the final state particles is $\propto (1 + \cos^2 \Theta)$ like in τ pair events. In the t-channel process, where electron and positron are scattered by only a small angle via γ exchange, the angular distribution is peaking in forward direction. To remove this event type, the following cuts were applied.

- **Barrel Region:**
  If the average $|\cos\Theta|$ as calculated from tracks and the clusters in the electromagnetic calorimeter is less than 0.7 (barrel region), the average cluster energy in the event plus 30% of the average energy as calculated from the tracks has to be larger than 80% of the beam energy.
- **Endcap Region:**
  In the endcap region the event is identified as a Bhabha event if the following criteria are not fulfilled:
  - ∗ The average energy as calculated from the tracks is less than 80% of the beam energy and the sum of the track energy plus the average energy as measured in the electromagnetic calorimeter is less than 1.05 times the beam energy.
  - ∗ The average energy as calculated from the tracks is greater than 80% of the beam energy and the average energy as deposited in the electromagnetic calorimeter is less than 25% of the beam energy.

Cosmic Muon Events:

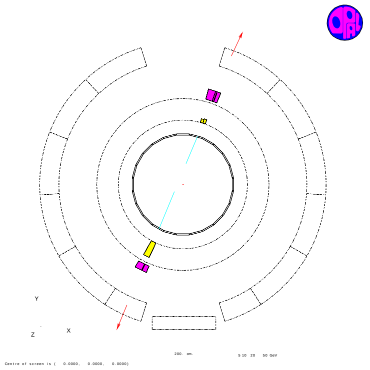

They are produced in the interaction of cosmic radiation with the atmosphere. They pass the detector from outside and leave one track in the jet chamber which will most probably be displaced from the primary vertex. For events in the central region of the detector ($|\cos\Theta| < 0.8$) the information from the Time-of-Flight counter is used. Events from τ decays are required to contain at least one TOF counter that measures a time within 10 ns of that expected for a particle coming from the interaction point. In addition the time difference between the signals from two opposite[4] modules is considered. Events were rejected as cosmic rays if $\Delta t > 10\,\mathrm{ns}$ for all such pairs. If an event is not classified as being in the barrel region and does not satisfy the TOF acceptance criteria, it is required to contain at least one pair of tracks with

$$\sum |d_0| < 0.6\,\mathrm{cm}$$
$$\sum |z_0| < 25\,\mathrm{cm}.$$

After the τ selection as described above, a total of 7.28% non-τ background events remain in the event sample. The Bhabha scattering events are recorded in the very forward direction ($|\cos\Theta| > 0.9$). The remaining background from μ-pairs is recorded at around $|\cos\Theta| \approx 0.8$, which is in the overlap region between the barrel and the endcaps of the detector. The two-photon events that pass the τ selection are also predominantly in the forward direction ($|\cos\Theta| \geq 0.6$). Since this analysis is restricted to the barrel region, their contribution is reduced to the permille level in the relevant range. The largest contribution to the non-τ background comes from $\mathrm{q\bar{q}}$ events (6.28%). By requiring that in each cone the sum of the charges of all good tracks is ±1 and that cones in opposite hemispheres have opposite net charge, this background is reduced to below 1%.

5.2 Selection of the Signal Channels

For the selection of the various final states, a cut based procedure is used. For all selected decay modes, the cone axis calculated from the momenta of all tracks and neutral clusters identified in the electromagnetic calorimeter have to have a polar angle within $|\cos\Theta| < 0.68$ for the reasons explained above. Each selected cone has to have at least one good track coming from the interaction point where the momentum sum of all tracks has to be less than the beam energy. Since there is at least one hadron in the final state, the energy deposit in the hadron calorimeter within the cone is required to exceed 1 GeV. In the following, the various final states are discussed individually.

5.2.1 $\tau^- \to \mathrm{K}^-\pi^0\nu_\tau$

In the $\mathrm{K}^-\pi^0\nu_\tau$ selection, exactly one good track coming from the primary vertex is required. This track has to have a minimum momentum of $p > 3\,\mathrm{GeV}$ for kinematic reasons. For the track, to be selected as a kaon, the pion weight has to satisfy $W_\pi < -0.98$ and the kaon weight $W_\mathrm{K} < 0.6$. Furthermore exactly one identified π^0 with $E_{\mathrm{min}}^{\pi^0} > 1.5\,\mathrm{GeV}$, selected using the algorithm explained in Chapter 4.2, is required. The variables used in this selection are shown in Figure 5.3.

---

[4] The two TOF modules have to have an azimuthal angle of $\phi > 165°$

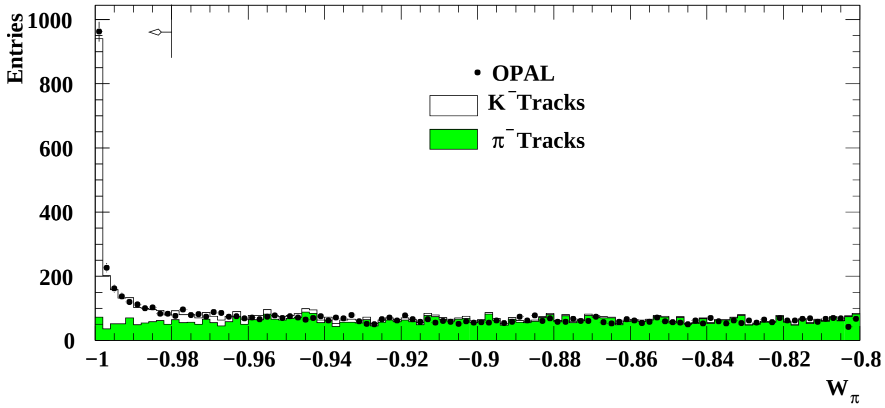

Fig. 5.2: The pion weight W_π for 1-prong τ decays in the range $(-1 : -0.8)$. The dots are the data points, the open histogram denotes the contribution from kaon tracks as predicted from the Monte Carlo simulation and the shaded area represents the contribution from pion tracks. Events on the side of the direction of the arrow are considered kaon candidates.

From this selection 360 events are seen in the data with 190.5 background events predicted from Monte Carlo. This corresponds to a background fraction of 54%. The invariant mass spectrum can be seen in Figure 5.8. The mass resolution in this channel is approximately 40 MeV. The main background comes from $\tau^- \rightarrow \mathrm{K}^-\nu_\tau$ decays where one fake neutral pion was reconstructed. Additional sources of background are $\tau^- \rightarrow \pi^-\pi^0\nu_\tau$, $\tau^- \rightarrow \mathrm{K}^-\mathrm{K}^0\nu_\tau$ and $\tau^- \rightarrow \mathrm{K}^0\mathrm{K}^-\pi^0\nu_\tau$ where the K^0 is a K^0_S decaying to two neutral pions or a K^0_L which does not decay within the jet chamber.

5.2.2 $\tau^- \rightarrow \mathrm{K}^0\pi^-\nu_\tau$

The selection is very similar to that for the $\mathrm{K}^-\pi^0\nu_\tau$ final state. Here exactly one identified K^0_S is required using the procedure from Chapter 4.3. There has to be one good track in the cone coming from the primary vertex. If the momentum of this track lies above the kinematically allowed minimum for a kaon, the same identification procedure as mentioned above is applied to veto decays $\tau^- \rightarrow \mathrm{K}^-\mathrm{K}^0\nu_\tau$. Only events with zero reconstructed π^0 are accepted. The variables used in the selection are shown in Figure 5.4.

From this selection 361 events are expected in the Monte Carlo with a background fraction of 47%, and 344 are seen in the data. The main background contribution comes from decays $\tau^- \rightarrow \mathrm{K}^0\overline{\mathrm{K}}^0\pi^-\nu_\tau$, $\tau^- \rightarrow \mathrm{K}^-\mathrm{K}^0\nu_\tau$

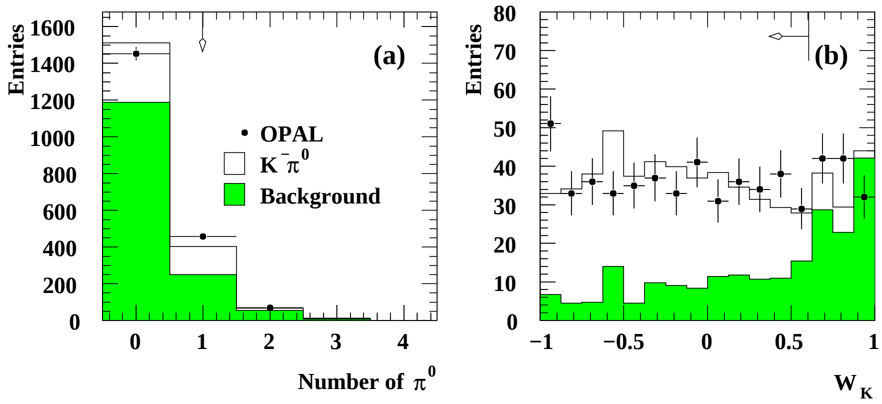

Fig. 5.3: Variables used in the $\mathrm{K}^-\pi^0\nu_\tau$ selection. The dots are the data points, the open histogram is the prediction from the Monte Carlo. Plot (a) shows the number of reconstructed neutral pions with $E > 1.5\,\mathrm{GeV}$. In this plot the shaded area is the background prediction from the Monte Carlo. Plot (b) shows the kaon weight as explained in the text. Here the shaded area represents the expected background from pion tracks. The arrows indicate the events kept in the selection. For all plots all selection cuts have been applied except for the cut on the variable shown.

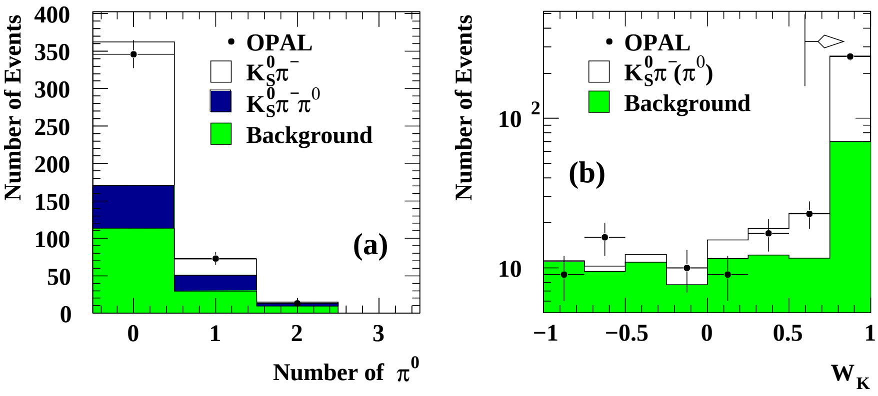

Fig. 5.4: Variables used in the $K^0\pi^-\nu_\tau$ and $K^0\pi^-\pi^0\nu_\tau$ selection. (a) shows the number of reconstructed π^0 mesons. The dots are the data, the open histogram is the signal. The dark-shaded area represents the contribution from $K^0\pi^-\pi^0\nu_\tau$ final states, the light-shaded area denotes other background channels. Plot (b) is the kaon weight of the primary track.

and $\tau^- \rightarrow K^0\pi^-\pi^0\nu_\tau$ where the π^0 escapes detection. The invariant mass spectrum for this channel is shown in Figure 5.8. The mass resolution in this channel is approximately 60 MeV.

5.2.3 $\tau^- \rightarrow K^-\pi^+\pi^-\nu_\tau$

The selection starts by requiring exactly three good tracks coming from the interaction point. These tracks are fitted to a common vertex and the fit probability is required to be larger than 10^{-7}. In addition, each pair of oppositely charged tracks has to fail the selection criteria for neutral kaons as defined in Chapter 4.3. These two requirements reduce the background from photon conversions and decays containing K^0_S.
To identify the kaon, the like-sign[5] candidate track has to have $p > 3$ GeV and $W_\pi < -0.9$. To further reduce the pion background among these candidate tracks, W_K and W_π are inputs to a neural network. The track is rejected if the output of the neural network is below 0.3 (see Figure 5.6(c)). Exactly one like-sign track is allowed to fulfill these requirements, otherwise the decay is treated as background. If the momentum of the unlike-sign track is consistent with the $\tau^- \rightarrow \pi^-K^-K^+\nu_\tau$ hypothesis, this τ decay is only accepted if $W_\pi > -0.95$ (see Figure 5.5).
The algorithm for identifying neutral pions explained in Chapter 4.2 is then applied to the selected cones. For this channel, the number of reconstructed π^0 mesons with an energy greater than 2 GeV is required to be zero (see Figure 5.6(b)). Otherwise this τ decay is treated as background. To further improve the

---

[5] Tracks with the same charge as the initial τ lepton.

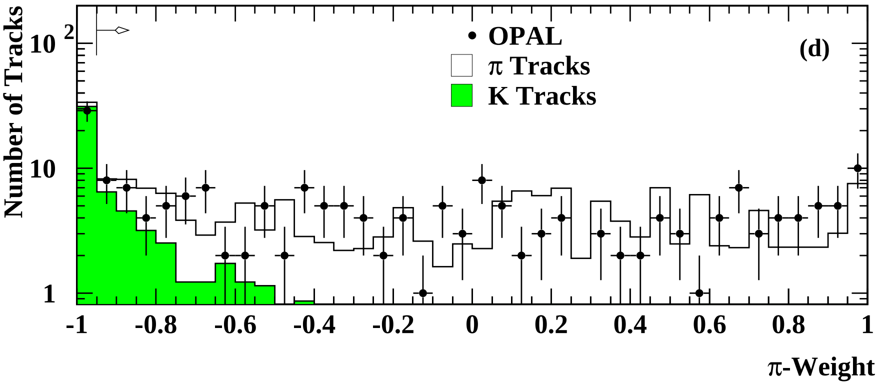

Fig. 5.5: Pion weight of the unlike-sign track. The dots are the data, the open histogram is the signal expected from pion track and the shaded area shows the background from kaon tracks. Here all selection cuts have been applied except for the one on the π-weight. Events on the side of the direction of the arrow are kept.

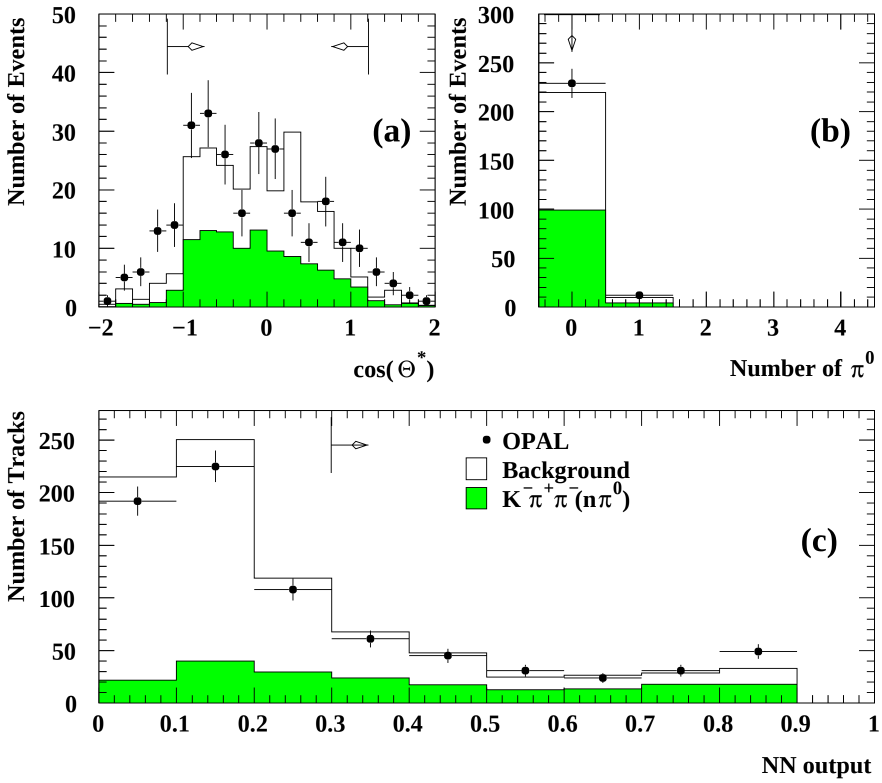

Fig. 5.6: Variables used in the $K^-\pi^+\pi^-\nu_\tau$ selection. Plot (a) shows the cosine of the Gottfried-Jackson angle Θ^*, (b) the number of reconstructed π^0 and (c) the output of the neural network. The dots are the data, the open histogram is the signal prediction from the Monte Carlo and the shaded area is the background. The number of reconstructed π^0 is required to be zero, except for (b). For all plots all selection cuts have been applied except for the cut on the variable shown. Events on the side of the direction of the arrow are kept.

purity of the selection the cosine of the decay angle in the rest frame of the τ lepton, the so-called Gottfried-Jackson angle Θ^* is calculated. The $\cos\Theta^*$ distribution is shown in Figure 5.6(a). For events where the kaon hypothesis was applied to the wrong track or the number of identified π^0 does not correspond to the true number, this calculation leads to unphysical values of that variable. Due to resolution effects, correctly identified signal events can also give values beyond ± 1. Therefore a cut was applied at $\cos\Theta^* = \pm 1.2$. The contribution from $\tau^- \to K^-\pi^+\pi^-(n\pi^0)\nu_\tau$ events is included in the background estimate.

From this selection 269 events are seen in the data with a contribution of 149.8 background events predicted from Monte Carlo. This corresponds to a background fraction of 63%. The main background contribution comes from decays $\tau^- \to \pi^-\pi^-\pi^+\nu_\tau$, $\tau^- \to \pi^-K^-K^+\nu_\tau$ and $\tau^- \to K^-\pi^+\pi^-\pi^0\nu_\tau$, where the π^0 meson escapes detection. The invariant mass spectrum can be found in Figure 5.9. The mass resolution in this channel is approximately 20 MeV.

5.2.4 $\tau^- \to K^0\pi^-\pi^0\nu_\tau$

Exactly one identified K^0_S and exactly one π^0 is required. The pion candidate track has to satisfy the same requirement as for $(K\pi)^-$ final states.

From this selection 65 events are expected in the Monte Carlo simulation of signal plus background and 67 seen in the data with a background fraction of 72%. The main background contribution comes from decays $\tau^- \to K^0\pi^-\nu_\tau$ where the π^0 escapes detection. The invariant mass spectrum can be seen in Figure 5.9. The mass resolution in this channel is approximately 100 MeV.

5.2.5 $\tau^- \to K^-\pi^+\pi^-\pi^0\nu_\tau$

The $(K\pi\pi\pi)^-$ signal consists of the following final states: $K^-\pi^+\pi^-\pi^0\nu_\tau$, $K^0\pi^-\pi^0\pi^0\nu_\tau$, $K^-\pi^0\pi^0\pi^0\nu_\tau$ and $K^0\pi^-\pi^+\pi^-\nu_\tau$. From these, only the first one which has the highest branching fraction is investigated.

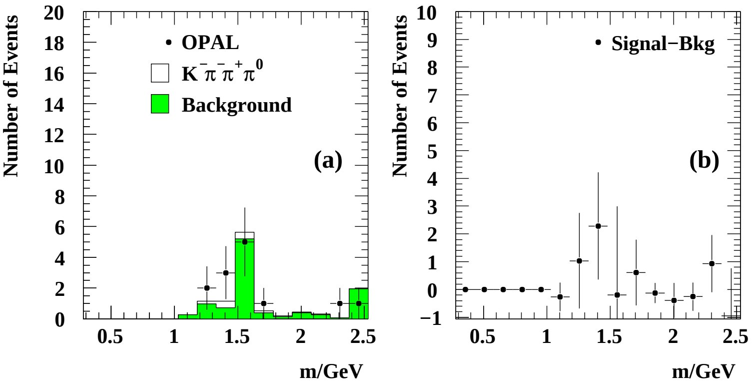

Fig. 5.7: Invariant mass spectra of the $K^-\pi^+\pi^-\pi^0\nu_\tau$ final states. Plot (a) shows the measured invariant mass spectrum. The dots are the data, the open histogram is the Monte Carlo signal and the shaded area is the background. Plot (b) shows the background subtracted spectrum.

The same procedure as for the $K^-\pi^+\pi^-\nu_\tau$ channel is used. In addition, one identified π^0 meson with an energy of more than 2 GeV is required. The invariant mass spectrum can be seen in Figure 5.7. From this selection, 14 events are seen in the data with a contribution of 10 events from background. The selection efficiency is of the order of 1%. The main background contribution comes from $\tau^- \to K^-\pi^+\pi^-\nu_\tau$ decays, where one fake neutral pion was identified.

Since the number of signal events in this final state is not significantly different from zero, this channel is not considered any further in this analysis. For the spectral function, the Monte Carlo prediction has been used instead.

5.3 Invariant Mass Spectra

From the selected events as described above, now the invariant mass spectra can be calculated. They are displayed in Figure 5.8 for the two meson final states, $K^-\pi^0\nu_\tau$ and $K^0\pi^-\nu_\tau$. For the three meson final states, $K^-\pi^+\pi^-\nu_\tau$ and $K^0\pi^-\pi^0\nu_\tau$, the invariant mass distributions are displayed in Figure 5.9. For all plots in all signal channels, a bin width of 150 MeV was chosen, which corresponds to at least 1.5 times the invariant mass resolution in the corresponding spectrum. In addition, the background subtracted spectrum is displayed. The selection efficiency for each signal channel is given in the last column as a function of the invariant mass of the corresponding spectrum. They are of the order of 10% or less. The efficiency correction is only applied to the individual spectrum after the unfolding procedure as described in Chapter 6.2.

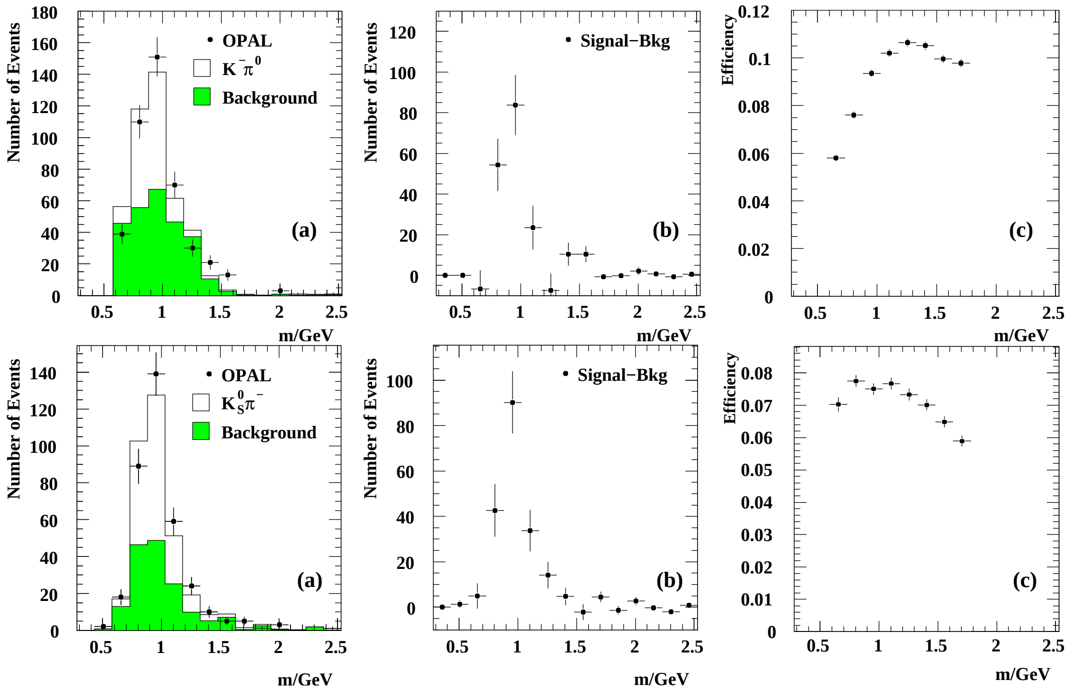

Fig. 5.8: Invariant mass spectra of the two meson final states. In the first (second) row, the plots for the $K^-\pi^0\nu_\tau$ ($K^0\pi^-\nu_\tau$) final states are shown. Plot (a) shows the measured invariant mass spectrum. The dots are the data, the open histogram is the Monte Carlo signal and the shaded area is the background. Plot (b) shows the background subtracted spectrum and plot (c) the selection efficiency as function of the invariant mass.

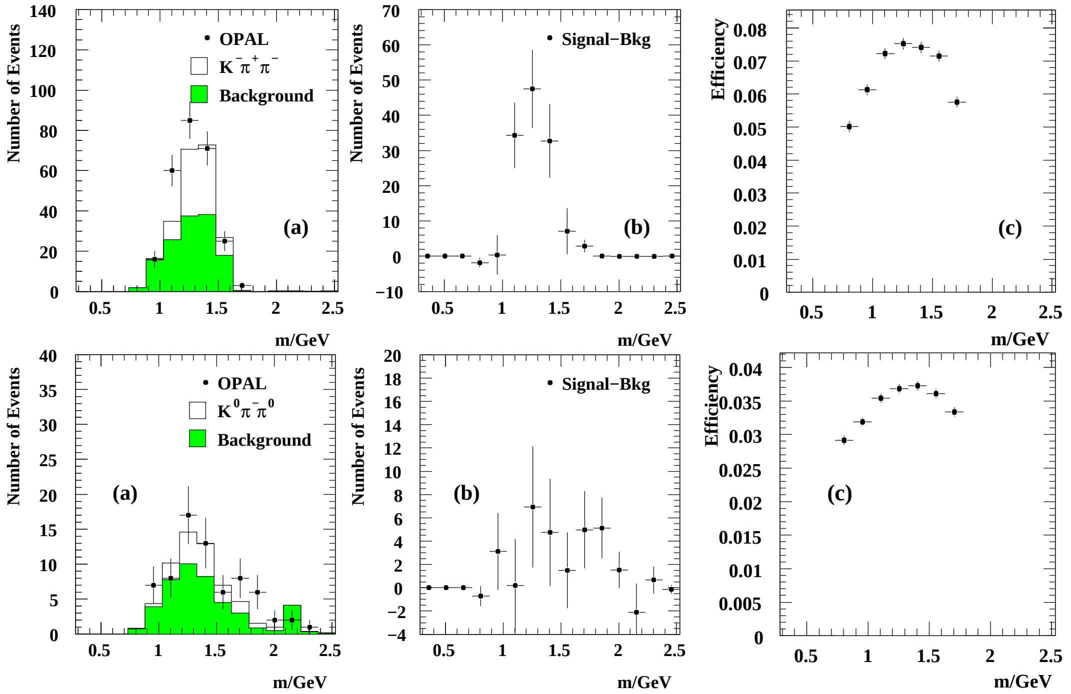

Fig. 5.9: Invariant mass spectra of the three meson final states. In the first (second) row, the plots for the $K^-\pi^+\pi^-\nu_\tau$ ($K^0\pi^-\pi^0\nu_\tau$) final states are shown. Plot (a) shows the measured invariant mass spectrum. The dots are the data, the open histogram is the Monte Carlo signal and the shaded area is the background. Plot (b) shows the background subtracted spectrum and plot (c) the selection efficiency as function of the invariant mass.

6. THE MASS CORRECTION PROCEDURE

Physical observables like the invariant mass spectra or angular distributions are usually distorted by the measurement procedure for several reasons. The probability of observing an event in the detector is usually less than one due to acceptance effects. The response of the measuring device might not be linear and thus distorting the measured observable, or the limited resolution of the detector leads to a smearing of the observed quantity. The measured observable therefore substantially depends on the properties of the detector. In order to be able to compare the results obtained from different experiments, to combine invariant mass spectra with different mass resolution or to theoretically evaluate the obtained results, a procedure to correct for these detector effects is necessary. This procedure is usually called unfolding, deconvolution or unsmearing. Apart from high energy physics, correcting measured observables from biasing effects is applied in various fields like medical imaging, radio astronomy or crystallography, to give some examples.

Any correction procedure has to fulfill certain quality criteria. It has to produce numerically stable results. An enhanced sensitivity to statistical fluctuations, either in the measured observable or in the Monte Carlo sample used in the correction procedure, is otherwise likely to produce artifacts in the 'corrected' spectrum. They could erroneously be interpreted as information from physics processes, or hide the wanted information. The result of the correction should be as independent as possible from the dynamics of the physics process used in the Monte Carlo simulation. In particular in those cases, where the dynamics in the data events are basically unknown, like in the case of invariant mass spectra in strange hadronic τ decays. The stability of the result when using Monte Carlo samples containing different models of the process under investigation, is vital for a useful physical interpretation. In addition, a good knowledge of the detector effects biasing the measurement is important. This means that the calibration and the resolution of the detector have to be well described by the Monte Carlo simulation.

Several correction procedures have been used in the analysis of high energy particle physics data. There are simple migration corrections, where each bin is assumed to be independent, unfolding procedures based on Singular Value Decomposition [58], methods using spline interpolations to parametrize the detector response [59] or methods based on Bayes Theorem [60]. Any correction procedure however in principle has a bias towards the model used in the Monte Carlo simulation. This bias has to be minimized, e.g. by 'regularization' of the result or by using iterative algorithms, where the model of the corresponding process in the Monte Carlo simulation is refined according to the results obtained after each iteration step. The remaining systematic uncertainty associated with the procedure chosen has to be reliably estimated.

In this analysis, a Matrix Unfolding method was used, where the inverse detector matrix was determined directly from Monte Carlo simulation, which avoids the instabilities of numerical matrix inversion. This correction procedure is used in an iterative algorithm, which leads to stable results within a few iteration steps. The result obtained for the corrected spectrum is independent of the dynamics of the physics process assumed in the Monte Carlo simulation within the statistical uncertainties of this analysis.

This chapter is organized as follows. It starts with a mathematical formulation of the unfolding problem followed by a brief discussion of other unfolding procedures. The Matrix Unfolding is introduced in Chapter 6.2 and the iteration procedure, applied in order to reduce the bias toward the model used in the Monte Carlo, is explained. Tests using events including full simulation of the OPAL detector and assuming various resonance structures for the invariant mass spectra is presented in 6.2.3. Finally the results obtained from the unfolding of the spectra from τ data events are presented in Chapter 6.3.

6.1 Introduction

Let $g(y)$ be the measured distribution which depends on some variable $y \equiv s_{\mathrm{meas}}$ and let $f(x)$ be the true distribution depending on $x \equiv s_{\mathrm{true}}$. The measured distribution $g(y)$ can then be written as

$$g(y) = \int_{x_{\min}}^{x_{\max}} \mathrm{d}x A(y,\, x)\varepsilon(x) f(x) + b(y). \tag{6.1}$$

Equation 6.1 is a Fredholm integral equation of first order. Mathematically, the function $A(y,\, x)$ is called kernel of the integral equation. It describes the effects of the detector on some true distribution x, leading to the measured distribution y. In other words, it gives the probability that for a certain event, $y = y_0$ is measured if $x = x_0$ were the true value. The detector response function is usually not known analytically and is therefore taken from a Monte Carlo simulation. The contribution from background events is denoted by $b(y)$, which is assumed to be known either from independent measurements or from calculations. The function $\varepsilon(x)$ describes efficiency and acceptance effects, which are determined using Monte Carlo simulations. In high energy physics, the measured distributions are usually given in the form of histograms. Therefore, the number of events observed in bin i is given by

$$g_i = \int_{y_{i-1}}^{y_i} g(y)\,\mathrm{d}y = \sum_{j=1}^{m} A_{ij} + b_i, \tag{6.2}$$

where

$$\begin{aligned} A_{ij} &= \int_{y_{i-1}}^{y_i} A_j(y)\,\mathrm{d}y \\ &= \int_{y_{i-1}}^{y_i} \left(\int_{x_{\min}}^{x_{\max}} A(y,x) f_{\mathrm{MC}}(x) \varepsilon(x)\,\mathrm{d}x \right) \mathrm{d}y \end{aligned}$$

and

$$b_i = \int_{y_{i-1}}^{y_i} b(y)\,\mathrm{d}y.$$

Equation 6.2 can be written as matrix equation

$$\mathbf{g} = \mathbf{A} \cdot \mathbf{f} + \mathbf{b}, \tag{6.3}$$

where $\mathbf{g}$ and $\mathbf{b}$ are n-vectors in detector space, $\mathbf{f}$ is an m-vector in tree-space and $\mathbf{A}$ is an $n \times m$ matrix. The vector, containing the unfolded distribution is then obtained by solving the set of Equations

$$\mathbf{f} = \mathbf{A}^{-1}(\mathbf{g} - \mathbf{b}). \tag{6.4}$$

To obtain the inverse of the detector response matrix, several procedures exist, which are briefly discussed here.

- Numerical Matrix Inversion: The determination of the detector matrix from Monte Carlo simulation and its numerical inversion leads to unsatisfactory results. Due to statistical fluctuations in the simulation and in the data set to be unfolded, this procedure is numerically unstable. The obtained distributions are wildly fluctuating. In addition, the number of bins has to be identical for the measured and for the unfolded spectrum, since only squared matrices can be numerically inverted. This includes, that there are events in the whole physically allowed range of the corresponding observable. Otherwise, the inverse matrix is undefined. For invariant mass spectra this is not usually the case, especially close to the kinematic limit.

- Bin-by-Bin Unfolding: This is a special case of the numerical inversion of the detector matrix. Here, each bin in the distribution to be unfolded is treated independently, i.e. the bins are assumed to be uncorrelated. Only the net migration of events from or into a particular bin is considered. The transfer matrix is diagonal and can therefore be inverted without the disadvantage of numerical instabilities. This method has a strong bias towards the model used in the Monte Carlo simulation. Since the resonance structure is not very accurately known, in particular in strange final states with three or more mesons, this method is not applicable here.

- Regularized Unfolding (see e.g. [58, 59]): These methods like e.g. Singular Value Decomposition, analyzes the measured spectrum in terms of eigenvalues and eigenvectors of the detector matrix, similar to a Fourier analysis. The unfolded spectrum is obtained by adding up the eigenvectors with the corresponding eigenvalues as relative weights. This procedure stops when the weight, i.e. the eigenvalue is

> no longer statistically significant and all higher contributions are neglected. This is called regularization or damping of the unfolded spectrum. The regularization parameter has to be determined using Monte Carlo simulations and the final result highly depends on this parameter. In the limit of no regularization, the same oscillating result is obtained as for the numerical matrix inversion.
>
> Using the regularized unfolding, only smooth deviations from the Monte Carlo prediction can be measured with reasonable accuracy. Otherwise eigenvectors representing ‘high frequencies’ would be needed to describe the spectrum. This enhances the statistical fluctuations in the spectrum and, depending on the given spectrum, may cause artifacts. To avoid this, the detector matrix is normalized to the prediction from the Monte Carlo and as a result, coefficients describing the deviation of the spectrum to be unfolded relative to the prediction from the Monte Carlo are obtained.

The resonance structure for the strange decay channels however is not very accurately known, in particular in cases with three or more mesons in the final state. Due to the limited statistics a detailed analysis of the resonance structure prior to the unfolding procedure is not possible. To keep the method simple and the systematic uncertainty small, a matrix unfolding procedure explained in the next section was used to correct for detector effects.

6.2 Matrix Unfolding

In this section, the matrix unfolding is explained in detail and tests of the method are presented. The following notation is used:

- g_i: Number of events in measured distribution
- f_i: Number of events in the unfolded distribution
- a_{ij}^{-1}: Elements of the inverse detector matrix

In the determination of the inverse detector matrix, the following quantities are required:

- N_{ij}: Number of events generated in bin i and reconstructed in bin j.
- X_i: Number of events generated in bin i
- Y_i: Number of events reconstructed in bin j.

In order to reduce the bias towards the Monte Carlo, this method is applied in an iterative procedure. After each unfolding step, the simulated events are reweighted:

- $w_i^{(n)}$: Reweighting factor.

The superscript denotes the iteration step, the reweighting factors belong to. In the Matrix Unfolding procedure, the inverse detector matrix is determined directly from Monte Carlo to avoid the instabilities of a numerical inversion. The elements a_{ij}^{-1} of the matrix are calculated according to

$$a_{ij}^{-1} = \frac{\#(\text{generated in bin } i \text{ and measured in bin } j)}{\#\text{measured in bin } j} = \frac{N_{ij}}{\sum_j N_{ij}} = \frac{N_{ij}}{Y_j}, \tag{6.5}$$

which is the number of events generated in bin i and reconstructed in bin j, normalized to the total number of events reconstructed in bin j. The elements of the matrix therefore represent the probability for a reconstructed event found in bin j, that it was originally generated in bin i. Unlike in the bin-by-bin unfolding discussed earlier, the correlation between the bins of the measured distribution is fully taken into account.

The coefficients a_{ij}^{-1} are calculated for each measured spectrum using the corresponding signal Monte Carlo. The events used in the calculation of the matrix have to fulfill the selection criteria for the corresponding signal channel. The inverse detector response matrix is then applied to the background subtracted spectrum to obtain the unfolded distribution. The number of events, observed in bin i of the distribution $g(y)$ is then given by

$$f_i = \varepsilon_i \sum_j a_{ij}^{-1}(g_j - b_j). \tag{6.6}$$

The efficiency corrections are then applied to these corrected distributions. Due to the limited statistics in the data set, a simultaneous unfolding including all signal channels and the dominant background contributions (like e.g. in [40]) is not possible here. In the unfolding procedure, the individual spectra are assumed to be independent.

6.2.1 Unfolding 'Ideal' Distributions

In the following example, the unfolding procedure is illustrated. In this example, the resonance structure is assumed to be exactly known. The identical distribution is used to calculate the smeared distribution and to set up the inverse detector matrix. Therefore, in this example, no statistical fluctuations occur and the tree-level distribution has to be exactly reconstructed in the unfolding procedure without iteration.
A background-free distribution is assumed, where on tree level 800 events are in the central bin and 100 events are on either side. To simulate the detector response, this distribution is folded with a resolution function. An arbitrary resolution function is assumed, where 80% of all events remain in the bin they were created in, 7% and 3% migrate to the neighboring and next-to-neighboring bin, respectively. This is illustrated in Figure 6.1. The inverse detector matrix can now be reconstructed using Equation 6.5:

$$\mathbf{A}^{-1} = (a^{-1})_{ij} = \begin{array}{r} \vdots \\ a_{3j}: \\ a_{4j}: \\ a_{5j}: \\ \vdots \end{array} \left(\begin{array}{ccccccc} & & & \mathbf{0} & & & \\ \frac{0.03\cdot 100}{3} & \frac{0.07\cdot 100}{31} & \frac{0.80\cdot 100}{139} & \frac{0.07\cdot 100}{654} & \frac{0.03\cdot 100}{139} & 0 & 0 \\ 0 & \frac{0.03\cdot 800}{31} & \frac{0.07\cdot 800}{139} & \frac{0.80\cdot 800}{654} & \frac{0.07\cdot 800}{139} & \frac{0.03\cdot 800}{31} & 0 \\ 0 & 0 & \frac{0.03\cdot 100}{139} & \frac{0.07\cdot 100}{654} & \frac{0.80\cdot 100}{139} & \frac{0.07\cdot 100}{31} & \frac{0.03\cdot 100}{3} \\ & & & \mathbf{0} & & & \end{array} \right). \tag{6.7}$$

Here, each row represents one bin on generator level and each column represents one bin on detector level. The inverse detector matrix can now be applied to the 'measured' distribution, yielding the unfolded spectrum

$$\begin{aligned} \mathbf{f} &= \mathbf{A}^{-1} \cdot \mathbf{g} \\ &= \begin{pmatrix} & & & \mathbf{0} & & & \\ 1.00 & 0.23 & 0.58 & 0.01 & 0.02 & 0 & 0 \\ 0 & 0.77 & 0.40 & 0.98 & 0.40 & 0.77 & 0 \\ 0 & 0 & 0.02 & 0.01 & 0.58 & 0.23 & 1.00 \\ & & & \mathbf{0} & & & \end{pmatrix} \cdot \begin{pmatrix} 3 \\ 31 \\ 139 \\ 654 \\ 139 \\ 31 \\ 3 \end{pmatrix} = \begin{pmatrix} 0 \\ 0 \\ 100 \\ 800 \\ 100 \\ 0 \\ 0 \end{pmatrix}. \end{aligned}$$

In this ideal case, the generated spectrum is precisely reproduced by construction. The covariance matrix in this case is calculated from the statistical error on the 'measured' distribution alone:

$$\mathrm{Cov}(\mathbf{f}) = \mathbf{A}^{-1} \cdot \Delta\mathbf{g} \cdot (\mathbf{A}^{-1})^{\mathrm{T}} = \cdots = \begin{pmatrix} & & & \mathbf{0} & & & \\ 0 & 0 & 52 & 45 & 3 & 0 & 0 \\ 0 & 0 & 45 & 709 & 45 & 0 & 0 \\ 0 & 0 & 3 & 45 & 52 & 0 & 0 \\ & & & \mathbf{0} & & & \end{pmatrix}. \tag{6.8}$$

The correlation between the bins, introduced by the resolution function is fully taken into account. The correlation coefficient is of the order 25% for the first off-diagonal elements, though only 7% of the events were assumed to migrate to either side of the corresponding bin in this example. The correlation is of the order of 5% for the second off-diagonal elements.

6.2.2 Iteration Procedure

The analysis of real data is different from the ideal case. The distribution realized in nature is usually not known and therefore the result of the correction procedure has to be independent from the dynamics assumed in the Monte Carlo simulation. In addition, statistical fluctuations cause deviations to the measured spectrum. They should be reflected in the unfolded distribution. The Matrix Unfolding procedure is applied

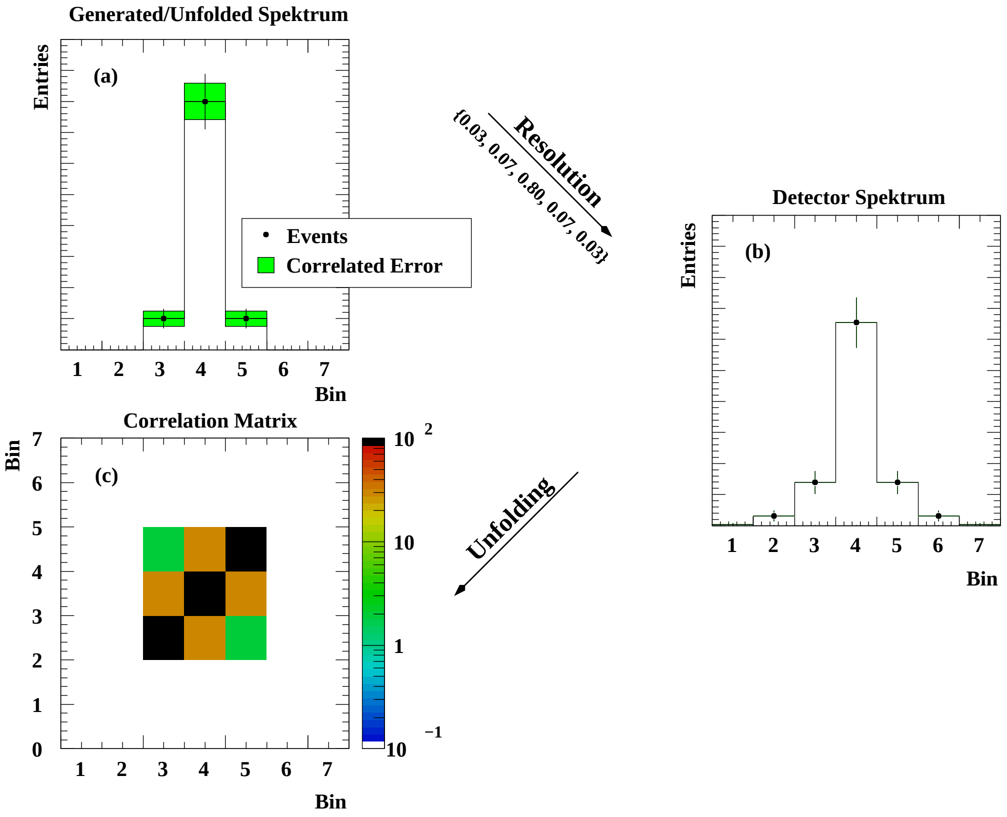

Fig. 6.1: Illustration of the unfolding procedure. Plot (a) shows the generated distribution on tree-level. By construction, it is identical to the spectrum after the unfolding procedure. The error bars represent the statistical uncertainty of the original spectrum. The shaded areas show the error as obtained from the diagonal elements of the covariance matrix after the unfolding procedure. Due to the correlation between neighboring bins, these errors are smaller than the original ones. For better visibility, the errors are multiplied by a factor three compared to the numerical example given in the text. The distribution on detector level is shown in plot (b), the correlation matrix is illustrated in plot (c). In this example the correlation is of the order of 25% (5%) for the first (second) off-diagonal elements.

in an iterative procedure to reduce the possible bias. After each unfolding step, the obtained result for the unfolded distribution is used to refine the Monte Carlo simulation. This adjusted Monte Carlo sample is then used to re-evaluate the inverse detector matrix and the unfolding is repeated.

After the n^{th} unfolding step, weights are calculated by comparing bin-by-bin the unfolded distribution to the distribution used in the Monte Carlo simulation on tree-level:

$$
\begin{aligned}
w_i^{(n)} &= N_X^f \cdot \frac{f_i}{X_i^{(0)}} = N_X^f \cdot \frac{\sum_j a_{ij}^{-1} g_j}{X_i^{(0)}} \\
&= N_X^f \cdot \frac{\sum_j w_i^{(n-1)} \frac{N_{ij}}{Y_j} g_j}{\sum_j N_{ij}} = N_X^f \cdot \frac{\sum_j w_i^{(n-1)} \frac{N_{ij}}{\sum_i N_{ij}} g_j}{\sum_j N_{ij}} .
\end{aligned}
$$

Here, N_X^f is a Monte Carlo normalization factor. The inverse detector matrix is then re-evaluated, now multiplying each event in the Monte Carlo with the corresponding weight, according to the bin i it was generated in. With this new detector matrix the unfolding is repeated.

To illustrate the iteration procedure the same distribution and resolution function as in the last chapter are used. However, here the dynamics in the Monte Carlo used in the set up of the detector matrix is assumed to produce flat mass distributions on generator level. This is illustrated in Figure 6.2(a), where the distribution on generator (detector) level is given as solid (dashed) line. If no statistical fluctuations are present, the true distribution is exactly reproduced in the limit of an infinite number of iterations. This is illustrated by the solid line in Figure 6.2(b), where the χ^2 as calculated from the original distribution and the result of the unfolding is plotted as a function of the number of iteration steps.

In the presence of statistical fluctuations, the situation is different. An infinite number of iterations in this case would lead to an enhancement of the fluctuations and thus to unsatisfactory results. This is discussed in detail in the next chapter. In order to study the performance of the Matrix Unfolding procedure in the presence of statistical fluctuations, fluctuations are applied to the detector spectrum as illustrated in Figure 6.2(c). The histogram with the shaded areas represent the original distribution and the error bars. The dots are the spectrum with the fluctuations applied.

The Matrix Unfolding Procedure is now applied using an iterative algorithm as explained above. Again, the χ^2 as calculated from the original distribution and the unfolded spectrum and is displayed as function of the iteration depth as a dotted line with full dots in Figure 6.2(b). This function shows a minimum after 4 iteration steps. The region around the minimum is flat, i.e. no significant change (given the assumed statistical uncertainty) is observed when changing the number of iterations from four to three or five. The variation stays well below 5%. For a larger number of iterations, the χ^2 increases again unlike in the ideal case, thus leading to an unsatisfactory result with enhanced statistical fluctuations. The result obtained after the optimal number of iteration steps is compared to the true distribution in Figure 6.2(d). Here the central bin is lower than in the original distribution. The left (right) neighboring bin has fewer (more) entries. This shape corresponds well to the statistical fluctuations applied on detector level, where altogether 55 events less have been observed in this particular example. This means that if the deviations were not just statistical fluctuations but were due to deviations from the dynamics assumed in the Monte Carlo simulation, it would have been retained after the unfolding.

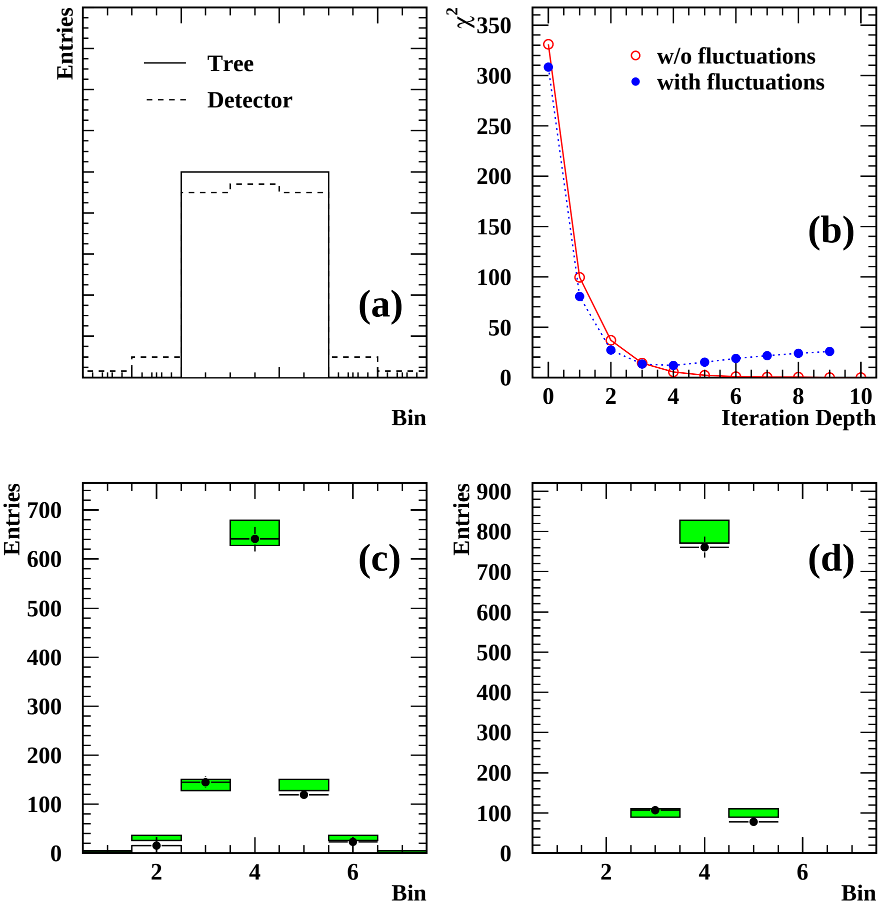

Fig. 6.2: Test of the iteration procedure. In plot (a), the input distribution as used to set up the inverse detector matrix is shown. The generator (detector) level is denoted by the solid (dashed) line. (b) shows the χ^2 as a function of the number of iteration steps. The full (open) dots illustrates the example without (with) statistical fluctuations. Plots (c) and (d) show the test sample on detector level and on generator level, respectively. The histogram represents the ideal case without statistical fluctuations, where the shaded area represents the statistical uncertainty. The dots are the corresponding distributions with the statistical fluctuations applied.

6.2.3 Test with τ Monte Carlo

To be able to apply the unfolding method explained above to the OPAL data, special Monte Carlo samples were generated. For the signal channels $\tau^- \to \mathrm{K}^-\pi^0\nu_\tau$, $\tau^- \to \mathrm{K}^0\pi^-\nu_\tau$ and $\tau^- \to \mathrm{K}^-\pi^+\pi^-\nu_\tau$ 200.000 events were generated for each decay mode. For the $\tau^- \to \mathrm{K}^0\pi^-\pi^0\nu_\tau$, due to the much lower selection efficiency, 600.000 events are produced. These events were processed through the full OPAL detector simulation.
The events in these samples are generated between the lower kinematic limit (which depends on the signal channel under investigation) and the upper limit of $m_\tau^2 = 3.154\,\mathrm{GeV}^2$ with a flat mass distribution. This allows for a precise determination of the inverse detector response matrix even in mass regions where the standard τ Monte Carlo does not provide a sufficient number of events. The uncertainty on the inverse detector response matrix due to the Monte Carlo statistic in these sample is of the order of a $(3-4)\%$ for the diagonal elements of the matrix and below 10% for the two first off diagonal elements. These events are also used for the determination of the selection efficiency.
In order to test the method, a flat mass distribution and a mass distribution according to phasespace was used to set up the inverse detector matrix. The latter is obtained from the flat distribution by reweighting the Monte Carlo events. Then, a subsample test was performed. For each signal channel, 200 subsamples of the size expected in the data for the corresponding channel were selected. The events were then unfolded using the iterative procedure as explained above.
The result of the unfolding procedure can be seen in Figures 6.3 and 6.4. In the first row in each figure, the results obtained after each iteration step are displayed using a phasespace distribution as initial guess to set up the inverse detector matrix. In the second row the same results are shown, now using a flat mass distribution as initial guess. In each row in the first plot, the mass distribution used as initial guess can be seen on generator level (dotted line) and detector level (dashed line). The dots show the distribution to be unfolded averaged over all subsamples. The next plots in the row, labeled '0^{th} Iteration Step', '1^{st} Iteration Step' and so on, compare the results of the corresponding iteration step (dots) to the original distribution on detector level (dashed line) and generator level (dotted line).
Using a phasespace distribution as initial guess, for all final states considered here, an agreement between the unfolded spectrum and the corresponding distribution on generator level of better than the expected statistical uncertainty was obtained after the second iteration step. Applying on additional iteration step changes the result only on the percent level, which can be seen by comparing the last and the second-to-last plot in the first row for each corresponding channel. Using a flat mass distribution as initial guess for the unfolding matrix, one additional iteration step is necessary to obtain a result which reproduces the corresponding tree distribution on the same level as for the phase space distribution. Also in this case, the obtained result is stable against one additional iteration step.
In all plots discussed here, the error bars do not correspond to the statistical uncertainty of the spectrum. They represent the spread obtained over the 200 subsamples.

6.3 Unfolding Data Events

The invariant mass spectra measured in Chapter 5.2 have different invariant mass resolutions, ranging from 20 MeV for the final state $\mathrm{K}^-\pi^+\pi^-\nu_\tau$, up to 100 MeV for the channel $\mathrm{K}^0\pi^-\pi^0\nu_\tau$. In order to be able to combine these signal channels (and the corrections from Monte Carlo) to obtain the strangeness spectral function, the invariant mass spectra are now subject to the mass correction procedure. Because of the large statistical uncertainty, a simultaneous unfolding of all signal channels like in [40] is not possible. Therefore, each channel is treated individually.
The inverse detector matrix is set up for each signal channel, using the special Monte Carlo as explained in the previous section. As initial guess, a phase space distribution is used for all spectra. The number of iteration steps is two for each channel. The corrected spectra for all signal channels are displayed on the left side of in Figure 6.5. The correlation matrices for the corresponding spectra are displayed on the right side. The size of the correlation is color-coded. The correlation between the bins varies from $\sim 20\%$ for the channel with the best invariant mass resolution ($\mathrm{K}^-\pi^+\pi^-\nu_\tau$) to about 50% for the two-meson final states. In the τ decay in the channel $\mathrm{K}^0\pi^-\pi^0\nu_\tau$, which has the worst resolution, the correlation bins is larger than 50% for neighboring bins and of the order of 50% to next-to-neighboring bins.

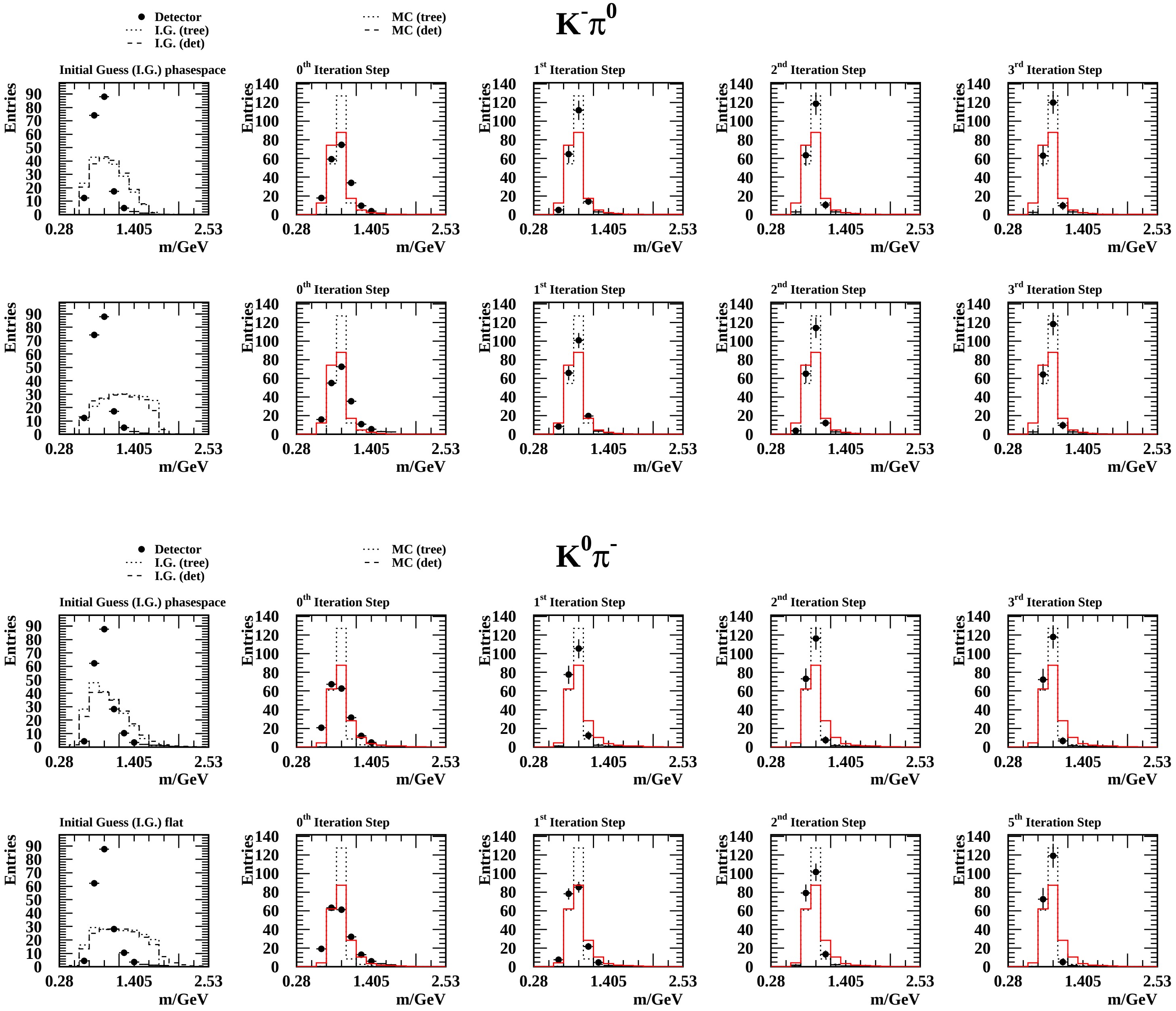

Fig. 6.3: Subsample test for the two meson final states. For each signal channel, in the first row, the result of the unfolding procedure using a phasespace distribution as initial guess is displayed. In the second row, a flat mass distribution was used. For further details, see explanation in the text.

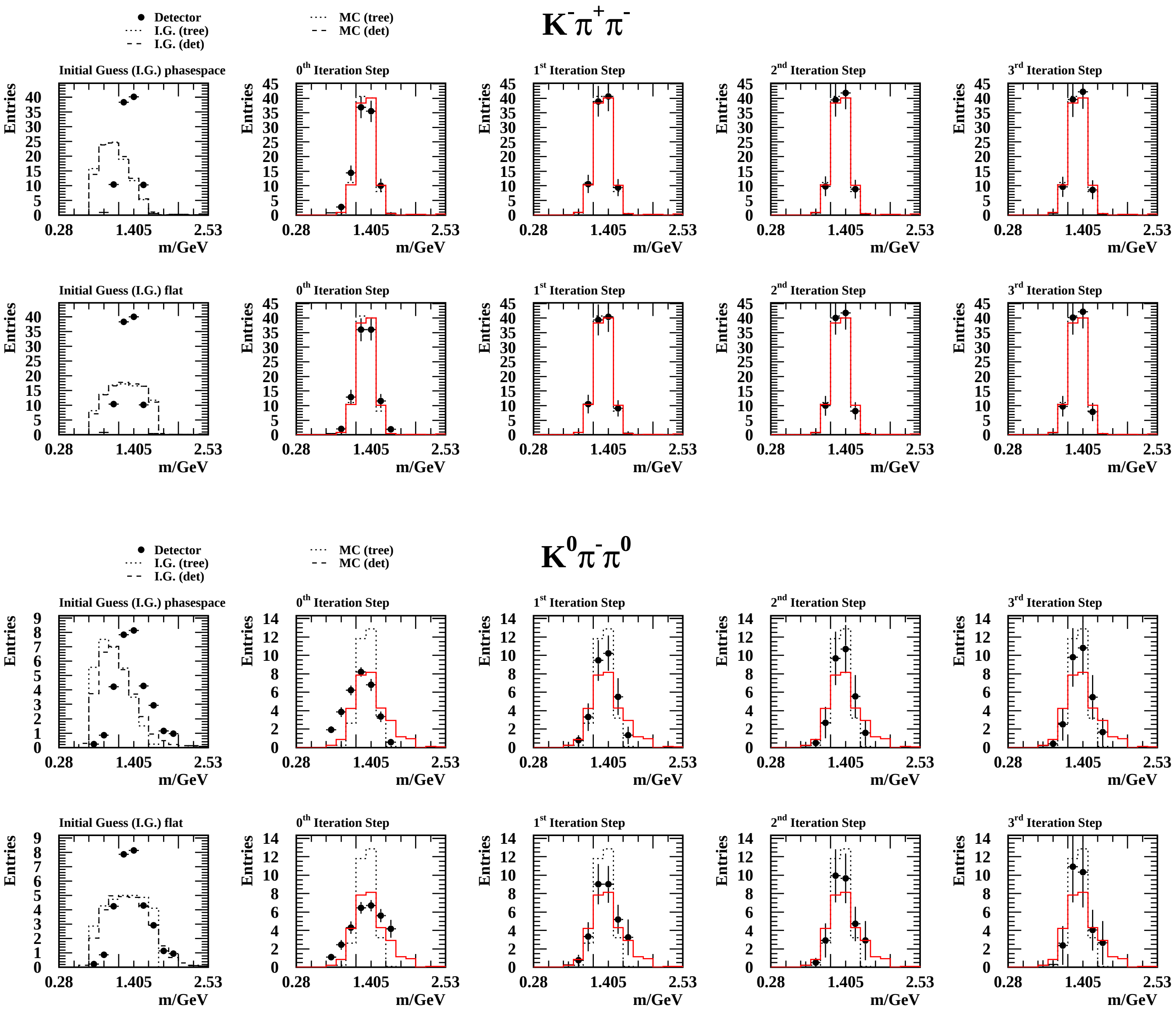

Fig. 6.4: Subsample test for the three meson final states. For each signal channel, in the first row, the result of the unfolding procedure using a phasespace distribution as initial guess is displayed. In the second row, a flat mass distribution was used. For further details, see explanation in the text.

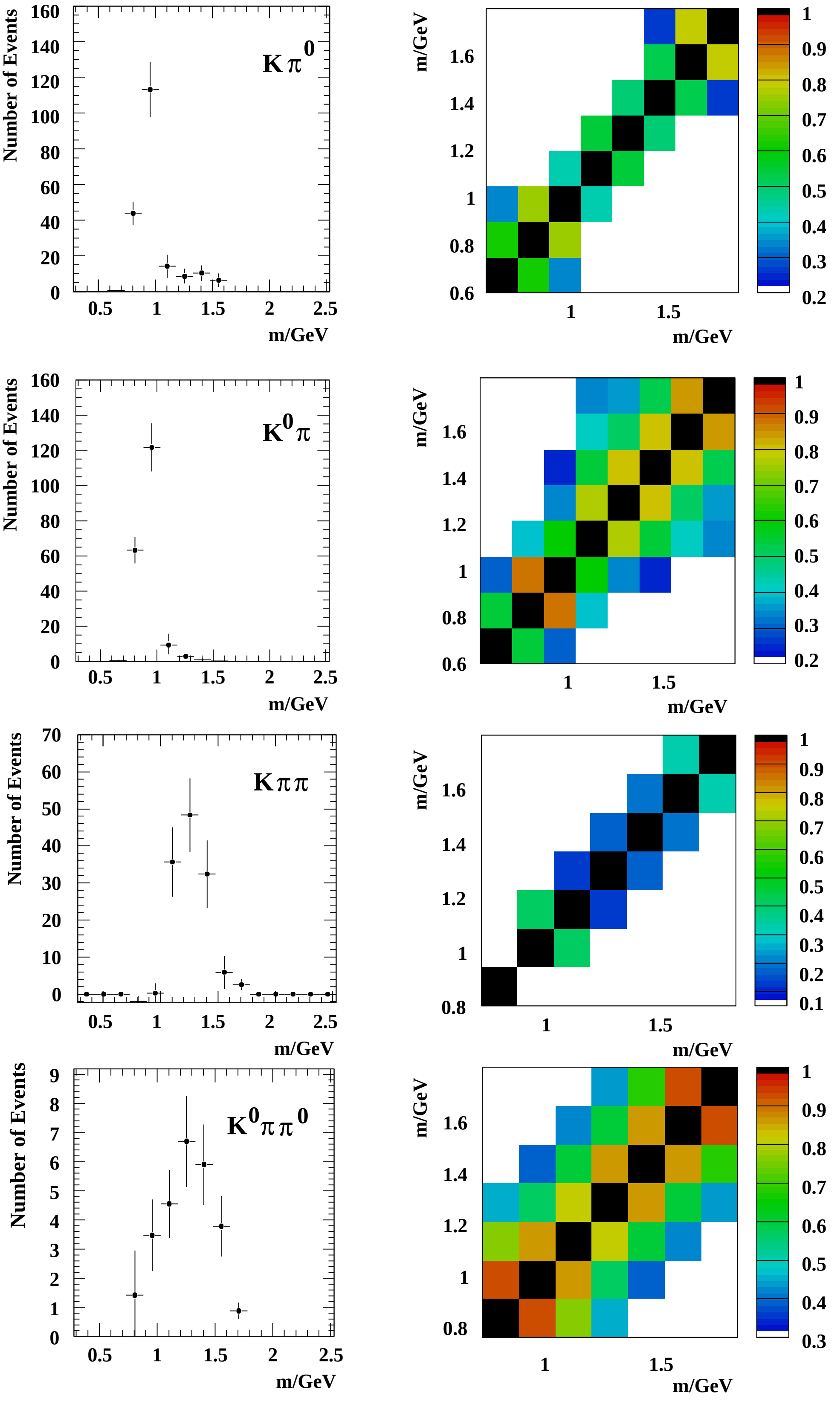

Fig. 6.5: Unfolded spectra and correlation matrices for the final states $K^-\pi^0\nu_\tau$, $K^0\pi^-\nu_\tau$, $K^-\pi^+\pi^-\nu_\tau$and $K^0\pi^-\pi^0\nu_\tau$. On the left side the unfolded spectra are displayed. On the right sight, the correlation matrices are given.

7. RESULTS

In this chapter, the results obtained from the measured invariant mass spectra are presented. At first, new branching fractions for the decay channels $\tau^- \to \mathrm{K}^-\pi^0\nu_\tau$ and $\tau^- \to \mathrm{K}^-\pi^+\pi^-\nu_\tau$ are determined in a simultaneous fit. Since the measured values change the present world averages, improved averages are calculated for these final states. In Section 7.2, the strangeness spectral function is presented and the systematic uncertainties associated with it are discussed. Spectral moments are then determined from the spectral function. In addition, the weighted difference of strange and non-strange spectral moments and their ratio are calculated. Finally, in Section 7.5, the mass of the strange quark is determined from this weighted difference and the obtained result is compared to previous analyses.

7.1 Branching Fractions

The channels $\tau^- \to \mathrm{K}^-\pi^0\nu_\tau$ and $\tau^- \to \mathrm{K}^-\pi^+\pi^-\nu_\tau$ allow the determination of competitive branching fractions from the measured data used in the spectral function analysis. The branching fractions are determined in a simultaneous χ^2-fit, taking all measured final states into account. The expected number of events is calculated by

$$N_i = N_i^{\not\tau} + (1 - f_{\mathrm{bkg}}^{\not\tau}) \cdot N^\tau \sum_j \varepsilon_{ij} B_j F_j^{\mathrm{Bias}},$$

where i is the signal channel under consideration and index j runs over all channels including background. The other quantities are

- $N_i^{\not\tau}$: the number of events expected from the non-τ background channels
- $f_{\mathrm{bkg}}^{\not\tau}$: the fraction of non-$\tau$ background in the corresponding decay channel.
- N^τ: the number of τ candidate events selected in the data
- ε_{ij}: the efficiency matrix as determined from Monte Carlo simulations
- F_j^{Bias}: the bias factor due to the τ selection cuts
- B_j: the fitted branching fractions.

While the branching fractions for the signal channels under consideration were allowed to vary freely, the branching fractions of all other τ decay modes contributing to the background prediction were allowed to vary only within their errors. An additional term is added to the fit function to account for the variation of the branching fractions not measured here. The fit function then reads

$$\chi^2 = \sum_{\mathrm{K}^-\pi^+\pi^-\nu_\tau}^{\mathrm{K}^-\pi^0\nu_\tau} \left(\frac{N_{\mathrm{meas}} - N_{\mathrm{exp}}}{\sigma}\right)^2 + \sum_{j\in\mathrm{other}} \left(\frac{B_j - B_{j,\,\mathrm{PDG}}}{\sigma_j}\right)^2 . \tag{7.1}$$

The shift in the branching fractions not measured here were found to be small. The selection quantities used in the fit are shown in Table 7.1(a/b) as well as contributions from the background channels and their branching fractions used in the Monte Carlo simulation. From the fit, the following results were obtained:

$$\begin{aligned} B(\tau^- \to \mathrm{K}^-\pi^0\nu_\tau) &= (0.471 \pm 0.064_{\mathrm{stat}} \pm 0.021_{\mathrm{sys}})\% \\ B(\tau^- \to \mathrm{K}^-\pi^+\pi^-(0\pi^0, \mathrm{ex.K}^0)\nu_\tau) &= (0.415 \pm 0.059_{\mathrm{stat}} \pm 0.031_{\mathrm{sys}})\%. \end{aligned}$$

It has been excluded that the $\pi^-\pi^+$ pair in the $\mathrm{K}^-\pi^+\pi^-\nu_\tau$ final state comes from a K^0_S decay.

$\tau^- \to \mathrm{K}^-\pi^0\nu_\tau$			
No. of Events	360		
Selection Efficiency /%	8.42 ± 0.17		
Preselection Bias Factor	1.016 ± 0.011		
Non-τ Background Fraction	0.006 ± 0.004		
τ Background Fraction	0.540 ± 0.027		
$\pi^-\pi^0\nu_\tau$	13.5%	0.051 ± 0.005	25.41 ± 0.14
$\mathrm{K}^-\mathrm{K}^0\pi^0\nu_\tau$	9.9%	6.0 ± 0.3	0.155 ± 0.020
$\mathrm{K}^-\nu_\tau$	8.1%	1.25 ± 0.06	0.686 ± 0.023
$\mathrm{K}^-\mathrm{K}^0\nu_\tau$	7.3%	4.5 ± 0.2	0.154 ± 0.016
$\pi^-\pi^0\pi^0\nu_\tau$	6.2%	0.07 ± 0.01	9.17 ± 0.14
$\mathrm{K}^-\pi^0\pi^0\nu_\tau$	5.0%	9.6 ± 0.5	0.058 ± 0.023
$\mathrm{K}^-\pi^0\pi^0\pi^0\nu_\tau$	2.6%	8.9 ± 0.6	0.037 ± 0.021
other	1.4%		
	Bkg. Fraction	Efficiency /%	B^{PDG}/%

$\tau^- \to \mathrm{K}^-\pi^+\pi^-\nu_\tau$			
No. of Events	269		
Selection Efficiency/%	6.59 ± 0.06		
Preselection Bias Factor	0.953 ± 0.013		
Non-τ Background Fraction	0.007 ± 0.006		
τ Background Fraction	0.631 ± 0.044		
$\pi^-\pi^+\pi^-\nu_\tau$	21.6%	0.15 ± 0.02	9.22 ± 0.10
$\mathrm{K}^-\mathrm{K}^+\pi^-\nu_\tau$	10.3%	3.9 ± 0.2	0.161 ± 0.019
$\pi^-\pi^+\pi^-\pi^0\nu_\tau$	8.1%	0.5 ± 0.1	4.24 ± 0.10
$\mathrm{K}^-\pi^+\pi^-\pi^0\nu_\tau$	6.7%	2.7 ± 0.2	0.064 ± 0.024
other	16.4%		
	Bkg. Fraction	Efficiency /%	B^{PDG}/%

Tab. 7.1: Quantities used in the fit for the branching fractions. The errors quoted for efficiency, bias factor and background fractions is from Monte Carlo statistics only. The last column contains the branching fractions for the background channels used in the Monte Carlo simulation [57].

	$\tau^- \to \mathrm{K}^-\pi^0\nu_\tau$	$\tau^- \to \mathrm{K}^-\pi^+\pi^-\nu_\tau$
Energy Loss Measurement $\Delta_{\mathrm{d}E/\mathrm{d}x}$	0.012	0.019
Energy Scale Δ_E	0.010	0.011
Momentum Scale Δ_p	0.003	0.003
MC Statistics Δ_{MC}	0.014	0.021
Bias Factor $\Delta_{F^{\mathrm{Bias}}}$	0.004	0.005
Total	0.022	0.031

Tab. 7.2: Individual contributions to the systematic uncertainty of the branching fraction measurements for the decay channels $\tau^- \to \mathrm{K}^-\pi^0\nu_\tau$ and $\tau^- \to \mathrm{K}^-\pi^+\pi^-\nu_\tau$. For the total error quoted, the individual contributions have been added in quadrature.

7.1.1 Systematic Studies for the Branching Fractions Measurement

For the estimation of the systematic uncertainty, the following sources are considered. They are summarized in Table 7.2. The total error is obtained by adding the individual contributions in quadrature.

- Energy loss measurement ($\Delta_{\mathrm{d}E/\mathrm{d}x}$):
  In the selection, the specific energy loss $\mathrm{d}E/\mathrm{d}x$ is used to separate pions from kaons. Cuts on corresponding weights are applied which are calculated from the pull distribution (see Figure 4.15). A possible shift in this quantity can lead to a systematic misidentification of tracks. The pull distribution is therefore shifted within the error on its mean and the selection procedure is repeated. The difference between the branching fractions obtain with and without the shift applied contributes to the systematic uncertainty.

- Energy scale in π^0 reconstruction (Δ_{E}):
  The energy resolution can be tested by measuring the invariant two-photon mass from π^0 decays. A systematic shift in the observed mass in the data compared to the detector simulation can be translated into a scale factor for the reconstructed photon energies. Deviations of $\Delta m_{\gamma\gamma}(0.5 \pm 0.9)\,\mathrm{MeV}$ from the nominal π^0 mass have been observed [40], corresponding to a scale factor of 1.004 ± 0.007. The energies of the reconstructed photons in the Monte Carlo samples were therefore varied by $\pm 0.7\,\%$. The difference between the branching fractions obtained with and without the variation is the systematic uncertainty.

- Momentum scale (Δ_{p}):
  The systematic uncertainty connected with the momentum scale was tested using $\mathrm{Z}^0 \to \mu^-\mu^+$ events [40]. The difference in momentum resolution between data and Monte Carlo as a function of $\cos\theta$ was studied. To assess the systematic uncertainty Δp in hadronic τ decays, all particle momenta in the Monte Carlo were varied accordingly. The difference in the result with and without this variation is quoted as a systematic uncertainty.

- Monte Carlo statistics (Δ_{MC}):
  The precision of the background prediction depends on the Monte Carlo statistics used in the selection procedure. Therefore, the number of background events selected is varied randomly within its statistical uncertainty. The observed spread in the branching fraction due to this variation is quoted as systematic uncertainty.

- Bias factor ($\Delta_{F^{\mathrm{Bias}}}$):
  The bias factors as determined from the Monte Carlo are varied by their known uncertainty and the branching fractions are then refitted. The observed spread observed due to this variation contributes to the total systematic uncertainty.

7.1.2 Improved Averages for $B(\tau^- \to \mathrm{K}^-\pi^0\nu_\tau)$ and $B(\tau^- \to \mathrm{K}^-\pi^+\pi^-\nu_\tau)$

For the determination of the spectral function and the moments described below, new average values for the branching fractions of the decays $\tau^- \to \mathrm{K}^-\pi^0\nu_\tau$ and $\tau^- \to \mathrm{K}^-\pi^+\pi^-\nu_\tau$ are determined. The same measurements are used as inputs for the calculation as in [57], but the older branching fractions from OPAL were replaced by those determined in this work. For the channel $\tau^- \to \mathrm{K}^-\pi^+\pi^-\nu_\tau$ in addition, the new measurement from CLEO [65] is included. For each measurement, first the total error is calculated by adding the statistical and systematic uncertainties in quadrature. The new average is then determined by calculating the weighted mean of the corresponding individual measurement, where the total error squared is used as weighting factor. The new averages are:

$$\begin{aligned} B_{\mathrm{av}}(\tau^- \to \mathrm{K}^-\pi^0\nu_\tau) &= (0.453 \pm 0.030)\% \\ B_{\mathrm{av}}(\tau^- \to \mathrm{K}^-\pi^+\pi^-\nu_\tau) &= (0.330 \pm 0.028)\%. \end{aligned}$$

The measurements used, together with the averages given in [57] and the improved value for the branching fractions obtained here, are displayed in Figure 7.1 (a/b) for the $(\mathrm{K}^-\pi^0\nu_\tau)$ and the $(\mathrm{K}^-\pi^+\pi^-\nu_\tau)$ final state, respectively.

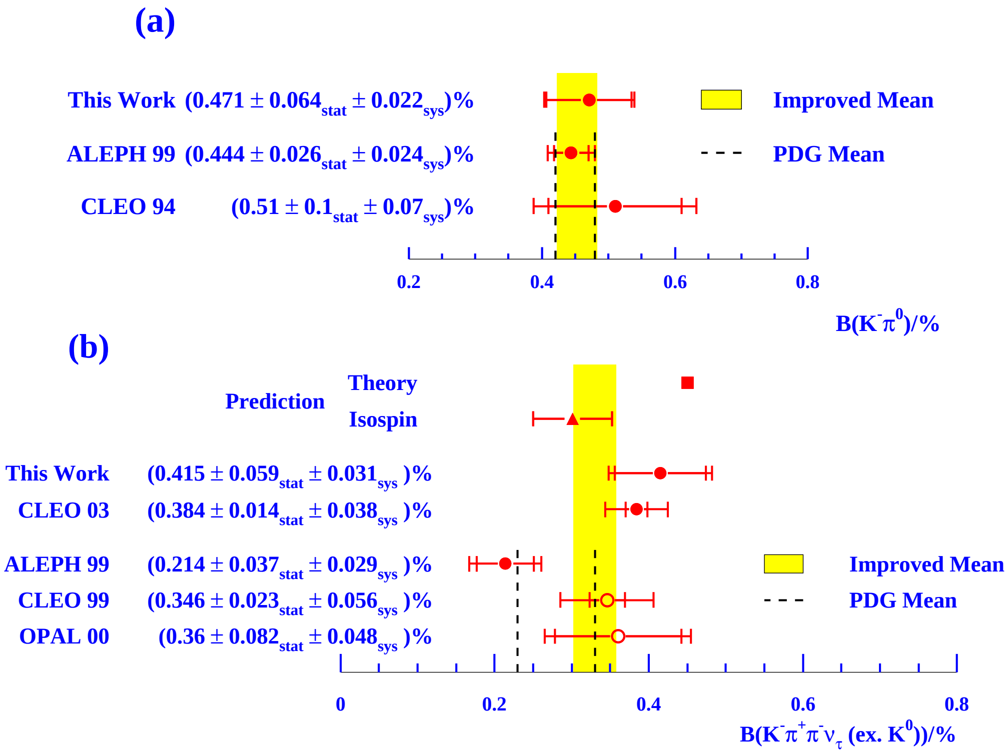

Fig. 7.1: Comparison of the Branching Ratio Measurements for the final states $\tau^- \to \mathrm{K}^-\pi^0\nu_\tau$ (a) and $\tau^- \to \mathrm{K}^-\pi^+\pi^-\nu_\tau$ (b). The full dots represent the measurements used in the calculation of the improved average. Previous measurements, which are not used in the calculation are marked with open dots. The error bars show the statistical uncertainty (inner error bar) and the systematic uncertainty added in quadrature (total error). The shaded band represents the new average and the PDG average is denoted by the dashed lines. In (b) the theoretical prediction from [78] is given by the square and the prediction from isospin relations [88] is given by the triangle.

7.1.3 Discussion

The branching fraction obtained from this analysis for the $\mathrm{K}^-\pi^0\nu_\tau$ channel is consistent with the previous measurements within the errors quoted. The value obtained for the $\mathrm{K}^-\pi^+\pi^-\nu_\tau$ channel is consistent with the new measurement from CLEO and the theoretical prediction in [78]. The ALEPH result differs from these values by roughly 2.5σ. The error on the PDG average contains a scaling factor of 1.4 due to the spread of the individual measurements.

The branching fraction for the $\mathrm{K}^-\pi^+\pi^-\nu_\tau$ final state can be predicted from the measured branching fraction of the final states $\mathrm{K}^0\pi^-\pi^0\nu_\tau$ and $\mathrm{K}^-\pi^0\pi^0\nu_\tau$ using isospin relations [88]:

$$B_{\mathrm{K}^-\pi^+\pi^-\nu_\tau} = \frac{1}{2}B_{\mathrm{K}^0\pi^-\pi^0\nu_\tau} + 2B_{\mathrm{K}^-\pi^0\pi^0\nu_\tau} \tag{7.2}$$

From the recent world averages taken from the PDG-Fit

$$B(\mathrm{K}^0\pi^-\pi^0\nu_\tau) = (0.37 \pm 0.04)\% \tag{7.3}$$

$$B(\mathrm{K}^-\pi^0\pi^0\nu_\tau) = (0.058 \pm 0.023)\%, \tag{7.4}$$

and taking into account the correlation, the following result is obtained:

$$B^{\mathrm{Isospin}}_{\mathrm{K}^-\pi^+\pi^-\nu_\tau} = (0.301 \pm 0.051)\%, \tag{7.5}$$

which is consistent with the improved average calculated in the previous section.

The PDG mean for the decay channel $\mathrm{K}^-\pi^+\pi^-\nu_\tau$ was calculated using the three measurements displayed at the bottom of Figure 7.1(b). This mean was dominated by the ALEPH value, which deviates by about 2σ from the other measurements. The two recent measurements labeled ‘This Work‘ and ’CLEO03’ favor a higher value for this branching fraction which is also preferred by isospin predictions and theoretical calculations.

7.2 The Strangeness Spectral Function

The hadronic decay of the τ lepton is commonly written in terms of the so-called spectral functions $v_1(s)$, $a_{0/1}(s)$ for the non-strange part and $v^{\mathrm{S}}_{0/1}(s)$ and $a^{\mathrm{S}}_{0/1}(s)$ for the strange part. The functions v and a are the vector (V) and the axial-vector (A) contributions, respectively, while the subscript denotes the angular momentum J in the hadronic rest frame. The variable s is the invariant mass squared of the hadronic system. The spectral function is experimentally determined by measuring the invariant mass spectra of the given hadronic modes and normalizing them to their respective branching fractions. The contributions to the total strangeness spectral function then read:

$$\begin{aligned} v^{\mathrm{S}}_1(s)/a^{\mathrm{S}}_1(s) = \frac{m_\tau^2}{6|V_{\mathrm{us}}|^2 S_{\mathrm{ew}}} \left(1-\frac{s}{m_\tau^2}\right)^{-2} \left(1+\frac{2s}{m_\tau^2}\right)^{-1} \\ \times \frac{B(\tau \to (\mathrm{V/A})^{(S=-1,J=1)}\nu_\tau)}{B(\tau \to e^-\bar{\nu}_e\nu_\tau)} \frac{1}{N_{\mathrm{V/A}}} \frac{\mathrm{d}N_{\mathrm{V/A}}}{\mathrm{d}s} \end{aligned} \tag{7.6a}$$

and

$$\begin{aligned} v^{\mathrm{S}}_0(s)/a^{\mathrm{S}}_0(s) = \frac{m_\tau^2}{6|V_{\mathrm{us}}|^2 S_{\mathrm{ew}}} \left(1-\frac{s}{m_\tau^2}\right)^{-2} \\ \times \frac{B(\tau \to (\mathrm{V/A})^{(S=-1,J=0)}\nu_\tau)}{B(\tau \to e^-\bar{\nu}_e\nu_\tau)} \frac{1}{N_{\mathrm{V/A}}} \frac{\mathrm{d}N_{\mathrm{V/A}}}{\mathrm{d}s} \end{aligned} \tag{7.6b}$$

where $|V_{\mathrm{us}}| = 0.2196 \pm 0.0023$ [57] is the CKM weak mixing matrix element, $m_\tau = (1\,776.99^{+0.29}_{-0.26})\,\mathrm{MeV}$ [89] is the mass of the τ lepton and $S_{\mathrm{ew}} = 1.0194 \pm 0.0040$ [31] is an electroweak correction factor.

The total strangeness spectral function $(v + a)$ is obtained by adding these individual contributions. To disentangle the vector and the axial-vector parts for the spin-1 part, a detailed analysis of the resonance structure of the measured spectra would be necessary which is not done here due to the limited statistics. The kaon pole contributes to the pseudoscalar spin-0 part $a_0^{(1)}$.

The Monte Carlo prediction of the total strangeness spectral function as a function of the invariant mass squared is displayed in Figure 7.2. The improved version of the τ Monte Carlo as explained in Chapter 4.4 has been used here. For illustration purposes the spectral function is shown using two different binnings. A non-equidistant binning is chosen which corresponds to a bin width of 50 MeV and 150 MeV in the invariant mass, respectively. The errors given here are from Monte Carlo statistics only.

The spectral function obtained from the data is displayed in Figure 7.3. For $\tau^- \to \mathrm{K}^-\pi^0\nu_\tau$ and $\tau^- \to \mathrm{K}^-\pi^+\pi^-\nu_\tau$, the new average branching fractions and their respective errors as given in Section 7.1.2 are used. The binning chosen in this plot corresponds to a bin width of 150 MeV in the invariant mass and

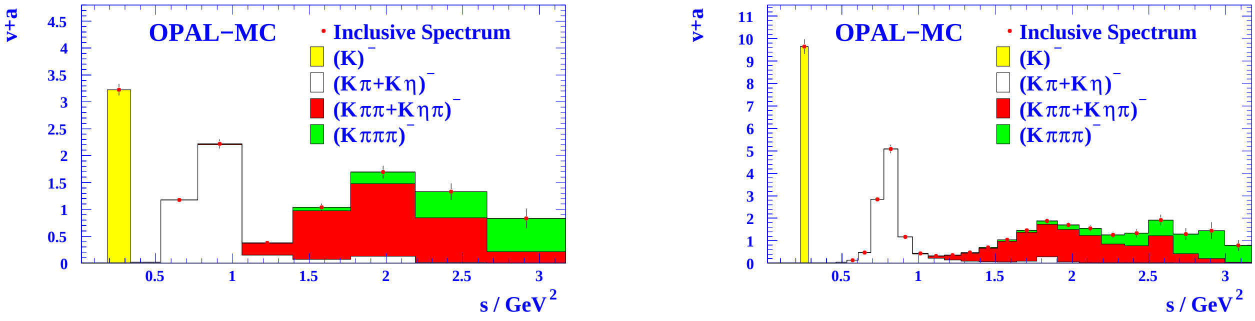

Fig. 7.2: The strangeness spectral function as predicted from Monte Carlo. For illustration purposes two different binnings were used – 150 MeV and 50 MeV in mass in the left and right plot, respectively. The dots represent the inclusive spectrum. The white histogram denotes the contribution from the $(\mathrm{K}\pi)^-$ and $(\mathrm{K}\eta)^-$ final states, the dark shaded histogram those from the $(\mathrm{K}\pi\pi)^-$ and $(\mathrm{K}\eta\pi)^-$ channels and the light shaded area shows the contribution from $(\mathrm{K}\pi\pi\pi)^-$ final states. The leftmost bin represents the kaon pole. The errors shown include the statistical uncertainty of the Monte Carlo as well as the uncertainties on the branching fractions.

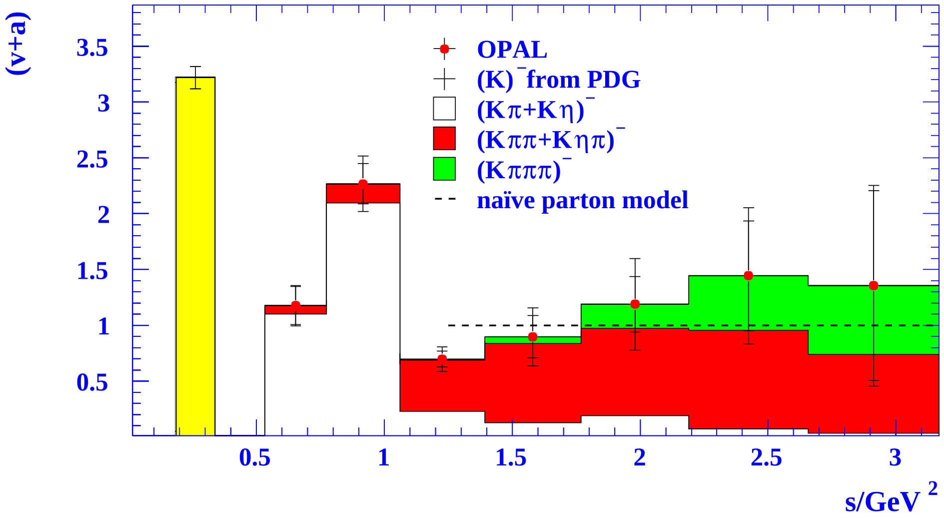

Fig. 7.3: The measured spectral function from strange τ decays. The dots show the inclusive spectrum as measured in OPAL. The white histogram shows the exclusive $(\mathrm{K}\pi)^-$ spectrum, the dark shaded area the $(\mathrm{K}\pi\pi)^-$ contribution and the light shaded area the contribution from the $(\mathrm{K}\pi\pi\pi)^-$ final states. The error bars show the statistical uncertainty (inner error bar) and the systematic uncertainty added in quadrature (total error). The kaon pole is calculated from the PDG branching fraction alone.

is governed by the mass resolution of the $\mathrm{K}^0\pi^-\pi^0\nu_\tau$ final state. The dots with error bars represent the inclusive spectrum. The inner error bars are the statistical uncertainties. They include the uncertainty on the efficiency and on Monte Carlo statistics. The total error is calculated by adding up the statistical and systematic uncertainties (explained in the next section) in quadrature. The numerical values are given in Table 7.3. The systematic uncertainty is dominated by the uncertainty on the branching fractions.
The kaon pole is not measured from the data. It was instead calculated from the branching fraction. For the $(\mathrm{K}\pi)^-$ final state, both τ decay channels $\mathrm{K}^0\pi^-\nu_\tau$ and $\mathrm{K}^-\pi^0\nu_\tau$ are measured. The channel $\mathrm{K}^-\eta\nu_\tau$ which also contributes to the two meson final state is taken from Monte Carlo simulation. For the $(\mathrm{K}\pi\pi)^-$ final state, the spectra $\mathrm{K}^0\pi^-\pi^0\nu_\tau$ and $\mathrm{K}^-\pi^+\pi^-\nu_\tau$ are measured. The contribution from the decay $\mathrm{K}^-\pi^0\pi^0\nu_\tau$ is added from Monte Carlo as well as the $\mathrm{K}^-\eta\pi^0\nu_\tau$ channel which also contributes to the three meson final states. For the $(\mathrm{K}\pi\pi\pi)^-$ spectrum, which consists of the channels $\mathrm{K}^-\pi^+\pi^-\pi^0\nu_\tau$, $\mathrm{K}^0\pi^-\pi^0\pi^0\nu_\tau$, $\mathrm{K}^-\pi^0\pi^0\pi^0\nu_\tau$ and $\mathrm{K}^0\pi^-\pi^+\pi^-\nu_\tau$, the prediction from the Monte Carlo is taken.

7.3 Systematic Uncertainties on the Spectral Function

The sources for possible systematic uncertainties listed below have been considered. Since the individual contributions are different for the different final states the error is given for each bin in s separately. The systematic uncertainties are summarized in Table 7.3.

- PDG errors on the branching fractions (Δ_B):
  The dominant contribution to the systematic uncertainty comes from the uncertainty in the τ branching fractions (see Table 5.1). A shift in the branching fractions can affect the measurement spectral function for two reasons. It influences the predicted contribution from background processes in the measurement of the invariant mass spectra. Furthermore, for the signal channels it influences the calculation of the strangeness spectral function since the branching fractions are used as weights for the individual channels. For $\tau^- \to \mathrm{K}^-\pi^0\nu_\tau$ and $\tau^- \to \mathrm{K}^-\pi^+\pi^-\nu_\tau$ the new average branching fractions and their respective errors as given in Section 7.1.2 are used. The channels which populate the region of high s have branching fractions with relative errors close to 100% leading to a large uncertainty in the spectral function itself. This error also covers the lack of knowledge on the details of the shape.

- Energy loss measurement ($\Delta_{\mathrm{d}E/\mathrm{d}x}$):
  One of the key elements in this analysis is the K-π separation via $\mathrm{d}E/\mathrm{d}x$. During the selection, cuts on kaon and pion weights are applied. A possible shift in the pull distribution from which the weights are

determined leads to systematic misidentification of tracks. The pull distributions were shifted within the errors on their mean value. The resulting change was found to be small compared to the statistical uncertainty. In particular no mass dependent effects are observed.

- $\mathrm{K^0_S}$ identification ($\Delta_{\mathrm{K^0_S}}$):
  A possible origin for systematic effects in the $\mathrm{K^0_S}$ identification is the estimation of the background using Monte Carlo. In particular the number of photon conversions found in τ decays is not perfectly modeled. The cut on the χ^2 probability of the 2-C constrained fit to $\mathrm{K^0_S}$ (see Section (4.3)) has been varied from 10^{-5} to 0.01 to estimate a possible systematic effect. This cut reduces the number photon conversions in the sample by one order of magnitude.

- Energy scale in π^0 reconstruction (Δ_{E}):
  The measured invariant mass spectrum may be distorted due to a bias in the measurement of the photon energies in π^0 decays. The energy resolution can be tested by measuring the invariant mass of the two photons from π^0 decays. A systematic shift in the observed mass in the data compared to the detector simulation can be translated into a scale factor for the reconstructed photon energies. Deviations of (0.5 ± 0.9) MeV from the nominal π^0 mass have been observed [40], corresponding to a scale factor of 1.004 ± 0.007. The energies of the reconstructed photons in the Monte Carlo samples were therefore varied by ±0.7 %.

- Momentum scale (Δ_{p}):
  The measurement of the particle momenta may have a bias which results in a distortion of the measured invariant mass spectra. The systematic uncertainty connected with the momentum scale was tested using $\mathrm{Z}^0 \rightarrow \mu^+\mu^-$ events. In these events, due to the event kinematics, the muons have to have an energy of $E_\mu = 45.6$ GeV, which corresponds to the beam energy. One muon is used to tag the event, the momentum resolution is then determined using the track from the second muon. The difference in momentum resolution between data and Monte Carlo as function of the $\cos\Theta$ was studied. To asses the systematic uncertainty Δ_p in hadronic τ decays, all particle momenta in the Monte Carlo were varied accordingly. The difference in the result with and without this variation is quoted as systematic uncertainty.

- Mass correction procedure (Δ_{mcorr}):
  In order to asses the systematic uncertainty associated with the mass correction procedure, two possible sources have to be considered: The effect due to different input mass spectra and the effect due to the choice of the number of iterations. Both have been studied using high statistics event samples. The systematic deviations using either flat, phase space, or resonance shaped input spectra (with an optimized number of iterations for each scenario) are about 5% in each mass bin. The deviations are largest when a flat input distribution is assumed. Because the true mass spectrum is certainly not flat, we consider 5% still a conservative estimate for Δ_{mcorr}. The effect due to the number of iterations was estimated using a phase space distribution as input spectrum and one additional iteration step was performed. The effect was found to be negligible compared to the effect from a change in the input distribution.

(s-range)/GeV^2	Δ_{B}	$\Delta_{\mathrm{d}E/\mathrm{d}x}$	$\Delta_{\mathrm{K^0_S}}$	Δ_{E}	Δ_{p}	Δ_{mcorr}	$\Delta^{\mathrm{tot}}_{\mathrm{sys}}$	Δ_{stat}	$V + A$
$(0.18, 0.34)$	–	–	–	–	–	–	–	–	3.22± 0.10
$(0.53, 0.77)$	0.04	0.006	0.006	0.007	0.003	0.06	0.07	0.17	1.17± 0.18
$(0.77, 1.06)$	0.13	0.011	0.011	0.014	0.001	0.11	0.17	0.18	2.27± 0.25
$(1.06, 1.39)$	0.08	0.003	0.003	0.004	0.001	0.03	0.09	0.07	0.69± 0.11
$(1.39, 1.77)$	0.18	0.005	0.005	0.005	0.002	0.05	0.18	0.19	0.90± 0.26
$(1.77, 2.19)$	0.32	0.006	0.007	0.007	0.003	0.06	0.33	0.25	1.22± 0.41
$(2.19, 2.66)$	0.35	0.007	0.009	0.009	0.003	0.07	0.36	0.49	1.44± 0.61
$(2.66, 3.17)$	0.30	0.007	0.008	0.008	0.003	0.07	0.31	0.85	1.35± 0.90

Tab. 7.3: Result for the strangeness spectral function. The table shows the values of the strangeness spectral function together with the statistical and the systematic uncertainties for every bin in s. The total uncertainty quoted is the quadratic sum of the statistical and systematic uncertainties. The first line corresponds to the contribution from the kaon pole. This value is not obtained from OPAL data but is calculated using the branching fraction from [57].

7.4 R_τ and the Spectral Moments

From the branching fractions in hadronic τ decays into strange and non-strange final states, the total hadronic width R_τ can be calculated. Exploiting in addition the shape of the spectral function, spectral moments can be determined, which are inputs to theoretical analyses.

7.4.1 The Measurement R_τ

Computing the ratio of the vector and axial-vector branching fractions to the electronic branching fraction, using the values from [57], the following hadronic width ratios were obtained

$$\begin{aligned} R_{\tau,\,V} &= 1.767 \pm 0.013 \\ R_{\tau,\,A} &= 1.702 \pm 0.012 \\ R_{\tau,\,V+A} &= 3.469 \pm 0.014 \\ R_{\tau,\,S} &= 0.1667 \pm 0.0050. \end{aligned}$$

For the non-strange final states, the individual values for vector and axial-vector currents are given separately. In addition, the sum of the two is given. In the calculation of $R_{\tau,\,V+A}$ the large anti-correlation is taken into account. This correlation is $\sim -40\%$ and it is due to the constraint of the sum of all branching fractions to unity. In the case of the strange final states, only the combined value $(V+A)$ is given, since the available statistics does not allow for a separation of vector and axial-vector part.
The values obtained here for the non-strange final states can now be compared to previously published results [40]. The results were found to be consistent within the experimental uncertainty. For the axial-vector final states however, the value obtained here differs from the published results by $\sim 1\sigma$. This is mainly due to the branching fraction in the $\pi^-\pi^0\pi^0\nu_\tau$ final state, which changed from $B = (9.27 \pm 0.14)\%$ to $B = (9.13 \pm 0.14)\%$.
The total strange branching fraction of the τ lepton, including the improved averages for the $\mathrm{K}^-\pi^0\nu_\tau$ and $\mathrm{K}^-\pi^+\pi^-\nu_\tau$ final states, is $B_{\mathrm{strange}} = (2.993 \pm 0.90)\%$. This corresponds to a total strange hadronic width of

$$R_{\tau,\,s} = 0.1677 \pm 0.0050. \tag{7.7}$$

The expectation value for a vanishing strange quark mass can be calculated using Equation 2.46, leading to $R_{\tau,S}(m_{\mathrm{s}} = 0) = 0.1766 \pm 0.0038$. The result obtained in this analysis differs significantly from the expectation in the chiral limit. This is evidence for a massive strange quark.
The corresponding values obtained by the ALEPH collaboration are $B^{\mathrm{ALEPH}}_{\mathrm{strange}} = (2.87 \pm 0.12)\%$ and $R^{\mathrm{ALEPH}}_{\tau} = 0.161 \pm 0.0066$ [63]. They differ from the OPAL values by about one standard deviation. This is mainly due to difference in the branching fractions for the decay channel $\tau^- \to \mathrm{K}^-\pi^+\pi^-\nu_\tau$. The value for the branching fraction obtained here is consistent with a previous OPAL analysis [64] and with the recent result from CLEO [65]. It differs however from the value published by ALEPH [67] by roughly three standard deviations. The improved average for the $\mathrm{K}^-\pi^+\pi^-\nu_\tau$ branching fraction used in the calculation of R_τ here and in the determination of the spectral function and the spectral moments is still about 1σ higher.
Adding the non-strange and strange contributions to the semileptonic width, the following result for the total hadronic width of the τ lepton is obtained:

$$R_\tau = 3.637 \pm 0.015. \tag{7.8}$$

A value for R_τ can also be obtained from the leptonic branching ratio of the τ lepton and from its lifetime.

- R_τ from the branching leptonic branching fractions:
  The total hadronic width can be calculated from the branching fraction of the τ lepton into electrons and into muons. The value for R_τ is then obtained via

$$R_\tau = \frac{1 - B(\tau^- \to \nu_\tau \mathrm{e}^-\overline{\nu}_{\mathrm{e}}) - B(\tau^- \to \nu_\tau \mu^-\overline{\nu}_\mu)}{B(\tau^- \to \nu_\tau \mathrm{e}^-\overline{\nu}_{\mathrm{e}})} = 3.632 \pm 0.016. \tag{7.9}$$

  It can be improved assuming lepton universality. The branching fraction of the τ lepton into muons is then calculated from the branching fraction into electrons via

$$B(\tau^- \to \nu_\tau \mu^-\overline{\nu}_\mu) = B(\tau^- \to \nu_\tau \mathrm{e}^-\overline{\nu}_{\mathrm{e}}) \cdot \frac{\Gamma_{\mathrm{e}}}{\Gamma_\mu}. \tag{7.10}$$

Using $\frac{\Gamma_\mathrm{e}}{\Gamma_\mu} = 0.9726$ [31] and $\Gamma_\mathrm{e} = 4.0329 \cdot 10^{-13}$ GeV [31, 32] this yields

$$R_\tau = \frac{1 - B(\tau^- \to \nu_\tau \mathrm{e}^- \overline{\nu}_\mathrm{e}) - B(\tau^- \to \nu_\tau \mathrm{e}^- \overline{\nu}_\mathrm{e})\frac{\Gamma_\mathrm{e}}{\Gamma_\mu}}{B(\tau^- \to \nu_\tau \mathrm{e}^- \nu_\mathrm{e})} = 3.633 \pm 0.013. \tag{7.11}$$

- R_τ from the τ lifetime:
  Another possibility is the calculation of R_τ from the mean lifetime of the τ lepton. Using $\tau_\tau = (290.6 \pm 1.1)$ fs one obtains:

$$R_\tau = \frac{\tau_\tau^{-1} - \Gamma_\mathrm{e} - \Gamma_\mu}{\Gamma_\mathrm{e}} = 3.644 \pm 0.021. \tag{7.12}$$

The values from the above calculations are independent from the result obtained using hadronic τ decays. They were found to be consistent with the result obtained here. The central value from ALEPH is about one standard deviation higher.

A graphical comparison of the results obtained here and in [70, 72] can be found in Figure 7.4. The value obtained in this work is marked by the full dot, the ALEPH result by the open dot. The crosses represent the values from the above calculations. The shaded band is the mean calculated from the values mentioned there. In the error on the mean, the correlation between the values obtained from the leptonic branching fraction is taken into account.

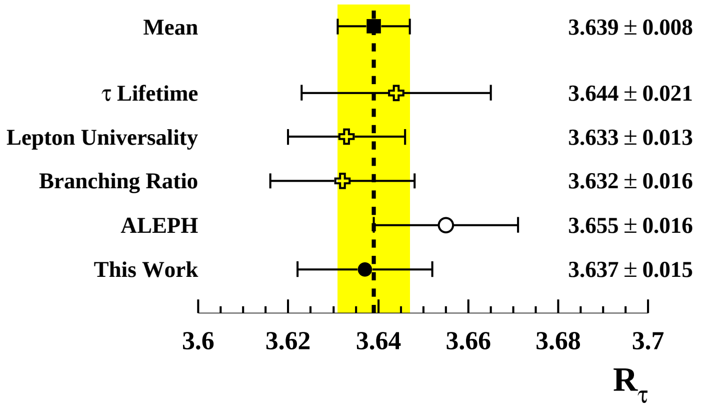

Fig. 7.4: Experimental results for R_τ. The result obtained from this work is represented by the full dot. The open dot represents the ALEPH measurement as calculated from [70, 72]. The values calculated from the mean lifetime of the τ lepton and from the leptonic branching fractions are represented by the open cross. The shaded band represents the weighted mean for R_τ as calculated from the values given here.

7.4.2 Measurement of the Spectral Moments

Spectral moments, which are input parameters for theoretical analyses, can be calculated from the measured spectral function. They are defined as

$$R_\tau^{kl}(m_\tau^2) = \int_0^{m_\tau^2} \mathrm{d}s \left(1 - \frac{s}{m_\tau^2}\right)^k \left(\frac{s}{m_\tau^2}\right)^l \sum_{\tau^- \to \nu_\tau X^-} \frac{B(\tau \to (\mathrm{V/A})^{(S=-1/0, J=0/1)} \nu_\tau)}{B(\tau^- \to e^- \overline{\nu}_e \nu_\tau)} \frac{1}{N_\mathrm{V/A}} \frac{\mathrm{d}N_\mathrm{V/A}}{\mathrm{d}s}, \tag{7.13}$$

where the sum runs over all hadronic final states. The values measured for the strange moments $kl = \{00, 10, 11, 12, 13, 20, 21, 30, 40\}$, their statistical and systematic uncertainties are given in Table 7.5. The various sources contributing have been discussed in Section 7.3. The value for $R_{\tau,S}^{00}$ is calculated from the branching fractions alone and is therefore independent of the measured spectra. In addition, the non-strange moments $kl = \{00, 10, 11, 12, 13\}$ published in [40] have been reevaluated using updated branching fractions. The non-strange moments $kl = 20, 21, 30, 40$ are also calculated, as they are later used in the determination of the strange quark mass. The values for $R_{\tau,V/A}$ and the correlations are given in Table 7.4. In Chapter 9.2 the individual contributions $R_{\tau,V}$, $R_{\tau,A}$ and their correlation coefficients are given.

In addition to the spectral moments, the CKM-weighted difference of the corresponding strange and non-strange moments are given:

$$\delta R_\tau^{kl} = \frac{R_{\tau,\mathrm{non-S}}^{kl}}{|V_{\mathrm{ud}}|^2} - \frac{R_{\tau,\mathrm{S}}^{kl}}{|V_{\mathrm{us}}|^2}, \tag{7.14}$$

where $R_{\tau,\mathrm{S}}^{kl}$ are the strange moments and $R_{\tau,\mathrm{non-S}}^{kl}$ is the sum of the updated vector plus axial-vector non-strange moments. The values of the matrix elements used as weights for the non-strange and strange moments are $|V_{\mathrm{ud}}| = (0.9734 \pm 0.0008)$ and $|V_{\mathrm{us}}| = (0.2196 \pm 0.0023)$, respectively [57]. Systematic errors which are common to both, strange and non-strange moments, as for instance the energy scale error and the momentum scale for tracks, are 100% correlated and are treated accordingly. A graphical comparison of the values obtained here with the ALEPH values for the moments $kl = \{00, 10, 20, 30, 40\}$ can be found in Figure 7.5. The values from ALEPH are denoted by the open dots. They stay rather constant. The values obtained from this analysis increase with increasing k. Since the total strange branching fraction is higher than the one determined by ALEPH, lower values for δR_τ^{kl} were expected. Since for higher values of k the low end of the mass spectrum becomes more pronounced, which has in general higher statistics and more accurately measured branching fractions, the errors decrease with increasing k. The CKM matrix elements used in the calculation of the weighted differences here and in [63] are different. In the latter, they fulfill the unitarity constraint for the mixing matrix. Using the same numerical values for these elements here, yields the results marked by the open crosses in Figure 7.5. A detailed discussion of these values and their impact on the result for the strange quark mass will be given in Section 7.5.3.

		Correlation/%								
kl	$R_{\tau,V+A}$	00	10	11	12	13	20	21	30	40
00	3.469 ± 0.014	100								
10	2.493 ± 0.013	66	100							
11	0.549 ± 0.004	68	65	100						
12	0.203 ± 0.002	51	9	74	100					
13	0.092 ± 0.002	33	-26	33	86	100				
20	1.944 ± 0.011	55	93	45	-11	-40	100			
21	0.346 ± 0.003	59	86	88	35	-13	71	100		
30	1.597 ± 0.009	48	85	28	-24	-44	93	58	100	
40	1.362 ± 0.008	42	77	14	-30	-43	87	43	92	100

Tab. 7.4: Spectral moments obtained from non-strange hadronic τ decays. These values are obtained from [40] using updated branching fractions. The correlation matrix for the spectral moments is given on the right side. The correlations are large, since all moments are based on the same measured spectral function.

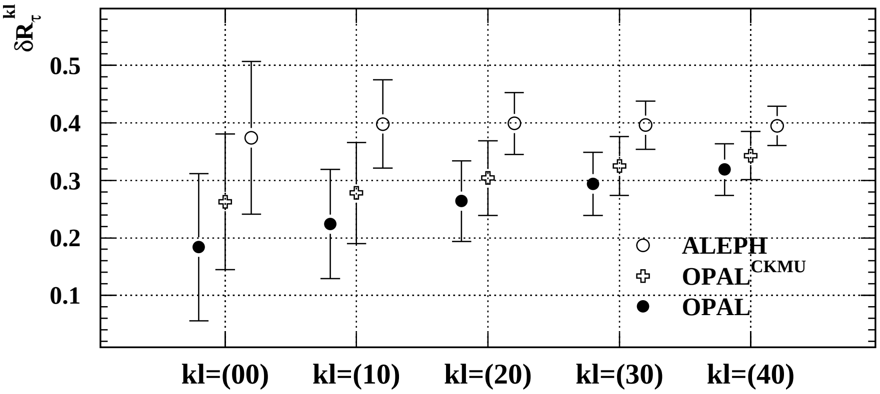

Fig. 7.5: Comparison of the values for the CKM weighted differences of strange and non-strange moments for $kl = \{00, 10, 20, 30, 40\}$ as used in the calculation of the strange quark mass. The open dots are the ALEPH results [63], the full dots represent the results obtained in this work using OPAL data. The open crosses represent the results obtained with the unitarity constraint applied to the CKM matrix elements. The errors include statistical and systematic uncertainties added in quadrature.

kl	$R^{kl}_{\tau,\mathrm{S}}$	Δ_{stat}	$\Delta_{\mathrm{d}E/\mathrm{d}x}$	$\Delta_{\mathrm{K^0_S}}$	Δ_{E}	Δ_{p}	Δ_{mcorr}	00	10	11	12	13	20	21	30	40
00	0.1677 ± 0.0050	–	–	–	–	–	–	100								
10	0.1161 ± 0.0038	0.0035	0.0006	0.0006	0.0005	0.0002	0.0011	89	100							
11	0.0298 ± 0.0012	0.0011	0.0001	0.0001	0.0001	0.0001	0.0004	97	83	100						
12	0.0107 ± 0.0006	0.0005	0.0002	0.0002	0.0002	0.0001	0.0002	86	54	91	100					
13	0.0048 ± 0.0004	0.0002	0.0002	0.0002	0.0002	0.0001	0.0001	74	36	78	97	100				
20	0.0862 ± 0.0028	0.0025	0.0006	0.0006	0.0006	0.0002	0.0008	75	97	66	32	13	100			
21	0.0191 ± 0.0007	0.0006	0.0001	0.0001	0.0001	0.0001	0.0002	92	96	92	66	47	87	100		
30	0.0671 ± 0.0022	0.0020	0.0005	0.0005	0.0004	0.0002	0.0006	66	92	54	19	1	99	78	100	
40	0.0539 ± 0.0018	0.0016	0.0003	0.0003	0.0003	0.0001	0.0005	60	87	46	11	-4	96	70	99	100

kl	δR^{kl}_{τ}	Δ_{exp}	$\Delta_{\lvert V_{\mathrm{us}}\rvert}$	00	10	11	12	13	20	21	30	40
00	0.184 ± 0.128	0.105	0.073	100								
10	0.224 ± 0.095	0.080	0.050	79	100							
11	-0.039 ± 0.028	0.025	0.013	88	67	100						
12	-0.008 ± 0.014	0.013	0.005	67	37	65	100					
13	-0.002 ± 0.009	0.009	0.000	49	20	48	53	100				
20	0.264 ± 0.070	0.059	0.037	64	74	51	20	5	100			
21	-0.031 ± 0.017	0.015	0.008	81	76	75	46	26	66	100		
30	0.294 ± 0.055	0.047	0.029	56	71	42	11	0	73	60	100	
40	0.320 ± 0.045	0.038	0.023	52	69	36	6	-4	74	55	77	100

kl	$R^{kl}_{\tau,\mathrm{S}}/R^{kl}_{\tau,\mathrm{non-S}}$	00	10	11	12	13	20	21	30	40
00	0.0484 ± 0.0015	100								
10	0.0466 ± 0.0015	79	100							
11	0.0543 ± 0.0022	88	67	100						
12	0.0527 ± 0.0030	67	37	66	100					
13	0.0518 ± 0.0045	49	20	48	53	100				
20	0.0444 ± 0.0015	64	74	51	20	5	100			
21	0.0552 ± 0.0021	80	76	75	46	26	66	100		
30	0.0420 ± 0.0014	57	71	42	12	0	73	59	100	
40	0.0400 ± 0.0013	53	69	36	7	-4	73	55	76	100

Tab. 7.5: The spectral moments for $kl = \{00, 10, 11, 12, 13, 20, 21, 30, 40\}$. The table includes the values for the strange spectral moments and the statistical and systematic uncertainty, where the statistical uncertainty also contains the uncertainty on the branching fractions. The moment R^{00}_{τ} is calculated from the branching fractions alone. It is therefore independent of the measured spectra. In addition, the weighted difference δR^{kl}_{τ} of the strange to non-strange moments are given. The corresponding elements of the weak mixing matrix $|V_{\mathrm{ud}}|^2$ and $|V_{\mathrm{us}}|^2$ are used as weighting factors. In bottom table, the ratio of strange to non-strange moments is given. On the right hand side of each table, the correlations are given in percent. The experimental errors for δR^{kl}_{τ} and the ratio include the statistical and systematic uncertainties added in quadrature. Contributions that are common to strange and non-strange moments are treated accordingly. For δR^{kl}_{τ} the error on the matrix element $\Delta_{|V_{\mathrm{us}}|}$ is given separately.

7.5 Measurement of the Strange Quark Mass m_s

The theoretical framework necessary to determine the mass of the strange quark was discussed already in Chapter 2. The principle is briefly repeated here.

The mass of the strange quark m_s is obtained from the analysis of the weighted integrals over the measured invariant mass spectra. Using the Operator Product Expansion, perturbative and non-perturbative contributions to R_τ can be separated and the corresponding expression for the moments read:

$$R_\tau = 3(|V_\mathrm{ud}|^2 + |V_\mathrm{us}|^2) S_\mathrm{ew} \left(1 + \delta_\mathrm{ew} + \delta^{(0)} + \sum_{D=2,4,\ldots} (\cos^2 \Theta_\mathrm{C} \delta^{(D)}_\mathrm{ud}) + \sin^2 \Theta_\mathrm{C} \delta^{(D)}_\mathrm{us}) \right), \tag{7.15}$$

where $|V_\mathrm{ud}| = 0.9734 \pm 0.0008$ and $|V_\mathrm{us}| = 0.2196 \pm 0.0023$ [57] are the corresponding elements of the weak mixing matrix (CKM Matrix) and $\sin^2 \Theta \equiv |V_\mathrm{us}|^2/(|V_\mathrm{ud}|^2 + |V_\mathrm{us}|^2)$. The electroweak corrections are split into a multiplicative part $S_\mathrm{ew} = 1.0194 \pm 0.0040$ [31] and an additive correction $\delta_\mathrm{ew} = 0.0010$. The purely perturbative correction is denoted by $\delta^{(0)}$. These are calculated neglecting the quark masses and are therefore identical for vector and axial-vector contributions and for strange τ decays.

By analyzing separately the Cabbibo-allowed and the Cabbibo-suppressed decay widths of the τ lepton, a sensitivity to the mass of the strange quark is induced (for details see Chapter 2). The quantity analyzed in this work is the CKM weighted difference of strange to non-strange moments

$$\delta R^{kl}_\tau \equiv \frac{R^{kl}_{\tau,V+A}}{|V_\mathrm{ud}|^2} - \frac{R^{kl}_{\tau,S}}{|V_\mathrm{us}|^2} = 3 S_\mathrm{ew} \sum_{D \geq 2} \left(\delta^{kl(D)}_\mathrm{ud} - \delta^{kl(D)}_\mathrm{us} \right). \tag{7.16}$$

In the limit of $\mathrm{SU}(3)_\mathrm{Flavor}$ symmetry, this quantity is expected to be exactly zero. Any deviation from this expectation is due to a massive strange quark. The dominant contribution to the $\mathrm{SU}(3)_\mathrm{Flavor}$ breaking effects comes from the dimension-2 corrections. They create the wanted sensitivity to the mass of the strange quark. The only other contribution (from dimension-4 operators) considered here is the quark condensate

$$\delta O_4(\mu^2) \equiv \langle 0 | m_\mathrm{s} \bar{\mathrm{s}}\mathrm{s} - m_\mathrm{d} \bar{\mathrm{d}}\mathrm{d} | 0 \rangle (\mu^2), \tag{7.17}$$

which was calculated using lowest order in Chiral Perturbation Theory [24]. It could in principle be determined from τ data using a combined fit to different moments R^{kl}_τ. However, given the large experimental uncertainties of the spectral moments, this is not sensible. The following estimate was obtained in [10]:

$$\langle \delta O_4(m^2_\tau) \rangle \simeq -(1.5 \pm 0.4) \times 10^{-3}\,\mathrm{GeV}^4, \tag{7.18}$$

Additional condensates contributing to the dimension-4 corrections are suppressed by a factor m^4_s. They are too small to be determined here, given the experimental uncertainty on the measured moments. The same is true for corrections of dimension $D \geqslant 6$ so that they don't have any significant impact on the result. The strange quark mass is then obtained from [10]

$$m^2_\mathrm{s}(m^2_\tau)\Big|_{kl} \simeq \frac{m^2_\tau}{(1-\epsilon^2_\mathrm{d})\Delta^{(2)}_{kl}(a_\tau)} \left(\frac{\delta R^{kl}_\tau}{24 S_\mathrm{ew}} + 2\pi^2 \frac{\langle \delta O_4(m^2_\tau) \rangle}{m^4_\tau} Q_{kl}(a_\tau) \right), \tag{7.19}$$

for each moment kl individually. Here $\Delta^{(2)}_{kl}(a_\tau)$ and $Q_{kl}(a_\tau)$ are the perturbative QCD series associated with the dimension-2 and dimension-4 corrections to δR^{kl}_τ, $a_\tau = \alpha_s(m^2_\tau)/\pi$ and $\epsilon_\mathrm{d} = m_\mathrm{d}/m_\mathrm{s} = 0.053 \pm 0.002$ [34] is the ratio of the mass of the d-quark to the mass of the strange quark. The numerical values used in the calculation of the mass of the strange quark are given in Table 7.6, where $\Delta^{(2)}_{kl}$ was calculated from the $L+T$ and the L contribution via

$$\Delta^{(2)}_{kl}(a_\tau) = \frac{1}{4} \left(3\Delta^{L+T}_{kl}(a_\tau) + \Delta^{L}_{kl}(a_\tau) \right). \tag{7.20}$$

In Chapter 2.7 it was discussed which considerations, either theoretical or experimental, should lead to a certain choice of moments to be analyzed in the determination of the mass of the strange quark. Given the actual experimental uncertainties on the $l \neq 0$ moments, their sensitivity on the strange quark mass is small. In addition for moments δR^{1l}_τ, the contributions from dimension-2 and dimension-4 operators have a theoretical uncertainty close to 100% [20], which leads to an increased sensitivity on higher dimension condensates. These are basically unknown. Therefore, in this work only moments δR^{k0}_τ are analyzed.

7.5.1 Measurement of m_{s} at the τ Mass Scale

The perturbative QCD contribution of dimension-2 is calculated up to third order for the $J = L$ part and up to second order for the $J = L + T$ part [19,20], using $\alpha_{\mathrm{s}} = 0.334 \pm 0.022$ for the strong coupling constant. An estimate of the third order contribution can be found in [26]. $\Delta^{(2)}_{kl}$ can therefore be displayed up to third order, which yields:

$$\begin{aligned}
\Delta^{(2)}_{00}(a_\tau) &= 0.9734 + 0.4811 + 0.3718 + 0.3371 + ...\\
\Delta^{(2)}_{10}(a_\tau) &= 1.0390 + 0.5576 + 0.4820 + 0.4771 + ...\\
\Delta^{(2)}_{20}(a_\tau) &= 1.1154 + 0.6432 + 0.6082 + 0.6470 + ...\\
\Delta^{(2)}_{30}(a_\tau) &= 1.1990 + 0.7374 + 0.7516 + 0.8507 + ...\\
\Delta^{(2)}_{40}(a_\tau) &= 1.2880 + 0.8404 + 0.9142 + 1.0928 + ...
\end{aligned}$$

where $a_\tau = \alpha_s(m_\tau^2)/\pi$. For $k \in \{0,\ 1\}$ the series converges reasonably well up to the third oder. However, for $k \in \{2\}$ and $k \in \{3,\ 4\}$, the contributions increase again, starting from the second order and first order, respectively. This is due to the bad convergence behavior of the $J = L$ series.

Therefore, the following truncation procedure is applied, which was adopted from [63]. The contributions from all orders up to the minimum term are kept in the calculation of $\Delta^{(2)}_{k0}$. The higher order terms are neglected. This means that $\Delta^{(2)}_{k=0/1,\,l=0}$ are summed up to third order, $\Delta^{(2)}_{k=2,\,l=0}$ up to second order and $\Delta^{(2)}_{k=3/4,\,l=0}$ up to first order only. The value of the last term considered is taken as systematic error to account for the uncertainty associated with the truncation procedure. The numerical values for the contributions from $\Delta^{(2)}_{k0}$ and the perturbative dimension-4 coefficient Q_{kl} are given in Table 7.6 [63].

The numerical values for the mass of the strange quark can now be calculated separately for the individual moments. The values are given in Table 7.7. They vary within the total uncertainty given from $\sim 75\,\mathrm{MeV}$ for $kl = 10$ up to $\sim 90\,\mathrm{MeV}$ for $kl = 30$. As k increases, the contribution from the theoretical uncertainty becomes more important. This is due to the limited validity of the OPE in the range of non-perturbative QCD. The experimental error decreases at the same time, since the spectra at the low mass end are easier to measure from the experimental point of view. To optimize the experimental and theoretical sensitivity, a weighted mean is calculated using all moments $l \neq 0$, taking into account the full covariance matrix. The variation of the final result on the strange quark mass when using different moments is given in Table 7.8. The observed variation is of the order of 5 MeV which is small compared to the total uncertainty quoted. Therefore, for the final result, all moments up to $kl = 40$ are used in the calculation of the weighted mean. The value obtained from this procedure is

$$\begin{aligned}
m_{\mathrm{s}}(m_\tau^2) &= (84 \pm 14_{\mathrm{exp}} \pm 6_{V_{\mathrm{us}}} \pm 17_{\mathrm{theo}})\,\mathrm{MeV} && (7.22\mathrm{a})\\
&= (84^{+20}_{-26})\,\mathrm{MeV}, && (7.22\mathrm{b})
\end{aligned}$$

where the individual contributions to the total uncertainty have been added in quadrature. The experimental uncertainty quoted is calculated from the uncertainty on the spectral moments alone. The theoretical uncertainty on the strange quark mass is given separately for the contribution from the CKM matrix element

kl	$\Delta^{(2)}_{kl}$	Q_{kl}	kl
00	2.16 ± 0.34	1.07 ± 0.02 ± 0.01	00
10	2.56 ± 0.48	1.50 ± 0.02 ± 0.01	10
20	2.37 ± 0.65	1.92 ± 0.01 ± 0.003	20
30	1.94 ± 0.73	2.33 ± 0.01 ± 0.01	30
40	2.13 ± 0.84	2.72 ± 0.03 ± 0.02	40

Tab. 7.6: Numerical values for the perturbative QCD series of dimension-2 ($\Delta^{(2)}_{kl}$) and dimension-4 (Q_{kl}), using $\alpha_{\mathrm{s}} = 0.334 \pm 0.022$. The error given for $\Delta^{(2)}_{kl}$ is the theoretical uncertainty associated with the truncation procedure. For Q_{kl}, the first error denotes the contribution from the theoretical uncertainty; the second error represent the contribution to the uncertainty from the experimental error on the strong coupling constant at the τ scale.

	m_{s}/ MeV	σ_{theo}/ MeV			σ/ MeV			Correlation/%				
kl		$\sigma(\alpha_s)$	$\sigma(\langle m_{\mathrm{s}}\bar{\mathrm{s}}\mathrm{s}\rangle)$	$\sigma(\text{Trunc.})$	σ_{theo}	$\sigma_{\lvert V_{\mathrm{us}}\rvert}$	σ_{exp}	00	10	20	30	40
00	79.5± 49.7	0.6	7.8	6.2	10.0	27.3	39.4	100	59	46	31	22
10	76.0± 34.7	0.5	9.7	7.1	12.0	16.7	26.7		100	53	38	29
20	82.4± 29.5	0.2	12.3	10.6	16.2	12.4	19.7			100	37	29
30	91.1± 32.3	0.3	16.5	17.3	24.0	10.7	17.1				100	24
40	85.6± 30.9	0.8	18.7	16.9	25.2	8.3	13.5					100

Tab. 7.7: The strange quark mass m_{s} as calculated from the CKM weighted differences δR_τ^{kl} of the measured strange and non-strange spectral moments for $kl = \{00, 10, 20, 30, 40\}$. The theoretical uncertainty σ_{theo} quoted includes the uncertainty on α_s, on the quark condensate $m_{\mathrm{s}}\langle\bar{\mathrm{s}}\mathrm{s}\rangle$ and on the truncation procedure added in quadrature. The uncertainty on the CKM matrix element $|V_{\mathrm{us}}|$ is given separately. In addition, the experimental uncertainty is given. The total error is obtained by adding the individual contributions in quadrature. The correlation between the values for the strange quark mass obtained from different moments is given on the right side of the table.

$|V_{\mathrm{us}}|$ and the theoretical uncertainty as given in Table 7.7. The theoretical uncertainty quoted in the final result contains two additional contributions.

1) An additional uncertainty $\Delta_{\text{OPE}} = 8\,\text{MeV}$ is assigned due to the limited validity of the operator product expansion in the low mass range. As k increases, the low mass end of the spectral function, where non-perturbative effects become more important and the operator product expansion might no longer be valid, dominates. The uncertainty is estimated from the variation of values obtained for the strange quark mass from different moments alone (see Table 7.7).

2) To split the total error as given above, the fit for the weighted mean is repeated. The contribution to be determined is subtracted from the total error. The total error obtained on the weighted mean was then compared to the original result and the difference is quoted as systematic uncertainty. Since the size of the errors vary with the moments used, the final result is different when considering different contributions to the total error. The variation on the mean obtained from the fit ($\Delta_{\text{Fit}} = 2\,\text{MeV}$) is assigned as additional systematic uncertainty.

The theoretical uncertainty as given in 7.22a was obtained by adding these two additional contributions in quadrature. The total error on final result for the strange quark mass is dominated by the theoretical uncertainty.

Moments	$(\bar{m}_{\mathrm{s}} \pm \Delta^{\text{tot}}_{\bar{m}_{\mathrm{s}}})$/ MeV	$\Delta^{\text{asym.}}_{m_{\mathrm{s}}}$/ MeV
$k = 0$ alone	79.5 ± 49.0	${}^{-117.9}_{+39.3}$
$k = 0$ to 1	76.5 ± 26.7	${}^{-23.2}_{+34.5}$
2	79.8 ± 23.2	${}^{-20.6}_{+28.2}$
3	83.0 ± 22.6	${}^{-20.2}_{+27.0}$
4	84.0 ± 21.7	${}^{-19.4}_{+25.5}$

Tab. 7.8: Variation of the strange quark mass as function of the moments used in the fit for the weighted mean. In the second column, the central value and the total error with the experimental and theoretical uncertainties added in quadrature is given. The error was symmetrized for reading convenience. In the last column the asymmetric errors are given.

7.5.2 The Strange Quark Mass at $\mu^2 = 1\,\text{GeV}^2$ and $\mu^2 = 4\,\text{GeV}^2$

The mass of the strange quark, measured at the τ mass scale, can now be evolved to different scales using the renormalization group β and γ functions. The mass of the strange quark can be evolved using the γ

function:

$$-\frac{\mu^2}{a_s}\frac{\mathrm{d}m_i}{\mathrm{d}\ln\mu^2} = \gamma(a_s) \tag{7.23a}$$

$$= +\gamma_0 a_s + \gamma_1 a_s^2 + \gamma_2 a_s^3 + \gamma_3 a_s^4 + \mathcal{O}(a_s^5), \tag{7.23b}$$

where $a_s = a_s(\mu^2) = \alpha_s(\mu^2)/(4\pi)$. The γ function is known to the 4-loop level [27]. The coefficients γ_i in the $\overline{\mathrm{MS}}$ scheme are given by

$$\gamma_0 = 4 \tag{7.24a}$$

$$\gamma_1 = \frac{202}{3} - \frac{20}{9}n_f \tag{7.24b}$$

$$\gamma_2 = 1249 + \Big(-\frac{2216}{27} - \frac{160}{3}\zeta(3)\Big)n_f - \frac{140}{81}n_f^2 \tag{7.24c}$$

$$\begin{aligned}\gamma_3 = {} & \frac{4603055}{162} + \frac{135680}{27}\zeta(3) - 8800\zeta(5) \\ & + \Big(-\frac{91723}{27} - \frac{34192}{9}\zeta(3) + 880\zeta(4) + \frac{18400}{9}\zeta(5)\Big)n_f \\ & + \Big(\frac{5242}{243} + \frac{800}{9}\zeta(3) - \frac{160}{3}\zeta(4)\Big)n_f^2 + \Big(-\frac{332}{243} + \frac{64}{27}\zeta(3)\Big)n_f^3,\end{aligned} \tag{7.24d}$$

where n_f is the number of active flavors and ζ is the Riemann ζ-function ($\zeta(3) = 1.20206...$, $\zeta(4) = 1.08232...$ and $\zeta(5) = 1.03693...$). This equation depends on the strong coupling constant at the same scale. It can be evaluated using the RGE β function:

$$-\mu^2\frac{\mathrm{d}a_s}{\mathrm{d}\ln\mu^2} = a_s\beta(a_s) \tag{7.25a}$$

$$= +\beta_0 a_s^2 + \beta_1 a_s^3 + \beta_2 a_s^4 + \beta_3 a_s^5 + \mathcal{O}(a_s^6). \tag{7.25b}$$

The β-function is also known to the 4-loop level [27], with the coefficients β_i in the $\overline{\mathrm{MS}}$ scheme given by

$$\beta_0 = 11 - \frac{2}{3}n_f \tag{7.26a}$$

$$\beta_1 = 102 - \frac{38}{3}n_f \tag{7.26b}$$

$$\beta_2 = \frac{2857}{2} - \frac{5033}{18}n_f + \frac{325}{54}n_f^2 \tag{7.26c}$$

$$\beta_3 = \Big(\frac{149753}{6} + 3564\zeta(3)\Big) - \Big(\frac{1078361}{162} + \frac{6508}{27}\zeta(3)\Big)n_f + \Big(\frac{50065}{162} + \frac{6472}{81}\zeta(3)\Big)n_f^2 + \frac{1093}{729}n_f^3. \tag{7.26d}$$

This differential equation can be solved at different scales using the Runge-Kutta procedure. In this procedure, the solution of a differential equation at some scale $\mu^2 = m_\tau^2 + h$, is obtained from a known solution (here $\alpha_s(m_\tau^2) = 0.334 \pm 0.022$) in an iterative procedure, where h is the step width. The error on this procedure scales with h^5. Thus by choosing sufficiently small intervals, the additional uncertainty from this procedure is negligible.
The solution of Equation 7.23a can be approximated by the Taylor expansion

$$m_i(\mu^2) = \hat{m}_\mathrm{q} a_s^{\frac{\gamma_0}{\beta_0}}\left(1 + A_1 a + \left(A_1^2 + A_2\right)\frac{a_s^2}{2} + \left(\frac{1}{2}A_1^3 + \frac{3}{2}A_1A_2 + A_3\right)\frac{a_s^3}{2} + \mathcal{O}(a_s^4)\right), \tag{7.27}$$

where $\hat{m}_\mathrm{q}$ is a renormalization group independent quark mass. The coefficients A_i are a function of the coefficients of the RGE β- and γ-functions. They are given by

$$A_1 = -\frac{\beta_1\gamma_0}{\beta_0^2} + \frac{\gamma_1}{\beta_0} \tag{7.28a}$$

$$A_2 = \frac{\gamma_0}{\beta_0^2}\left(\frac{\beta_1^2}{\beta_0} - \beta_2\right) - \frac{\beta_1\gamma_1}{\beta_0^2} + \frac{\gamma_2}{\beta_0} \tag{7.28b}$$

$$A_3 = \left(\frac{\beta_1\beta_2}{\beta_0} - \frac{\beta_1}{\beta_0}\left(\frac{\beta_1^2}{\beta_0} - \beta_2\right) - \beta_3\right)\frac{\gamma_0}{\beta_0^2} + \frac{\gamma_1}{\beta_0^2}\left(\frac{\beta_1^2}{\beta_0} - \beta_2^2\right) - \frac{\beta_1\gamma_2}{\beta_0^2} + \frac{\gamma_3}{\beta_0}. \tag{7.28c}$$

Using the above definitions, the following expansion for the running strange quark mass in the $\overline{\mathrm{MS}}$ scheme at the 4-loop level is obtained:

$$m_\mathrm{s}(\mu^2) = \widehat{m}_\mathrm{s}\left(\frac{\alpha_s}{\pi}\right)^{\frac{4}{9}}\left(1 + 0.895062\left(\frac{\alpha_s}{\pi}\right) + 1.37143\left(\frac{\alpha_s}{\pi}\right)^2 + 1.95168\left(\frac{\alpha_s}{\pi}\right)^3\right). \tag{7.29}$$

The value for the renormalization group independent mass $\widehat{m}_\mathrm{s}$ is chosen in a way that the measured mass of the strange quark ($(84^{+20}_{-26})\,\mathrm{MeV}$) is obtained when setting $\mu^2 = m_\tau^2$. This leads to

$$\widehat{m}_\mathrm{s} = (204 \pm 56)\,\mathrm{MeV}. \tag{7.30}$$

Using Equation 7.29 with $\alpha_s(m_\tau^2) = 0.334 \pm 0.022$ and $m_\mathrm{s}(m_\tau^2) = (0.084 \pm 0.023)\,\mathrm{GeV}$, the following values are obtained for the strange quark mass at the scales $\mu^2 = 1\,\mathrm{GeV}^2$ and $\mu^2 = 4\,\mathrm{GeV}^2$:

$$m_\mathrm{s}(1\,\mathrm{GeV}^2) = (111^{+26}_{-35})\,\mathrm{MeV} \tag{7.31}$$

$$m_\mathrm{s}(4\,\mathrm{GeV}^2) = (82^{+19}_{-25})\,\mathrm{MeV}. \tag{7.32}$$

These results are displayed in Figure 7.6. The above values are shown together with the one obtained at $\mu^2 = m_\tau^2$. The errors shown in the plot were symmetrized. The shaded band represents the uncertainty on the evolution from the error on the strong coupling constant. In addition, the values obtained by the ALEPH collaboration are shown [63]. All results are obtained, assuming three active quark flavors. The values for the strange quark mass obtained here are significantly lower at all scales than the one from ALEPH in the publication mentioned above.

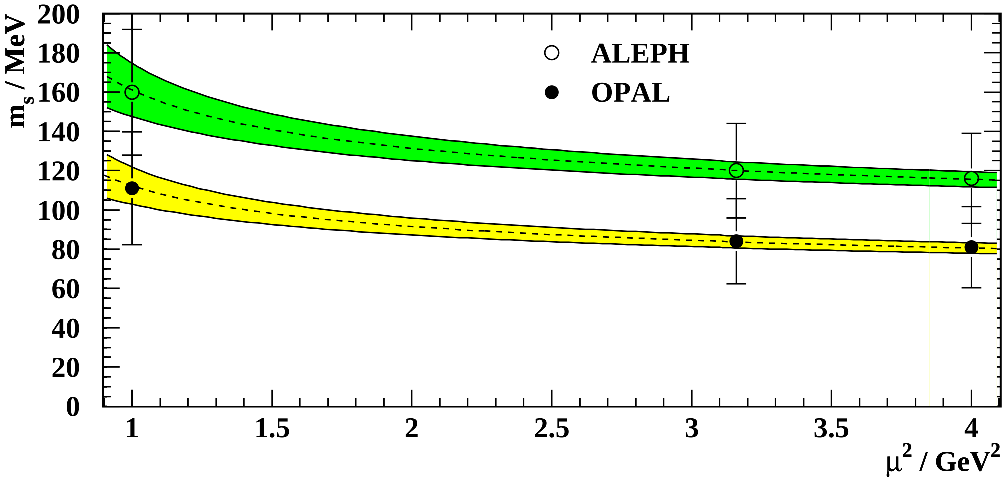

Fig. 7.6: Running of the strange quark mass. The value of m_s is evaluated at the scales $\mu^2 = \{1\,\mathrm{GeV}^2,\, m_\tau^2,\, 4\,\mathrm{GeV}^2\}$. The value at $\mu^2 = m_\tau^2 = (1.777\,\mathrm{GeV})^2$ was obtained from experiment. The two other values were calculated using the RGE equation at the 4-loop level. The open dots represent the OPAL result, the full dots the measurement from ALEPH [63]. The error bars denote the total uncertainty with the experimental and theoretical uncertainties added in quadrature. For this plot, the errors were symmetrized. The shaded band represents the uncertainty from the strong coupling constant α_s alone.

7.5.3 Discussion

The value obtained for the strange quark mass m_s at $\mu^2 = 4\,\mathrm{GeV}^2$ can be compared to previous analyses. A graphical comparison is shown in Figure 7.7 with additional remarks on the type of analysis the result is based on. The mass of the strange quark obtained in this work is represented by the full dots. The open dots represent the analyses based on the ALEPH spectral function which are therefore correlated. Other analyses, not based on τ spectral functions are given as open crosses. In addition, the preferred range for the strange quark mass using QCD sum rules (QCDSR) and Lattice QCD (LQCD) predictions are given by the dashed and dotted lines, respectively [69]. The shaded band represents the preferred region as given by the Particle Data Group fit. This fit includes additional results from theoretical calculations, which are not mentioned here. In this comparison, only results based on experimental data are discussed. The value obtained in this work favors the preferred range from Lattice QCD calculations. However it is also consistent with the prediction from QCD sum rules within the errors quoted. The analyses based on the ALEPH spectral functions slightly favor the range covered by QCD sum rules. Analyses not based on spectral functions from τ decays usually tend to yield higher mass values.

Comparison with ALEPH Results:
The various analyses based on ALEPH data (GAMIZ03, MALTMAN02, CHEN01B, KOERNER01, BARATE99R, MALTMAN99, PICH99) display some differences in their treatment of the truncation procedures for the dimension-2 correction, in their treatment of the dimension-4 correction and in the moments used in the calculation. Since there is a high degree of cancellation between the weighted integrals of the strange and the non-strange spectral function, the result of m_s is also very sensitive to differences in $R_{\tau,\mathrm{s}}$, $R_{\tau,\,non-\mathrm{s}}$ and on the values used for the matrix elements $|V_\mathrm{ud}|$ and $|V_\mathrm{us}|$ in the two analyses. These differences have to be taken into account, when comparing the results obtained here to the ALEPH based analyses. The comparison with CHEN01B is of particular interest, since the same truncation procedure for the perturbative series of dimension-2 was used here and the treatment of the dimension-4 condensate is identical. The values obtained here are consistent in the sense that the error bars overlap. However the central values differ by 1.5 standard deviation. The differences in these two analyses are discussed in more detail.

1) The Elements of the CKM Matrix:
The values of the weak mixing matrix used here do not satisfy the unitarity constraint

$$|V_\mathrm{ud}|^2 + |V_\mathrm{us}|^2 + |V_\mathrm{ub}|^2 = 1. \tag{7.33}$$

Taking the measured values from [57]

$$|V_\mathrm{ud}|^2 + |V_\mathrm{us}|^2 + |V_\mathrm{ub}|^2 = 0.9957 \pm 0.0019, \tag{7.34}$$

reveals a 2.3σ deviation from unity. The matrix elements can be reevaluated using an unitarity constraint for the elements which yields the following results

$$V_\mathrm{ud}^\mathrm{CKMU} = 0.9749 \pm 0.0004 \tag{7.35a}$$

$$V_\mathrm{us}^\mathrm{CKMU} = 0.2225 \pm 0.0019 \tag{7.35b}$$

$$V_\mathrm{ub}^\mathrm{CKMU} = (3.604 \pm 0.7) \cdot 10^{-3}. \tag{7.35c}$$

Compared to the unconstrained values, this means a shift of roughly 2σ for $|V_\mathrm{ud}|$ and $\sim 1\sigma$ for $|V_\mathrm{us}|$. The results obtained for the weighted difference of strange and non-strange moments are compared to the original values and the results obtained in [70] in Figure 7.5. The dependence of δR_τ^{kl} on the matrix elements becomes smaller with increasing k. The strange quark mass obtained in this analysis can be reevaluated using the constraint matrix elements, which yields

$$m_\mathrm{s}(m_\tau^2) = (95 \pm 15_\mathrm{exp} \pm 4_{V_\mathrm{us}} + 14_\mathrm{theo})\,\mathrm{MeV} \tag{7.36a}$$

$$= (95^{+18}_{-22})\,\mathrm{MeV}. \tag{7.36b}$$

Evolving this to the scales $\mu^2 = 1\,\mathrm{GeV}^2$ and $\mu^2 = 4\,\mathrm{GeV}^2$, one obtains

$$m_\mathrm{s}(1\,\mathrm{GeV}^2) = (125^{+24}_{-29})\,\mathrm{MeV} \tag{7.36c}$$

$$m_\mathrm{s}(4\,\mathrm{GeV}^2) = (91^{+17}_{-21})\,\mathrm{MeV}. \tag{7.36d}$$

Considering the results obtained with and without unitarity constraint for the matrix elements at $\mu^2 = 4\,\mathrm{GeV}^2$, a shift of the strange quark mass by $\sim 10\,\mathrm{MeV}$ is observed.

In CHEN01B, $|V_{\mathrm{us}}| = 0.2225 \pm 0.0021$ was used, which corresponds to the value obtained above with the unitarity constraint applied to the elements of the CKM matrix. The value for $|V_{\mathrm{ud}}|$ is not given in [70]. It can however be reconstructed from the δR_τ^{kl} and their results on the non-strange spectral moments taken from [41]. It was found to be $|V_{\mathrm{ud}}| = 0.9759$. These matrix elements differ by roughly 4σ from the unconstrained values in the case of $|V_{\mathrm{ud}}|$ and 1σ in the case of $|V_{\mathrm{us}}|$. The sensitivity of m_{s} on a shift of that size in $|V_{\mathrm{ud}}|$ however produces negligible variation. The observed shift is of the order of $1\,\mathrm{MeV}$ in m_{s}.

2) The Branching Fractions:
The total strange branching fraction used in this analysis was $B_{\mathrm{s}} = (2.993 \pm 0.90)\%$. This differs from the total strange branching fraction used in [70] ($B_{\mathrm{s}}^{\mathrm{ALEPH}} = (2.900 \pm 0.102)\%$) by about one standard deviation. The largest difference was observed for the decay channel $\tau^- \to \mathrm{K}^-\pi^+\pi^-\nu_\tau$. The branching fraction for this final state was measured in this analysis using OPAL data:

$$B(\tau^- \to \mathrm{K}^-\pi^+\pi^-\nu_\tau) = (0.415 \pm 0.059_{\mathrm{stat}} \pm 0.031_{\mathrm{sys}})\%. \tag{7.37}$$

This value was found to be consistent with previous OPAL publications [64] and the recent result from the CLEO collaboration [65]. For the determination of the spectral function and the calculation of the spectral moments, the improved average as calculated in Section 7.1.2 was used. It differs from the value used in CHEN01B ($B(\tau^- \to \mathrm{K}^-\pi^0\nu_\tau) = (0.276 \pm 0.048)\%$) by two standard deviations. For the strange spectral moments, this difference results in a shift of 0.0017 for R_τ^{00}. This translates into a shift in the mass of the strange quark of $\sim +5\,\mathrm{MeV}$ at $\mu^2 = 4\,\mathrm{GeV}^2$.

3) Update of Non-Strange Spectral Moments $R_{\tau,\,\mathrm{non-s}}$:
For the calculation of the weighted difference of strange and non-strange spectral moments δR_τ^{kl}, the results from [40] were updated using recent branching fractions. The value for R_τ was found to be

$$R_{\tau,\,\mathrm{non}-s} = 3.469 \pm 0.014. \tag{7.38}$$

This differs from the previously published value $R_{\tau,\,\mathrm{non}-s} = 3.484 \pm 0.025$ by 1.1σ. This is mainly due to the axial-vector part. The branching ratio for the decay channel $\tau^- \to \pi^-\pi^0\pi^0\nu_\tau$, which contributes to $R_{\tau,\,A}$ changed by more than one standard deviation from $B = 9.27\%$ to $B = 9.13\%$.

The value for R_τ used in CHEN01B is $R_\tau = 3.492 \pm 0.014$. Taking the moments $kl = \{00\}$ and $kl = \{10\}$ (since these were the only $l = 0$-moments previously published) one observes a shift in the strange quark mass of $\sim +5\,\mathrm{MeV}$ at $\mu^2 = 4\,\mathrm{GeV}^2$.

Implications on ε'/ε:
The mass of the strange quark is an important parameter which enters, among other quantities like the elements of the weak mixing matrix or the strong coupling constant, in the calculation of the ratio ε'/ε. This ratio parametrizes the size of the direct CP violation in $\mathrm{K}_{\mathrm{L}}^0 \to \pi^+\pi^-$ decays with respect to the CP violation in mixing or so-called indirect CP violation. Deviations of the experimental results from the theoretical calculations can be a sign of new physics beyond the Standard Model. As an example, in supersymmetric models, charginos or charged Higgs bosons contributing in loop diagrams change the value for ε'/ε. The current world average is based on the recent experimental results from NA48 [90], KTeV [91], NA31 [92] and E731 [93] which yields:

$$\frac{\varepsilon'}{\varepsilon} = (16.6 \pm 1.6) \cdot 10^{-4}. \tag{7.39}$$

Assuming that ε'/ε is fully dominated by Standard Model contributions, this experimental results can be reproduced in next-to-leading-order calculations assuming that the mass of the strange quark lies in the region $m_{\mathrm{s}}(m_{\mathrm{c}}^2) \leqslant 100\,\mathrm{MeV}$ or equivalently $m_{\mathrm{s}}(4\,\mathrm{GeV}^2) \leqslant 85\,\mathrm{MeV}$ [94]. The results obtained in this analysis from hadronic τ decays complies with this limit.

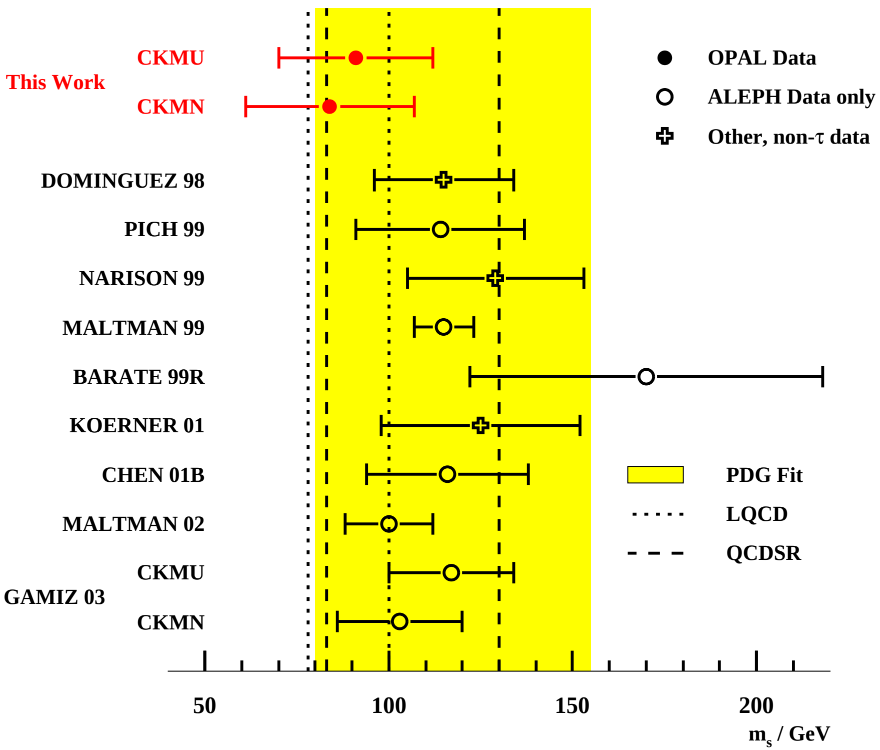

	$m_s(4\,\mathrm{GeV}^2)/\,\mathrm{MeV}$	Remarks
GAMIZ 03 [68]	117 ± 17	Determination of m_s from SU(3)$_{\mathrm{Flavor}}$ breaking effects in τ hadronic width. A fit to δR_τ^{kl} for $kl = \{00, 10, 20, 30, 40\}$ has been performed with and without imposing unitarity constraints on the CKM matrix elements.
MALTMAN 02 [69]	100 ± 17	Extract m_s from finite energy sum rules of the flavor breaking difference of light-strange quark vector plus axial-vector correlators, using spectral functions determined from hadronic τ decays.
CHEN 01B [70]	116 ± 22	Determines m_s using spectral moments of the strange spectral function in hadronic τ decays.
KOERNER 01 [71]	125 ± 27	Determines m_s from $kl = \{00\}$ spectral moment of the τ spectral function employing contour improved resummation.
BARATE 99R [72]	170 ± 48	A combination of strange and non-strange spectral functions is used to determine m_s and non-perturbative contributions to the strange hadronic width.
MALTMAN 99 [73]	115 ± 8	The strange quark mass is determined from a study of the correlator using finite energy sum rules.
NARISON 99 [74]	129 ± 24	Extracting the strange quark mass from decay sum rules for the Φ meson and hadronic τ decays.
PICH 99 [75]	114 ± 23	Determination of m_s from SU(3)$_{\mathrm{Flavor}}$ breaking effects in τ hadronic width. A fit to δR_τ^{kl} for $kl = \{00, 10, 20\}$ has been performed.
DOMINGUEZ 98 [76]	115 ± 19	Using data from radial excitations of the kaon and the spectral function reconstructed using threshold normalization from chiral symmetry, the mass of the strange quark is determined.

Fig. 7.7: Comparison of m_s measurements at $\mu^2 = 4\,\mathrm{GeV}^2$. The full dots represent the values from this work. The result labeled 'CKM Unitarity' is obtained employing an unitarity constraint on the elements of the weak mixing matrix. The open dots represent the results based on the analysis of the spectral function in hadronic τ decays from the ALEPH collaboration. These results are therefore correlated. The dashed and dotted lines denote the preferred region for the strange quark mass from lattice QCD calculations and QCD sum rules, respectively. The shaded band represents the preferred region for the strange quark mass from the PDG evaluation.

8. CONCLUSION

The measurement of the spectral function in τ lepton decays into vector or axial vector final states with open strangeness, using data taken with the OPAL detector during the years 1991 to 1995 operating on the Z^0 resonance, has been presented. A total of $121\,\mathrm{pb}^{-1}$ of data have been analyzed. The analysis of the strangeness spectral function requires a detailed understanding of the energy loss measurement $\mathrm{d}E/\mathrm{d}x$ in the OPAL central drift chamber, the efficient identification of neutral kaons and the reconstruction of neutral pions from measured shower profiles in the electromagnetic calorimeter.

- In this work, the energy loss measurement in the OPAL central drift chamber has been studied for τ lepton decays to optimize the separation of charged kaons and pions in this particular environment. A drift time dependent correction on a hit-by-hit basis has been developed using data events only. In addition, cross-talk corrections and corrections due to inhomogeneities of the drift field have been optimized for τ lepton decays.
- Neutral Pions in τ lepton decays are reconstructed comparing measured shower shapes in the electromagnetic calorimeter. The selection procedure for photon candidates has been optimized for strange τ lepton decays to account for the different background fraction and energy distribution compared to the non-strange case. In addition, the JADE jet-pairing algorithm with the P0 option has been used to combine neutral objects to photon candidates. This has led to an improvement in the energy and momentum resolution.
- An efficient identification procedure for neutral kaons has been developed. A simultaneous 2-C kinematic fit to the invariant K^0_S mass and the secondary vertex has been implemented. This has lead to an improvement in the resolution of the invariant mass spectrum for final states including neutral kaons.

The invariant mass spectra of 93.4% of the τ decay channels $\tau^- \to (\mathrm{K}\pi)^-\nu_\tau$, $(\mathrm{K}\pi\pi)^-\nu_\tau$ and $(\mathrm{K}\pi\pi\pi)^-\nu_\tau$ have been reconstructed in the analysis. For the remaining 6.6% and for the final states including η mesons, Monte Carlo simulations have been used. To obtain a better description of the signal channels and the prediction from background channels, the standard Monte Carlo has been extended to include the four-meson final states with kaons. Since the resonance structure for those final states is unknown, phase space distributions have been used here.

For the decay channels $\tau^- \to \mathrm{K}^-\pi^0\nu_\tau$ and $\tau^- \to \mathrm{K}^-\pi^+\pi^-\nu_\tau$, from the selected number of events, competitive branching fractions are obtained in a simultaneous χ^2-fit. The following results were obtained

$$\begin{aligned} B(\tau^- \to \mathrm{K}^-\pi^0\nu_\tau) &= (0.471 \pm 0.064_{\mathrm{stat}} \pm 0.021_{\mathrm{sys}})\% \\ B(\tau^- \to \mathrm{K}^-\pi^+\pi^-\nu_\tau) &= (0.415 \pm 0.059_{\mathrm{stat}} \pm 0.031_{\mathrm{sys}})\%, \end{aligned}$$

where experimental and systematic uncertainties are given separately.

The measured invariant mass spectra have been corrected for resolution effects, using the matrix unfolding procedure. The dependence of the corrected spectra on the assumed resonance structure in the simulated spectra has been studied. Monte Carlo samples for the signal channels containing either a flat mass distributions or a distributions according to phase space have been generated. The results obtained were compared to those using the standard Monte Carlo.

From the measured invariant mass spectra, corrected for efficiency and resolution effects, the spectral function of strange τ lepton decays is obtained by adding the individual spectra, weighted with their respective branching fractions and unfolding them from the phase space factors.

The spectral moments $R^{kl}_{\tau,S}$ for $kl = \{10,\ 11,\ 12,\ 13,\ 20,\ 21,\ 30,\ 40\}$ as well as the ratio of strange and non-strange moments, updated from [40], and the weighted differences δR^{kl}_{τ} which are useful quantities for further theoretical analyses of the data are calculated from the strange spectral function. The following results were obtained

kl	$R^{kl}_{\tau,S}$	δR^{kl}_{τ}	$R^{kl}_{\tau,S}/R^{kl}_{\tau,non-S}$
00	0.1677 ± 0.0050	0.184 ± 0.128	0.0484 ± 0.0015
10	0.1161 ± 0.0038	0.224 ± 0.095	0.0466 ± 0.0015
11	0.0298 ± 0.0012	-0.039 ± 0.028	0.0543 ± 0.0022
12	0.0107 ± 0.0006	-0.008 ± 0.014	0.0527 ± 0.0030
13	0.0048 ± 0.0004	-0.002 ± 0.009	0.0518 ± 0.0045
20	0.0862 ± 0.0028	0.264 ± 0.070	0.0444 ± 0.0015
21	0.0191 ± 0.0007	-0.031 ± 0.017	0.0552 ± 0.0021
30	0.0671 ± 0.0022	0.294 ± 0.055	0.0420 ± 0.0014
40	0.0539 ± 0.0018	0.319 ± 0.045	0.0400 ± 0.0013

These results have been published by the OPAL collaboration [95].
Using the weighted differences δR^{kl}_{τ} for the moments $kl = \{10,\ 20,\ 30,\ 40\}$, a value for the strange quark mass at the scale $\mu^2 = m^2_{\tau}$ is obtained

$$\begin{aligned} m_{\rm s}(m^2_{\tau}) &= (84 \pm 14_{\rm exp} \pm 6_{V_{\rm us}} \pm 17_{\rm theo})\,{\rm MeV} \\ &= (84^{+20}_{-26})\,{\rm MeV}. \end{aligned}$$

The error on the strange quark mass is dominated by the theoretical uncertainty. Evolving this result to customary scales, using the renormalization group equation at the 4-loop level, yields

$$\begin{aligned} m_{\rm s}(1\,{\rm GeV}^2) &= (111^{+26}_{-35})\,{\rm MeV} \\ m_{\rm s}(4\,{\rm GeV}^2) &= (82^{+19}_{-25})\,{\rm MeV}. \end{aligned}$$

where the experimental and theoretical uncertainties have been added in quadrature.

9. APPENDIX

9.1 Branching Fractions used in Monte Carlo Simulation

The τ decay modes realized in the updated Monte Carlo sample is summarized. The PDG code of the τ decay is given together with the possible decay modes and the corresponding branching fractions. In the last column, detail can be found either on the branching fraction or on its implementation in the τ Monte Carlo.

PDG Code	**τ Decay**	**Final States**		**B/%**	**Remarks**
${}^{a}\Gamma_5$	$\tau \to e\bar{\nu}_e\nu_\tau$		e	17.83 ± 0.06	
${}^{a}\Gamma_3$	$\tau \to \mu\bar{\nu}_\mu\nu_\tau$		μ	17.37 ± 0.07	
${}^{a}\Gamma_{10}$	$\tau \to \pi\nu_\tau$		π	11.09 ± 0.12	
${}^{a}\Gamma_{14}$	$\tau \to \rho\nu_\tau$		$\pi\pi^0$	25.40 ± 0.14	ex. $\mathrm{B}(\text{non-}\rho)=(3 \pm 3.2) \cdot 10^{-3}$
	$\tau \to a_1\nu_\tau$				
$\Gamma_{61} =^{a} \Gamma_{63} + 0.0221^{a}\Gamma_{144}$			$\pi\pi\pi$	9.18 ± 0.11	TAUOLA a_1 only
					ex. K^0
${}^{a}\Gamma_{20}$			$\pi\pi^0\pi^0$	9.13 ± 0.14	ex. K^0
${}^{a}\Gamma_{11}$	$\tau \to \mathrm{K}\nu_\tau$		K	0.699 ± 0.027	
Γ_{110}	$\tau \to \mathrm{K}^*(892)\nu_\tau$			1.29 ± 0.05	
${}^{a}\Gamma_{16}$			$\mathrm{K}\pi^0$	0.454 ± 0.033	
${}^{a}\Gamma_{35}$		$\mathrm{K}^0\pi$		0.90 ± 0.04	
			$\pi\pi\pi$		$\frac{2}{3}B(\tau \to \mathrm{K}^*(892)\nu_\tau)$
			$\pi\pi^0\pi^0$		$\frac{1}{3}B(\tau \to \mathrm{K}^*(892)\nu_\tau)$
$\Gamma_{70} =^{a} \Gamma_{71} + 0.888^{a}\Gamma_{144} + 0.021^{a}\Gamma_{145}$	$\tau \to 3\pi\pi^0\nu_\tau$		$\pi\pi\pi\pi^0$	4.20 ± 0.08	TAUOLA (70%ω + 30% ph.-sp.) ex. K^0, incl. ω
${}^{a}\Gamma_{26}$	$\tau \to \pi 3\pi^0\nu_\tau$		$\pi\pi^0\pi^0\pi^0$	1.08 ± 0.10	ex. K^0
${}^{a}\Gamma_{103}$	$\tau \to 5\pi\nu_\tau$		$\pi\pi\pi\pi\pi$	0.078 ± 0.006	5h ex. K^0
${}^{a}\Gamma_{104}$	$\tau \to 5\pi\pi^0\nu_\tau$		$\pi\pi\pi\pi\pi\pi^0$	0.022 ± 0.005	5hπ^0 ex. K^0
${}^{a}\Gamma_{95}$	$\tau \to \mathrm{KK}\pi\nu_\tau$		$\mathrm{KK}\pi$	0.161 ± 0.018	
${}^{a}\Gamma_{46}$	$\tau \to \mathrm{K}^0\overline{\mathrm{K}}^0\pi\nu_\tau$	$\mathrm{K}^0\overline{\mathrm{K}}^0\pi$		0.119 ± 0.020	
			$\pi^0\pi^0\pi^0\pi^0\pi$		$\frac{1}{3} \cdot \frac{1}{3}\mathrm{B}(\tau \to \mathrm{K}^0\overline{\mathrm{K}}^0\pi)$
			$\pi\pi\pi^0\pi^0\pi$		$\frac{1}{3} \cdot \frac{2}{3} \cdot 2\mathrm{B}(\tau \to \mathrm{K}^0\overline{\mathrm{K}}^0\pi)$
			$\pi\pi\pi\pi\pi$		$\frac{2}{3} \cdot \frac{2}{3}\mathrm{B}(\tau \to \mathrm{K}^0\overline{\mathrm{K}}^0\pi)$
${}^{a}\Gamma_{42}$	$\tau \to \mathrm{KK}^0\pi^0\nu_\tau$	$\mathrm{KK}^0\pi^0$		0.157 ± 0.021	
			$\mathrm{K}\pi^0\pi^0\pi^0$		$\frac{1}{3}B(\tau \to \mathrm{KK}^0\pi^0\nu_\tau)$
			$\mathrm{K}\pi\pi\pi^0$		$\frac{2}{3}B(\tau \to \mathrm{KK}^0\pi^0\nu_\tau)$
${}^{a}\Gamma_{23}$	$\tau \to \mathrm{K}2\pi^0\nu_\tau$		$\mathrm{K}\pi^0\pi^0$	0.060 ± 0.024	ex. K^0
${}^{a}\Gamma_{88}$	$\tau \to \mathrm{K}\pi\pi\nu_\tau$		$\mathrm{K}\pi\pi$	0.27 ± 0.05	ex. K^0
${}^{a}\Gamma_{40}$	$\tau \to \pi\mathrm{K}^0\pi^0\nu_\tau$	$\pi\mathrm{K}^0\pi^0$		0.38 ± 0.04	
			$\pi\pi^0\pi^0\pi^0$		$\frac{1}{3}B(\tau \to \pi\mathrm{K}^0\pi^0\nu_\tau)$
			$\pi\pi\pi\pi^0$		$\frac{2}{3}B(\tau \to \pi\mathrm{K}^0\pi^0\nu_\tau)$
${}^{a}\Gamma_{73} + 0.888^{a}\Gamma_{145}$	$\tau \to 3\pi 2\pi^0\nu_\tau$		$\pi\pi\pi\pi^0\pi^0$	0.49 ± 0.05	TAUOLA ω only
					3h2π^0, ex. K^0, η

PDG Code	**τ Decay**	**Final States**	**B/%**	**Remarks**
$^a\Gamma_{124}$	$\tau \to \eta\pi\pi^0\nu_\tau$	$\eta\pi\pi^0$	0.174 ± 0.024	
		$\pi\pi\pi\pi^0\pi^0$		$0.230 \cdot B(\tau \to \eta\pi\pi^0\nu_\tau)$
		$\pi\pi^0 2\gamma$		$0.3933 \cdot B(\tau \to \eta\pi\pi^0\nu_\tau)$
		$\pi\pi^0\pi^0\pi^0\pi^0$		$0.3224 \cdot B(\tau \to \eta\pi\pi^0\nu_\tau)$
		$\pi\pi^0\pi\pi\gamma$		$0.0475 \cdot B(\tau \to \eta\pi\pi^0\nu_\tau)$
Γ_{81}	$\tau \to 3\pi 3\pi^0\nu_\tau$	$\pi\pi\pi\pi^0\pi^0\pi^0$	0.029 ± 0.008	3h3π^0
$^a\Gamma_{144} \cdot 0.085$	$\tau \to \pi\pi^0\gamma\nu_\tau$	$\pi\pi^0\gamma$	0.164 ± 0.011	$\tau \to \omega\pi\nu_\tau \overset{0.085}{\to} \pi\pi^0\gamma\nu_\tau$
				hω
$^a\Gamma_{37}$	$\tau \to \mathrm{KK}^0\nu_\tau$	KK^0	0.155 ± 0.017	
		$\mathrm{K}\pi^0\pi^0$		$\frac{1}{3}B(\tau \to \mathrm{KK}^0\nu_\tau)$
		$\mathrm{K}\pi\pi$		$\frac{2}{3}B(\tau \to \mathrm{KK}^0\nu_\tau)$
$^a\Gamma_{92}$	$\tau \to \mathrm{K}\pi\pi\pi^0\nu_\tau$	$\mathrm{K}\pi\pi\pi^0$	0.060 ± 0.024	ex. K^0, η
Γ_{44}	$\tau \to \mathrm{K}^0\pi\pi^0\pi^0\nu_\tau$		0.026 ± 0.024	
		$\pi^0\pi^0\pi\pi^0\pi^0$		$\frac{1}{3}B(\tau \to \mathrm{K}^0\pi\pi^0\pi^0\nu_\tau)$
		$\pi\pi\pi\pi^0\pi^0$		$\frac{2}{3}B(\tau \to \mathrm{K}^0\pi\pi^0\pi^0\nu_\tau)$
$^a\Gamma_{27}$	$\tau \to \mathrm{K}\pi^0\pi^0\pi^0\nu_\tau$	$\mathrm{K}\pi^0\pi^0\pi^0$	0.039 ± 0.022	ex. K^0, η
Γ_{53}	$\tau \to \mathrm{K}^0\pi\pi\pi\nu_\tau$		0.023 ± 0.020	$\mathrm{K}^0$3h
		$\pi^0\pi^0\pi\pi\pi$		$\frac{1}{3}B(\tau \to \mathrm{K}^0\pi\pi\pi\nu_\tau)$
		$\pi\pi\pi\pi\pi$		$\frac{2}{3}B(\tau \to \mathrm{K}^0\pi\pi\pi\nu_\tau)$
$^a\Gamma_{96}$	$\tau \to \mathrm{KK}\pi\pi^0\nu_\tau$	$\mathrm{KK}\pi\pi^0$	0.040 ± 0.016	
Γ_{49}	$\tau \to \mathrm{K}^0\overline{\mathrm{K}}^0\pi\pi^0\nu_\tau$		0.031 ± 0.023	
		$\pi^0\pi^0\pi^0\pi^0\pi\pi^0$		$\frac{1}{3} \cdot \frac{1}{3}\mathrm{B}(\mathrm{K}^0\overline{\mathrm{K}}^0\pi\pi^0\nu_\tau)$
		$\pi\pi\pi^0\pi^0\pi\pi^0$		$\frac{1}{3} \cdot \frac{2}{3} \cdot 2\mathrm{B}(\mathrm{K}^0\overline{\mathrm{K}}^0\pi\pi^0\nu_\tau)$
		$\pi\pi\pi\pi\pi\pi^0$		$\frac{2}{3} \cdot \frac{2}{3}\mathrm{B}(\mathrm{K}^0\overline{\mathrm{K}}^0\pi\pi^0\nu_\tau)$
?	$\tau \to \mathrm{KK}^0\pi\pi\nu_\tau$		? ± ?	
Γ_{45}	$\tau \to \mathrm{KK}^0\pi^0\pi^0\nu_\tau$		¡0.016	
$^a\Gamma_{126}$	$\tau \to \mathrm{K}\eta\nu_\tau$		0.027 ± 0.006	
		$\mathrm{K}\pi\pi\pi^0$		$0.230 \cdot B(\tau \to \mathrm{K}\eta\nu_\tau)$
		$\mathrm{K}2\gamma$		$0.3933 \cdot B(\tau \to \mathrm{K}\eta\nu_\tau)$
		$\mathrm{K}\pi^0\pi^0\pi^0$		$0.3224 \cdot B(\tau \to \mathrm{K}\eta\nu_\tau)$
		$\mathrm{K}\pi\pi\gamma$		$0.0475 \cdot B(\tau \to \mathrm{K}\eta\nu_\tau)$
Γ_{128}	$\tau \to \mathrm{K}\eta\pi^0\nu_\tau$		0.018 ± 0.009	
		$\mathrm{K}\pi\pi\pi^0\pi^0$		$0.230 \cdot B(\tau \to \mathrm{K}\eta\pi^0\nu_\tau)$
		$\mathrm{K}\pi^0 2\gamma$		$0.3933 \cdot B(\tau \to \mathrm{K}\eta\pi^0\nu_\tau)$
		$\mathrm{K}\pi^0\pi^0\pi^0\pi^0$		$0.3224 \cdot B(\tau \to \mathrm{K}\eta\pi^0\nu_\tau)$
		$\mathrm{K}\pi^0\pi\pi\gamma$		$0.0475 \cdot B(\tau \to \mathrm{K}\eta\pi^0\nu_\tau)$

9.2 Update of the Non-Strange Spectral Moments

The non-strange spectral moments $k \in \{00, 10, 11, 12, 13\}$ for vector and axial vector final states have been reevaluated using updated branching fractions. In addition the moments $kl \in \{20, 21, 30, 40\}$ have been calculated which are used in the determination of the strange quark mass. The updated moments are given in the table below. In addition, the correlations between the moments are given in percent. They are not negligible, since the moments are calculated from identical spectra.

		Correlation/%								
kl	$R_{\tau, V}$	00	10	11	12	13	20	21	30	40
00	1.767 ± 0.013	100								
10	1.271 ± 0.011	65	100							
11	0.299 ± 0.004	69	74	100						
12	0.094 ± 0.002	67	35	82	100					
13	0.040 ± 0.001	57	2	49	89	100				
20	0.972 ± 0.009	53	95	52	9	-17	100			
21	0.205 ± 0.002	54	87	89	48	5	72	100		
30	0.767 ± 0.007	47	87	33	-4	-23	97	55	100	
40	0.616 ± 0.006	41	77	18	-12	-23	91	38	98	100

		Correlation/%								
kl	$R_{\tau, A}$	00	10	11	12	13	20	21	30	40
00	1.702 ± 0.012	100								
10	1.222 ± 0.008	68	100							
11	0.250 ± 0.003	87	65	100						
12	0.109 ± 0.002	75	19	85	100					
13	0.052 ± 0.001	63	-5	64	94	100				
20	0.972 ± 0.006	43	93	34	-15	-36	100			
21	0.141 ± 0.002	71	93	82	39	9	76	100		
30	0.830 ± 0.005	29	84	14	-32	-48	98	60	100	
40	0.746 ± 0.004	21	76	2	-41	-52	93	48	99	100

Due to the correlation of the branching fractions and due to the unfolding procedure, vector and axialvector moments are not independent. The cross-correlations are given in the table below. The correlations are up to 40% for $kl = 00$. They become negligible for higher moments.

V/A	Correlation/%								
kl	00	10	11	12	13	20	21	30	40
00	-40	-19	-34	-35	-34	-8	-21	-3	0
10	-15	-6	-15	-15	-14	0	-9	3	5
11	-32	-20	-30	-30	-28	-10	-20	-5	-3
12	-43	-25	-39	-39	-36	-15	-25	-10	-8
13	-41	-23	-36	-37	-35	-15	-24	-10	-9
20	-5	-4	-6	-6	-6	4	-4	6	8
21	-16	-11	-16	-16	-14	-5	-11	0	2
30	-1	-1	-2	-2	-2	0	-1	7	9
40	1	1	0	0	-1	1	1	1	9

9.3 Kinematic Fit

To improve the invariant mass resolution in τ final states containing neutral kaons, a kinematic fit is applied. It constrains the two tracks to a common secondary vertex and the invariant two-track mass under pion hypothesis has to correspond to the nominal K^0_S mass. First the general formalism of kinematic fitting is briefly explained. This formalism is then adapted to the constraints described above.

General Formalism

The kinematic fitting technique is based on the Lagrangian multiplier method. It is assumed that the constraint equations can be linearized and summarized into matrices. The function describing the constraints can be written as

$$\mathbf{H}(\boldsymbol{\alpha}) = 0, \tag{9.1}$$

where $\mathbf{H} = \{H_1, ..., H_n\}$ are the n constraint equations and $\boldsymbol{\alpha} = \{\alpha_1, ..., \alpha_m\}$ is the set of m parameters in the fit. Expanding 9.1 around a convenient point $\boldsymbol{\alpha_A}$ using a Taylor expansion, yields the linearized equations

$$\begin{aligned} 0 &= \left(\frac{\partial \mathbf{H}(\boldsymbol{\alpha}_A)}{\partial \boldsymbol{\alpha}}\right)(\boldsymbol{\alpha} - \boldsymbol{\alpha}_A) + \mathbf{H}(\boldsymbol{\alpha}_A) && (9.2)\\ &\equiv \mathbf{D}\delta\boldsymbol{\alpha} + \mathbf{d}, && (9.3)\end{aligned}$$

where $\delta\boldsymbol{\alpha} = \boldsymbol{\alpha} - \boldsymbol{\alpha}_A$ and

$$\mathbf{D} = (\mathbf{D})_{ij} = \frac{\partial H_i}{\partial \alpha_j} \qquad \mathbf{d} = (\mathbf{d})_i = H_i(\boldsymbol{\alpha}). \tag{9.4}$$

The constraints are implemented using Lagrangian multipliers $\boldsymbol{\lambda}$. The expression for χ^2 consists of two terms. One from the parameters and their covariance matrix and one from the constraint equations. The expression then reads:

$$\chi^2 = (\boldsymbol{\alpha} - \boldsymbol{\alpha}_0)^T \mathbf{V}^{-1}_{\boldsymbol{\alpha}_0}(\boldsymbol{\alpha} - \boldsymbol{\alpha}_0) + 2\boldsymbol{\lambda}^T(\mathbf{D}\delta\boldsymbol{\alpha} + \mathbf{d}). \tag{9.5}$$

The vector $\boldsymbol{\alpha}_0$ contains the initial, unconstrained parameters and $\mathbf{V}_{\boldsymbol{\alpha}_0}$ represents their covariance matrix. Equation 9.5 is now minimized with respect to $\boldsymbol{\alpha}$ and $\boldsymbol{\lambda}$ which yields the two equations

$$\mathbf{V}^{-1}_{\boldsymbol{\alpha}_0}(\boldsymbol{\alpha} - \boldsymbol{\alpha}_0) + \mathbf{D}^T\boldsymbol{\lambda} = 0 \tag{9.6a}$$

$$\mathbf{D}\delta\boldsymbol{\alpha} + \mathbf{d} = 0. \tag{9.6b}$$

The solution for the new parameter vector $\boldsymbol{\alpha}$ and the Lagrangian multipliers is then

$$\boldsymbol{\alpha} = \boldsymbol{\alpha}_0 - \mathbf{V}_{\boldsymbol{\alpha}_0}\mathbf{D}^T\boldsymbol{\lambda} \tag{9.7a}$$

$$\boldsymbol{\lambda} = (\mathbf{D}\mathbf{V}_{\boldsymbol{\alpha}_0}\mathbf{D}^T)^{-1}(\mathbf{D}\delta\boldsymbol{\alpha}_0 + \mathbf{d}). \tag{9.7b}$$

The covariance matrix for the new parameter set is the calculated via

$$\mathbf{V}_{\boldsymbol{\alpha}} = \mathbf{V}_{\boldsymbol{\alpha}_0} - \mathbf{V}_{\boldsymbol{\alpha}_0}\mathbf{D}^T(\mathbf{D}\mathbf{V}_{\boldsymbol{\alpha}_0}\mathbf{D}^T)^{-1}\mathbf{D}\mathbf{V}_{\boldsymbol{\alpha}_0}. \tag{9.8}$$

The χ^2 for the individual iteration steps is then calculated from the Lagrangian multipliers via

$$\chi^2 = \boldsymbol{\lambda}^T(\mathbf{D}\delta\boldsymbol{\alpha} + \mathbf{d}). \tag{9.9}$$

Invariant Mass and 3D Vertex Constraint

In this work, a combined constrained fit to the invariant two track mass and the unknown position of the secondary vertex is performed. The formalism explained above can be easily adapted to this problem.

- The constrained equation of the two track invariant mass to the nominal mass of the K^0_S reads

$$\sum_i (E_i)^2 - \sum_i (p'_{xi})^2 - \sum_i (p'_{yi})^2 - \sum_i (p'_{zi})^2 - m^2_{\mathrm{K}^0} = 0, \tag{9.10}$$

  where the prime denotes the momentum of the track calculated with respect to the production point

$$p'_{x_i} = p_{x_i} - a_i \Delta y_i \qquad \Delta y_i = y_c - y_i \tag{9.11a}$$

$$p'_{y_i} = p_{y_i} - a_i \Delta x_i \qquad \Delta x_i = x_c - x_i. \tag{9.11b}$$

- For the constraint to a common secondary vertex, for each of the two tracks there are two equations, corresponding to the constraint in the bend and non-bend planes respectively. In the solenoidal magnetic field of the OPAL jet chamber, the following equations are obtained

$$0 = p_{x_i}\Delta y_i - \frac{a_i}{2}(\Delta x_i^2 + \Delta y_i^2) \tag{9.12a}$$

$$0 = \Delta z_i - \frac{p_{z_i}}{a_i}\sin^{-1}\Big(a_i\frac{(p_{x_i}\Delta x_i + p_{y_i}\Delta y_i)}{p_{\mathrm{T}i}^2}\Big), \tag{9.12b}$$

  where $\Delta x_i = (x_x - x)$ is the distance to the secondary vertex position. The quantities Δy_i and Δz_i are defined accordingly. The parameter a is defined as $a_i = c\cdot 10^{-6}BQ_i$, where c is the speed of light, B the strength of the magnetic field and Q_i the charge of the particle under consideration.

The problem then is the following. The parameter vector $\boldsymbol{\alpha}$ contains the five track parameters $\mathbf{t}_i$ of each of the two tracks and the position $\mathbf{v}$ of the secondary vertex to be determined.

$$\begin{aligned}\boldsymbol{\alpha} &= (\mathbf{t}_1,\, \mathbf{t}_2,\, \mathbf{v}) \\ &= (\kappa_1,\, \phi_1,\, \mathrm{d}_{0,1},\, \tan\lambda_1,\, z_{0,1},\, \kappa_2,\, \phi_2,\, \mathrm{d}_{0,2},\, \tan\lambda_2,\, z_{0,2},\, x_{\mathrm{vtx}},\, y_{\mathrm{vtx}},\, z_{\mathrm{vtx}}).\end{aligned} \tag{9.13}$$

For each individual track, the covariance matrix consist of a 3-by-3 submatrix and a 2-by-2 submatrix. This is due to the procedure of the track fit in the OPAL jet chamber. It is performed separately for the $r-\phi$ plane and the $x-z$ plane. Therefore, $(\kappa,\, \phi,\, \mathrm{d}_0)$ are correlated and $(\tan\lambda,\, z_0)$ are correlated.
There is no correlation among the track parameters for different tracks. The covariance matrix for the unconstrained parameters therefore reads

$$\mathbf{V}_{\boldsymbol{\alpha}_0} = \begin{pmatrix} \mathbf{V}_{\mathbf{t}_1} & 0 & 0 \\ 0 & \mathbf{V}_{\mathbf{t}_2} & 0 \\ 0 & 0 & \mathbf{V}_{\mathrm{vtx}} \end{pmatrix}. \tag{9.14}$$

The matrix $\mathbf{D}$ which contains the derivatives of the constraint equations with respect to the track parameters is a 5×15 matrix and it reads

$$\mathbf{D} = \begin{pmatrix} \mathbf{D}_{\mathrm{t}_1} & \mathbf{0} & \mathbf{E}_1 \\ \mathbf{0} & \mathbf{D}_{\mathrm{t}_2} & \mathbf{E}_2 \\ \mathbf{D}_{\mathrm{mass1}} & \mathbf{D}_{\mathrm{mass2}} & \mathbf{E}_{\mathrm{mass}} \end{pmatrix}, \tag{9.15}$$

where the components $\mathbf{D}_{\mathrm{t}_{1/2}}$ is the derivatives of the vertex constraint equations with respect to the track parameters, $\mathbf{E}_{1/2}$ is the derivative with respect to the vertex position, $\mathbf{D}_{\mathrm{mass1/2}}$ is the derivative of the mass constraint equation 9.10 with respect to the track parameters and $\mathbf{E}_{\mathrm{mass}}$ is the derivative of the mass constraint equation with respect to the vertex position. The explicit expression for these matrices are

$$\begin{aligned}
\mathbf{D}_i &= \begin{pmatrix} \Delta y_i & -\Delta x_i & 0p_{y_i} + a + i\Delta x_i & -p_{x_i} + a_i\Delta y_i & 0 & \\ -p_{z_i}p_{\mathrm{T}_i}S_iR_{x_i} + U_i\frac{p_{x_i}}{p_{\mathrm{T}_i}} & -p_{z_i}p_{ti}S_iR_{yi} + U_i\frac{p_{yi}}{p_{ti}} & -\frac{1}{a_i}(p_{\mathrm{T}_i}\sin^{-1}B_i) & p_{x_i}p_{z_i}p_{\mathrm{T}_i}S_i & p_{y_i}p_{z_i}p_{\mathrm{T}_i}S_i & -p_{ti} \end{pmatrix} \\
\mathbf{E}_i &= \begin{pmatrix} -p_{y_i} - a_i\Delta x_i & p_{x_i} - a_i\Delta y_i & 0 \\ -p_{x_i}p_{z_i}p_{\mathrm{T}_i}S_i & -p_{y_i}p_{z_i}p_{\mathrm{T}_i}S_i & p_{\mathrm{T}i} \end{pmatrix} \\
\mathbf{d}_i &= \begin{pmatrix} A_{1i} - \frac{a_i}{2}(\Delta x_i^2 + \Delta y_i^2) \\ U_ip_{\mathrm{T}i} \end{pmatrix} \\
\mathbf{D}_{\mathrm{mass},i} &= \begin{pmatrix} -2p'_x + 2E\frac{p'_{x1}}{E_i} & -2p'_y + 2E\frac{p'_{y1}}{E_i} & -2p'_z + 2E\frac{p'_{z1}}{E_i} & 2a_i\Big(p'_y - E\frac{p'_{y_i}}{E_i}\Big) & 2a_i\Big(p'_x - E\frac{p'_{x_i}}{E_i}\Big) & 0 \end{pmatrix} \\
\mathbf{E}_{\mathrm{mass}} &= \begin{pmatrix} 2E\sum_i\frac{p'_{y_i}a_i}{E_i} - 2p'_y\sum_i a_i & 2E\sum_i\frac{p'_{x_i}a_i}{E_i} - 2p'_s\sum_i a_i & 0 \end{pmatrix}.
\end{aligned}$$

The following addition definitions are used

$$E = \sum_i E_i$$

$$p'_x = \sum_i p'_{x_i}$$

and

$$\begin{aligned}
A_{1i} &= p_{x_i}\Delta y_i - p_{y_i}\Delta x_i \\
A_{2i} &= p_{x_i}\Delta x_i - p_{y_i}\Delta y_i \\
B_i &= a_i \frac{A_{2i}}{p_{\mathrm{T}i}^2} \\
R_{x_i} &= \Delta x_i - 2p_{x_i}\frac{A_{2i}}{p_{\mathrm{T}i}^2} \\
R_{y_i} &= \Delta y_i - 2p_{y_i}\frac{A_{2i}}{p_{\mathrm{T}i}^2} \\
S_i &= \left(p_{\mathrm{T}i}^2\sqrt{1-B_i^2}\right)^{-1} \\
U_i &= \Delta z_i - \frac{p_{z_i}}{a_i}\sin^{-1} B_i
\end{aligned}$$

This fit is a constrained fit with two degrees of freedom. The number of degrees of freedom of a kinematic fit is calculated as

$$N_{\mathrm{D.o.F.}} = N_{\mathrm{meas}} - N_{\mathrm{fitted}} + N_{\mathrm{constr.}}, \tag{9.16}$$

where N_{meas} is number of measured parameters that are inputs to the fit. In this case, these are all together ten track parameters for the two tracks. N_{fitted} is the number of fitted parameters. Here, this number is 13, the ten track parameters and the 3D position of the vertex. $N_{\mathrm{const.}}$ is the number of constraints. It is five in this case. Two for each track from the vertex constraint plus the constraint to the invariant mass.

9.4 Updated Parametrizations of the Three Meson Final States

	A	$G_1 \quad (Q^2, s_2, s_3)$	$G_2 \quad (Q^2, s_1, s_3)$
$K^- \pi^- K^+$	$\frac{-\cos\theta_c}{2}$	$\mathrm{BW}_{a_1}(Q^2) T_\rho^{(2m)}(s_2)$	$\mathrm{BW}_{a_1}(Q^2) T_{K^\star}^{(2m)}(s_1)$
$K^0 \pi^- \overline{K^0}$	$\frac{-\cos\theta_c}{2}$	$\mathrm{BW}_{a_1}(Q^2) T_\rho^{(2m)}(s_2)$	$\mathrm{BW}_{a_1}(Q^2) T_{K^\star}^{(2m)}(s_1)$
$K_S \pi^- K_S$	$\frac{-\cos\theta_c}{4}$	$\mathrm{BW}_{a_1}(Q^2) T_{K^\star}^{(2m)}(s_3)$	$\mathrm{BW}_{a_1}(Q^2)\times$ $[T_{K^\star}^{(2m)}(s_1) + T_{K^\star}^{(2m)}(s_3)]$
$K_S \pi^- K_L$	$\frac{-\cos\theta_c}{4}$	$\mathrm{BW}_{a_1}(Q^2)\times$ $[2T_\rho^{(2m)}(s_2) + T_{K^\star}^{(2m)}(s_3)]$	$\mathrm{BW}_{a_1}(Q^2)\times$ $[T_{K^\star}^{(2m)}(s_1) - T_{K^\star}^{(2m)}(s_3)]$
$K^- \pi^0 K^0$	$\frac{3\cos\theta_c}{2\sqrt{2}}$	$\mathrm{BW}_{a_1}(Q^2)\times$ $\left[\frac{2}{3}T_\rho^{(2m)}(s_2) + \frac{1}{3}T_{K^\star}^{(2m)}(s_3)\right]$	$\frac{1}{3}\mathrm{BW}_{a_1}(Q^2)\times$ $\left[T_{K^\star}^{(2m)}(s_1) - T_{K^\star}^{(2m)}(s_3)\right]$
		$G_3 \quad (Q^2, s_1, s_2, s_3)$	
$K^- \pi^- K^+$	$-\cos\theta_c$	$T_\rho^{(3m)}(Q^2)(\sqrt{2}-1)\left[\sqrt{2}T_\omega(s_2) + T_{K^\star}^{(2m)}(s_1)\right]$	
$K^0 \pi^- \overline{K^0}$	$\cos\theta_c$	$T_\rho^{(3m)}(Q^2)(\sqrt{2}-1)\left[\sqrt{2}T_\omega(s_2) + T_{K^\star}^{(2m)}(s_1)\right]$	
$K_S \pi^- K_S$	$\frac{-\cos\theta_c}{2}$	$T_\rho^{(3m)}(Q^2)(\sqrt{2}-1)\left[T_{K^\star}^{(2m)}(s_1) - T_{K^\star}^{(2m)}(s_3)\right]$	
$K_S \pi^- K_L$	$\frac{\cos\theta_c}{2}$	$T_\rho^{(3m)}(Q^2)(\sqrt{2}-1)\left[2\sqrt{2}T_\omega(s_2) + T_{K^\star}^{(2m)}(s_1) + T_{K^\star}^{(2m)}(s_3)\right]$	
$K^- \pi^0 K^0$	$\frac{-\cos\theta_c}{\sqrt{2}}$	$T_\rho^{(3m)}(Q^2)(\sqrt{2}-1)\left[T_{K^\star}^{(2m)}(s_3) - T_{K^\star}^{(2m)}(s_1)\right]$	

	A	$G_1 \quad (Q^2, s_2, s_3)$	$G_2 \quad (Q^2, s_1, s_3)$
$\pi^0 \pi^0 K^-$	$\frac{\sin\theta_c}{4}$	$T_{K_1}^{(a)}(Q^2) T_{K^\star}^{(2m)}(s_2)$	$T_{K_1}^{(a)}(Q^2) T_{K^\star}^{(2m)}(s_1)$
$K^- \pi^- \pi^+$	$\frac{-\sin\theta_c}{2}$	$T_{K_1}^{(a)}(Q^2) T_{K^\star}^{(2m)}(s_2)$	$T_{K_1}^{(b)}(Q^2) T_\rho^{(1)}(s_1)$
$\pi^- \overline{K^0} \pi^0$	$\frac{3\sin\theta_c}{2\sqrt{2}}$	$\frac{2}{3}T_{K_1}^{(b)}(Q^2) T_\rho^{(2m)}(s_2)$ $+\frac{1}{3}T_{K_1}^{(a)}(Q^2) T_{K^\star}^{(2m)}(s_3)$	$\frac{1}{3}T_{K_1}^{(a)}(Q^2)\left[T_{K^\star}^{(2m)}(s_1) - T_{K^\star}^{(2m)}(s_3)\right]$
		$G_3 \quad (Q^2, s_1, s_2, s_3)$	
$\pi^0 \pi^0 K^-$	$\sin\theta_c$	$\frac{1}{4}T_{K^\star}^{(3m)}(Q^2)\left[T_{K^\star}^{(2m)}(s_1) - T_{K^\star}^{(2m)}(s_2)\right]$	
$K^- \pi^- \pi^+$	$\sin\theta_c$	$\frac{1}{2}T_{K^\star}^{(3m)}(Q^2)\left[T_\rho^{(2m)}(s_1) + T_{K^\star}^{(2m)}(s_2)\right]$	
$\pi^- \overline{K^0} \pi^0$	$\sqrt{2}\sin\theta_c$	$\frac{1}{4}T_{K^\star}^{(3m)}(Q^2)\left[2T_\rho^{(2m)}(s_2) + T_{K^\star}^{(2m)}(s_1) + T_{K^\star}^{(2m)}(s_3)\right]$	

Tab. 9.2: Updated parametrizations of the 3 meson final states. The upper table corresponds to the background channels involving kaons and the lower table corresponds to the strange final states.

LIST OF FIGURES

2.1 The optical theorem 17
2.2 Integration path 18
2.3 Feynman diagrams for the dimension-0 operators 19
2.4 Feynman diagrams for the dimension-4 operators 21
2.5 Feynman diagrams for the dimension-6 operators 21

3.1 The LEP storage ring 27
3.2 The OPAL detector 28
3.3 The tracking system of the OPAL detector 30

4.1 Energy loss as a function of the momentum for different particle species 34
4.2 Landau distribution for minimum ionizing pions 35
4.3 Illustration of the tail subtraction procedure 38
4.4 Distribution of the drift time differences in τ decays compared to $\mathrm{q\bar{q}}$ events 38
4.5 Comparison between old and new normpulse 39
4.6 Measured energy loss normalized to the expectation as a function of time difference 40
4.7 Systematic bias in $(\mathrm{d}E/\mathrm{d}x)_{\mathrm{meas}}/(\mathrm{d}E/\mathrm{d}x)_{\mathrm{exp}}$ 40
4.8 Illustration of the cross talk correction 42
4.9 The measured mean energy loss for tracks from $\mathrm{Z}^0 \to \mu^+\mu^-$ events 43
4.10 Anode plane corrections 43
4.11 Cathode plane corrections 44
4.12 Correlation to the standard correction 44
4.13 Expected residuals 46
4.14 Test of the fit procedure using tracks from Monte Carlo simulation 47
4.15 Pull distribution obtained under a pion hypothesis 48
4.16 Fraction of the total energy deposited in each block 52
4.17 Block energy in cluster with and without associated tracks 53
4.18 Number of blocks in cluster with and without associated tracks 54
4.19 Energy distribution of cluster with and without associated track 54
4.20 Illustration of the iteration procedure for the Find Photon algorithm 55
4.21 Determination of the y_{cut} value for cluster without associated tracks 57
4.22 Resolution of reconstructed Photons 58
4.23 Energy of reconstructed photons 59
4.24 Invariant two-photon mass 60
4.25 Energy distribution of reconstructed neutral pions 60
4.26 Number of reconstructed neutral pions 61
4.27 Event display of τ decays involving neutral kaons. 62
4.28 Illustration of selection quantities in $\mathrm{K^0_S}$ decays. 63
4.29 Variables used in the $\mathrm{K^0_S}$ selection 64
4.30 Result of the $\mathrm{K^0_S}$ selection 65
4.31 Comparison of the invariant mass spectra 67
4.32 Comparison between old and new Monte Carlo spectra 68

5.1 Event display of typical τ decay 73
5.2 The pion weight W_π for 1-prong τ decays 77
5.3 Variables used in the $\tau^- \to \mathrm{K}^-\pi^0\nu_\tau$ selection 77
5.4 Variables used in the $\tau^- \to \mathrm{K}^0\pi^-\nu_\tau$ selection 78
5.5 Variables used in the $\tau^- \to \mathrm{K}^-\pi^+\pi^-\nu_\tau$ selection 78

5.6 Variables used in the $\tau^- \rightarrow \mathrm{K}^-\pi^+\pi^-\nu_\tau$ selection . . . 79
5.7 Invariant mass spectra of the four-meson final states . . . 80
5.8 Invariant mass spectra of the two meson final states . . . 81
5.9 Invariant mass spectra of the three meson final states . . . 81

6.1 Illustration of the unfolding procedure . . . 87
6.2 Test of the iteration procedure . . . 88
6.3 Subsample test for the two meson final states . . . 90
6.4 Subsample test for the three meson final states . . . 91
6.5 Unfolded spectra and correlation matrices . . . 92

7.1 Comparison of the branching ratio measurements for $\tau^- \rightarrow \mathrm{K}^-\pi^0\nu_\tau$ and $\tau^- \rightarrow \mathrm{K}^-\pi^+\pi^-\nu_\tau$. 96
7.2 The strangeness spectral function as determined from Monte Carlo . . . 97
7.3 The spectral function from strange τ decays . . . 98
7.4 Experimental results for R_τ . . . 101
7.5 Comparison of the values for δR_τ^{kl} . . . 102
7.6 Running of the strange quark mass m_s . . . 108
7.7 Comparison of m_s measurements at $\mu^2 = 4\,\mathrm{GeV}^2$ . . . 111

LIST OF TABLES

1.1 The Standard Model of particle physics . . . 10

2.1 Resonances involved in τ decays with open strangeness . . . 16

4.1 Corrections applied to the energy loss measurement . . . 37
4.2 Parameters of the optimized pulse shape . . . 41
4.3 Parameters for the cross talk correction . . . 42
4.4 Result of the fit to the residuals . . . 47
4.5 Table of coefficients for the parametrization of the shower shape . . . 52
4.6 Selection of the pairing algorithms . . . 56
4.7 Summary of the non-τ background Monte Carlo samples . . . 69

5.1 Overview of all channels with net strangeness . . . 71

7.1 Quantities used in the fit for the branching fractions . . . 94
7.2 Individual contributions to the systematic uncertainty of the branching fraction measurements 94
7.3 Result of the spectral function analysis . . . 99
7.4 Spectral moments obtained from non-strange hadronic τ decays . . . 102
7.5 The spectral moments for $kl = \{00, 10, 11, 12, 13, 20, 21, 30, 40\}$ . . . 103
7.6 Numerical values for the perturbative QCD series of dimension-2 ($\Delta_{kl}^{(2)}$) and dimension-4 (Q_{kl}) 105
7.7 Summary of the m_s measurement . . . 106
7.8 The strange quark mass using different moments . . . 106

9.2 Updated parametrizations of the 3 meson final states . . . 121

BIBLIOGRAPHY

[1] M. L. Perl *et al.*, Phys. Rev. Lett. **35**, (1975) 1489.

[2] M. L. Perl *et al.*, Phys. Lett. **B70**, (1977) 487.

[3] J. E. Augustin *et al.*, Phys. Rev. Lett. **34**, (1975) 233; G. J. Feldman and M. L. Perl, Phys. Repl. **190**, (1975) 233.

[4] J. Burmester *et al.*, Phys. Lett. **B68**, (1977) 297; J. Burmester *et al.*, Phys. Lett. **B68**, (1977) 301.

[5] R. Brandelik *et al.*, Phys. Lett. **B70**, (1977) 125.

[6] E. Braaten, S. Narison and A. Pich, Nucl. Phys. **B373**, 581 (1992).

[7] E. Braaten, Phys. Rev. Lett. **60** (1988) 1606.

[8] E. Braaten, Phys. Rev. **D39** (1989) 1458.

[9] S. Narison and A. Pich, Phys. Lett. **B211** (1988) 183.

[10] F. Le Diberder and A. Pich, Phys. Lett. **B286** (1992) 147.

[11] F. Le Diberder and A. Pich, Phys. Lett. **B289** (1992) 165.

[12] A. A. Pivovarov, Z. Phys. C **53** (1992) 461 [Sov. J. Nucl. Phys. **54** (1991 YAFIA,54,1114.1991) 676].

[13] L.E. Adam and K.G. Chetyrkin, Phys. Lett. **B 329**, (1994) 129.

[14] L.V. Lanin, V.P. Spiridonov, and K.G. Chetyrkin, Sov. J. Nucl. Phys. **44**, (1986) 892.

[15] K. G. Chetyrkin, J. H. Kuhn and A. A. Pivovarov, Nucl. Phys. B **533** (1998) 473.

[16] K.G. Chetyrkin and A. Kwiatkowski , Z. Phys. **C 59** (1993) 525.

[17] K.G. Chetyrkin , Phys. Lett. **B 390** (1997) 309.

[18] K.G. Chetyrkin and J.H. Kuhn, Phys. Lett. **B 406** (1997) 102.

[19] K. Maltman, Phys. Rev. **D 58** (1998) 093015.

[20] A. Pich and J. Prades, JHEP **9910** (1999) 004.

[21] K. Maltman, eConf **C0209101** (2002) WE05.

[22] see for example A. Pich, 'QCD predictions for the tau hadronic width: Determination of $\alpha_s(m_\tau)$' in *Proceedings of the 2nd Workshop on Tau Lepton Physics*, edited by K. K. Ghan, Columbus, Ohio, 1992.

[23] H. Leutwlyer, in Proc. of the NATO Advanced Study Institute on Masses of Fundamental Particles (Cargese, 1996), M. Levy, J. Illiopoulos, R. Gastmans, and J.-M. Gerard (eds), NATO ASI Series B:Physics, Vol. 363 (Plenum Press, New York, 1997),p.149 [hep-ph/9609467].

[24] J. Gasser and H. Leutwyler, Nucl. Phys. **B 250**, (1985) 465; Ann. Phys. (NY) **158** (1984) 142.

[25] J. Bijnens, J. Prades, and E. de Rafael, Phys. Lett. **B348** (1995) 226, J. Prades, Nucl. Phys. (Proc. Suppl.) **B 64** (1998) 253.

[26] A. Pich and J. Prades ,JHEP **9806** (1998) 013; J. Prades and A. Pich, Nucl. Phys. B (Proc. Suppl.) **74** (1999) 309; J. Prades, Nucl. Phys. B (Proc. Suppl.) **76** (1999) 341.

[27] J. A. M. Vermaseren, S. A. Larin and T. van Ritbergen, Phys. Lett. B **405**, (1997) 327.

[28] V. P. Spiridonov and K. G.hetyrkin, Sov. J. Nucl. Phys., **47**, (1988) 522; S. G. Gorishny, A. L. Kataev, and S. A. Larin, Phys. Lett., **B 259**, (1991) 144.

[29] L. -E. Adam and K. G. Chetyrkin, Phys. Lett. **B 329**, (1994) 129; L. V. Lanin, V. P. Spiridonov, and K. G. Chetyrkin, Sov. J. Nucl. Phys. **44**, (1986) 892; M. Jamin and M. Münz, Z. Physik **C 60**, (1993) 569; M. Jamin and M. Münz, Z. Physik **C 66**, (1995) 633; D. J. Broadhurst and S. C. Generalis, Phys. Lett. **B 165**, (1985) 175; S. C. Generalis and D. J. Broadhurst, Phys. Lett. **B 139**, (1984) 85; W. Hubschmid and S. Mallik, Nucl. Phys. **B 207**, (1982) 29; S. C. Generalis, J. Phys. **G 16**, (1990) 367.

[30] D. J. Broadhurst and S. C. Generalis, Phys. Lett. **B 165**, (1985) 175.

[31] W. Marciano and A. Sirlin, Phys. Rev. Lett. **61** (1988) 1815; Phys. Rev. Lett. **56** (1986) 22.

[32] Y. Tsai , Phys. Rev. **D4**, (1971) 2821.

[33] E. Braaten and C.S. Li, Phys. Rev. **D42** (1990) 3888.

[34] H. Leutwlyer, hep-ph/9609467.

[35] M. A. Shifman, A. I. Vainshtein, and V. I. Zakharov, Nucl. Phys. **B147** (1979) 385.

[36] M. A. Shifman, A. I. Vainshtein, and V. I. Zakharov, Nucl. Phys. **B147** (1979) 448.

[37] M. A. Shifman, A. I. Vainshtein, and V. I. Zakharov, Nucl. Phys. **B147** (1979) 519.

[38] K. G. Wilson, Phys. Rev **179** (1969) 1499.

[39] OPAL Collaboration, R. Akers et al., Phys. Lett. **B328** (1994) 207.

[40] OPAL Collaboration, K. Ackerstaff *et al.*, Eur. Phys. J. **C7**, (1999) 571.

[41] ALEPH Collaboration, R. Barate *et al.*, Eur. Phys. J. **C4**, (1998) 409.

[42] CLEO Collaboration, T. Coan *et al.*, Phys. Lett. **B356**, (1995) 580.

[43] OPAL Collaboration, G. Abbiendi *et al.*, Eur. Phys. J. **C13**, (2000) 197.

[44] OPAL Collaboration, K. Ahmet *et al.*, Nucl. Instr. and Meth. **A 305** (1991) 275.

[45] M. G. Vincter and A. Astbury and R.K. Keeler and R. Sobie, A Study of Electromagnetic Shower Profiles in EB,TN 174, University of Victoria , 1993.

[46] H. Hillemanns and W. Krenz and D. Schmitz, Fast Simulation of Electromagnetic Showers in a Homogeneous Crystal Calorimeter, Technical Report 12, RWTH Aachen, December 1993

[47] P. Mättig, OPAL Internal Note **TN324** (1995).

[48] H.A. Bethe, Handbuch der Physik 24/1, J.Springer Verlag, Berlin (1933) 491.

[49] E. Fermi, Phys. Rev. Lett. **57** (1940) 485.

[50] D. Jeanne *et al.*, Nucl. Instr. and Meth. 111 (1973) 287.

[51] M. Hauschild *et al.*, Nucl. Inst. Meth. **A314**, (1992) 74.

[52] H. Breuker *et al.*, Nucl. Instrum. Meth. A **260**, (1987) 329.

[53] M. Hauschild, Nucl. Instrum. Meth. A **379**, (1996) 436.

[54] S. Bethke, Z. Kunszt, D.E. Soper and W.J. Stirling: Nucl. Phys. **B370** (1992) 310, erratum ibid. **B523** (1998) 681.

[55] W. R. Nelson *et al.* , Phys. Rev. **149** (1966) 201; G. Bathow *et al.*, Nucl. Phys. **B20** (1970) 592.

[56] G. A. Akopdjanov *et al.*, Nucl. Instrum. Meth. **140** (1977) 441.

[57] K. Hagiwara et al., Phys. Rev. D 66, 010001 (2002).

[58] A. Hocker and V. Kartvelishvili, Nucl. Instrum. Meth. A **372** (1996) 469 [arXiv:hep-ph/9509307].

[59] V. Blobel, arXiv:hep-ex/0208022.

[60] G. D'Agostini, 'A multidimensional Unfolding Method Based on Bayes Theorem' DESY 94-099 (1994)

[61] M. G. Vincter, A. Astbury, R. Keeler, and R. Sobie, A Study of Electromagnetic Shower Profiles in EB, TN 174, University of Victoria, 1993.

[62] S. Weinberg, Phys. Rev. **112**, (1958) 1375.

[63] S. Chen, M. Davier, E. Gamiz, A. Hocker, A. Pich and J. Prades, Eur. Phys. J. C **22**, (2001) 31.

[64] OPAL Collaboration ,G. Abbiendi *et al.*, Eur. Phys. J. C **13**, (2000) 197.

[65] CLEO Collaboration, R. A. Briere *et al.*, Phys. Rev. Lett. **90**, (2003) 181802.

[66] CLEO Collaboration, M. Bishai *et al.*, Phys. Rev. Lett. **82**, (1999) 281

[67] ALEPH Collaboration, R. Barate *et al.*, Eur. Phys. J. C **1**, (1998) 65.

[68] E. Gamiz et al., **JHEP 0301** 060.

[69] K. Maltman, J. Kambor, Phys. Rev., **D65** 074013.

[70] S. Chen et al., EPJ, **C22** 31.

[71] J.G. Koerner, F. Krajewski, A.A. Pivovarov, EPJ, **C20** 259.

[72] R. Barate et al. (ALEPH Collab.), EPJ, **C11** (1998) 599.

[73] K. Maltman, Phys. Lett., **B462** 195.

[74] S. Narison, Phys. Lett., **B466** 345.

[75] A. Pich, J. Prades JHEP 9910 004.

[76] C.A. Dominguez, L. Pirovano, K. Schilcher, Phys. Lett., **B425** 193.

[77] M. Finkemeier and E. Mirkes, Z. Phys. C **69**, (1996) 243.

[78] M. Finkemeier, J. H. Kühn and E. Mirkes, Nucl. Phys. Proc. Suppl. **55C**, (1997) 169.

[79] J. Allison et al., Nucl. Instrum. Methods **A317**, (1992) 47.

[80] S. Jadach, B.F.L. Ward, and Z. Wąs, Comp. Phys. Comm. **79**, (1994) 503.

[81] S. Jadach, Z. Wąs, R. Decker, and J.H. Kühn, Comp. Phys. Comm. **76**, (1993) 361.

[82] T. Sjöstrand, Comp. Phys. Comm. **82**, (1994) 74.

[83] S. Jadach, W. Placzek and B. F. Ward, Phys. Lett. B **390**, (1997) 298.

[84] R. Engel, and J. Ranft Phys. Rev. **D54**, (1996) 4244.

[85] A. Buijs, W. G. Langeveld, M. H. Lehto and D. J. Miller, Comput. Phys. Commun. **79**, (1994) 523.

[86] R. Battacharya, J. Smith, and G. Grammer, Phys. Rev. **D15**, (1977) 3267.

[87] J. Smith, J.A.M. Vermaseren, and G. Grammer, Phys. Rev. **D15**, (1977) 3280.

[88] A. Rouge, hep-ph/0303212.

[89] BES Collaboration, J.Z. Bai *et al.*, Phys. Rev. **D53**, (1996) 20.

[90] The NA48 collaboration, J. R. Batley *et al.*, Phys. Lett. **B544**, (2002) 97; NA48 collaboration, A. Lai *et al.*, Eur. Phys. J. **C22**, (2001) 231.

[91] The KTeV Collaboration, A. Alavi-Harati *et al.* Phys. Rev. **D67**, (2003) 012005; The KTeV Collaboration, A. Alavi-Harati *et al.* Phys. Rev. Lett. **83**, (1999) 22.

[92] The NA31 Collaboration, J. Burkhardt *et al.* Phys. Lett. **B206**, (1988) 169; The NA31 Collaboration, G. D. Barr *et al.* Phys. Lett. **B317**, (1993) 233.

[93] The E731 Collaboration, L. K. Gibbons *et al.* Phys. Rev. Lett. **70**, (1993) 1203.

[94] A. J. Buras and M. Jamin, arXiv:hep-ph/0306217.

[95] OPAL Collaboration, G. Abbiendi *et al.*, *Submitted to Eur.Phys.J. C*

Acknowledgments

A large number of people helped and gave me guidance during my Ph.D. studies. I would like to take the opportunity to thank all of them.

First of all, I would like to thank my supervisor Prof.Dr. Norbert Wermes. He offered me the possibility to work on this interesting subject and he gave me the opportunity to spend 18 months at CERN. Without this experience, this analysis would not have been possible. His continuous support and guidance, in particular during the last two years, made my Ph.D. studies an outstanding experience.

I'm thankful to Prof.Dr. Achim Stahl for his support and all the fruitful discussions we had, especially during our stay at CERN.

The work in the Opal Collaboration at CERN was a great experience. I would like to thank everyone for the friendly atmosphere and the numerous inspiring discussions at any day or night time. In particular, I would like to thank Dr. Michael Hauschild. With his knowledge of the Jet Chamber and his experience in energy loss measurement and detector calibration he made important contributions to this analysis. Without his support this thesis would not have been possible.

I would like to thank Thorsten Kuhl, my room-mate at CERN. His willingness to discuss any subject at almost any time was extremely helpful. I would also like to thank all the other people I had the pleasure to meet at CERN. Thank you David and Pam, Brigitte, Hagar, Dirk, Anna, Helge, Rolf, Thorsten and Jo, everyone from the famous Opal soccer team and all those I forgot to mention here.

I would like to say 'Thank you' to everyone from the Bonn High Energy Physics group (Opal, ATLAS and DØ) and everyone from SiLAB. I enjoyed very much the time here in Bonn and I will surely remember the friendly atmosphere and all the help I received.

I would like to thank the friends I met during my years of study here in Bonn. They helped me to enjoy life outside physics. Thank you Johannes and Marion, Markus, Ruth, Reinhard and Petra, Vera and many others.

And last but not least, I would like to express my gratitude to my family. They have always supported me and they encouraged me to make the most out of the opportunities without even knowing the details of my work. This thesis would not have been possible without you.

Thank you, Vielen Dank and Merçi Bien to all of you!